

# UC Berkeley

## UC Berkeley Electronic Theses and Dissertations

### Title

Modulating Condensed Phase Thermophysical and Thermochemical Transition Temperatures Using Chemical and Electrochemical Methods

### Permalink

<https://escholarship.org/uc/item/6630b2jh>

### Author

Lilley, Drew

### Publication Date

2023

Peer reviewed|Thesis/dissertation

Modulating Condensed Phase Thermophysical and Thermochemical  
Transition Temperatures Using Chemical and Electrochemical Methods

By

Drew Lilley

A dissertation submitted in partial satisfaction of the

requirements for the degree of

Doctor of Philosophy

In

Engineering – Mechanical Engineering

in the

Graduate Division

of the

University of California, Berkeley

Committee in charge:

Professor Ravi Prasher, Co-Chair

Professor Chris Dames, Co-Chair

Professor Van Carey

Professor Ahmad Omar

Spring 2023

© Copyright by

Drew Lilley

2023

## Abstract

# Modulating Condensed Phase Thermophysical and Thermochemical Transition Temperatures Using Chemical and Electrochemical Methods.

By

Drew Lilley

Doctor of Philosophy in Mechanical Engineering

Energy Science and Technology – Heat Transfer

University of California, Berkeley

Professor Ravi Prasher, Co-Chair

Professor Chris Dames, Co-Chair

Refrigeration, heat pumping, and thermal energy storage will play a critical role in decarbonizing the residential and industrial sectors. Refrigeration and heat pumping are abundant but employ refrigerants with high global warming potential. Thermal energy storage can provide low cost solutions for load-shifting and demand side flexibility to enable a more renewable grid, but implementation in the real world has been slowed by economic barriers. Thus, shifting to new heating and cooling technologies with zero global warming potential and connecting those technologies to affordable thermal storage solutions is an important step toward carbon neutrality. This thesis takes a critical look at the fundamental principles governing thermal energy storage from the material level up to the system level, specifically focusing on the solid to liquid phase transition. Both equilibrium material properties and non-equilibrium material behavior are treated in relation to their applications in thermal energy storage systems. In addition, we analyze up and coming thermal storage technologies, such as thermochemical reaction-based storage, wherein we demonstrate design rules, equilibrium, and non-equilibrium stability criteria for hydration/dehydration based storage, along with a novel liquid-solubilized reactant storage. Finally, we show how fundamental understanding of the solid to liquid transition leads to insight on phase stabilization, from which we develop the ionocaloric effect. We then show how we can embed the ionocaloric effect in various thermodynamic cycles, and demonstrate how a novel, condensed-phase and zero global warming potential heat pumping cycle emerges.

This dissertation is dedicated to my beloved family

## Table of Contents

<b>Chapter 1.</b>	<b><i>Introduction .....</i></b>	<b><i>1</i></b>
<b>Chapter 2.</b>	<b><i>Description of the Equilibrium Thermodynamics of Solid/Liquid Transition .....</i></b>	<b><i>5</i></b>
<b>Chapter 2.</b>	<b><i>Defining an upperbound on solid/liquid transition enthalpy.....</i></b>	<b><i>27</i></b>
<b>Chapter 3.</b>	<b><i>Modeling of metastability in the condensed phase.....</i></b>	<b><i>54</i></b>
<b>Chapter 4.</b>	<b><i>Manipulation of thermochemistry for enhanced thermal fluids and pumpable thermal energy storage .....</i></b>	<b><i>83</i></b>
<b>Chapter 5.</b>	<b><i>Nonequilibrium stabilization of Thermochemical Energy Materials during Hydration/Dehydration .....</i></b>	<b><i>96</i></b>
<b>Chapter 6.</b>	<b><i>Ionocaloric Refrigeration.....</i></b>	<b><i>111</i></b>
<b>Chapter 7.</b>	<b><i>Final Thoughts .....</i></b>	<b><i>175</i></b>

## List of Figures

Figure 2.1 Dynamics in liquids. (a) Profile of a potential experienced by a test particle in a liquid at different times, taken from molecular dynamics simulations(31). The equilibrium position (zero derivative of the potential) changes with time, indicating a changing center of oscillation. (b) The implications of a changing center of oscillation on the mechanical model of an atom in a liquid. (a) Reproduced with permission from J. Chem. Phys. **101**, 693 (1994). Copyright 1994 Journal of Chemical Physics .....8

Figure 2.2: (a) Predicted vs experimental liquid entropy at melt. The solid red line represents equivalence and the dashed lines represent 10% error. In order of increasing experimental entropy entropy, the dots represent Li, Ga, Na, Hg, Al, Mg, In, K, Zn, Cu, Rb, Ag, Si, Cs, Pb, and Au. (b) Predicted vs experimental entropy of fusion using equation 3. The blue asterisks denote exact predictions using liquid Debye frequencies from (41, 42). The black circles represent approximate predictions where the liquid and solid Debye frequencies were evaluated at their respective densities. In order of increasing predicted enthalpy of fusion, the dots represent Li, K, Cs, Na, Rb, In, Pb, Ag, Cu, Mg, Hg, Au, Zn, and Al. The solid red line is the 45o line, and the dashed lines represent 10% error..... 10

Figure 2.3: Theory and experimental entropies of various monatomic liquids versus temperature. Experimental entropy values were taken from Selected Values of the Thermodynamic Properties of the Elements[18] at a pressure of 1 atm. Solid lines represent theory, whereas dots represent experimental data. .... 12

Figure 2.4: Predicted vs experimental entropy of vaporization. The solid red line is the 45o line, and the dashed lines indicate 10% error. The black dashed horizontal line shows Trouton’s Rule. In order of increasing predicted entropy, the dots represent Ga, Sn, Pb, In, Cs, Rb, Hg, Na, and K. .... 13

Figure 2.5:A comparison of the predicted heat capacity at constant pressure and constant volume to experimental data using equation 4 in the main text. .... 16

Figure 2.6:Predicted enthalpy of fusion vs. experimental data..... 19

Figure 2.1 Phase Space for changing spring constant .....37

Figure 2.2 Phase space for changing mass ..... 37

Figure 2.3. Physical constraints on atom during phase transition.....39

Figure 2.4 LJ Potential – Visualization of parameters.....43

Figure 2.5 Heat Map of optimized enthalpy of fusion per unit volume vs temperature and atomic mass.....48

Figure 2.6 Heat map of optimized enthalpy of fusion per unit mass vs atomic mass .....49

Figure 2.7 Final optimization result for enthalpy of fusion per unit volume.....52

Figure 3.1 Differences in experimental conditions for lab-scale and system-scale PCMs that affect the degree of supercooling ( $\theta_s$ ) of a PCM. (a) A schematic of PCM sample contained in a pan for lab-scale DSC analysis. The volume ( $V$ ) of a PCM sample for DSC is typically less than 100  $\mu\text{L}$ , which makes the Biot number ( $Bi$ ) less than 0.1 and the temperature ( $T$ ) distribution of the PCM spatially uniform. (b) A schematic of PCM-embedded building envelopes. PCMs in system-scale applications such as buildings, on the other hand, typically have much larger volume that results in  $Bi$  much higher than 0.1 and spatially non-uniform temperature distribution of the PCM. Color gradients in the schematic represents the non-uniform temperature distribution. (c) The literature data of  $\theta_s$  of  $\text{MgCl}_2 \cdot 6\text{H}_2\text{O}$  as a function of volume. Generally,  $\theta_s$  decreases with volume; however, limited understanding of the effects of size and thermal conditions on  $\Delta T_s$  makes the relationship between the lab-scale and system-scale  $\theta_s$  unclear.....56

Figure 3.2. Discretization of a material into multiple non-homogeneous poisson distributions for metastable analysis .....60

Figure 3.3 (a) Raw DSC data for 150 cooling cycles of 10 mg of NPG at  $\beta=10^\circ\text{Cmin}$ . Each cooling curve exhibits a phenomenon known as recalescence, in which immediately after the onset of a phase transition the rate of heat released is temporarily greater than the rate of cooling, so the material heats itself up for a short time. From these curves, the distribution of supercooling temperatures is recorded. (b) shows the survivor function (magenta) discussed in Section 1, which was calculated from the distribution of supercooling temperatures given by the DSC data in (a). A 95% confidence interval using the DKW inequality is shown in blue surrounding the empirical survivor function. The solid black line shows the fitted CDF from the nucleation parameters,  $\gamma$  and  $n$  using equation 9. (c) The PDF computed from the survivor function,  $PDF_t = dCDF(t)/dt$ . (d) shows the pointwise nucleation rate (magenta) calculated using a two-point finite difference form of equation 2, and its fit (black solid line) using equation 3. Panels (b)-(d) are referred to  $T_m = 40.8^\circ\text{C}$ .....66

Figure 3.4: Experimental vs. predicted supercooling temperatures (relative to  $T_m$ ) for NPG at different volumes and cooling rates for the uniform temperature distribution approximation. The black dots represent the experimental averages and the vertical lines their standard deviations, all for an experimental cooling rate of  $\beta=0.1^\circ\text{Cmin}$ . The shaded blue region and the dashed blue lines represent the average predicted supercooling temperatures from equation 10a for a cooling rate of  $0.1^\circ\text{Cmin}$ , bounded by one predicted standard deviation, using  $\gamma = 4.2 * 10^{-33}$  and  $n = 35.87$  determined from Fig. 2, The red point is another experiment using a faster cooling rate of  $101^\circ\text{Cmin}$ . .....67

Figure 3.5: Experimental setup to test the general non-lumped theory of Section 4. NPG (blue) was cast into cylinders of varying lengths and diameters, but constant volume. The cylinders were suspended between two foam insulation columns such that the end faces were insulated. Heat transfer is in the radial direction (red arrows) during these cooling experiments.....68

Figure 3.6: Experimental (points) vs predicted (lines) supercooling times for NPG at fixed volume with varying aspect ratio (unitless). See figure 3 for schematic of the experiment. The black points represent the experimental averages and their standard deviations on the vertical. The solid blue

line represents the predicted supercooling times from equations 5-8 using  $\gamma = 4.2 * 10^{-33}$  and  $n = 35.87$ . The blue shaded zone represents  $\pm 1$  standard deviation from equation 8. The gray dashed and dotted lines show predictions for lumped convective and lumped constant cooling cases, and are included to highlight the importance of taking into account temperature gradients (non-lumped) to correctly predict the supercooling behavior of a system..... 70

Figure 3.7 Statistical distributions of  $\theta_s$  and nucleation rates of  $MgCl_2 \cdot 6H_2O$  and decanoic acid obtained by DSC analysis. (a) Survival function and (b) probability distribution function of  $MgCl_2 \cdot 6H_2O$  as a function of  $\theta_s$ . Sample 1 (blue) and Sample 2 (red) have the same  $\beta$  of  $10 \text{ }^\circ\text{C}/\text{min}$  but different  $m$  of 1.4 and 19.8 mg, respectively. In contrast, Sample 2 (red) and Sample 3 (yellow) have the same  $m$  of 19.8 mg but different  $\beta$  of 10 and  $1 \text{ }^\circ\text{C}/\text{min}$ , respectively.  $\theta_s$  distributions of three samples show that  $\theta_s$  decreased with the increase of  $m$  and decrease of  $\beta$ . Data points are experimental data. Solid lines show the fitting results of the experimental data with the power law function of  $J_V$ . (c) Volume-specific nucleation rate  $J_V$  of  $MgCl_2 \cdot 6H_2O$  calculated from the survival function. Fitting (black solid line) of all experimental data with the power law  $J_V \theta_s = \gamma \theta_s^n$  results in  $\gamma = 3.17 \times 10^{-10} \text{ }^\circ\text{C}^{-n} \text{min}^{-1} \text{m}^{-3}$  and  $n = 12.38$ . (d) Survival function and (e) probability distribution function of decanoic acid. Sample 1 (blue), Sample 2 (red), and Sample 3 (yellow) have  $m$  of 0.99, 11.82, and 11.82 mg and  $\beta$  of 10, 10, and  $1 \text{ }^\circ\text{C}/\text{min}$ , respectively. While the decrease of  $\theta_s$  from Sample 2 to Sample 3 by the decrease of  $\beta$  is not as apparent as  $MgCl_2 \cdot 6H_2O$ , a similar decreasing trend of  $\theta_s$  was found with the increase of  $m$ . (f)  $J_V$  of decanoic acid calculated from the survival function. The black solid line shows the power-law fit of experimental data with  $\gamma = 4.85 \times 10^4 \text{ }^\circ\text{C}^{-n} \text{min}^{-1} \text{m}^{-3}$  and  $n = 6.44$ . ..... 72

Figure 3.8: Prediction of  $\theta_s$  for lumped thermal capacitance cases. (a) Experimental setup to measure  $\theta_s$  values of large but lumped thermal capacitance samples. An Alodine<sup>®</sup>-coated aluminum tubing was filled with  $MgCl_2 \cdot 6H_2O$  and vertically hung in an oven. Tubing dimensions were chosen to make sure the  $Bi$  of  $MgCl_2 \cdot 6H_2O$  in the tubing is less than 0.1. Two different  $m$  (265.7 and 1776 mg) and  $\beta$  (8 and  $0.1 \text{ }^\circ\text{C}/\text{min}$ ) were tested. Four thermocouples were attached to the outer wall to detect the phase change. (b) Experimental results of  $\theta_s$  values (y-axis) measured for large samples in an oven (squares) as well as DSC samples (circles) compared with our prediction (x-axis). A black solid line indicates the equivalence of experiments and prediction. Grey dashed lines show the  $\pm 20\%$  deviation range. Error bars for prediction were evaluated based on the DKW analysis (further details in Section III of Supplemental Information). Error bars for experimental data are standard deviations of measurements. (c) Contour maps of average and (d) standard deviation of  $\theta_s$  as a function of  $V$  and  $\beta$  in log-log scale. Both the average and standard deviation follow the scaling relationship with  $V$  and  $\beta$  as  $\sim V^{-1n+1}$  and  $\sim \beta^{1n+1}$ . ..... 74

Figure 3.9: Prediction of  $\tau_{avg}$  and experimental validation for a PCM ( $MgCl_2 \cdot 6H_2O$ ) with non-uniform temperature distribution. (a) A PCM-embedded plate-fin heat exchanger. The heat exchanger is made of aluminum with  $\approx 50$ -nm-thick Parylene C covering the entire surface to protect from corrosion. Four thermocouples were inserted into the fins to measure the temperature change. (b) A schematic of heating-cooling cycle experiments. During heating, the PCM melts and the whole device thermalizes at  $130 \text{ }^\circ\text{C}$  in an oven; then, the device was cooled at room temperature by natural convection for nucleation. (c) A temperature profile of a heating-cooling cycle measured by embedded thermocouples. The red shadow region between 45 and

67 min shows the phase transition from solid to liquid at the melting temperature, and the yellow shadow region around 228 min shows the temperature spike due to the freezing. (d) A COMSOL simulation of temperature distribution in the PCM after 354 sec of cooling from the initial temperature of 130 °C. (3) A PDF of nucleation calculated from COMSOL simulation. The  $t_{avg}$  for nucleation was calculated as 354.3 sec with the  $t_{std}$  of 18.1 sec. (f) Comparison of experimental data of the first cooling experiment with our prediction. Four lines show the temperature profile measured by thermocouples. The freezing point (temperature spike) at 358 sec shows an excellent agreement with our prediction of 354.3 sec.....76

**Figure 4.1:** The heat capacity of a heat transfer fluid is enhanced by adding reactants that absorb energy when heated and release energy when cooled. (a) shows the physical mechanism of the enhancement in which the reactants break weak covalent bonds to form a rigid ring (b) depicts the thermodynamic effect on the heat capacity where the transition enthalpy is distributed over a large temperature range as a result of equilibrium between the reactants and products. (c) shows how the heat transfer fluid behaves at the system level, absorbing extra energy from the heat source by breaking the ring structure of the reaction product, and subsequently transferring extra energy to the heat sink by re-forming the ring structure. ....85

Figure 4.2 a) Effective heat capacity of 3.5M maleic anhydride and 2-methylfuran in DMF (solid blue) compared to the heat capacities of common thermal fluids (water, ethylene glycol, propylene glycol, mineral oil, and pure DMF). The blue shaded region indicates the enhancement provided by the chemical reaction taking place between the maleic anhydride and 2-methylfuran. (b) Viscosity of the 3.5M mixture over shear rates 20-600 1/s showing a Newtonian response. We include water, mineral oil, ethylene glycol, and propylene glycol data for comparison.....87

**Figure 4.3** (a) NMR data (triangles) showing the concentration vs time of the maleic anhydride and 2-methylfuran isothermal reaction at 26°C. The solid lines indicate the predictions given by Eq. SI.1 using inputs determined from density functional theory calculations. (b-d) DSC measurements of 2M, 3M, and 3.5M mixtures. The blue solid line indicates the first measurement, and the red solid line shows the performance after 10 heating and cooling cycles. The black dashed line shows the predicted heat capacity using equation 1 (see Methods) and the green dashed line shows the predicted equilibrium heat capacity from previous work<sup>17</sup>. The thermodynamic inputs were determined from density functional theory calculations. ....89

**Figure 4.4:** Viscosity of DMF with respect to concentration of diels alder reactants. As can be seen, the increase is approximately linear with reactant concentration .....93

Figure 5.1 (a) Energy density comparison between various thermal energy storage materials including phase change materials (PCM), water-based adsorption and absorption thermochemical materials (TCM). (b) Illustration for use of TCMs in buildings and charge-discharge cycle of salt hydrates where the salt hydrates can be dehydrated using the energy generated through solar power and then rehydrated at night with outside humid air or a humidifier. (c) SEM image and illustration of the change in salt hydrate (SrCl<sub>2</sub>.6H<sub>2</sub>O) morphology and size during cycling.....97

Figure 5.2. (a) Model along with experimental data on the critical particle size of salt hydrates. Two set of material constant values were taken to represent the range of mechanical and intrinsic

properties for various salt hydrates. Size distribution and SEM image for pristine (as received) to post 10 cycles of (b)  $K_2CO_3 \cdot 1.5H_2O$  (c)  $MgSO_4 \cdot 7H_2O$ , (d)  $SrCl_2 \cdot 6H_2O$ , and (e)  $Na_3PO_4 \cdot 12H_2O$ . Cycling was done between 25°C, 60% RH and 80°C, 0% RH at 1°C/min ramp rates. ....103

Figure 5.3: Dehydration and hydration behavior of  $SrCl_2 \cdot 6H_2O$  with various average starting size and ramp rates. (a) Dehydration time from  $6H_2O$  to anhydrous of as-received particles at various temperature ramp rates. (b) Dehydration time from  $6H_2O$  to anhydrous of pre-conditioned particles close to  $R_{crit}$  at various temperature ramp rates. (c) Relation between mass generation rate and ramp rates for as received and pre-conditioned particles. (d) Hydration times for pre-conditioned and as-received particles with different temperature and relative humidity conditions. (e) Hydration times for particles with different initial sizes. (f) Effect of particle size on power density. As the relative humidity and/or temperature were increased, the hydration rate for small particles increased whereas large particles lagged behind owing to slower water transport. Thus, having the salt hydrates within the critical size not only allows for increased mechanical stability but also provides more flexibility in parametric space of operations at the reactor level for both dehydration and hydration processes.....104

Figure 5.4: Gravimetric data of (a) as-received  $SrCl_2 \cdot 6H_2O$  and (b) pre-conditioned  $SrCl_2 \cdot 6H_2O$  cycled 10 times. Mass vs. time evolution of (c) as received  $SrCl_2 \cdot 6H_2O$  and (d) pre-conditioned  $SrCl_2 \cdot 6H_2O$  cycled 20 times at 1°C/min between 25°C, 60% RH and 80°C, 0% RH. Change in dehydration time for (e) as-received  $SrCl_2 \cdot 6H_2O$  and (f) pre-conditioned  $SrCl_2 \cdot 6H_2O$ . Change in hydration time for (g) as-received  $SrCl_2 \cdot 6H_2O$  and (h) pre-conditioned  $SrCl_2 \cdot 6H_2O$ .....108

Figure 6.1. Magnitude of Applied field strength needed to shift waters melting point by 10 degrees using magnetic, electric, elastic, and pressure fields.....113

Figure 6.2 Voltage modulated ion concentration fo dynamic tunability of a solid to liquid phase transition .....116

Figure 6.3: Overview of the ionocaloric cycle. (A) Schematic of the 4 steps involved in ionocaloric refrigeration (separation, crystallization, mixing, and melting). (B) T-S diagram for an ideal, reversible ionocaloric cycle. (C) The T- $\eta$  binary phase equilibria for the ethylene carbonate-sodium iodide system, along with state points corresponding to various points on the T-S diagram and schematic in (A). ....119

Figure 6.4: The ionocaloric effect of the ethylene carbonate-sodium iodide system. (A) Comparison of the maximum entropy change (per kg and L) and adiabatic temperature change of EC/NaI to the state of the art in magnetocaloric (MCE), electrocaloric (ECE), elastocaloric (eCe), and barocaloric (BCE) literature<sup>22-25</sup>, along with the applied field strengths to achieve the effect. The data shown for other caloric materials are typical values based on three criteria: (i) simultaneous measurement of entropy and adiabatic temperature change on the same system (ii) measurement taken near room temperature and (iii) reversible material changes. Detailed data sets for all other possible cases are available in references<sup>26,28,29</sup> (B) Ionocaloric entropy change for various mass fractions of NaI. (C) Directly measured adiabatic temperature change of ethylene carbonate as a function of the applied electrochemical potential (bottom axis) and mass fraction (top axis). ....121

Figure 6.5: Experimental setup and results. (A) Electrodialysis cell used for the separation process of the ionocaloric cycle. (B and C) Relative Carnot efficiency vs temperature span and relative Carnot efficiency vs cooling power per liter of the device compared against that of other elastocaloric magnetocaloric, electrocaloric, and electrochemical prototypes reported in literature <sup>15,19,20,35-40</sup> . The data shown were curated from the literature where COP, Temperature Span and Cooling power were simultaneously reported. Detailed data sets for other conditions can be obtained from <sup>29</sup> .....	124
Figure 6.6 DSC Thermograms .....	132
Figure 6.7 EC + NaI Binary Phase Equilibria .....	133
Figure 6.8: Enthalpy Path relative to reference curve.....	136
Figure 6.9 Schematic of Regenerative Ionocaloric Cycle .....	139
Figure 6.10 TS Diagram of and Ideal Regenerative Ionocaloric Cycle.....	140
Figure 6.11 Traversal of Phase Diagram for Ideal Regenerative Ionocaloric Cycle.....	141
Figure 6.12 Ideal Material COP and Carnot Efficiency for Ethylene Carbonate and Sodium Iodide System .....	145
Figure 6.13 Activity Coefficients of EC in EC + NaI mixture .....	146
Figure 6.14 Entropy vs Temperature for various NaI concentrations in EC.....	147
Figure 6.15 Electrodialysis Experimental Setup.....	149
Figure 6.16 Output of a typical electrodialysis experiment.....	152
Figure 6.17: Temperature-composition representation of a non-ideal regenerative system....	154
Figure 6.18 Comparison of Eqn. 6.47 with calorimetry data for $T_h = 36.4$ °C. ....	156
Figure 6.19 Experimental COP vs Temperature Span for various experiments operating using different concentrations.....	157
Figure 6.20 Carnot Efficiency vs Temperature Span for various experimental conditions.....	158
Figure 6.21 COP vs Cooling Power for experiments run at different concentrations .....	159
Figure 6.22 Relative Carnot Efficiency vs Cooling Power for experiments run at different concentrations.....	160
Figure 6.23 Hot Disc Experimental Setup .....	162
Figure SI.6.24 Nyquist Plot created using electrochemical impedance spectroscopy to determine the ionic conductivity of the membranes used in electrodialysis .....	163
Figure 6.25 Nyquist Plots created using electrochemical impedance spectroscopy with an H cell using Graphite Felt electrodes at various current densities.....	165
Figure 6.26 Kinetic Resistance of the Graphite Felt electrodes as a function of current density .....	166

Figure 6.27 Viscosity of Ethylene Carbonate as a function of shear rate taken at 25 degrees celsius for 1m, 1.5m and 2m concentrations .....167

Figure 6.28. Cyclic Voltammetry of Ethylene Carbonate and sodium iodide + triiodide system, showing reversible reactions.....168

Figure 7.1 Efficiency vs temperature span of vapor compression vs ionocaloric cycle .....181

## Acknowledgements

I'd first like to acknowledge my advisor Ravi Prasher and express my sincere gratitude for the incredible mentorship I received over the last 5 years. Beyond the technical and academic support, his guidance on how to identify and choose the most important and high impact problems in a given field will be invaluable for me moving forward. For the countless late night calls, key research and career guidance, and meticulous line-by-line review of every equation I've ever written, I truly thank you.

And of course, there's the whole rest of the research team I could not have done it without. Sumanjeet Kaur, I thank you for your patience with me regarding all lab matters – I know I didn't make your life any easier; Chris Dames, for the amazing support and valuable insights; Divya Chalise, Nate Weger, Alondra Perez for always bouncing ideas around in the office, and pioneering the Prasher lab PhD cohort together; Sean Lubner, Mahmoud Elzouka, Akanksha Mennon, Peiyuan Yu, Jonathan Lau, Youngsup Song, Andrew Haddad, and Lin Yang for getting me up to speed in the lab, teaching me valuable research skills, and providing mentorship and friendship on my journey. Each of you have made a huge impact on my career and life outlook, and I will be forever grateful; Chen Fang, Dion Hubble, Tianyu Zhu, Nhan Tran, Joseph Papp, and Daniel Collins for all chemistry and electrochemistry help – I truly couldn't have done my research without the help and guidance you provided, and for saving me from dying a horrible chemical death once or twice along the way.

Finally, I would like to express my deepest gratitude to my family and friends who have supported me throughout my PhD journey. Their unwavering encouragement, patience, and understanding have been indispensable to my success.

First and foremost, I would like to thank my family for their unwavering love, support, and encouragement. My mom has been my pillar of strength, providing me with emotional support and motivation to pursue my dreams. Her sacrifices and guidance have been invaluable to my success. Her dedication to my well-being and academic pursuits has been a source of inspiration and motivation. Regardless of how boring or abstract my research may have sounded, she made me feel wonderful and special and gave me nothing but encouragement and excitement, especially when I needed it most. I would also like to thank my brother for always being there for me, providing a listening ear and cheering me up during difficult times, and Mike and Jessie for creating the part of my world I will always call home. Finally, I want to extend my heartfelt thanks to my grandma for always being there for me, and I give her full credit for my interests in math, as she quizzed me on multiplication before I could even walk upright.

I am grateful to my friends who have supported me during my academic journey. Their companionship and encouragement have made this journey easier. They have been there for me during difficult times, and I am fortunate to have them in my life. Once again, I express my sincere gratitude to everyone who has supported me throughout my PhD journey. Without their love, support, and guidance, this achievement would not have been possible

## Chapter 1. Introduction

One of the central challenges of this century is mitigating and reversing anthropogenic climate change. Reducing and ultimately eliminating greenhouse gas emissions to solve this problem will necessitate decarbonizing our entire energy infrastructure. This means that regardless of the diversity of down-stream forms of energy and end-uses for that energy, all primary energy sources will need to be carbon-free. It is expected that a significant fraction of this carbon-free energy will come from renewable sources such as solar and wind energy. Unfortunately, these sources are inherently intermittent, while our energy infrastructure and economy are predicated on reliable, dispatchable, and 24/7 consistent sources of energy. This creates a considerable timing mismatch between energy supply and demand for a carbon-free future. As a consequence, it will be impossible to switch to all-renewable primary energy sources without large scale (> 100 kW), long duration (10 to 100 hours), and inexpensive (levelized cost of storage (LCOS) < \$0.05/kWh-cycle) energy storage technologies to bridge the gap between supply and demand.<sup>1</sup>

Among the many energy storage technology options, thermal energy storage (TES) is very promising as more than 90% of the world's primary energy generation is consumed or wasted as heat<sup>2</sup>. TES entails storing energy as either sensible heat through heating of a suitable material, as latent heat in a phase change material (PCM), or as the heat of a reversible chemical reaction in a thermochemical material (TCM) as shown in Figure 1. The stored energy can then be supplied directly as process heat to industrial applications and to buildings for thermal comfort<sup>3</sup> as needed, providing a steady energy output while receiving intermittent energy inputs<sup>4,5</sup>. The development of TES materials and systems was highlighted as one of the top five grand challenges for decarbonization<sup>2</sup>, and it is particularly well suited for large scale and long duration storage: TES technology is not constrained by specific geographic requirements and can be made modular and deployable to most regions. For example, TES does not require terrain with large height differentials like pumped hydro does. Furthermore, heat and non-gaseous phase change are among the safest forms of stored energy. TES does not have a catastrophic failure mode that could suddenly and destructively release all of its stored energy at once, unlike many other forms of energy storage such as high-speed flywheels, electrochemical batteries, gravitational potential energy storage, or compressed air. Finally, the additional capital cost to increase storage capacity of TES can be very low, due to the abundance of inexpensive materials such as molten silicon for high temperatures<sup>6</sup> or polymeric phase change materials for low temperatures<sup>7</sup>. Additionally, in TES most atoms comprising the storage material play a direct role in storing energy, so there is very little inactive material adding to the weight and cost. However, this can also create challenges in modeling the physics of TES systems, because all constituent parts of the (frequently messy and complex) material are participatory and therefore must be considered along with their full degrees of freedom, rather than being able to restrict analysis to smaller subcomponents that are doing all the work. Improving these TES material modeling capabilities would help provide insight that accelerates material design.

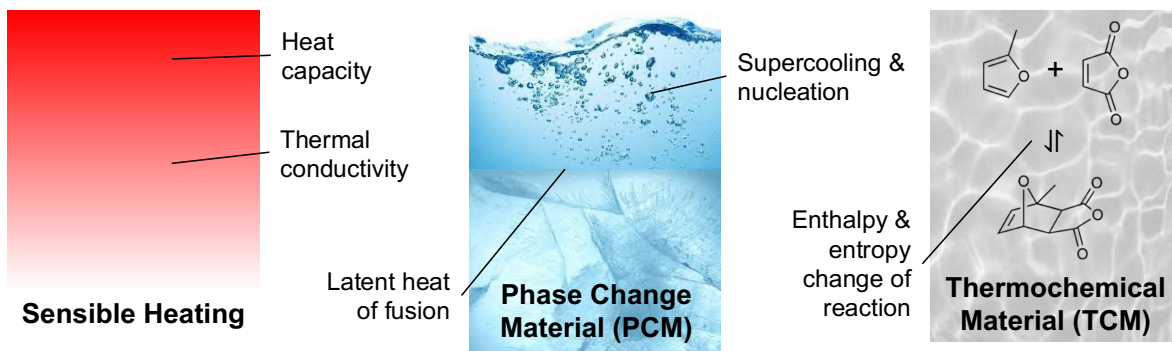


**Fig. 1.1:** Overview of different thermal energy storage materials and the key properties that require prediction and control for optimal performance over a range of applications.

Realizing large scales of integrated TES will require solving technological challenges associated with material design and thermal transport, which in turn vary with the application. For instance, industrial process heat for manufacturing requires TES at temperatures ranging from 200 – 1500 °C, solar-thermal energy harvesting typically uses molten salts at temperatures ~400 °C, while several applications such as residential and commercial building HVAC, water desalination, typical sorbent regeneration for the direct air capture of CO<sub>2</sub>, thermal management of batteries, and personal thermoregulation all require low temperatures <150 °C. Thermal energy storage materials and associated properties that govern thermal transport need to be tailored to these specific applications, which may include controlling transition temperatures, energy density (*i.e.*, heat capacity or latent heat of fusion), thermal conductivity, nucleation dynamics, and overall enthalpies and entropies of reactions (Figure 1). Efficient control of these properties first requires an understanding of their fundamental mechanisms and associated governing physics, but this is often still lacking.

While the physics of sensible heating of solids is well known with a high degree of confidence using the Debye Theory of Solids, physics of phase change and solid to liquid phase change in particular is still not a completely solved problem. One often needs to resort to computational methods such as molecular dynamics combined with density functional theory to understand the solid-liquid phase transition.

Phase Change Materials (PCM) based on solid to liquid phase transition are one of the most promising TES material for both low and high temperature applications<sup>8</sup>. Despite their potential, many fundamental and applied questions remain unanswered, such as: *(i)* how do we model and predict thermodynamic properties such as the latent heat of fusion to design new phase change materials? *(ii)* how do kinetic processes such as supercooling impact the metastability of PCMs at different length scales? And *(iii)* how do transport properties such as thermal conductivity impact the thermal power output from such a storage system?

The first half of this thesis endeavors to answer these questions.

## Design of thermal energy storage materials and systems

The storage properties of a thermal energy storage material are governed by equilibrium thermodynamics and can be represented by the Gibbs free energy:

$$\Delta G = \Delta H - T\Delta S \quad (1)$$

For a first order phase transition in PCMs, solid-liquid equilibria exists when the chemical potential of the liquid phase is equal to that of the solid phase such that  $\Delta\mu_{L\rightarrow S} = 0$ , yielding the relation  $\Delta H_{fus} = T_m\Delta S_{fus}$ , where  $\Delta S$  is the change in entropy between the solid and liquid phases. The melting temperature,  $T_m$  dictates the range of temperatures that the PCM can operate effectively at, while the enthalpy of phase change (latent heat of fusion,  $\Delta H_{fus}$ ) is a measure of the energy storage density of the PCM as shown in Figure 2. Selecting the right material requires knowing two of these three terms; entropy change is challenging to accurately predict owing to multiple entropy contributions associated with the melting process (*e.g.*, vibrational, configurational, mixing, intra-molecular dynamics, etc.). As a result, thermodynamic properties of storage materials are experimentally determined using various thermophysical characterization techniques -  $\Delta H_{fus}$  is typically measured using differential scanning calorimetry, and  $T_m$  is based on the application. The full suite of experimental techniques required to sufficiently characterize the equilibrium properties for TES applications is time-consuming and often expensive. Thus, the development of simple analytical models to down-select materials with promising thermophysical properties is needed.

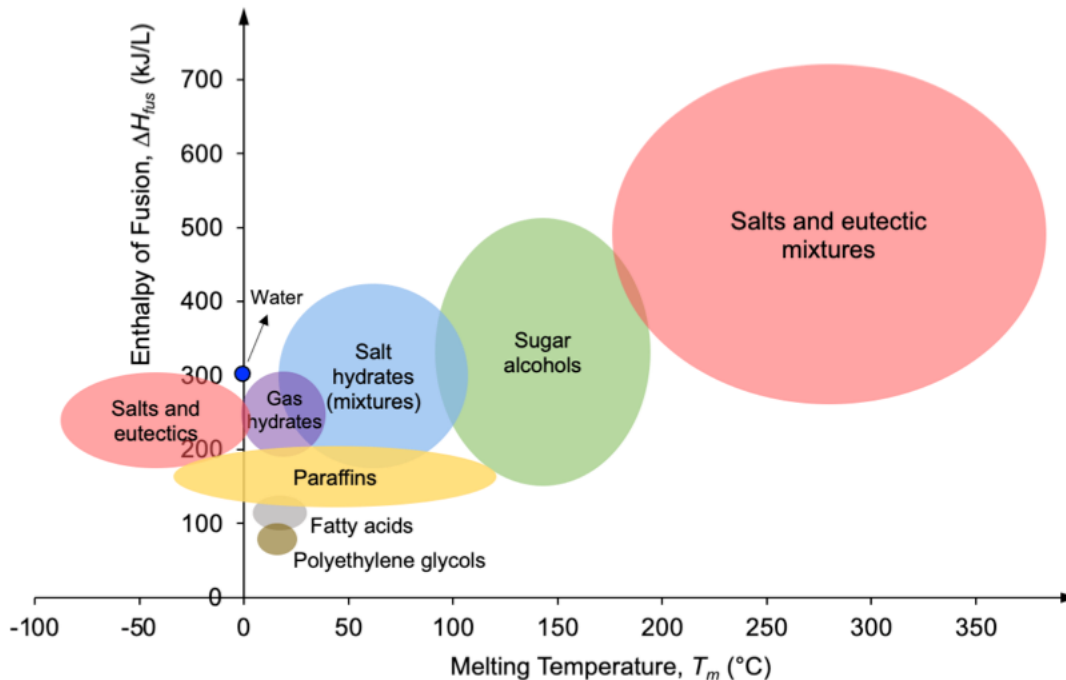


**Fig. 2.2:** Melting temperature and Enthalpy of Fusion of various PCM-based thermal energy storage materials, adapted from references [9-11].

While latent heat of fusion, heat capacity, density, and other equilibrium thermophysical properties are critical for material selection, it is the non-equilibrium properties that drive the system-level design and determine the overall TES performance. Among the various non-equilibrium properties

relevant to phase change materials, thermal conductivity and supercooling are the most important. Thermal conductivity determines the thermal energy charge/discharge rate or the power output, in addition to the storage system architecture and boundary conditions. Most high-energy density PCMs have correspondingly low thermal conductivities and – by design – high heat capacities, resulting in exceptionally low thermal diffusivities. For thermal reservoir type applications, moving the heat in and out can therefore be particularly challenging while keeping capital costs of heat exchangers low. This tradeoff has recently been analyzed using thermal Ragone plots to optimize the design<sup>9</sup>. Low thermal conductivity can be addressed by techniques such as the addition of nanoparticles and the impregnation of PCM into graphite matrices or other composite architectures. However, approaches to reduce supercooling by using either nucleating or thickening agents have met with limited and unreliable success. If unanticipated supercooling persists in PCM applications, the system may never nucleate the solid state, and the system utilization factor decreases to zero. Conversely, if the TES system is overdesigned, an unnecessary temperature bias may be introduced, which reduces the storage round-trip efficiency.

In the first half of this thesis, I highlight different physics-based models that describe equilibrium thermodynamic properties of the liquid state, their implications for thermal energy storage, and identify future directions for research. I then discuss physics and statistics-based frameworks to explain metastable behavior and show that thermal transport strongly affects nonequilibrium TES performance.

The second half of this thesis focuses on manipulating the phase transition of phase change materials in a novel condensed-phase refrigeration cycle that utilizes what we call the ionocaloric effect to enable simultaneous thermal energy storage and thermal energy generation.

#### References:

- <sup>1</sup> P. Albertus, J.S. Manser, and S. Litzelman, *Joule* **4**, 21 (2020).
- <sup>2</sup> A. Henry, R. Prasher, and A. Majumdar, *Nat. Energy* **5**, 635 (2020).
- <sup>3</sup> C. Booten, P. Rao, V. Rapp, R. Jackson, and R. Prasher, *Joule* **5**, 24 (2021).
- <sup>4</sup> B.A. Babb and M.K. Pruetz, *Fam. Court Rev.* **57**, 459 (2019).
- <sup>5</sup> C.W. Forsberg, D.C. Stack, D. Curtis, G. Haratyk, and N.A. Sepulveda, *Electr. J.* **30**, 42 (2017).
- <sup>6</sup> C. Amy, H.R. Seyf, M.A. Steiner, D.J. Friedman, and A. Henry, *Energy Environ. Sci.* **12**, 334 (2019).
- <sup>7</sup> P. Khomein, A. Nallapaneni, J. Lau, D. Lilley, C. Zhu, S. Kaur, R. Prasher, and G. Liu, *Sol. Energy Mater. Sol. Cells* **225**, 111030 (2021).
- <sup>8</sup> D. Zhou, C.Y. Zhao, and Y. Tian, *Appl. Energy* **92**, 593 (2012).
- <sup>9</sup> J. Woods, A. Mahvi, A. Goyal, E. Kozubal, A. Odukomaiya, and R. Jackson, *Nat. Energy* **6**, 295 (2021).

## Chapter 2. Description of the Equilibrium Thermodynamics of Solid/Liquid Transition

### The Challenge:

For solid-liquid phase change materials (*e.g.*, ice and paraffin wax) or pumpable sensible storage (*e.g.*, hot water and molten salts), the thermodynamic properties of liquids are paramount in the modeling of these TES systems. Valuable insights into these properties can be made by simple physical models describing the equilibrium solid and liquid states that are important for thermal storage. These models offer selection rules and help reduce the number of experiments needed for full thermodynamic characterization.

To predict the melting point of a material, the enthalpy and entropy of both the solid and liquid phases must be known. Historically, quantifying the absolute value of the enthalpy and entropy of the liquid phase independent of the solid phase has been challenging. Consequently, simple melting “rules” formulated from experimental observation have been popular. The Lindemann melting criterion(1–3) is perhaps the most widely used melting rule, and it states that melting occurs when the root mean amplitude of vibration exceeds a threshold value in relation to the nearest neighbor distance (originally stated to be 10%). At melt, all atoms vibrate at the Einstein frequency so the equipartition theorem can be used to equate the amplitude of vibration to the temperature, yielding  $T_m = \frac{4\pi^2 m c_l a^2}{k_b}$ , where  $m$  is the atomic mass,  $c_l$  is the Lindemann constant, and  $a$  is the nearest neighbor distance. The Lindemann constant changes with crystal structure, and the Lindemann melting rule provides only modest agreement with experimentally recorded melting points. There have been many sophisticated attempts to improve upon the Lindemann rule, but to date there is no universally successful model for melting. Moreover, the exact mechanism responsible for the lattice instability that drives the transition to the liquid state remains a mystery, and no self-consistent solid-state model predicts it.

Historically, a general approach to calculating the thermodynamic properties of liquids has been a long-standing problem in condensed matter physics(4). The solid-state is partially to blame. Phase equilibria is built right into statistical mechanics, and the complete and correct partition function of a system should have the phase-change behavior encoded into the equations, such that as you traverse an extensive-thermodynamic path, an instability in the equations causes a discontinuity in the free energy curve (i.e phase transition). This is partially what makes the van der Waals theory of liquids/gasses so attractive: It describes both the liquid (near vapor) and gas phases. From a specific assumption about molecular interactions, a single partition function leads directly to the liquid-vapor phase transition. However, in almost all other cases first-order phase equilibria are more easily studied by adopting different models for each phase and finding the conditions under which the separate models yield equilibrium among the phases. For the solid-liquid transition, this must be done. A major failure of crystal thermodynamics / solid-state theory is that it cannot predict melting. In general, this is blamed on the inability to handle anharmonicity near melting, which is believed to provide the instability driving the discontinuity in the free energy curve.

### Previous Attempts

Although no solid-state model exhibits explicit solid-liquid equilibria like the Van der Waals equation of state does for the liquid-gas transition, they do describe the solid-state thermodynamic properties reasonably well. Specifically, the Einstein and Debye models provide an excellent balance between accuracy and ease-of-use. However, a major failure of crystal thermodynamics theory is that it cannot predict melting. This is attributed to the inability to handle anharmonicity near melting, which is believed to cause instability that drives the discontinuity in the free energy curve. As mentioned, the Debye model and/or its variants are adequate to describe the solid phase, but a robust mechanical model to describe the liquid phase has been elusive. In fact, a general approach to calculate the thermodynamic properties of liquids has been a long-standing problem in condensed matter physics(4). On the fundamental side, the Vibration-Transit (VT) model(5–10) elucidates much of the fundamental statistical mechanics underlying liquid phenomena, but application of this model requires sophisticated Molecular Dynamics (MD) simulations with high-fidelity interatomic potentials of the system. Wallace formulated the VT theory by building upon Stillinger and Weber's work(11–14) on the multi-atomic potential energy surface. By building upon their concept of inherent structures, Wallace re-casts the configurational partition function into the product of partition functions of independent liquid "structures"(8, 15). Each "structure" has a distinct contribution to the partition function and therefore the system thermodynamics, and the degeneracy of that structure provides the appropriate weighting function. The degeneracy, or the number of random structures per given energy level, is an unknown parameter. Only detailed MD simulations – whereby the system is repeatedly quenched, and the energy levels calculated and "binned" – can determine the number of random structures existing at each energy level. However, Wallace did find that for simple monatomic liquids, the average degeneracy was well-defined, and the standard deviation of that value is relatively small(8).

Less fundamental but more easily applied and quantitatively fairly accurate, Eyring developed a purely analytical model(16–19) that provides a quantitative description of the liquid state. Qualitatively, Eyring assumes that a liquid has a mixture of solid-like and gas-like characteristics such that it supports both conventional solid-like phonon transport and gas-like ballistic transport. The model assumes that any atoms next to a vacancy behave as gas-like, and then uses the vacancy concentration along with atom-coordination number to determine the fraction of gas-like atoms in the liquid. Once this fraction is established, Eyring employs what is essentially an interpolation between solid and liquid partition functions, weighted by the "gas-like" fraction; the percentage of gas-like particles is a fitting parameter, and it is phenomenological. Although this model provides an excellent fit for many liquids, it has little predictive power for TES applications because there is no way to know the fraction of gas-like molecules that will appear a priori. Eyring's work has, however, been extended by Henry Frank(20–22) in his formulation of a free volume theory to describe entropy changes upon isothermal expansions (e.g. phase transitions). Although its focus is mainly on the liquid to vapor transition, for which free volume theory has many merits and has seen much success, it can also be applied to the solid-liquid phase transition. To use it in the condensed state, details of crystal structure and bonding are necessary, along with the density change upon melting. If these are known, the free volume theory can be used to estimate the entropy of fusion, and in addition, it can be used to evaluate Eyring's fraction of "gas-like" molecules, enabling quantitative prediction of the rest of the liquid's thermodynamic functions vs temperature and volume.

Both Eyring and Wallace's models lean on phonon theory to describe microscopic dynamics. Modern molecular dynamics approaches, such as the instantaneous normal mode theory(23) and the two-phase thermodynamic model(24), are consonant with the phonon picture. The instantaneous mode theory employs lattice dynamics at short time scales to resolve the eigen frequencies governing the lattice dynamics. Real frequencies correspond to normal, solid-like modes, and imaginary frequencies signal instability whereby the lattice will re-arrange. This picture is closely related to Wallace's vibration-transit view of liquid dynamics. The two-phase model abides much more closely to Eyring's microscopic view; in the two phase-model, a fourier-transform of a particle's velocity autocorrelation function yields the liquids density of states, which they decompose into a solid-like part and a gas-like part, just as Eyring did in his analytical model. Both approaches are useful in extracting thermodynamic properties for molecular dynamics simulations but are quite complex to implement.

### **My Attempt**

Lacking a simple model without fitting parameters, scientists and engineers have traditionally looked towards empirical rules to estimate thermodynamic properties in the liquid phase. Empirical rules, such as Richard's rule of melting(25), Lindemann's melting criteria, and Trouton's rule of vaporization(26), are practical rules of thumb, but they lack the fine-ness to offer design or selection rules for TES. In my recent work(27), I proposed a simple model for the entropy of melting of monatomic liquids, which – when combined with the Debye model for the solid phase – can be used to predict the entropy and enthalpy of fusion without fitting parameters. Furthermore, this model – under the appropriate limits – recovers Richard's rule of melting. The simple, physics-based model considers a particle's liquid phase dynamics in a rough potential energy surface. The dynamics of a particle in the liquid state include (i) lattice vibrations, which are solid-like, except they generally exhibit anharmonicity due to large displacements from meta-stable equilibrium; (ii) large scale diffusion, which is gas like and describes the hopping motion of the atom from one lattice cage to another as described by Frenkel (4); and (iii) small scale diffusion corresponding to movement within a local lattice cage and without significant or lasting change to neighbor atoms.

First, we'll take a high-level view of the atomistic dynamics; the lattice vibrations are well-described by the conventional Debye model, and large-scale diffusion can generally be ignored at the melting point for elements with high viscosity upon melting(28, 29). Due to small-scale diffusion, the center of oscillation of the traditional lattice-like vibrations changes(30, 31), as shown in Figure 2.1. This changing center of oscillation is a consequence of the complex, time-dependent nature of the atom's multi-atomic potential energy surface, so employing traditional lattice dynamics methods to resolve these effects on particle motion is impractical(32). However, molecular dynamics simulations have shown that the changing center of oscillation occurs at a frequency similar to the lattice vibrations, and that they are often oscillatory in nature.

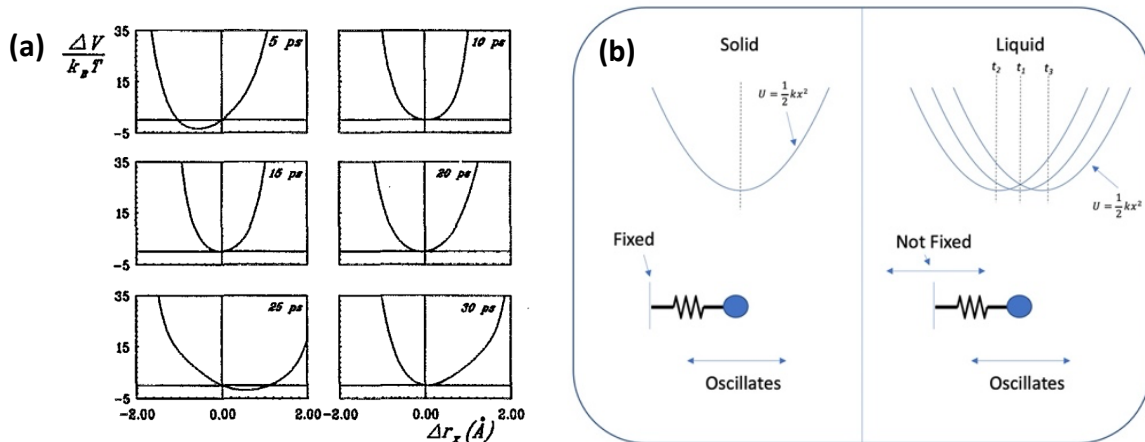


Figure 2.1 Dynamics in liquids. (a) Profile of a potential experienced by a test particle in a liquid at different times, taken from molecular dynamics simulations(31). The equilibrium position (zero derivative of the potential) changes with time, indicating a changing center of oscillation. (b) The implications of a changing center of oscillation on the mechanical model of an atom in a liquid. (a) Reproduced with permission from J. Chem. Phys. **101**, 693 (1994). Copyright 1994 Journal of Chemical Physics

In this analysis we'll systematically go through each dynamic component and make simplifying assumptions to resolve a coarse-grained dynamical description of an atom in a liquid state.

We begin the analysis by considering the solid-like local vibrations of a particle about its instantaneous equilibrium point for times less than the Maxwell relaxation time ( $t < \tau_m$ ). In general, liquid particles vibrate in a potential well described by both harmonic and higher order (anharmonic) terms that act to soften the spring constant at larger displacements. The anharmonicity associated with lattice vibrations in liquids is not well understood, but it has been shown that it can be neglected for calculating the total entropy near melting(29) , so for now we will assume the particle vibrates in a harmonic potential. Anharmonicity is later included as a correction factor for  $T > T_m$  where  $T_m$  is the melting temperature.

To demonstrate the significant need for the harmonic assumption, we can attempt to evaluate the spring constant associated with an interatomic interaction between two atoms, where the first atom is oscillating at high amplitudes and we include anharmonic contributions to its potential energy, and the other atom is oscillating at small amplitudes, where we assume its potential energy is completely harmonic. We note that if we assume that both are anharmonic, the problem quickly becomes intractable.

We begin by defining  $y_1$  as the displacement of the point connecting the linear spring and the nonlinear spring, and  $y_2$  as the displacement of the end of the nonlinear spring. From this, we can construct the system's lagrangian:

$$\mathcal{L} = T - V \tag{2.1}$$

where T refers to the system's kinetic energy and V refers to the systems potential energy. In the linear spring system, these are defined as:

$$T = \frac{1}{2} m \dot{y}_2^2(t) \quad 2.2$$

$$V = \frac{1}{2} k_1 y_1(t)^2 + \frac{1}{2} k_2 (y_2(t) - y_1(t))^2 - k_8 (y_2(t) - y_1(t))^8 \quad 2.3$$

where we have chosen an 8th order anharmonic term for this exercise. This yields two coupled equations of motion:

$$k_1 y_1(t) - k_2 (y_2(t) - y_1(t)) + 8k_8 (y_2(t) - y_1(t))^7 \quad 2.4$$

$$k_2 (y_2(t) - y_1(t)) - 8k_8 (-y_1(t) + y_2(t))^6 + m \ddot{y}_2(t) \quad 2.5$$

Using the change of variables,  $v(t) = y_2(t) - y_1(t)$ , and solving the system we get

$$v''(t) = \left\{ \frac{8k_1 k_8 v(t)^7}{M(k_1 + k_2 - 56k_8 v(t)^6)} - \frac{k_1 k_2 v(t)}{M(k_1 + k_2 - 56k_8 v(t)^6)} + \frac{336k_8 v(t)^5 v'(t)^2}{k_1 + k_2 - 56k_8 v(t)^6} \right\} \quad 2.6$$

Which can be integrated with respect to v(t) to get the systems potential:

$$U(v) = ((-7)^{\frac{2}{3}} k_1 (k_1 - 6k_2) (\log(-2\sqrt[3]{-7^3 k_8^3 \sqrt{k_1 + k_2}} (tv)^2 + (k_1 + k_2)^{2/3} + 2\sqrt{3} (1 - \frac{4\sqrt[3]{-7^3 k_8} (tv)^2}{\sqrt[3]{k_1 + k_2}})) + 4(-7)^{2/3} k_8^{2/3} (tv)^4) - 2(\log(\sqrt[3]{k_1 + k_2} + 2\sqrt[3]{-7^3 k_8} (tv)^2)) + \frac{1}{\sqrt{3} \tan} \quad 2.7$$

$$* \frac{1}{\sqrt[3]{k_8} (k_1 + k_2)^{2/3}}$$

As can be seen, obtaining a simple spring constant from even the simplest of anharmonic interatomic interactions is already incredibly complex. **Thus, without the harmonic assumption, there is very little analytical operating space.**

Next, we address the large-scale, slow diffusion by describing the hopping motion of the atom from one lattice cage to another, resulting in a large and lasting change in the atoms neighbor list. The hopping rate is described by the Maxwell relaxation time (4) (also known as the Frenkel frequency),  $\omega_F(T) = \frac{G}{\eta(T)}$ , where  $G$  is the high strain rate shear modulus and  $\eta(T)$  is the temperature-dependent shear viscosity (33). At  $T_m$ , the viscosity of metallic liquids is very high; under these conditions, the hopping frequency is small compared to the Debye frequency,  $\omega_D$ , and has been shown to be on the order of  $\frac{\omega_D}{10}$  or less(4, 33, 34). Thus, at  $T_m$ , we assume the dynamics are dominated by small-scale *fast* diffusion and lattice-like vibrations and we neglect large-scale diffusion in our model. We emphasize that for liquids with  $\omega_D \approx \omega_F$  at melt, this assumption fails, as is the case for noble gasses where density changes are large upon melt(33). When  $T > T_m$ , large-scale diffusion will be accounted for using the phonon theory of liquids.

Finally, we consider small-scale, fast diffusion, or the hopping of small energy barriers ( $< k_B T$ ) corresponding to the particles' changing center of oscillation (30, 31, 35). The particle's equation of motion can be written as  $m\ddot{x}_p = -k\nabla U$  and expanded such that  $m\ddot{x}_p = -k(x_p(t) - x_o(t))$  where  $x_p(t)$  describes the position of the particle, and  $x_o(t)$  describes the time-dependent position of the center of the particle's potential well. Describing the particle coordinate with respect to its displacement from the center of oscillation ( $\Delta x$ ),  $x_p(t) = x_o(t) + \Delta x(t)$ , the equation of motion

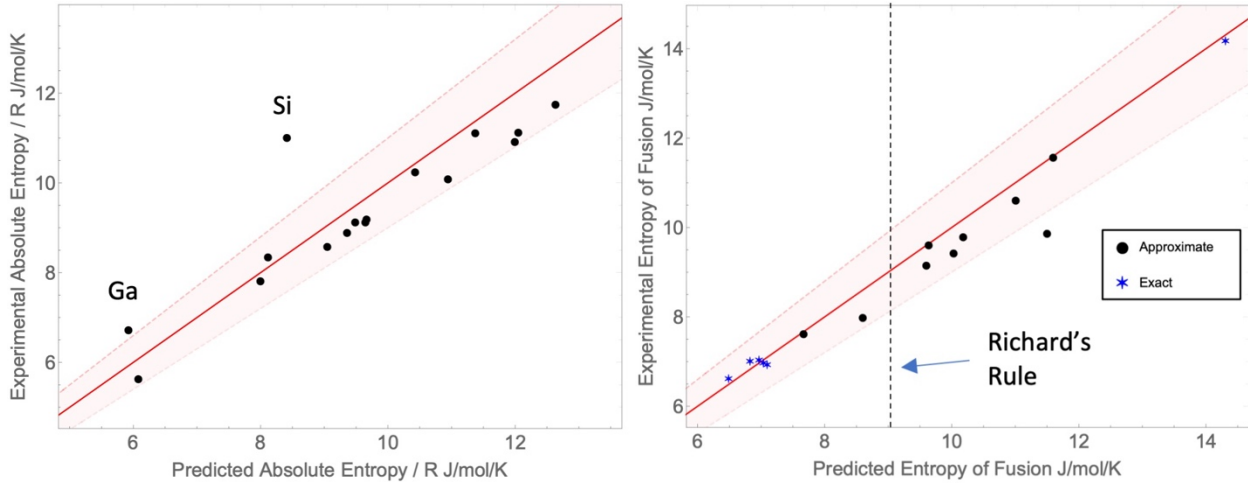


Figure 2.2: (a) Predicted vs experimental liquid entropy at melt. The solid red line represents equivalence and the dashed lines represent 10% error. In order of increasing experimental entropy entropy, the dots represent Li, Ga, Na, Hg, Al, Mg, In, K, Zn, Cu, Rb, Ag, Si, Cs, Pb, and Au. (b) Predicted vs experimental entropy of fusion using equation 3. The blue asterisks denote exact predictions using liquid Debye frequencies from (41, 42). The black circles represent approximate predictions where the liquid and solid Debye frequencies were evaluated at their respective densities. In order of increasing predicted enthalpy of fusion, the dots represent Li, K, Cs, Na, Rb, In, Pb, Ag, Cu, Mg, Hg, Au, Zn, and Al. The solid red line is the 45° line, and the dashed lines represent 10% error.

becomes  $m(\ddot{x}_o + \Delta\ddot{x}) = -k\Delta x(t)$ . Small-scale fast diffusion is responsible for changing  $x_o$ , giving it its time dependence (30, 31, 35).

The particle undergoes simple harmonic motion about its center of oscillation, so a harmonic trial solution is chosen such that  $\Delta x(t) = Ae^{i\omega_{eff}t}$ . The trial solution of  $x_o(t)$  is more nuanced; molecular dynamics simulations have demonstrated that the center of oscillation also oscillates(30, 31, 35) with similar amplitude to the particle's vibration. The hopping of small barriers that give rise to this oscillation does not significantly alter the character of the system configuration. Indeed, Rabani et al.(36) were unable to distinguish between the small-scale diffusion and solid-like vibrations when observing the decay of neighbor list correlation functions. Provided that the small-scale diffusion energy barriers are small, they thus lumped these mechanisms together, both being local perturbations occurring within the domain of a particular particle's local minima. Our model is motivated by MDS that have shown rapid re-crossing of these small barriers on time scales associated with lattice vibrations. In these simulations, a particle's neighbor list correlation function returns to its initial state after  $t \approx \frac{2\pi}{\omega_D}$  (30, 36, 37), thus we choose  $x_o(t) = Ae^{i\omega_{eff}t}$  as an ansatz. Plugging this into the equation of motion yields  $m(A + A)\omega_{eff}^2 = k(A)$ . *We note that  $k$ , the intermolecular spring constant, is governed by the nature of the intermolecular bond and is therefore fixed. The frequency of the oscillation then becomes*

$$\omega_{eff} = \frac{1}{\sqrt{2}} \sqrt{\frac{k}{m}} = \frac{1}{\sqrt{2}} \omega_D^L \quad 2.8$$

Where  $\omega_D^L$  is the Debye frequency characterizing the atomic vibration in the liquid phase. We remark that this result is equivalent to putting two springs with spring constants corresponding to the Debye frequency in series. Thus, we argue that the dynamics of the particle near melting can be simplified by modeling the small-scale diffusive translational motion as a harmonic spring in series with harmonic lattice-like vibration.

We note that Girifalco(38), after analyzing root mean square vibrational amplitudes in simple metals and fitting to Eyring's Liquid model, also concludes empirically that the effective liquid Debye temperature is  $\frac{\omega_{L,Tm}}{\sqrt{2}}$  under the approximation that  $\omega_l = \omega_s$ , confirming that equation 2.8 also works with Eyring's model.

Using the Debye model, we can calculate the entropy associated with the effective Debye frequency at melt as  $S_{Tm} = 4RD \left( \frac{\theta_{D,eff}}{Tm} \right) - 3R \ln \left( 1 - e^{-\frac{\theta_{D,eff}}{Tm}} \right)$ , where  $\theta_{D,eff}$  is the effective

Debye temperature corresponding to  $\omega_{eff}$  in Eq. 2.8 and  $D$  is the Debye function. We emphasize that the Debye model is used for its simplicity, and note that the Debye approximation is a simplification of the real density of states of monatomic liquids, which in reality exhibits a much flatter transverse phonon dispersion for small wavevectors at high temperatures (39). Because we are modeling the liquid state, we can use the high temperature Debye expansion to obtain the entropy of the liquid at melt:

$$S_{T_m} = 4R + 3R \ln \left( \frac{k_b T_m}{\hbar \omega_{eff}} \right) \quad 2.9$$

A comparison of the entropy at melt (equation 2.9 with  $\omega_{eff}$  from equation 2.8) to experimental data from Selected Values of the Thermodynamic Properties of the Elements (40) for 16 monatomic liquids is plotted in Figure 2.3. Debye temperatures evaluated at the crystal melt and density were taken from (29), and we observe that with just this single input property equation 2 predicts entropy at melt to within 10% of experimental values for 14 of the 16 liquids. The notable

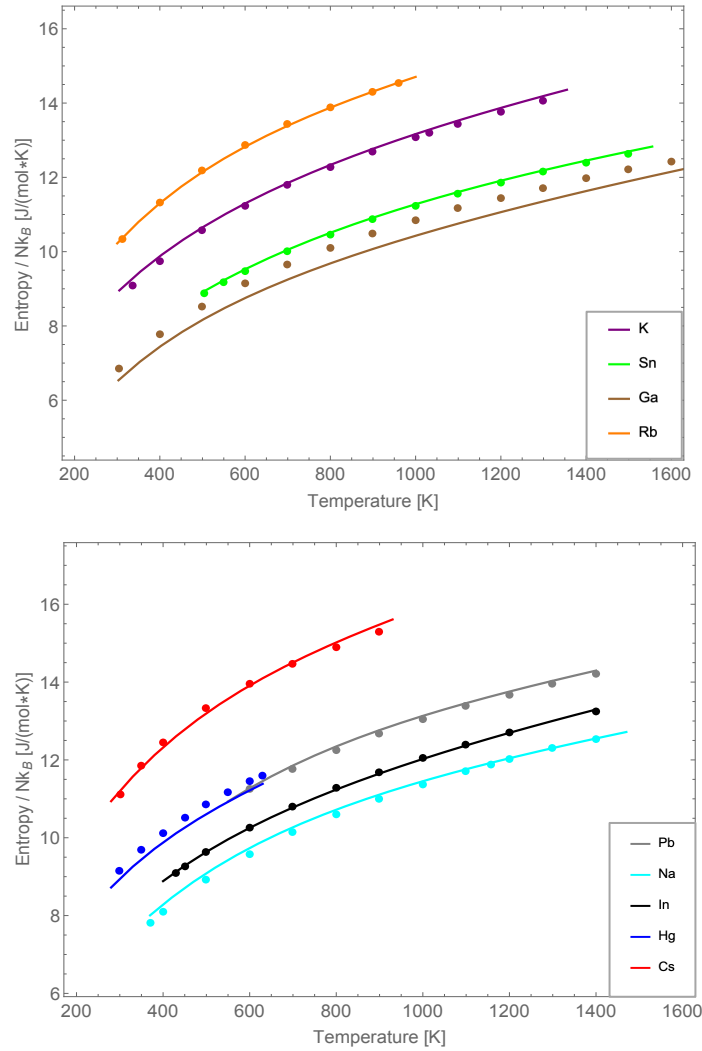


Figure 2.3: Theory and experimental entropies of various monatomic liquids versus temperature. Experimental entropy values were taken from Selected Values of the Thermodynamic Properties of the Elements[18] at a pressure of 1 atm. Solid lines represent theory, whereas dots represent experimental data.

outliers are silicon and gallium. Wallace identifies silicon, as well as Ge, Bi, Ga, and Sb, as “anomalous melting” elements because they are shown to undergo significant change in electronic structure from crystal to liquid (8, 29), which impacts the Debye frequency and our model does not account for this.

In addition, equation 2.9 can be combined with the Debye model for crystals to calculate the entropy and enthalpy of fusion:

$$\Delta S_M = 3R \ln \left( \frac{\omega_{D,T_m}^S}{\omega_{eff}^L} \right) = 3R \ln \left( \frac{\sqrt{2} \omega_{D,T_m}^S}{\omega_{D,T_m}^L} \right) \quad 2.10$$

where  $\omega_{D,T_m}^S$  is the Debye frequency in the solid state and  $\omega_{D,T_m}^L$  is the Debye frequency in the liquid state at melt. It has been shown (41)) that for many metals  $\omega_{D,T_m}^L \approx \omega_{D,T_m}^S$ . In this case, equation 3 reduces to  $\Delta S \approx 1.1R$  which is the empirical value used in Richard’s Melting Rule(25).

The true value for  $\Delta S$  of metals ranges from 0.8R-1.5R. Equation 2.10 converges to a single value (1.1R) when we assume  $\omega_{D,T_m}^L \approx \omega_{D,T_m}^S$ . In reality,  $\omega_{D,T_m}^L$  differs from that  $\omega_{D,T_m}^S$  because of the density changes on melt, and the nature of the liquid dynamics change from that of the solid. The true liquid Debye frequencies for Ar, Cs, Rb, K, Li, and Na were determined in (41, 42), and were used to evaluate equation 2.10 without approximation. Figure 2.2 compares the exact predictions

of equation 2.10 with experimental values (identified by blue asterisks), The exact predictions give a root mean squared error of 1.64%, showing excellent agreement with experimental entropy of fusion values. When the exact value of  $\omega_{D,T_m}^L$  is not available, equation 2.10 can be evaluated using the quasiharmonic phonon approximation, whereby the change in Debye frequency can be related to the change in density from the solid to the liquid state. For small density changes, this can be approximated as  $\theta_D(\rho) \approx \theta(\rho_o) \left( \frac{\rho}{\rho_o} \right)^\gamma$ , where  $\rho_o$  is the density at which the original Debye temperature was evaluated,  $\rho$  is the density at which the new Debye temperature is to be evaluated, and  $\gamma$  is the grüneisen parameter. Debye frequencies evaluated at liquid state densities are tabulated in (41) and were used to evaluate equation 2.10. The approximate results are shown in Figure

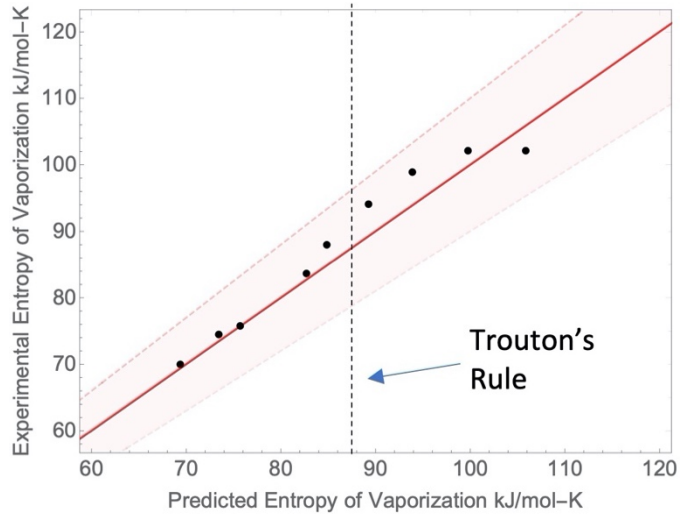


Figure 2.4: Predicted vs experimental entropy of vaporization. The solid red line is the 45° line, and the dashed lines indicate 10% error. The black dashed horizontal line shows Trouton’s Rule. In order of increasing predicted entropy, the dots represent Ga, Sn, Pb, In, Cs, Rb, Hg, Na, and K.

2.2, identified by black circles, and excluding the elements for which exact predictions were made (Ar, Cs, Rb, K, Li), the approximate predictions give an RMSE of 6.35%, compared to a 19.1% RMSE given by Richard's rule. Thus, equation 3 provides an excellent material dependent correction to Richard's rule of melting. The results for enthalpy of fusion  $\Delta H_m$ , given by  $\Delta H_M = T_M \Delta S_M$  are shown in Figure 2.6.

We note that the viscosity of Ar is low at melt such that  $\omega_{F,T_m} \approx \omega_{D,T_m}$ , so large scale diffusive dynamics should become important. However, although our model neglects the large-scale diffusion, it still predicts the entropy of fusion of Ar with less than 1% error, suggesting that the large scale diffusion does not strongly influence the entropy at melt in this case. More accurate values for  $\omega_{D,T_m}^L$ , which can be computed from Molecular Dynamics (41), are needed to test this model against a larger set of the known 0.8R-1.5R entropy jump seen in metals.

Our model for the entropy at melt does not explain thermodynamic properties at higher temperatures. To do this, one can incorporate prior models for the temperature dependent heat capacity of liquids (28, 43). To illustrate this, we use the results of Trachenko, Brazhkin, and coworkers' phonon theory of liquid thermodynamics to predict the thermodynamic properties at  $T > T_m$  under constant pressure. We must include the entropy increase due to expansion and anharmonicity, and the entropy decrease associated with the loss of transverse phonons, which account for the effect of large-scale diffusion. This can be written as  $S(T) = S_{T_m} + \int_{T_m}^T \frac{C_p}{T} dT$ , where  $C_p = 3R + C_{exp} + C_{anharmonic} - C_{loss}$ . [20] Expansion heat capacity is expressed as  $C_{exp} = MB\alpha_V^2 T$  where  $M$  is the molar volume,  $B$  is the fluid's bulk modulus and  $\alpha_V$  is the fluid's volumetric thermal expansion coefficient. The anharmonic heat capacity can be approximated as  $C_{anharmonic} = 3R\alpha_V T$ . [10,21] The heat capacity associated with the large-scale diffusion, or the loss of transverse phonons is approximated as  $C_{loss} = \frac{d}{dT} \left[ RT \left( \frac{\omega_F(T)}{\omega_D} \right)^3 \right]$ . [10] Therefore  $S(T)$  can then be written as:

$$S(T) = S_{T_m} + 3R \ln \left( \frac{T}{T_m} \right) + MB\alpha_V^2 (T - T_m) + 3R\alpha_V (T - T_m) - R \int_{T_m}^T \left\{ \frac{1}{T} \frac{d}{dT} \left[ RT \left( \frac{\omega_F(T)}{\omega_D} \right)^3 \right] \right\} dT \quad 2.11$$

with  $S_{T_m}$  from the model described in this work. The phonon loss term (final term in equation 2.11) can be approximated as  $S_{Loss}(T) = -R \left( \frac{\omega_F(T)}{\omega_D} \right)^3$  with less than 2% total error on  $S(T)$ .

*Phonon Loss term:*

According to the phonon theory of liquids by Brazhkin and Trachenko (33), the energy loss associated with the loss of transverse phonon is given by:

$$E_{loss} = -RT \left( \frac{\omega_F}{\omega_D} \right)^3 \quad 2.12$$

and the loss of heat capacity associated with  $E_{loss}$  is the temperature derivative of  $E_{loss}$ :

$$C_{loss}(T) = -R \left( \frac{\omega_F}{\omega_D} \right)^3 - 3RT \left( \frac{\omega_F}{\omega_D} \right)^2 \frac{d\omega_F}{dT} \quad 2.13$$

where  $\omega_F$  is the frenkel frequency and is given by:

$$\omega_F = \frac{G}{\eta(T)} \quad 2.14$$

and  $\eta(T)$  is the liquid viscosity which is a function of temperature. The liquid viscosity is typically modeled using the Arrhenius relation:

$$\eta(T) = Ae^{-\frac{B}{T}} \quad 2.15$$

We can estimate the entropy loss term as:

$$S(T) = \int dT' \frac{C_{loss}(T')}{T'} \quad 2.16$$

Substituting in our expression for  $C_{loss}$ , we get:

$$S_{loss} = -\frac{G^3 R \left( e^{-\frac{3B}{T}} - \text{Ei} \left( -\frac{3B}{T} \right) \right)}{A^3 \omega_D^3} + C \quad 2.17$$

We assume that large-scale diffusion is negligible, *i.e.*,  $S_{loss} = 0$  at  $T = T_m$ . Thus, C can be evaluated such that:

$$C = \frac{G^3 R \left( e^{-\frac{3B}{T_m}} - \text{Ei} \left( -\frac{3B}{T_m} \right) \right)}{A^3 \omega_D^3} \quad 2.18$$

We have also found that using  $C = 0$  provides a good approximation. The argument to both the exponential integral and the exponential functions in equation 2.18 is  $-\frac{3B}{T}$ , where B comes from

the Arrhenius function  $Ae^{-\frac{B}{T}}$ . In the Arrhenius function, the factor B is often larger than the melting temperature ( $\sim 1.5-2x$ ), so the argument near melting is  $-\frac{3B}{T_m} \approx -6$ . The ratio of the exponential integral term to the exponential term in equation 2.18 near melt is then  $\frac{Ei(-6)}{e^{-6}} \approx 0.1$ , so the exponential integral term is roughly 1/10<sup>th</sup> of the exponential term near melt. Therefore, we can ignore that term such that

$$S_{loss} = -\frac{G^3 R \left( e^{-\frac{3B}{T}} - Ei\left(-\frac{3B}{T}\right) \right)}{A^3 \omega_D^3} \approx -\frac{G^3 R \left( e^{-\frac{3B}{T}} \right)}{A^3 \omega_D^3} \approx -R \left( \frac{\omega_F}{\omega_D} \right)^3 \quad 2.19$$

As T increases, the approximation becomes less accurate, but for the 6 metals depicted in the  $C_p$  vs  $C_v$  plots in *Figure 1.5*, the largest error (at boiling point) remains less than 20% for the  $S_{loss}$  term.  $S_{loss}$  is roughly 10% of total entropy at boiling, so this approximation should produce less than a 2% error in the total entropy throughout the entire liquid domain.

All other thermodynamic properties of interest can be determined using appropriate thermodynamic relations (4).

Finally, we note that for  $S(T)$  at constant volume, the expansion term (3<sup>rd</sup> term) in Eqn. 2.11 should be neglected. Comparison of equation 2.11 to experimental entropy data as a function of temperature is plotted in *Figure 2.3*. Besides gallium, which also has a significant change in electronic structure like silicon (29), there is excellent agreement between experiment and model.

Constant pressure and constant volume heat capacities evaluated as  $C_{p,v} = T \left( \frac{\partial S}{\partial T} \right)_{v,p}$  are compared to experimental data in *Figure 2.5*

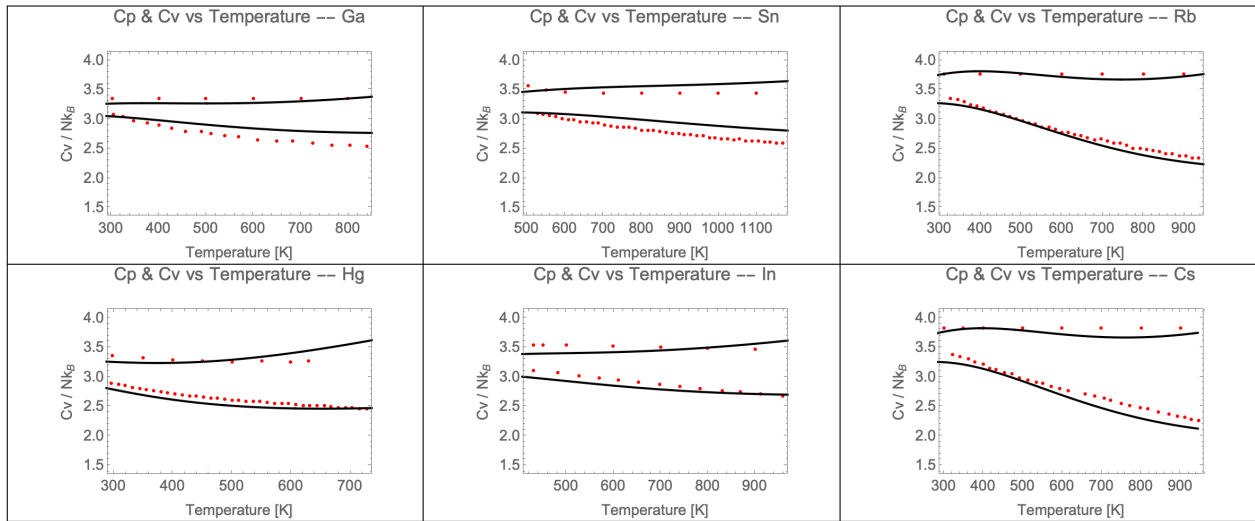


**Figure 2.5:** A comparison of the predicted heat capacity at constant pressure and constant volume to experimental data using equation 4 in the main text.

The input parameters are listed in Table 2.2. We note that the experimental shear modulus is difficult to obtain, so we calculated it as  $G = \frac{\omega_D}{\eta(T_b)}$ . We believe this is a good approximation because  $\omega_F$  approaches  $\omega_D$  as the liquid approaches its boiling point(33, 34). The viscosity at the boiling point is known, so if we assume  $\omega_F(T_b) = \omega_D$ , it becomes possible to calculate the shear modulus, assuming the shear modulus is not a strong function of temperature.

To demonstrate that the previous results are valid even near the boiling point, we compare our combined model with experimental data for the entropy of vaporization ( $\Delta S_V$ ), which is typically given by the well-known Trouton' rule (26) that states  $\Delta S_V \approx 88 \text{ J/mol-K}$ . We used experimental entropy data for the gas phase(40) and subtracted it from equation 2.11 evaluated at the boiling temperature to predict  $\Delta S_V$ , as plotted in Figure 2.4. Examination of Figure 2.4 reveals that our model predicts  $\Delta S_V$  very well (mean absolute error of 2.42 J/mol-K) whereas Trouton' rule, which is independent of material properties, gives a constant value. Thus, we have shown that equation 2.11 gives accurate thermodynamic values over the entire liquid range at atmospheric pressure.

In summary we have developed a simple analytical model to predict thermodynamic properties of monatomic liquids. It requires input of the Debye frequency in the liquid state for precise evaluation, or density-corrected Debye frequencies for approximate use. Data for  $\omega_D^L$  is rare, and future efforts in determining  $\omega_D^L$  are needed to test the model more accurately for such liquids. In addition, our model uses the Debye approximation, but future modelling efforts should focus on more realistic dispersion for transverse phonons, which in reality are far more complex (39). Our model also assumes  $\omega_F \ll \omega_D$  at melt so that large-scale diffusion is much slower than interatomic vibration, which may break down for low viscosity liquids. Moreover, we restricted our analysis to monatomic systems to isolate the thermodynamic contributions from the inter-molecular interactions, and therefore make a simpler and more meaningful comparison to our model.

However, applications usually involve multi-atomic materials; for multi-atomics, intra-molecular interactions in the liquid state are well-described using Einstein oscillators for vibrational modes and the Debye density of states for librational modes, which are the hindered rotational modes along the molecules three principle rotational axes. Intra-molecular vibrations are straightforward when the characteristic frequency, determined by the intra-molecular potential, is known. Librational modes are more nuanced - in addition to the intra-molecular potential, the nature of the librational modes depends on the molecular geometry and the lattice coordination in the liquid state at small time scales. Thus, making predictions without detailed knowledge of the molecule and lattice structure become quite complex. Future work must be done to simplify the inclusion of intra-molecular contributions in the calculation of enthalpy/entropy in the liquid state to predict the enthalpy of fusion of more complex materials.

### *Model Input Parameters*

The Debye temperatures listed in Ta of (29) were used for inputs to all equations. In Table II of [3],  $\theta_o$  is the Einstein temperature and  $\theta_2$  is the high temperature Debye temperature using the quasiharmonic phonon approximation. To determine the Debye frequency,  $\omega$ , from  $\theta_2$ , we used

the relation given in (29) to solve for  $\langle (\hbar\omega)_{BZ}^2 \rangle$  which is the average vibrational frequency in the high temperature Debye limit,  $\omega$ :

$$k_b\theta_2 = \left[ \frac{5}{3} \langle (\hbar\omega)_{BZ}^2 \rangle \right]^{\frac{1}{2}} = \omega_{D,T_m} \hbar \sqrt{\frac{5}{3}} \quad 2.20$$

In Table 2.1,  $\theta_{D,T_m} = \frac{\hbar\omega_{D,T_m}}{k_b}$  is the temperature associated with  $\omega$  calculated from  $\theta_2$  in equation 2.20.

Element	$\theta_{D,T_m}$ (K)
Li	308
Cu	244
Ag	164
Mg	246.4
Zn	186.34
Al	311.08
Cd	161
Au	141.7
Si	527.45
Ga(46)	181.6
Sn	132.44
K	78.617
Pb	71.92
Hg	81.62
Na	128.6
In	106.8
Cs	38.4
Rb	49.6
Ar	54

Table 2.1 :Tabulated Debye Temperatures

The curves for Figure 2.3 were generated by using the following parameters as inputs into equation 2.21 (33, 47, 56, 48–55):

$$S(T) = S(T_m) + 3R \ln \left( \frac{T}{T_m} \right) + M\beta\alpha^2(T - T_m) - R \left( \frac{\omega_F(T)}{\omega_D} \right)^3 + 3R\alpha(T - T_m) \quad 2.21$$

Where  $\omega_F(T) = \frac{G}{\eta(T)}$  and we fitted the viscosity curves to an Arrhenius equation,  $\eta(T) = Ae^{\frac{B}{T}}$  and the fits are listed below.

	$\beta$ (Pa)	$\alpha$	A	B	$V$ ( $\frac{m^3}{mol}$ )	G (Pa)
K	2.60E+09	2.10E-04	5.00E-04	733.00	4.57E-05	1.00E+09
Sn	3.50E+10	9.00E-05	6.92E-04	950.80	1.62E-05	2.60E+09
Ga	3.00E+10	1.30E-04	4.09E-04	487.50	1.18E-05	2.00E+09
Rb	2.00E+09	3.50E-04	9.29E-05	616.60	5.58E-05	1.91E+08
Pb	3.00E+10	1.80E-04	7.05E-04	800.00	1.83E-05	2.40E+09
Na	5.30E+09	2.60E-04	8.86E-05	761.40	2.38E-05	4.80E+08
In	3.20E+10	1.20E-04	4.34E-04	556.60	1.57E-05	1.26E+09
Hg	2.70E+10	1.80E-04	5.58E-04	304.50	1.48E-05	1.30E+09
Cs	1.40E+09	4.00E-04	1.13E-04	620.30	7.07E-05	1.73E+08

Table 2.2 Model input parameters

### Enthalpy of Fusion

The plot below shows the predictions of equation 2.10 for the entropy of fusion, multiplied by the elements' melting temperature to calculate the enthalpy of fusion.

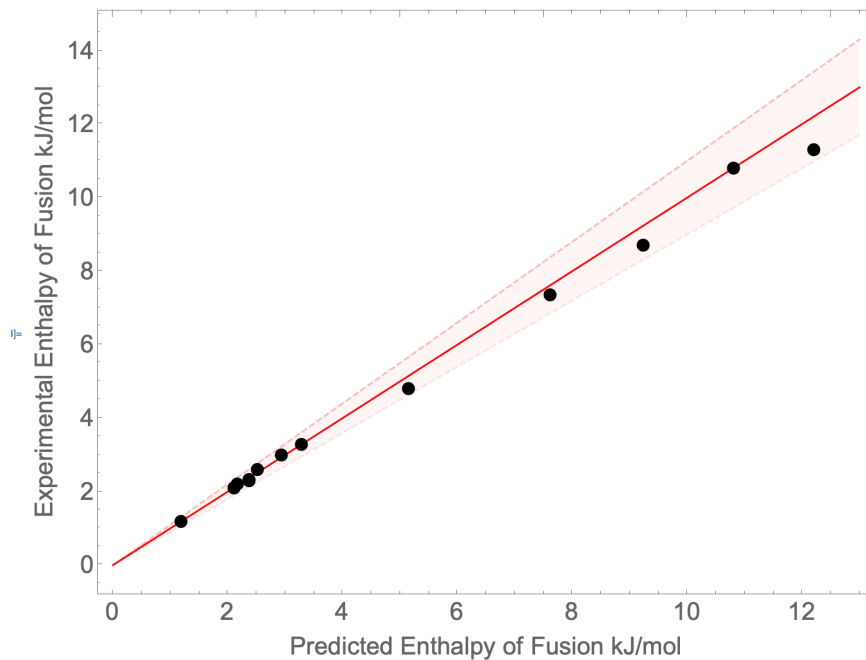


Figure 2.6: Predicted enthalpy of fusion vs. experimental data.

### Thermal conductivity of Liquids:

The thermal conductivity of liquids is difficult to describe from the microscopic picture(57). In 1964, Mclaughlin(58) reviewed 18 physics-based models that describe liquid thermal conductivity, yet none accurately capture the temperature and pressure dependent behavior over a wide range of liquids governed by different interatomic potentials. Since his review, Molecular Dynamics simulations (e.g. Modal contributions via Green-Kubo modal analysis)(59) have dominated the field, and few new analytical models have been proposed. In the solid phase, phonon gas models have been successfully applied to various types of solids(60). Most phonon gas models begin with the Boltzmann transport equation or kinetic theory and perform a modal analysis of the relevant energy carriers. In the case of non-metallic solids, the energy carriers are predominantly phonons, or quantized vibrations propagating through the lattice. In liquids, there is some debate over the appropriate quantization. Many have championed the phonon picture at short timescales(61) while recent work(34) has suggested local atomic re-arrangements, which they referred to as ananeons(62), as the more fundamental quantization in liquids. It is not yet clear how ananeons can be incorporated into traditional statistical mechanics schemes for thermodynamic predictions, which is needed before they can be evaluated as energy carriers for analyzing thermal conductivity. During the interim, perhaps insight can be gleaned from the work of Allen and Feldman(63) on the concepts of locons, propagons, and diffusions, which are responsible for thermal transport in amorphous solids. More work is needed in this direction to see if it will prove fruitful, and until then we believe the phonon picture has the most merit. For each polarization, the typical modal analysis reads like(60):

$$k = \int_0^{\infty} \frac{1}{3} C_v(\omega) v_g(\omega) \lambda(\omega) d\omega \quad 2.22$$

Where  $C_v$  is the constant volume heat capacity,  $v_g$  is the phonon group velocity, and  $\lambda$  is the mean free path of the phonon. There have been many attempts to evaluate this integral for amorphous solids, which are similar in structure to liquids in that they exhibit short-range but not long-range order. The temperature-dependent behavior of constant-volume heat capacity in liquids, however, exhibits a difficult trend to account for monatomic decrease up until the liquid-gas transition(44).

Eyring accounted for the decrease in constant-volume heat capacity with his solid-gas interpolation of the liquid state(16, 38). As the liquid increases in temperature, the fraction of gas-like molecules increases. The gas-like molecules are immune to the intermolecular potential, so when a molecule converts from solid-like to gas-like via vacancy formation, it loses its potential energy, or  $\frac{k_b}{2}$  of energy via the equipartition theorem. At the melting point when there is low vacancy formation, Eyring's equation predicts that of Dulong Petit,  $3k_b$ . At the gas transition when vacancies dominate, it predicts that of an ideal gas,  $\frac{3}{2}k_b$ . At intermediate temperatures, it uses the vacancy formation to determine the fraction of gas-like molecules, which modulates the constant-volume heat capacity between the solid and gas limits.

Wallace also accounted for the decrease in constant-volume heat capacity with his vibration-transit theory(28). By re-casting the configurational partition function into the partition function of independent structures, he argued that the integral of the partition function should no longer be from  $-\infty$  to  $\infty$ , as is customary. Instead, the structures have distinct boundaries, after which they

begin to impinge on each other. As the temperature increases and atoms vibrate with larger amplitudes, the boundaries get closer and closer so that the atom's configurational phase space becomes increasingly more restricted. Thus, in his integral of the partition function for each structure, he bounds the configurational space and thus the integrand. That bound gets smaller with temperature, and the heat capacity concomitantly decreases.

More recently, Trachenko and colleagues(33, 44, 64) have re-championed Frenkel's picture of liquid dynamics in which transverse phonons, previously believed to disappear in the liquid state, can persist so long as they are above the "Frenkel frequency", or the Maxwell relaxation time of a molecule subjected to a simple spring and damper in parallel. The spring is given by the shear modulus of the liquid, and the damper is given by the viscosity. Using this postulate, Trachenko et al. re-counted the number of phonons existing at each temperature. If each phonon contributes  $k_b$  of energy to the system, then the final energy will be equal to  $Nk_b$ , where  $N$  is the number of phonons. By assuming a Debye density of states, the number of transverse phonons having frequencies below the Frenkel frequency can be evaluated, and then subtracted from  $Nk_b$  for the energy. The kinetic energy of those atoms can be added back into the account, and the result is the total energy of the system, with its derivative giving the constant volume heat capacity. The result of this model agrees fairly well with experimental data for many simple liquids.

It is difficult to reconcile Trachenko and Wallace's model under a single physical picture; Trachenko et al. relied on a phonon-gas model, where they assume the thermodynamic functions of each phonon are independent of one another, and use traditional lattice-dynamical approaches, including the Frenkel modification, to prescribe the appropriate thermodynamic weighting to each phonon in the gas comprising the liquid. Wallace also assumes a phonon gas, but instead of employing a mechanical modification to the dynamics, as Trachenko did with the vanishing transverse phonons, he prescribes a limit on the available amplitude (and therefore volume) occupied by each phonon, imposing a restriction on the system's configurational phase space. It is unclear how the configurational restriction relates to the vanishing of transverse phonons; however, both certainly predict a decreasing constant volume heat capacity as a function of temperature in the liquid state. We note that for PCMs, Trachenko et. al's model seems more promising because it can be directly evaluated from material properties, whereas Wallace's model requires experimental fitting parameters.

To evaluate the thermal conductivity of liquids, several models must be chosen to evaluate each of the contributing terms:  $C_v(\omega, T)$ ,  $v_g(\omega)$  and  $\lambda(\omega)$ . A recent model with reasonably good predictions for a large variety of liquids relative to experiment (within 15% error for Argon, Water, Potassium Nitrate, and Sodium Nitrate) was proposed by Zhao(65) et al. In this model, Trachenko's model for  $C_v(\omega, T)$  was employed, which re-formats the modal analysis into a sum of integrals:

$$k = \int_0^{\omega_{D,Longitudinal}} \frac{1}{3} C_v(\omega) v_g(\omega) \lambda(\omega) d\omega + \int_{\omega_F}^{\omega_{D,Transverse}} \frac{2}{3} C_v(\omega) v_g(\omega) \lambda(\omega) d\omega \quad 2.23$$

The Debye model was used for the group velocity, which equates the group velocity to the speed of sound. Finally, instead of using the Cahill-Pohl model for the mean free path, they posit that dominant energy carriers are short-wavelength, high-energy modes, and that they scatter frequently so that the mean free-path can be taken as the intermolecular distance. This is perhaps their biggest assumption, and more experimental evidence is needed to resolve the mean-free path of high energy phonons in liquids. Nevertheless, predictions match experimental data fairly well, so that assumption is likely valid for the class of liquids they compared to.

## References

1. A. C. Lawson, Physics of the Lindemann melting rule. *Philos. Mag.* **89**, 1757–1770 (2009).
2. S. Sarkar, C. Jana, B. Bagchi, How universal is the Lindemann criteria in melting of Lennard-Jones polydisperse solids? *J. Chem. Sci.*, 833–840 (2017).
3. A. V Granato, D. M. Joncich, V. A. Khonik, Melting, thermal expansion, and the Lindemann rule for elemental substances. *Appl. Phys. Lett.* **97**, 12–538 (2010).
4. K. Trachenko, V. Brazhkin, Collective Modes and Thermodynamics of the liquid State. *Reports Prog. Phys.* **1**, 016502 (2016).
5. G. De Lorenzi-Venneri, E. D. Chisolm, D. C. Wallace, Vibration-transit theory of self-dynamic response in a monatomic liquid. *Phys. Rev. E - Stat. Nonlinear, Soft Matter Phys.* **78** (2008), doi:10.1103/PhysRevE.78.041205.
6. D. C. Wallace, S. Rudin, G. De Lorenzi-Venneri, T. Sjostrom, Vibrational theory for monatomic liquids. *Phys. Rev. B.* **99**, 104204 (2019).
7. T. Sjostrom, G. De Lorenzi-Venneri, D. C. Wallace, Potential energy surface of monatomic liquids. *Phys. Rev. B.* **98**, 54201 (2018).
8. D. C. Wallace, Statistical mechanics of monatomic liquids. *Phys. Rev. E - Stat. Physics, Plasmas, Fluids, Relat. Interdiscip. Top.* **55**, 4179–4186 (1997).
9. G. De Lorenzi-Venneri, D. C. Wallace, A model for transits in dynamic response theory. *J. Chem. Phys.* **123**, 244513 (2005).
10. E. E. Chisolm, B. B. Clements, D. D. Wallace, Mean-atom-trajectory model for the velocity autocorrelation function of monatomic liquids. *Phys. Rev. E - Stat. Physics, Plasmas, Fluids, Relat. Interdiscip. Top.* **63** (2001), doi:10.1103/PhysRevE.63.031204.
11. F. H. Stillinger, T. A. Weber, Hidden structure in liquids. *Phys. Rev. A.* **25**, 978–989 (1982).
12. F. H. Stillinger, T. A. Weber, Dynamics of structural transitions in liquids. *Phys. Rev. A.* **28**, 2408–2416 (1983).
13. T. F. Middleton, D. J. Wales, Energy landscapes of some model glass formers. *Phys. Rev. B - Condens. Matter Mater. Phys.* **64** (2001), doi:10.1103/PhysRevB.64.024205.
14. F. H. Stillinger, "Liquids at Thermal Equilibrium" in *Energy Landscapes, Inherent Structures, and Condensed-Matter Phenomena* (2019), pp. 134–194.
15. D. C. Wallace, Entropy of liquid metals. *Proc. R. Soc. London. Ser. A Math. Phys. Sci.* **433**, 615–630 (1991).
16. H. Eyring, D. Henderson, E. M. Eyring, B. J. Stover, *Statistical mechanics and dynamics* (Wiley, 1964).
17. J. Walter, H. Eyring, A Partition Function for Normal Liquids. *J. Chem. Phys.* **9**, 393–397 (1941).
18. J. Walter, H. Eyring, A Partition Function for Normal Liquids ARTICLES YOU MAY BE INTERESTED IN Structure and Partition Function of Liquid Water. III. Development of the Partition Function for a A Partition Function for Normal Liquids. *A Theory Liq. Struct. J. Chem. Phys.* **9**, 896 (1941).
19. D. R. McLaughlin, H. Eyring, SIGNIFICANT STRUCTURE THEORY OF MOLECULES HAVING HINDERED INTERMOLECULAR ROTATION IN THE CONDENSED PHASES. *Proc. Natl. Acad.*

- Sci.* **55**, 1031–1037 (1966).
20. H. S. Frank, Free volume and entropy in condensed systems I. General principles. Fluctuation entropy and free volume in some monatomic crystals. *J. Chem. Phys.* **13**, 478–492 (1945).
  21. H. S. Frank, Free volume and entropy in condensed systems II. Entropy of vaporization in liquids and the pictorial theory of the liquid state. *J. Chem. Phys.* **13**, 493–507 (1945).
  22. H. S. Frank, M. W. Evans, Free volume and entropy in condensed systems III. Entropy in binary liquid mixtures; Partial molal entropy in dilute solutions; Structure and thermodynamics in aqueous electrolytes. *J. Chem. Phys.* **13**, 507–532 (1945).
  23. G. Seeley, T. Keyes, Normal-mode analysis of liquid-state dynamics. *J. Chem. Phys.* **91**, 5581 (1998).
  24. S.-T. Lin, M. Blanco, W. A. G. III, The two-phase model for calculating thermodynamic properties of liquids from molecular dynamics: Validation for the phase diagram of Lennard-Jones fluids. *J. Chem. Phys.* **119**, 11792 (2003).
  25. G. P. Tiwari, Modification of richard’s rule and correlation between entropy of fusion and allotropic behaviour. *Met. Sci.* **12**, 317–320 (1978).
  26. D. W. Reager, Daniel L and Goode, Scott R and Ball, *Chemistry: principles and practice* (Cengage Learning, 2009).
  27. D. Lilley, A. Jain, R. Prasher, A simple model for the entropy of melting of monatomic liquids. *Appl. Phys. Lett.* **118**, 083902 (2021).
  28. D. C. Wallace, Liquid dynamics theory of high-temperature specific heat. *Phys. Rev. E - Stat. Physics, Plasmas, Fluids, Relat. Interdiscip. Top.* **57**, 1717–1722 (1998).
  29. D. C. Wallace, Evaluation of thermodynamic functions of elemental crystals and liquids. *Phys. Rev. E - Stat. Physics, Plasmas, Fluids, Relat. Interdiscip. Top.* **56**, 1981–1986 (1997).
  30. A. Magro, D. Frezzato, A. Polimeno, G. J. Moro, R. Chelli, R. Righini, Dynamics of liquid benzene: A cage analysis. *J. Chem. Phys.* **123**, 6851 (2005).
  31. G. J. Moro, P. L. Nordio, M. Noro, A. Polimeno, A cage model of liquids supported by molecular dynamics simulations. I. The cage variables. *J. Chem. Phys.* **101**, 693–702 (1994).
  32. K. Trachenko, V. V. Brazhkin, Collective modes and thermodynamics of the liquid state. *Reports Prog. Phys.* **79** (2015), doi:10.1088/0034-4885/79/1/016502.
  33. D. Bolmatov, V. V. Brazhkin, K. Trachenko, The phonon theory of liquid thermodynamics. *Sci. Rep.* **2**, 1–6 (2012).
  34. T. Iwashita, D. M. Nicholson, T. Egami, Elementary excitations and crossover phenomenon in liquids. *Phys. Rev. Lett.* **110**, 205504 (2013).
  35. A. Polimeno, G. J. Moro, A cage model of liquids supported by molecular dynamics simulations. II. The stochastic model. *J. Chem. Phys.* **101**, 703–712 (1994).
  36. E. Rabani, J. D. Gezelter, B. J. Berne, Calculating the hopping rate for self-diffusion on rough potential energy surfaces: Cage correlations. *J. Chem. Phys.* **107**, 6867–6876 (1997).
  37. J. D. Gezelter, E. Rabani, B. J. Berne, Calculating the hopping rate for diffusion in molecular liquids: CS<sub>2</sub>. *J. Chem. Phys.* **110**, 3444–3452 (1999).
  38. M. Luban, H. Novogrodsky, Statistical mechanics of solids. *Phys. Rev. B.* **6**, 1130–1134 (1972).

39. N. P. Kryuchkov, L. A. Mistryukova, A. V Sapelkin, V. V Brazhkin, S. O. Yurchenko, Universal effect of excitation dispersion on the heat capacity and gapped states in fluids. *Phys. Rev. Lett.* **125**, 125501 (2020).
40. K. K. Hultgren, Ralph and Desai, Pramod D and Hawkins, Donald T and Gleiser, Molly and Kelley, *Selected values of the thermodynamic properties of the elements* (1973).
41. D. C. Wallace, Liquid dynamics theory of the velocity autocorrelation function and self-diffusion. *Phys. Rev. E - Stat. Physics, Plasmas, Fluids, Relat. Interdiscip. Top.* **58**, 538–545 (1998).
42. K. N. Lad, A. Pratap, Atomic dynamics in liquid alkali metals at the melting point. *Phys. Rev. B - Condens. Matter Mater. Phys.* **73** (2006), doi:10.1103/PhysRevB.73.054204.
43. E. I. Andritsos, E. Zarkadoula, A. E. Phillips, M. T. Dove, C. J. Walker, V. V. Brazhkin, K. Trachenko, The heat capacity of matter beyond the Dulong-Petit value. *J. Phys. Condens. Matter.* **25**, 235401 (2013).
44. M. T. Dove, K. Trachenko, V. V Brazhkin, C. J. Walker, A. E. Phillips, E. I. Andritsos, E. Zarkadoula, The heat capacity of matter beyond the Dulong–Petit value. *J. Phys. Condens. Matter.* **25**, 235401 (2013).
45. D. Bolmatov, K. Trachenko, Liquid heat capacity in the approach from the solid state: Anharmonic theory. *Phys. Rev. B.* **84**, 54106 (2011).
46. F. Demmel, Slow structural relaxation process facilitates solidification in liquid gallium. *Phys. Rev. B.* **101**, 1–6 (2020).
47. A. V Grosse, Viscosities of liquid sodium and potassium, from their melting points to their critical points. *Science (80-. ).* **147**, 1438–1441 (1965).
48. P. E. . Turchi, Viscosity and Surface Tension of Metals, 73 (2018).
49. M. J. Assael, I. J. Armyra, J. Brillo, S. V Stankus, J. Wu, W. A. Wakeham, Reference Data for the Density and Viscosity of Liquid Cadmium, Cobalt, Gallium, Indium, Mercury, Silicon, Thallium, and Zinc. *J. Phys. Chem. Ref. Data.* **41**, 33105 (2012).
50. G. R. Stewart, Measurement of low-temperature specific heat. *Rev. Sci. Instrum.* **54**, 1–11 (1983).
51. D. R. Chipman, Temperature dependence of the Debye temperatures of aluminum, lead, and beta brass by an X-ray method. *J. Appl. Phys.* **31**, 2012–2015 (1960).
52. P. Hu, P.-P. Zhao, Y. Jin, Z.-S. Chen, Experimental study on solid–solid phase change properties of pentaerythritol (PE)/nano-AlN composite for thermal storage. *Sol. Energy.* **102**, 91–97 (2014).
53. S. P. Srivastava, I. D. Singh, Debye Temperature of Molecular Crystals. *J. Phys. Soc. Japan.* **44**, 2005–2006 (1978).
54. R. W. Powell, L. P. E., Thermal Conductivity of the Elements: A Comprehensive Review. *J. Phys. Chem. Ref. Data.* **3** (1973).
55. T. Chi, Electrical Resistivity of Alkali Elements. *J. Phys. Chem. Ref. Data.* **8**, 339–438 (1979).
56. C. Author, E. N. da C Andrade, E. R. Dobbs, “The Viscosities of Liquid Lithium” (1952), (available at <https://www.jstor.org/stable/pdf/98838.pdf?refreqid=excelsior%3A528a6474ad6a6b5fcec3888564eefb05>).
57. G. Chen, Perspectives On Molecular-Level Understanding of Thermophysics of Liquids

- and Future Research Directions. *J. Heat Transfer* (2021), doi:10.1115/1.4052657.
58. E. McLaughlin, The thermal conductivity of liquids and dense gases. *Chem. Rev.* **64**, 389–428 (1964).
  59. W. Lv, A. Henry, Direct calculation of modal contributions to thermal conductivity via Green–Kubo modal analysis. *New J. Phys.* **18**, 013028 (2016).
  60. G. Chen, *Nanoscale energy transport and conversion: a parallel treatment of electrons, molecules, phonons, and photons* (Oxford university press, 2005).
  61. K. Trachenko, V. V. Brazhkin, Duality of liquids. *Sci. Rep.* **3**, 1--5 (2013).
  62. T. Egami, Elementary excitation and energy landscape in simple liquids. *Mod. Phys. Lett. B.* **28** (2014), p. 1430006.
  63. P. B. Allen, J. L. Feldman, J. Fabian, F. Wooten, Diffusons, locons and propagons: Character of atomic vibrations in amorphous Si. *Philos. Mag. B Phys. Condens. Matter; Stat. Mech. Electron. Opt. Magn. Prop.* **79**, 1715–1731 (1999).
  64. V. V. Brazhkin, K. Trachenko, Between glass and gas: Thermodynamics of liquid matter. *J. Non. Cryst. Solids.* **407**, 149–153 (2015).
  65. A. Z. Zhao, M. C. Wingert, R. Chen, J. E. Garay, Phonon gas model for thermal conductivity of dense, strongly interacting liquids. *J. Appl. Phys.* **129**, 235101 (2021).

## Chapter 2. Defining an upperbound on solid/liquid transition enthalpy

This chapter pays homage to the very first problem my advisor gave me upon entering the PhD. Although I never tried to publish this attempt at a solution, I think going through it represents a unique exercise in applying all the fundamental descriptions of the solid/liquid transition that were outlined in chapter 1, and I hope someone may continue the attempt at a solution that I began, but hopefully with a more informed beginning after reading this.

### The Problem:

The goal is to determine the maximum enthalpy of transition for a system of atoms in the condensed state at 1 atm in contact with a thermal reservoir of some arbitrary temperature.

In other words, given a temperature, is there a maximum enthalpy for a first-order transition for an arbitrary condensed atomic system at that temperature?

### Motivation

We need an upper-bound on the enthalpy of transition in the condensed state to determine the potential for thermal energy storage, and to define efficiencies for phase change systems. Moreover, evaluating the efficiencies for current phase change materials will give research in thermal energy storage materials a clearer direction. Is it worth it to seek new materials with higher enthalpy of transition, or are we already close to the fundamental limit so that we should focus on other pressing problems (e.g. thermal transport of these materials)?

### Thermodynamic Preamble

It is tempting to hope that the answer to this problem will be an equation akin to the Carnot efficiency. That will not happen. The Carnot efficiency is derived from the thermodynamic relations between macroscopic variables/potentials. It is pure thermodynamics that relies on nothing but energy conservation and entropy maximization.

This problem can also be related to pure thermodynamics, but it cannot be bounded. In terms of macroscopic thermodynamic variables, the problem statement reads:

$$\text{Maximize } T_m \left( \frac{\partial F^\alpha}{\partial T} \Big|_{T_m} - \frac{\partial F^\beta}{\partial T} \Big|_{T_m} \right) \text{ such that } F^\alpha(T_m) = F^\beta(T_m)$$

Where  $F$  is the appropriate chemical potential (we'll be operating within the Helmholtz potential),  $\alpha$  and  $\beta$  are the high and low temperature phases, respectfully, and  $\frac{\partial F^\alpha}{\partial T} \Big|_{T_m}$  gives the entropy of the  $\alpha$  phase at  $T_m$ , so that the maximized quantity reads  $T_m \Delta S$ , or  $\Delta H$ . At a glance, the solution appears fairly obvious: maximize the slope of the free energy (i.e entropy) in the  $\alpha$  phase and minimize it in the  $\beta$  phase while constraining the chemical potentials such that they are equal. **This is the most insight macroscopic thermodynamics can give for this problem. The**

**macroscopic formalism cannot impose any limits on the potentials, or the derivatives of the potentials.** To determine limits on the entropies of each phase at constant chemical potential, we must depart from the macroscopic formalism and treat the system in terms of discrete states.

The workflow would look like:

Quantum Mechanics → Available Energy Levels → Statistical Mechanics → Ensemble Averages / Macroscopic Properties → Constraints on Macroscopic Properties

Quantum mechanics constrains the available energy states of the system, and statistical mechanics determines how the system will distribute the available energy from the environment to those allowed energy states. The most likely distribution will be the ensemble average, giving the macroscopic quantity we seek. The constraints on the maximization problem come from atomistic considerations governing the systems available energy states.

### **Most Fundamental Approach**

It should come as no surprise that I'll have to make quite a few approximations to arrive at a reasonable limit while following this workflow. Before I do that, I think it's important to see what it would take to fundamentally solve this problem.

First, you'd have to consider a system of  $N$  atoms for an arbitrary set of protons, neutrons, and electrons, and then solve the many-body Schrodinger equation. This will determine the energy states available to the system, and then you would look at every possible way of distributing the available energy across those states, and from the set of possible distributions you would turn the statistical mechanical crank and calculate the thermodynamic potential for a given amount of available energy. As you increase the amount of available energy, you would eventually notice a discontinuity in the free energy curve, indicating a first-order phase transition. You could then correlate the available energy and the distribution of that energy to the temperature of your system ( $dS/dE$ ).

You would do this for every possible combination of protons, neutrons, and electrons, and from repeating this procedure for all possible combinations you would get a set of all possible phase transitions at a given temperature, and you would identify the proton/neutron/electron combination that had the maximum entropy change at that temperature.

Of course, this is impractical, but I bring it up because I don't think there will ever be a "true" and "fundamental" limit to this problem as there is to the carnot efficiency. The best we can hope for is a "practical" limit.

### **First Simplification:**

As mentioned in Chapter 1, the possibility of phase equilibria is built right into statistical mechanics. The complete and correct partition function of a system should have the phase-

change behavior encoded into the equations, such that as you traverse an extensive thermodynamic path, an instability in the equations causes a discontinuity in the free energy curve (i.e phase transition). This is partially what makes the van der Waals theory of liquids/gasses so attractive: It describes both the liquid (near vapor) and gas phases. From a specific assumption about molecular interactions, a single partition function leads directly to the liquid-vapor phase transition.

However, in almost all other cases first-order phase equilibria are more easily studied by adopting different models for each phase and finding the conditions under which the separate models yield equilibrium among the phases. For the solid-liquid transition, this must be done. A major failure of crystal thermodynamics / solid-state theory is that it cannot predict melting. In general, this is blamed on the inability to handle anharmonicity near melting, which is believed to provide the instability driving the discontinuity in the free energy curve.

**For this reason, to study the solid-liquid transition, we have to adopt different mechanical models for each phase. This is the first assumption**

### **Mechanical Model of Solids**

I'm going to go through the full derivation for the free energy of a crystal of N atoms. **In the end, I arrive at the expression for the free energy of a harmonic solid with arbitrary dispersion**, but I am going through the full derivation to make all further assumptions clear, and to argue that this approach is still very general. The derivation can be skipped without loss of continuity in the subsequent sections.

*Classic textbook Derivation:*

-----  
-----

If we have a system of N atoms, we must have 3N DOF. **We assume that each DOF can be described by a simple harmonic oscillator. This is the 2<sup>nd</sup> major assumption I make. There is no possible analytical solution without making this assumption.** So we begin by assuming we have a system of 3N independent harmonic oscillators.

The possible energy for each oscillator is given by the quantum solution to a particle in a harmonic well:

$$E(n_j) = \left(n_j + \frac{1}{2}\right) \hbar v_j \quad 2.1$$

Where the  $j^{th}$  oscillator has frequency  $\nu_j$  and  $n_j$  is a positive integer. The total energy of the crystal system is:

$$E_{crystal} = E_{static} + E_{Dynamic} \quad 2.2$$

Where  $E_{static}$  is the potential energy when all atoms are at their equilibrium positions, and  $E_{Dynamic}$  is the sum of the energy corresponding to each of the  $3N$  harmonic oscillators:

$$E_{crystal}\{n_j\} = U_o + \sum_{j=1}^{3N} (n_j + \frac{1}{2})\hbar\nu_j \quad 2.3$$

$\{n_j\} = \{n_1, n_2, n_3 \dots n_{3N}\}$  refers to a particular state, or a possible ordering of the distribution of energies across the harmonic oscillators.  $U_o$  is the static lattice energy (sometimes called electronic energy). The partition function is the sum over all states, or all the possible different ways to divide the total energy available from the environment across the different harmonic oscillators of the system:

$$Z = \sum_{\{n_j\}} e^{-\frac{E_{crystal}\{n_j\}}{k_b T}} \quad 2.4$$

Summing over all “states” or configurations of excitations must be performed over all sets of integers (all possible excitation values), so each excitation can vary between 0 and infinity. This means that in the set  $\{n_j\} = \{n_1, n_2, n_3 \dots n_{3N}\}$   $n_1$  must be varied from 0 to infinity,  $n_2$  must be varied from 0 to infinity.... Etc, and the partition function sums every possible combination resulting from varying each parameter. Mathematically, this reads as:

$$Z = \sum_{\{n_j\}} e^{-\frac{E_{crystal}\{n_j\}}{k_b T}} = \sum_{\{n_j\}} e^{-\frac{U_o}{k_b T}} e^{-\frac{\sum_{j=1}^{3N} (n_j + \frac{1}{2})\hbar\nu_j}{k_b T}} \quad 2.5$$

$$\sum_{\{n_j\}} = \sum_{n_1}^{\infty} \sum_{n_2}^{\infty} \sum_{n_3}^{\infty} \dots \sum_{n_{3N}}^{\infty} e^{-\frac{U_o}{k_b T}} e^{-\frac{\sum_{j=1}^{3N} (n_j + \frac{1}{2})\hbar\nu_j}{k_b T}} \quad 2.6$$

If we take  $E_0 = U_0 + \frac{1}{2} \sum_{j=1}^{3N} \hbar \nu_j$  and rewrite  $e^{-\frac{\sum_{j=1}^{3N} n_j \hbar \nu_j}{k_b T}} = \prod_{j=1}^{3N} e^{-\frac{n_j \hbar \nu_j}{k_b T}} = e^{-\frac{n_1 \hbar \nu_1}{k_b T}} e^{-\frac{n_2 \hbar \nu_2}{k_b T}} e^{-\frac{n_3 \hbar \nu_3}{k_b T}} \dots e^{-\frac{n_{3N} \hbar \nu_{3N}}{k_b T}}$

We can group the sums so that:

$$Z = e^{-\frac{E_0}{k_b T}} \sum_{n_1}^{\infty} e^{-\frac{n_1 \hbar \nu_1}{k_b T}} \sum_{n_2}^{\infty} e^{-\frac{n_2 \hbar \nu_2}{k_b T}} \sum_{n_3}^{\infty} e^{-\frac{n_3 \hbar \nu_3}{k_b T}} \dots \sum_{n_{3N}}^{\infty} e^{-\frac{n_{3N} \hbar \nu_{3N}}{k_b T}} \quad 2.7$$

Notice that each n is just an integer counter in each sum. We can re-write this where all the sums are summing over the same index:

$$Z = e^{-\frac{E_0}{k_b T}} \sum_n^{\infty} e^{-\frac{n \hbar \nu_1}{k_b T}} e^{-\frac{n \hbar \nu_2}{k_b T}} e^{-\frac{n \hbar \nu_3}{k_b T}} \dots e^{-\frac{n \hbar \nu_{3N}}{k_b T}} \quad 2.8$$

Which looks like a product of sums, so we can re-arrange such that:

$$Z = e^{-\frac{E_0}{k_b T}} \prod_{j=1}^{3N} \sum_n^{\infty} e^{-\frac{n \hbar \nu_j}{k_b T}} \quad 2.9$$

This is the canonical partition function of 3N independent harmonic oscillators. It can be evaluated with the routine-trick where we set  $x_j = e^{-\frac{\hbar \nu_j}{k_b T}}$  so that Z becomes a geometric series whose sum is  $\frac{1}{1-x_j}$ . This yields:

$$Z = e^{-\frac{E_0}{k_b T}} \prod_{j=1}^{3N} \left( \frac{1}{1 - e^{-\frac{\hbar \nu_j}{k_b T}}} \right) \quad 2.10$$

-----  
-----

*End of Derivation:*

The Helmholtz free energy is found directly from the partition function using the relationship  $F = -k_b T \ln(Z)$ :

$$F = E_o + k_b T \sum_j^{3N} \ln \left( 1 - e^{-\frac{\hbar \nu_j}{k_b T}} \right) \quad 2.11$$

Thus, if we know the frequencies of the  $3N$  states, you could perform the sum and get the exact solution for the free energy of the crystal. **This gives a complete theory of the thermodynamic properties of a harmonic crystal, provided we know the values of the complete frequency distribution within the system.** This can be put into integral form by multiplying the sum by  $Ng(\nu)d\nu$  and integrating for all frequencies:

$$F = E_o + Nk_b T \int_0^\infty g(\nu) \ln \left( 1 - e^{-\frac{\hbar \nu_j}{k_b T}} \right) d\nu \quad 2.12$$

In other words, if the density of states,  $g(\nu)$  is known, the thermodynamics are completely known. Describing  $g(\nu)$  is a problem for lattice dynamics, which is directly related to the microscopic details of the system (e.g. constraints).

At this point we can try to come up with a function for  $g(\nu)$  that satisfies the optimization criteria from macroscopic thermodynamics. I tried this using variational principles and failed because  $g(\nu)$  is not analytic. It suffers from “van hof singularities” which means that no smooth function, or even superposition of smooth functions, could span the entire set of possible  $g(\nu)$ , so this makes functional based optimization impractical.

**The 3<sup>rd</sup> assumption is that the system is classical at the melting point.** This allows a high temperature expansion of the free energy to simplify the equation a little. Taking:

$$F = E_o + k_b T \sum_j^{3N} \ln \left( 1 - e^{-\frac{\hbar \nu_j}{k_b T}} \right) \quad 2.13$$

And setting  $x = \frac{\hbar \omega}{k_b T}$ , we can expand  $e^x \approx 1 + x$  so that  $\ln(1 - e^{-x}) \approx \ln(1 - 1 - x) \approx \ln(-x)$  and

$$F = E_0 + k_b T \sum_j^{3N} \ln \left( \frac{\hbar \nu_j}{k_b T} \right) \quad 2.14$$

Which represents a superposition of Einstein oscillators. Fortunately, the optimization problem only concerns the value of the free energy and its temperature-derivative at a single point. Thus, we must demonstrate that a single characteristic temperature can be used to represent the thermodynamics of any possible frequency distribution at a single temperature. Across all temperatures, this cannot be done because the thermodynamic path depends strongly on the density of states. But at a single temperature it is less obvious. **To show that it can, we need to show that both the absolute value and the temperature-derivative of the free energy described by an arbitrary frequency distribution can be written as a single characteristic temperature.**

First, we equate the free energies of the generalized free energy and the single-frequency free energy:

$$E_0 + k_b T \sum_j^{3N} \ln \left( \frac{\theta_j}{T} \right) = E_0 + k_b T \ln \left( \frac{\theta_{eff}}{T} \right) \quad 2.15$$

Which simplifies to:

$$\ln(\theta_{eff}) = \frac{1}{3N} \sum_j^{3N} \ln \left( \frac{\theta_j}{T} \right) \quad 2.16$$

Next, we equate the derivatives of the free energies:

$$\frac{\partial}{\partial T} \left( E_0 + k_b T \sum_j^{3N} \ln \left( \frac{\theta_j}{T} \right) \right) = \frac{\partial}{\partial T} \left( 1 + k_b T \ln \left( \frac{\theta_{eff}}{T} \right) \right) \quad 2.17$$

Which also simplifies to:

$$\ln(\theta_{eff}) = \frac{1}{3N} \sum_j^{3N} \ln \left( \frac{\theta_j}{T} \right) \quad 2.18$$

So this says that by choosing  $\theta_{eff}$  using the relation above, then for any frequency distribution / density of states, a single effective frequency/temperature can be used that will reproduce both the absolute value and the derivative of the free energy curve at a single temperature. **For this**

reason, all of the thermodynamics at a given temperature can be described with an appropriate average temperature. So long as we choose an effective temperature equal to the natural log weighted average of the frequency distribution, this will hold true in any harmonic solid, irrespective of the nature of any other microscopic quantities. The temperature-dependence, however, cannot be represented using this coarse-graining trick.

In other words, given  $N$  atoms, regardless if they are isotropic, 1D, 2D, 3D, arranged in unit cells, undergo librational/torsional/bending vibrations etc – an effective temperature can be chosen that will give both the correct value and the derivative of the free energy at a given temperature for that arbitrary system.

This is important because in our optimization problem, the free energy and its derivative at the melting point are the only thermodynamic quantities needed. *The implication here is that by varying the effective characteristic temperature, we can check the optimization condition for the thermodynamic output of every possible density of states.*

### Mechanical Model of Liquids

Now we need a model to represent the free energy of the liquid. The only modern analytical theories are

1. Wallace- V-T Model
2. Our Diffusion-oscillator model from Chapter 1
3. Phonon Theory of Liquids
4. Eyring's theory of significant structures

There are some older (pre 1960s) theories, but most were intractable or valid more for gas-like liquids. For reference, these are the Guggenheim, Devenshire-Cellular, Mie, and Kirkwood models.

Eyring's theory of significant structures is essentially just a linear interpolation between a solid model and a gas model. It asks, "how gas like is this liquid?" and then multiplies the gas partition function by the percentage of atoms you say behave gas-like. Likewise, it then multiplies the solid partition function by the percentage of molecules you say are solid-like. The percentage of gas-like particles is a fitting parameter, and is phenomenological. With that said, it gives an excellent fit for a lot of liquids. Although it hasn't been in the spot light for ~40 years (mostly because it doesn't comment on any new physics), I'd say most sources deem Eyring's model the most successful analytical model to describe liquid thermodynamics. The problem is that it has no predictive power – there's really no way to know the fraction of gas-like molecules that will appear a priori. Instead, it must be fit to experimental data in which case the equation shows excellent agreement to experimental results once you've made the fit.

Thus, we will move ahead by using Eyring's model to represent the thermodynamics of the liquid state.

The chemical potential in the Eyring model is expressed as:

$$F_L = f_g k_b T \ln \left( \frac{z_l \Lambda^3}{e(z_l + 1) \bar{V}_L} \right) + f_g \bar{E}_o^g + f_s \bar{E}_o^s + 3 f_s k_b T \ln \left( \frac{\theta_D^L}{T} \right) + \frac{f_g}{z_l} k_b T \quad 2.19$$

Where  $f_g$  is the fraction of molecules that are gas-like,  $f_s$  is the fraction of molecules that are solid-like ( $f_s = 1 - f_g$ ),  $\Lambda$  is the thermal DeBroglie wavelength,  $e$  is eulers number,  $z_l$  is the molecules coordination number (varies between 8-12),  $\bar{V}_L$  is the volume per molecule in the liquid state,  $\bar{E}_o^g$  and  $\bar{E}_o^s$  are the zero point energies per gas-like and solid-like molecules respectively, and  $\theta_D^L$  is the debye temperature evaluated in the liquid state, which is  $\theta_{D,L} = \frac{\theta_{D,L}^0}{\sqrt{2}}$  as shown in chapter 1. I'd also like to note that  $\Lambda$  is implicitly dependent on the Mass of the system, so  $M$  must be specified.

I'd like to further note that this can be put in the form of the equations I derived in chapter 1. In fact, I can equate the two expressions and derive a relation for the gas-fraction Eyring proposed in terms of grunesian parameters, density changes, and the Frenkel frequencies. However, as we'll see later in the derivations, the gas-fraction is actually more convenient for the optimization problem, because I can relate it to free-volume theory which will prove useful in the numerical optimization of these expressions.

### Phase Equilibria and Maximization

The melting point occurs when  $F_S(T_m) = F_L(T_m)$

And we've shown:

$$F_s = E_0^s + 3 N k_b T \ln(\theta_{eff}^s) \quad 2.20$$

$$F_L = f_g k_b T \ln \left( \frac{z_l \Lambda^3}{e(z_l + 1) \bar{V}_L} \right) + f_g \bar{E}_o^g + f_s \bar{E}_o^s + 3 f_s k_b T \ln \left( \frac{\theta_D^L}{T} \right) + \frac{f_g}{z_l} k_b T \quad 2.21$$

Where  $f_g \bar{E}_o^g + f_s \bar{E}_o^s - E_s = \Delta H$

With great generality. Equating them we get:

$$\Delta H = -\frac{f_g N k_b T_m}{z_l} + 3 N k_b T_m \ln\left(\frac{\theta_D^S}{\theta_D^L}\right) - 3 f_g N k_b T_m \ln\left(\frac{\theta_D^L}{T_m}\right) + f_g N k_b T_m \ln\left(\frac{\Lambda^3 z_l}{e \bar{V}_L (1 + z_l)}\right) \quad 2.22$$

Note: This essentially reads  $\Delta H = T \Delta S$  where  $\Delta S = -\frac{f_g N k_b}{z_l} + 3 N k_b \ln\left(\frac{\theta_D^S}{\theta_D^L}\right) - 3 f_g N k_b \ln\left(\frac{\theta_D^L}{T_m}\right) + f_g N k_b \ln\left(\frac{\Lambda^3 z_l}{e \bar{V}_L (1 + z_l)}\right)$ . The maximization problem then boils down to this one incredibly simple, yet reasonably fundamental/broad equation.

How do we bound  $\frac{\theta_D^S}{\theta_D^L}$ ?

**Bounding**  $\frac{\theta_{eff}^S}{\theta_{eff}^L}$

To bound this ratio, we're going to go back to the fundamental idea of entropy and how it relates to its phase space.

Remember, the entropy of an atom is simply  $S = k_b \ln(\Omega)$ .  $\Omega$  is the number of possible states the atom can be in when it's given a fixed stipend of energy. An atom's energy can be distributed across two independent coordinates, which are its momentum and position coordinates. In other words,

$$E = \frac{p^2}{2m} + \frac{1}{2} k x^2 \quad 2.23$$

For fixed E, how many combinations of p and x will make this true if I discretize p and x by  $\hbar$ ? If you ask this question for every atom, and you add up all the combinations, you get the entropy of the system. The combinations can be envisioned as a 3N "hyperspace," and at any instant in time, the material is at a point in this space that gives all positions and momenta of its atoms. The point moves around as the atoms vibrate, and the larger the volume explored during vibration, the greater the number of ways of finding the system, and thus the larger the entropy.

To determine the differences in vibrational entropy between two phases, all we have to do is find the change in volume explored in the hyperspace between those phases.

If we assume two phases are at the same temperature (necessary condition for phase equilibria), then each atom in both phases will have  $k_b T$  of energy (if they are classical). This means that

- 1.) Each atom has the same kinetic energy as it passes through its equilibrium point of its vibrational cycle
- 2.) Each atom has the same potential energy as it passes through its turning points in its cycle

However, the range of travel in each case depends on the strength of the interatomic springs and on its interatomic masses. So, if  $m$  is fixed, then a change in  $k$  will change how far the atom can go in phase space. This is visualized below:

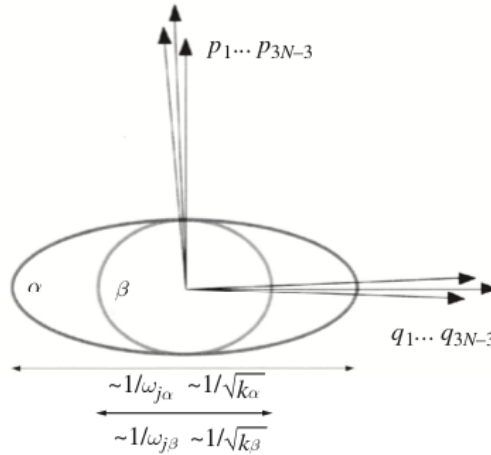


Figure 2.1 Phase Space for changing spring constant

Because the mass is the same, the momenta coordinates are unchanged. In the above picture,  $\alpha$  has a smaller spring constant, so that its amplitude of vibration is larger for fixed energy, and it can explore more of phase space, thus having larger entropy. Conversely, if  $k$  is fixed but  $m$  can vary:

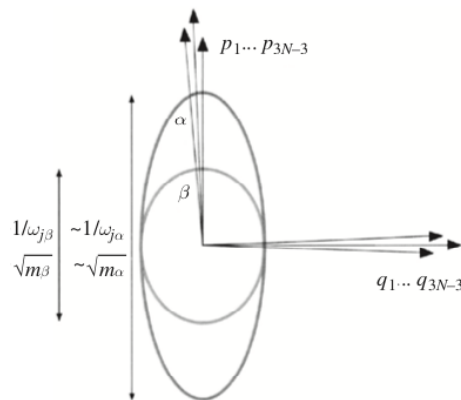


Figure 2.2 Phase space for changing mass

The change in hyperspace would be rotated.

So how does this relate to bounding  $\frac{\theta_D^s}{\theta_D^l}$ ?

Let's assume that the 2 phases  $\alpha$  and  $\beta$  have the same atoms, but different structures and bonding. This means that the mass of the atoms is fixed (which is true in phase transitions), but the spring constants vary because the changes in chemical forces between the two bonds alter the forces between the atoms, so they vibrate with different frequencies. **Both  $\alpha$  and  $\beta$  have  $k_b T$  of thermal energy available from the environment, so the total energy of each oscillator in  $\alpha$  and  $\beta$  is the same. This means we can set the potential energies of the atoms in each phase equal to each other at the amplitude of their vibrations:**

$$PE^\alpha = PE^\beta \quad 2.24$$

$$\frac{1}{2} k^\alpha A_\alpha^2 = \frac{1}{2} k^\beta A_\beta^2 \quad 2.25$$

$$\frac{A_\alpha}{A_\beta} = \sqrt{\frac{k_\beta}{k_\alpha}} = \sqrt{\frac{m\omega_\beta^2}{m\omega_\alpha^2}} = \frac{\theta_\beta}{\theta_\alpha} \quad 2.26$$

So we can bound  $\frac{\theta_\beta}{\theta_\alpha}$  by bounding  $\frac{A_\alpha}{A_\beta}$ .

**How do we bound  $\frac{A_\alpha}{A_\beta}$ ?**

We know that in the solid state, the amplitude of vibration is some fraction of the interatomic spacing. We'll quantify that fraction in a minute. Physically, the interatomic potential is stronger in solids such that an atom uses up all its  $k_b T$  of thermal energy before it can reach the full interatomic spacing.

**In the condensed state, the furthest it could possibly travel is half its interatomic spacing minus the diameter of the molecule, purely based on geometric arguments. This isn't an assumption; this is a physical constraint.** As we said before, the vibrational entropy change is exclusively due to changes in amplitude, and we have a physical constraint to bound the largest possible amplitude of vibration. Using the picture below to guide us, we can calculate  $\frac{A_\alpha}{A_\beta}$

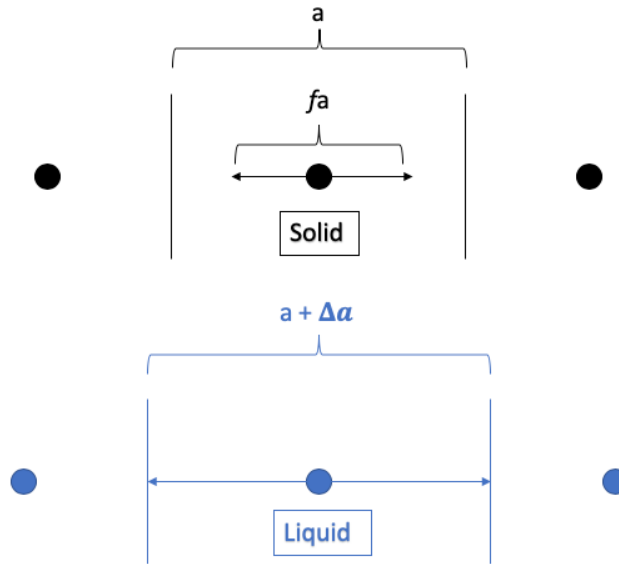


Figure 2.3. Physical constraints on atom during phase transition

$$\frac{A_L}{A_S} = \frac{a + \Delta a}{fa} = \frac{1}{f} \left( 1 + \frac{\Delta a}{a} \right) \quad 2.27$$

Where  $a$  is the interatomic spacing minus the “exclusion diameter” (Minimum separation distance between two particles based on pauli repulsive forces – will dive deeper into this shortly).  $\Delta a$  is the expansion/contraction of the lattice upon transition, and  $f$  is the fraction of the interatomic spacing the lower-temperature phase atom vibrates at. Now, we just need to determine  $f$ , or the amplitude of vibration of the atom before transition. Fortunately, this is fairly easy to quantify:

To do this, we’ll use harmonic vibration theory to determine the average amplitude of vibration at the melting point. Let’s denote the amplitude for each normal mode in a monatomic crystal as  $A_k$ . The displacement of an atom at  $R$  is:

$$u = \frac{1}{\sqrt{N}} \sum_k A_k e^{ik \cdot R} \quad 2.28$$

The magnitude of the square of the displacement is:

$$u^2 = \frac{1}{N} \sum_K A_k^2 \quad 2.29$$

Now, for a simple harmonic oscillator of angular frequency  $\omega$ , the amplitude can be related to the total energy by:

$$E = \frac{1}{2}m\omega^2 A^2 \quad 2.30$$

So the mean square amplitude of the  $k^{th}$  oscillator is related as:

$$A_k^2 = \frac{2}{M\omega_k^2} E_k^2 \quad 2.31$$

If we're above the characteristic temperature of the crystal, each oscillator has an energy  $k_b T$ , so subbing in for  $E_k$  we get:

$$u^2 = \frac{2k_b T}{MN} \sum_k \frac{1}{\omega_k^2} \quad 2.32$$

Converting this sum to an integral using the debye density of states, this gives:

$$u^2 = \frac{18T\hbar^2}{Mk_b\theta_D^2} \quad 2.33$$

**I will justify the use of the Debye density of states later, but for now let's consider this another assumption.**

Now, to get the fraction of interatomic spacing the atom vibrates at, we just divide the above equation by  $a^2$  and take the square root:

$$f = \frac{3\hbar}{a\theta_D} \sqrt{\frac{2T}{k_b M}} \quad 2.34$$

And plugging this back into the amplitude ratio equation, we get:

$$\frac{A_L}{A_S} = \frac{a + \Delta a}{fa} = \frac{1}{f} \left(1 + \frac{\Delta a}{a}\right) = \frac{a\theta_D \sqrt{\frac{k_b M}{2T}}}{3\hbar} \left(1 + \frac{\Delta a}{a}\right) \quad 2.35$$

First, we note that at the melting point,  $T = T_m$ . Next, we observe that this ratio is maximized when  $\theta_D$  is largest (which corresponds to a tighter crystal, or smaller amplitude of vibration in the first phase). **We haven't explicitly placed an upper-bound on  $\theta_D$ , but here we bound  $\theta_D$  by the melting point to ensure that we're only dealing with classical liquids. Thus, we assume that**

$\theta_D = T_m$  . If we don't do this, then each oscillator would not have  $k_b T$  of energy, and our amplitude analysis would get a lot more complicated. I think this is a very fair assumption, because it is assumed that melting occurs from phonon-phonon interactions, which require anharmonicity which kicks in after the solid goes classical.

Our only toggles, then, are the atomic mass,  $M$ , and the maximum amplitude,  $a$ , given by the interatomic spacing and molecular diameter (pauli exclusion forces). Plugging into our enthalpy of transition equation, the final formula for the max enthalpy of transition for 1 mole of atoms reads:

$$\Delta H \left[ \frac{J}{mol} \right] = -\frac{f_g N k_b T_m}{z_l} + 3N k_b T_m \ln \left( \frac{\theta_D^S}{\theta_D^L} \right) - 3f_g N k_b T_m \ln \left( \frac{\theta_D^L}{T_m} \right) + f_g N k_b T_m \ln \left( \frac{\Lambda^3 z_l}{e \bar{V}_L (1 + z_l)} \right) \quad 2.36$$

$$\Delta H \left[ \frac{J}{mol} \right] = -\frac{f_g N k_b T_m}{z_l} + 3RT_M \ln \left( \frac{a}{3\hbar} \sqrt{\frac{k_b T_m M}{2}} \left( 1 + \frac{\Delta a}{a} \right) \right) - 3f_g N k_b T_m \ln \left( \frac{\theta_D^L}{T_m} \right) + f_g N k_b T_m \ln \left( \frac{\Lambda^3 z_l}{e \bar{V}_L (1 + z_l)} \right) \quad 2.37$$

Where  $\theta_D^L = \theta_D^S \left( \frac{A_s}{A_L} \right) = T_m \left( \frac{A_s}{A_L} \right) = T_m \frac{3\hbar}{a \theta_D \sqrt{\frac{k_b M}{2T} \left( 1 + \frac{\Delta a}{a} \right)}}$  .

J/mol isn't very useful for practical applications. Instead, we care about the max enthalpy of fusion per unit volume and/or mass:

$$\Delta H_{max,V} = \frac{\Delta H_{max,unit\ cell}}{V_{unit\ cell}(a)} \quad 2.38$$

$$\Delta H_{max,Mass} = \frac{\Delta H_{max,atomic}}{M_{atomic}} \quad 2.39$$

**Maximizing  $\Delta H_{max,V}$  and  $\Delta H_{max,Mass}$**

To maximize, we need to identify the independent variables. Right now, it looks like:

$$\Delta H_{\max,V}, \Delta H_{\max,M} = f(M, a, T_m) \quad 2.40$$

This is because fraction of gas-like molecules,  $f_g$  can be solved for by setting the expansion,  $\Delta a$ , and then  $\Delta a$  can be optimized independently to maximize  $\Delta H$  (more on that later Remember, the goal is to get  $\Delta H_{\max,V}(T_m)$ . This means that we must relate “a” and M to  $T_m$ . This won’t be possible for M, so for now let’s lower our ambition and seek  $\Delta H_{\max,V}(T_m, M)$

So how do we relate “a” to  $T_m$ ? Remember, “a” describes the max amplitude of a particles oscillation which is equal to the interatomic distance between nearest neighbors minus the “closest” approach distance between the two particles.

The interatomic distance is determined by the interatomic potential describing the force interactions between the two particles (e.g. when the derivative of the potential goes to zero). Moreover, the interatomic potential determines the Debye temperature. So already we can see that “a” cannot be varied independently of  $\theta_D$ .

The closest approach distance is dictated by the interatomic potential and the total energy of both particles. So “a” and  $k_b T_m$  must be related.

**The common link here is that we need an interatomic potential to tell us how a and  $T_m$  are related (remember it is assumed  $T_m = \theta_D$ )**

Once we have “a”, we can calculate  $\Delta H_{\max}$  at a given temperature and for a given mass. We can then use “a” to calculate the volume of a unit cell and determine its enthalpy per unit volume. We set M independently so we can then calculate the enthalpy per unit mass.

### **Relating “a” to $T_m$ with an Interatomic Potential**

The goal is to use a pair potential,  $U(r)$  to relate the interatomic spacing, max separation, and spring constants. By far, the most popular and easiest to use is the Lennard-Jones 6-12 potential. *I’m going to carry out the rest of this calculation using the LJ 6-12 potential, but I’d like to note that the following steps can use any potential.*

First, LJ pair-potential looks like:

$$U(r) = 4\epsilon \left( \left( \frac{\sigma}{r} \right)^{12} - \left( \frac{\sigma}{r} \right)^6 \right) \quad 2.41$$

Where

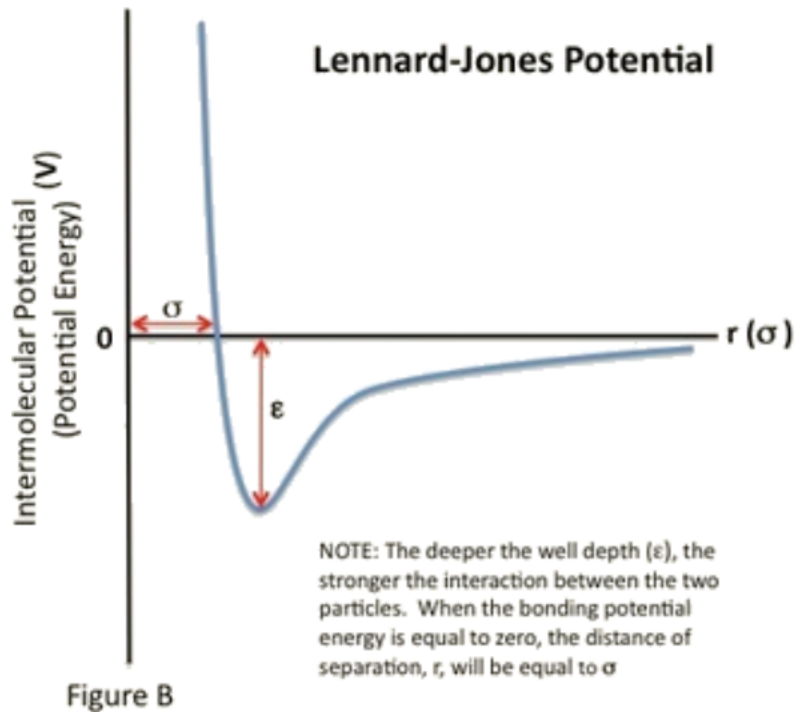


Figure 2.4 LJ Potential – Visualization of parameters

We can solve for the equilibrium interatomic spacing by setting the force equal to zero,  $\frac{dU}{dr} = 0$  and solving for  $r_0$ . This gives us

$$r_0 = 2^{\frac{1}{6}}\sigma \quad 2.42$$

And the lattice spacing is  $d = cr_0$  where  $c$  is a constant that depends on the specific lattice geometry. For FCC it is  $\sqrt{2}$ . The volume per atom is then  $V_{atom} = d^3c_1$  where  $c_1$  is a geometric constant specific to the lattice type. For FCC  $c_1 = \frac{1}{4}$ . The molar volume is then

$$V_{molar} = Nc_1 \left( c2^{\frac{1}{6}}\sigma \right)^3 \quad 2.43$$

Next, we can determine the spring constant by evaluating  $k = \frac{d^2U}{dr^2} \Big|_{r_0}$ . For the LJ system,  $k = \frac{72\epsilon}{r_0^2}$ . This is for a single particle pair interaction. The net spring constant is approximately equal to the single spring constant multiplied by the coordination number of the lattice. We'll call this

$$k_{net} = \frac{c_l 72\epsilon}{r_o^2} \quad 2.44$$

Where  $c_l$  is the coordination number of the lattice. For FCC,  $c_l = 12$ . We can relate the spring constant to the Einstein temperature which we can then relate to the Debye temperature by equating the classical Einstein and Debye models at high temperatures:

$$\theta_D = e^{\frac{1}{3}} \theta_E \quad 2.45$$

$$\theta_E = \frac{\hbar}{k_b} \omega_E \quad 2.46$$

$$\omega_E = \sqrt{\frac{k}{m}} \quad 2.47$$

Putting it all together we get:

$$\theta_D = \frac{e^{\frac{1}{3}} \hbar}{k_b} \sqrt{\frac{k_{net}}{m}} \quad 2.48$$

And subbing in for  $k_{net}$  we get:

$$\theta_D = \frac{e^{\frac{1}{3}} \hbar}{k_b} \sqrt{\frac{c_l 72\epsilon}{m r_o^2}} \quad 2.49$$

From our assumption that the liquid has to be classical at the melting point, we enforce  $\theta_D = T_m$ , so

$$k_b T_m = e^{\frac{1}{3}} \hbar \sqrt{\frac{c_l 72\epsilon}{m r_o^2}} \quad 2.50$$

Solving for  $r_o$  we get:

$$r_o = \frac{6\hbar e^{\frac{1}{3}}}{k_b T_m} \sqrt{\frac{2\epsilon c_l}{M}} \quad 2.51$$

Which gives us the interatomic spacing as a function of the well-depth  $\epsilon$ , Mass, and melting point temperature.

We've almost got "a", the maximum amplitude for a particle at  $T_m$ . At first glance, it might appear that the max amplitude is equal to the interatomic spacing. However, if two particles are at their max amplitudes there will exist a strong pauli repulsive force from the electron clouds overlapping that will prevent both from reaching the maximum amplitude. That repulsive force is baked right into the Lennard Jones potential. So the question becomes, "what's the minimum separation distance two particles can achieve at a given temperature?". That minimum separation distance will denote the "exclusion zone" that we'll have to shave off of the interatomic spacing. This one's easy, let's just equate the total energy of both particles  $2k_b T$  to the pair particle potential energy function:

$$2k_b T_m = 4\epsilon \left( \left( \frac{r_o}{\frac{1}{2^6} r_{min}} \right)^{12} - \left( \frac{r_o}{\frac{1}{2^6} r_{min}} \right)^6 \right) \quad 2.52$$

So if we set  $r_o$  by choosing  $\epsilon$ , we can solve for  $r_{min}$ . The above equation has a lot of solutions and it's not obvious which ones positive and real until you plug in numbers, but can easily be solved numerically. "a" Then equals:

$$a(\epsilon) = r_o - r_{min} \quad 2.53$$

From this procedure, we get "a" and we get the molar volume as a function of the energy parameter,  $\epsilon$ . Later we'll optimize  $\Delta H$  over  $\epsilon$  To remind ourselves what we're evaluating, copying the formula below:

$$\Delta H = -\frac{f_g N k_b T_m}{z_l} + 3RT_M \ln \left( \frac{a}{3\hbar} \sqrt{\frac{k_b T_m M}{2}} \left( 1 + \frac{\Delta a}{a} \right) \right) - 3f_g N k_b T_m \ln \left( \frac{\theta_D^L}{T_m} \right) \quad 2.54$$

$$+ f_g N k_b T_m \ln \left( \frac{\Lambda^3 z_l}{e \bar{V}_L (1 + z_l)} \right)$$

All that's left is to determine  $f_g$ , the fraction of gas-like molecules. This is pretty straightforward and comes right out of Eyring's analysis (using his definitions here).

$$f_g = \frac{N_g}{N} \quad 2.55$$

Where the fraction of gas molecules is equal to the number of gas molecules divided by avogadros number. The number of gas-like molecules is equal to the number of vacancies,  $N_v$ , multiplied by the coordination number. This says that any particle next to a vacancy becomes gas-like.

$$N_g = N_v Z_l \quad 2.56$$

We can determine the number of vacancies by calculating the total volume available to the gas and dividing it by the volume per vacancy, which is approximately equal to the volume per particle,  $\bar{V}_L$ :

$$N_v = \frac{V_g}{\bar{V}_L (z_l + 1)} \quad 2.57$$

The total gas volume is equal to the free volume introduced during the phase transition. The free volume is often evaluated to be the volume difference between the solid and liquid state. So

$$V_g = V_l - V_s \quad 2.58$$

The liquid volume is just scaled from the solid volume by the lattice expansion on melting ( $\Delta a$ )

$$V_L = V_s + \Delta a^3 \quad 2.59$$

So  $V_g = \Delta a^3$ , or the expansion upon melting. Combing, we get:

$$f_g = \frac{N_g}{N} = \frac{N_v Z_l}{N} = \frac{N_v Z_l}{N} = \frac{V_g}{\bar{V}_L (z_l + 1)} = \frac{\Delta a^3}{\bar{V}_L (z_l + 1)} = \frac{\Delta a^3}{c_1 \left( c 2^{\frac{1}{6}} \sigma \right)^3 (z_l + 1)} \quad 2.60$$

We can see that by setting  $\epsilon$  we get  $\sigma$  and if we set the volume expansion,  $\Delta a$ , we can get  $f_g$  The conclusion is that

$$f_g = f_g(\epsilon, \Delta a) \quad 2.61$$

Now we have everything that we're after. I'm going to re-write the enthalpy equation and highlight some functional dependencies :

$$\Delta H = -\frac{f_g(\epsilon, \Delta a) N k_b T_m}{z_l} + 3RT_M \ln \left( \frac{a(\epsilon)}{3\hbar} \sqrt{\frac{k_b T_m M}{2}} \left( 1 + \frac{\Delta a}{a} \right) \right) \quad 2.62$$

$$- 3f_g(\epsilon, \Delta a) N k_b T_m \ln \left( \frac{\theta_D^L(\epsilon)}{T_m} \right) + f_g(\epsilon, \Delta a) N k_b T_m \ln \left( \frac{\Lambda(M, T_m)^3 z_l}{e \bar{V}_L (1 + z_l)} \right)$$

And if we want it per unit volume, we divide by the molar volume which has the dependence  $V_L = V_L(\epsilon, \Delta a)$ .

### Maximization of $\Delta H_V$

The maximization is very straightforward. We have the objective function  $\Delta H_V(M, T_m, \epsilon, \Delta a)$  and we expect there to be a maximum as we vary  $\epsilon, \Delta a$ , whereas we expect a monotonic increase in  $\Delta H_V$  with  $T_m$  and  $M$ . The maximization looks something like this:

$$\text{Max } H_v(M, T_m, \epsilon, \Delta a) \text{ such that } \frac{\partial H_v}{\partial \epsilon} = 0 \ \&\& \ \frac{\partial H_v}{\partial \Delta a} = 0 \quad 2.63$$

This might be able to be done analytically), but it was very straightforward to implement this numerically. I just meshed the enthalpy function for appropriate ranges of  $\epsilon$  and  $\Delta a$  and took the maximum value. The result is  $\Delta H_{v,max}(T_m, M)$ .

## Results

First, I computed  $\Delta H_{max,V}$  as a function of  $M$  and  $T_m$ . I did this by setting  $M$  and  $T_m$  and varying  $\epsilon$ . There was a clear maximum with respect to epsilon. Then, using that  $\epsilon$  I varied  $\Delta a$ . Again, there was a clear maximum with respect to  $\Delta a$  (usually around 0.25-0.3).

Both can be maximized independently from one another (it gives the same result if I maximize over both simultaneously). The result is shown below: (note the MJ label in the plot title should be GJ).

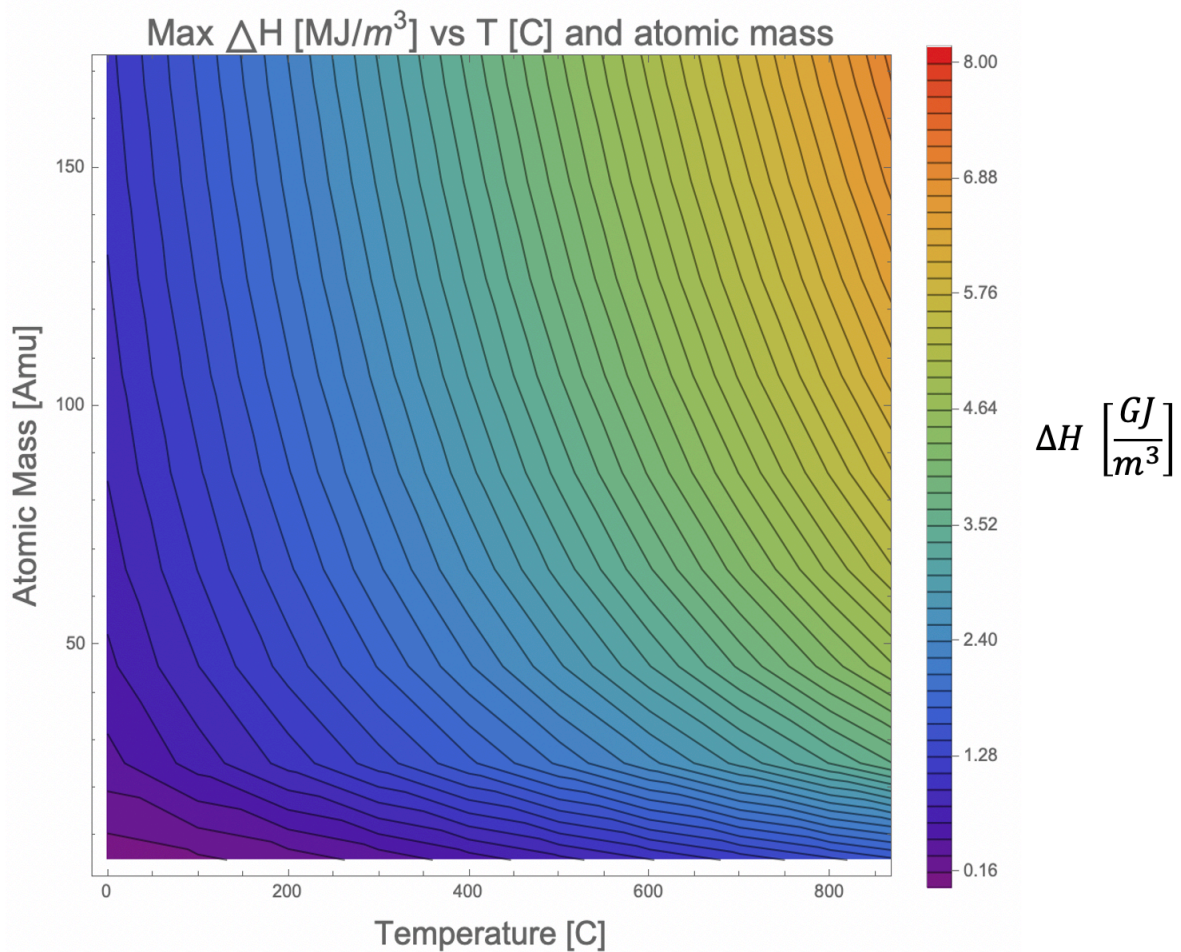


Figure 2.5 Heat Map of optimized enthalpy of fusion per unit volume vs temperature and atomic mass

**It can be seen that at any given temperature, the enthalpy of fusion increases monotonically with Atomic mass.** This makes sense because if you have a larger mass for a given volume, it takes more energy to change its amplitude of vibration.

Next, I computed  $\Delta H_M$  as a function of  $M$  and  $T_m$ . I did this by setting  $M$  and  $T_m$  and varying  $\epsilon$ . There was a clear maximum with respect to epsilon. Then, using that  $\epsilon$  I varied  $\Delta\alpha$ .

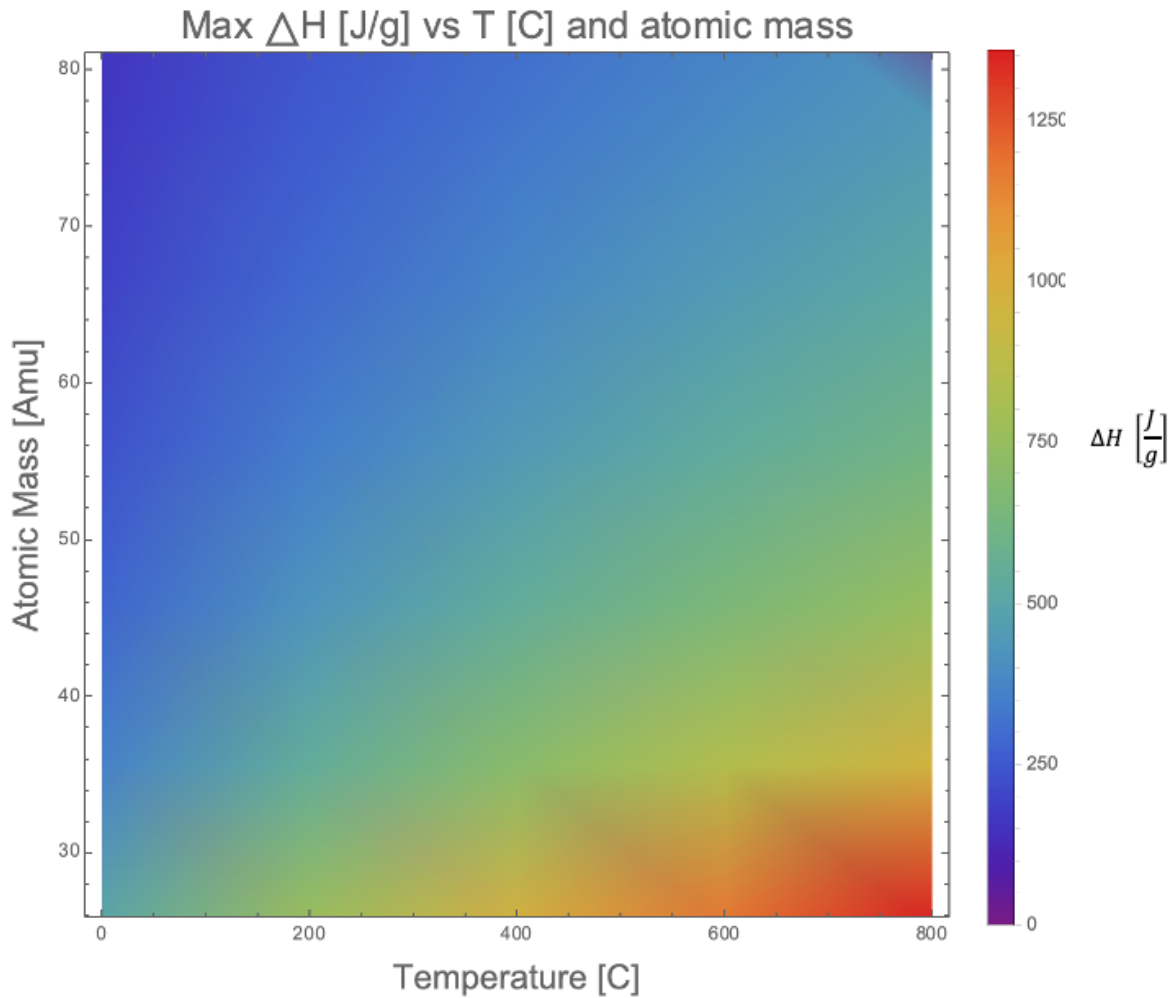


Figure 2.6 Heat map of optimized enthalpy of fusion per unit mass vs atomic mass

**It can be seen that at any given temperature, the enthalpy of fusion decreases monotonically with Atomic mass.**

### **Arriving at a practical limit to $\Delta H_V$ and $\Delta H_M$**

The above plots don't answer the original question:

*What is the maximum enthalpy of transition for a system of atoms in the condensed state at 1 atm in contact with a thermal reservoir?*

As it stands, I require a temperature and mass to give you a maximum enthalpy of melting. However, we just showed that to maximize  $\Delta H_V$  we want to pick a mass as large as possible. Likewise, to maximize  $\Delta H_m$  we want to pick a mass as small as possible.

Let's start with  $\Delta H_V$  – what is the largest mass we can choose in a practical system?

First, I'll argue that the best-case  $\Delta H_V$  scenario comes from a monatomic solid. The argument goes something like this:

If I have  $3N$  atoms, I can get all  $3N$  oscillators to increase the vibrational entropy. But if I have  $3N$  atoms, and I place constraints on those atoms, for example, the system of  $3N$  atoms is composed of molecules, with 4 atoms per molecule, then we automatically reduce the number of oscillators that can increase vibrational entropy.

For 4 atoms per molecule, we get  $3N/4$  oscillators that change vibrational entropy, and  $3N/4$  oscillators that increase librational entropy. So in total you get:

$$\frac{3N}{4} + \frac{3N}{4} = \frac{3N}{2} \quad 2.64$$

In general, this reads:

$$\frac{3N}{n} + \frac{3N}{n} = \frac{6N}{n} \text{ when } n > 3 \text{ and nonlinear} \quad 2.65$$

And

$$\frac{3N}{n} + \frac{2N}{n} = \frac{5N}{n} \text{ when } n = 2 \text{ or linear} \quad 2.66$$

In both cases, the resulting number of oscillators that can increase their vibrational entropy is less than  $3N$ , which you would get in the monatomic case. So, when  $n > 1$ , you always get a smaller entropy change per mole of atoms because there are fewer oscillators available to re-distribute the energy (volume of hyperspace decreases).

The same is true for macromolecules (e.g. polymers), but now anisotropy simply adds a further constraint, decreasing the number of oscillators further.

To get back the same entropy change, you would need to add more atoms. For example, if we have diatomic molecules, 1 mole of those molecules would give you  $\frac{N}{2}$  oscillators. To get  $N$  oscillators, you would need  $2N$  moles. So now you have the same number of oscillators changing entropy at melt, but you've increased your molar volume. Now you have 2 atoms per oscillator (albeit with increased oscillator mass), whereas in a monatomic case you had 1 atom per oscillator for the same entropy change.

**This established then that the best-case  $\Delta H_v$  scenario comes from a monatomic solid.** So what is the max molar mass of a monatomic solid?

We could look at the periodic table and just choose the highest mass possible of a single atom. This would give us Ununbium, element 112, with a mass of 277 amu. However, this isn't very practical because many of the higher atomic weight elements are extremely short-lived or radioactive and will never be used for phase change materials. This is where we have to make a "practical" decision. From scanning the periodic table, it looks like lead is the highest atomic mass element that is non-exotic / radioactive. 1 lead atom has 207.2 amu. So for the best case  $\Delta H_v$  scenario, we set  $M = 207.2$  amu. Now we can carry out the same optimization over  $\epsilon$  and  $\Delta a$  as a function of melting point only. The result is shown below.

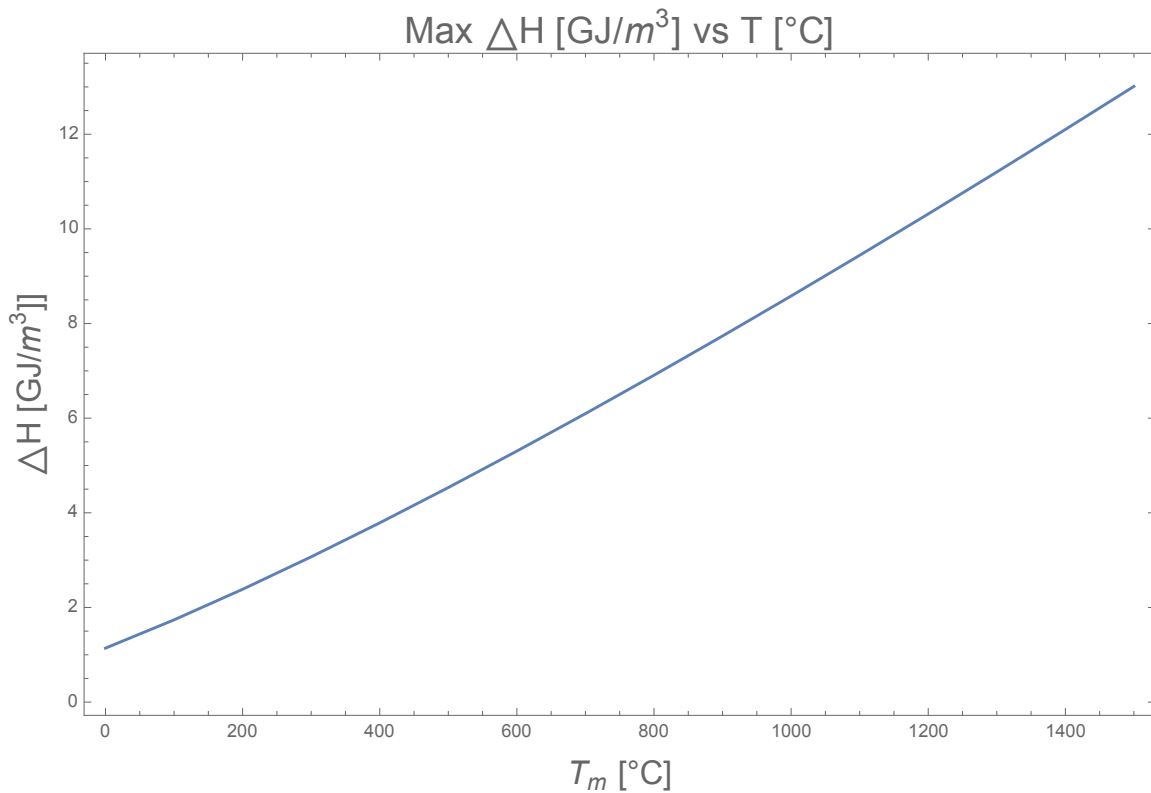


Figure 2.7 Final optimization result for enthalpy of fusion per unit volume

For some context, at 0 celsius water's volumetric enthalpy of melting is about 0.33 GJ/m<sup>3</sup>, or about 33% of the limit. Silicon melts at about 1420 celsius with roughly 4 GJ/m<sup>3</sup>, or again about 33% of the limit. These are two of the highest enthalpy of melting elements/molecules that I've come across, so the limit above at least isn't beaten and seems very reasonable.

### **Maximum $\Delta H_m$**

To maximize  $\Delta H_m$  we want to pick a mass as small as possible. Contrary to maximizing  $\Delta H_v$ , maximizing  $\Delta H_m$  does not require a monatomic solid. For  $\Delta H_v$  we argued that adding extra atoms that don't contribute to the entropy change at melt only serves to add volume, which hurts  $\Delta H_v = \frac{\Delta H}{V}$  because V is increased while  $\Delta H$  nominally stays the same (minus the minor increase you get from increasing the mass from adding atoms). Now, we don't care about the molar volume, so we can add as many non-oscillator-contributing atoms as we want, and increase the molar volume to as large as we want, so long as we maximize  $\Delta H_m = \frac{\Delta H}{M}$ .

This makes it very difficult to come up with a limit for  $\Delta H_m$  without making a suite of assumptions. For this reason, I'll choose to avoid  $\Delta H_m$  for now, because I think any list of assumptions I make will be strongly contested and muddle the discussion of  $\Delta H_v$ , which is of more practical importance for PCM applications

## Full List of of Assumptions made to achieve practical limit

- 1.) Two different mechanical models to represent the free energies of the solid and liquid phases
  - a. Very standard, there is no equation of state that describes both the solid and liquid states. I can provide references for this justification
- 2.) We ignore anharmonicity in our energy states / partition function (each DOF can be described by a harmonic oscillator)
  - a. Very standard, pretty much the only way people can analyze crystals.
- 3.) We assume that the liquid is classical at the melting point.
  - a. Never seen anyone consider liquids using quantum partition functions. Should be very standard.
- 4.) We assume a debye density of states to calculate the average amplitude of vibration in the solid state.
  - a. Weakest assumption
- 5.) We assume a Lennard Jones pair potential to calculate lattice constants
  - a. LJ pair potential can be used to model almost any pair interaction with appropriate choice of constants

**These are the only assumptions we've made. The first 3 are standard and should be completely defensible. The worst assumptions are the last two (Debye DOS / Lennard Jones Pair Potential). There is no good "one size fits all" choice of an intermolecular potential – just ask the MD guys.**

## Chapter 3. Modeling of metastability in the condensed phase

All condensed phase transitions exhibit some sort of metastability (i.e. non-equilibrium behavior) that results in thermal hysteresis. The thermal hysteresis can be understood through proper examination of both the material and system level details. In this chapter, we dive into how the metastability of a material can be theoretically and experimentally characterized, and then tie it to system level details and transport modelling so that we can fully understand the material's metastable behavior in real world applications. We specifically focus on phase change materials (PCM) in condensed systems, and we will use examples in both solid-solid and solid-liquid systems, both of which are relevant for PCM thermal storage applications.

### Introduction

PCM implementation is lagging relative to the abundance of thermal energy, application and opportunity. The lag is in part due to economics, but in larger part is caused by technological barriers, which are widely identified [4,8,9] as (1) low PCM thermal conductivity and (2) excessive supercooling, i.e. the undesirable difference between a material's thermodynamic equilibrium phase change temperature  $T_m$  and the actual value seen in a cooling process with non-zero cooling rate. Low thermal conductivity has been addressed recently by many novel and promising techniques such as the addition of nanoparticles and the impregnation of PCM into graphite matrices [10]. However, the approaches to reduce supercooling by using either nucleating or thickening agents have met with limited success.

In a broader context, fundamental understanding of supercooling – or metastability – remains a grand challenge in the sciences. Phenomenological models, such as classical nucleation theory [10] and its various extensions, provide excellent physical insight into the nucleation process. Although physically successful, the inputs to such models (e.g surface energies, surface shape, free energy barriers) are difficult to know a-priori. For this reason, classical nucleation theory has traditionally been limited to applications requiring experimental fitting, as opposed to experimental prediction [11].

Supercooling changes with just about every material and system parameter: geometry, volume, material, microstructure, purity, discharge rate, etc. Due to the fickle nature of nucleation, predicting the performance of any large-scale practical system based on lab scale data from small scale samples is a difficult task. Phase change is stochastic in nature, and there often exist numerous nucleation pathways that yield the same outcome [12]. As a result, when researchers report a supercooling temperature from lab-scale experiments, that temperature means little beyond that specific experimental system, size, material, and environment. This hampers system-level modeling of PCMs in applications. Given such uncertainty, most numerical models neglect the effect of supercooling entirely [13–15], which results in overly-optimistic predictions of system performance [16]. Thus, from a practical point of view for successful implementation of large-scale PCM systems, there is a pressing need to develop techniques to accurately predict their supercooling temperatures.

For applications with narrow temperature ranges (i.e buildings, refrigeration, medicine), supercooling can be even more limiting. As an example, consider a PCM with a transition temperature of 20 °C used in building applications. If the lowest temperature the building can reach is 15 °C, then the PCM cannot supercool more than 5 degrees. If it does, the PCM will never crystallize and the material will be rendered inert, so that the only thermal energy storage comes from sensible – as opposed to latent – heat. Lacking predictive power, industry often cannot rely on lab-scale supercooling data reported in the literature, and instead find it necessary to perform their own time-consuming and expensive large-scale testing before installations. The inability to use lab-scale data to predict supercooling behavior for larger systems is the key bottleneck in translating research into application.

To overcome the bottleneck, this chapter explores how nucleation theory is inherently coupled to system size and thermal transport phenomena. We first establish a method to characterize the nucleation rate in PCMs using common lab-scale thermal analysis instrumentation (DSC, DTA, T-History). Using the nucleation rate from lab-scale, we show how to predict the supercooling temperature as a function of volume and cooling rate for isothermal (slow) cooling. We then generalize that analysis to calculate the supercooling temperature for an arbitrary geometry, volume, and thermal boundary conditions which result in transient temperature gradients in the system. This enables more accurate supercooling predictions for any system given lab-scale data. The analysis can in principle be used in conjunction with existing numerical methods to accurately incorporate supercooling into phase change models, thus combining material modeling with system modeling. Finally, we validate the methodology outlined by comparing to experimental results in neopentyl glycol (NPG), which shows how the model successfully predicts the changes in subcooling temperature across a large range of cooling rates (2 orders of magnitude) and volumes (3 orders of magnitude).

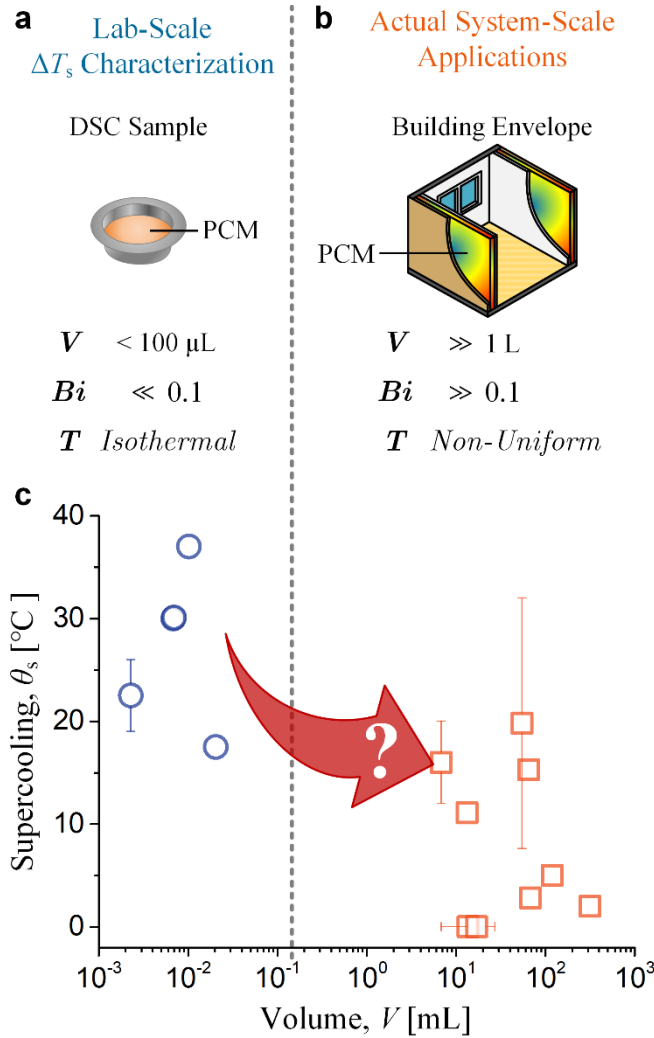


Figure 3.1 Differences in experimental conditions for lab-scale and system-scale PCMs that affect the degree of supercooling ( $\theta_s$ ) of a PCM. (a) A schematic of PCM sample contained in a pan for lab-scale DSC analysis. The volume ( $V$ ) of a PCM sample for DSC is typically less than  $100 \mu\text{L}$ , which makes the Biot number ( $Bi$ ) less than  $0.1$  and the temperature ( $T$ ) distribution of the PCM spatially uniform. (b) A schematic of PCM-embedded building envelopes. PCMs in system-scale applications such as buildings, on the other hand, typically have much larger volume that results in  $Bi$  much higher than  $0.1$  and spatially non-uniform temperature distribution of the PCM. Color gradients in the schematic represents the non-uniform temperature distribution. (c) The literature data of  $\theta_s$  of  $\text{MgCl}_2 \cdot 6\text{H}_2\text{O}$  as a function of volume. Generally,  $\theta_s$  decreases with volume; however, limited understanding of the effects of size and thermal conditions on  $\Delta T_s$  makes the relationship between the lab-scale and system-scale  $\theta_s$  unclear.

## 1. Determining the Nucleation Rate of a lumped PCM

Nucleation is a stochastic process and as such can be described with an appropriate statistical distribution. As mentioned, phenomenological models exist (e.g. Classical Nucleation

theory [10]) to describe that distribution but are difficult to apply in practice for experimental characterization given that multiple input parameters are unknown for the systems of current interest. It is instead more convenient to describe nucleation as a non-homogeneous Poisson process [11,17–21]. A Poisson process is a purely statistical model for a series of discrete events where the average time between events is known, but the exact timing of events is random and memoryless. These assumptions are consonant with nucleation theory, where the average time between nucleation events is given by the reciprocal of the average nucleation rate, but the process is stochastic so that the exact timing of nucleation events is random. The Poisson process further assumes that the nucleation events are independent and cannot occur at the same time. Nucleation is said to be a “*non-homogeneous*” Poisson process because the rate parameter, which in this case is the nucleation rate, may not be constant over time (e.g. when the temperature changes with time). Note that this use of “non-homogenous” is completely different from the nucleation itself being homogeneous or heterogeneous.

The non-homogeneous Poisson distribution has been used in fundamental nucleation studies of metals [11,21], and in solution-crystallization processes [22,23], but not previously for characterizing PCMs. Here we tailor the application of the non-homogeneous Poisson distribution for the workflow of PCM characterization.

We begin by introducing the properties of the distribution of subcooling temperatures. The cumulative distribution function is described by  $CDF(t) = 1 - e^{-\int_0^t \lambda(t') dt'}$ , and the survivor function is  $\chi(t) = 1 - CDF(t)$ , where  $\lambda(t)$  is the Poisson rate parameter which corresponds to the system-wide nucleation events per second, at time  $t$ . In general,  $\lambda(t)$  depends on the number of nucleation sites at the surface and within the volume. Thus,  $\lambda(t)$  is the sum of two contributions so that  $\lambda(t) = VJ_V(t) + AJ_A(t)$  where  $V$  is the system volume,  $A$  is the system surface area, and  $J_V(t)$  and  $J_A(t)$  are the volume-specific and area-specific nucleation rates, respectively. In a given system, normally either  $J_V(t)$  or  $J_A(t)$  will dominate so the nucleation rate can be normalized by only the surface area or the volume. Thus, for a sufficiently large system,  $J(t) = \frac{\lambda(t)}{V}$ , while for a sufficiently small system,  $J(t) = \frac{\lambda(t)}{A}$ . We further note that  $J_V(t)$  has contributions from both heterogeneous and homogeneous nucleation sites within the volume of the system, whereas  $J_A(t)$  has contributions only from heterogeneous nucleation sites at the surface of the system. For the rest of this chapter we will assume the system is large enough so that  $VJ_V(t) \gg AJ_A(t)$ , such that the system’s nucleation physics scales only with the system volume. We also note that in principle, most modeling results obtained below could be easily translated to a system with surface area-dominated nucleation physics ( $AJ_A(t) \gg VJ_V(t)$ ) by suitable exchanges  $J_V(t) \leftrightarrow J_A(t)$  and  $V \leftrightarrow A$ .

To further clarify the scope of the analysis below, we note that in addition to the aforementioned restriction  $VJ_V \gg AJ_A$ , the framework holds only when the system size is much larger than the size of a typical crystal nucleus ( $\sim 10$  nm) for the statistical approach to be valid. We emphasize this restriction because in a typical material there are numerous nucleation pathways that lead to phase transitions, so when the material is characterized at the lab-scale ( $\sim$ mm), the statistical framework draws upon the average of all possible nucleation pathways. If the system size were then reduced such that the original nucleation pathways are suppressed, the determined statistical

distribution would no longer be representative of the true population of nucleation sites and the framework would no longer hold.

In PCM characterization, the independent variable of interest is the temperature rather than the time. Moreover, our goal is to couple nucleation with thermal transport, so we make a change of variables from  $t$  to  $T$  as the independent variable, such that  $T(t) = T$  and  $\frac{dT}{dt} = \dot{T}$ . We also assume that the entire system is initially at the equilibrium phase transition temperature,  $T_m$ , so that the initial condition becomes  $T(t = 0) = T_m$ . In DSC, the most popular PCM characterization technique, the cooling rate is typically constant and the system is “thermally lumped,” such that there are no spatial gradients in temperature. We can then simplify by assuming  $\dot{T} = -\beta$ , where  $\beta$  is the constant cooling rate in degrees Celsius per second, defined to be a positive quantity. If  $\beta$  is not constant,  $\dot{T} = \dot{T}(t)$  in the integration. Applying this change of variables to the survivor function yields:

$$\chi(T) = e^{-\frac{V}{\beta} \int_{T_m}^T J(T') dT'} \quad 3.1$$

The goal is to compute the volume-specific nucleation rate,  $J_V(T)$ , from experimental data, so we invert the survivor function,  $\chi(T)$  [18] :

$$J_V(T) = -\frac{1}{V} \frac{\beta}{\chi(T)} \frac{d\chi(T)}{dT} \quad 3.2$$

The distribution of supercooling temperatures,  $\chi(T)$ , can be determined for a given PCM sample from cooling experiments, and thus from Eq. (2) the nucleation rate can be calculated for the material given the sample volume and the experimental cooling rate. It is crucial that the sample volume be cooled uniformly during supercooling experiments, such that the Biot Number ( $Bi = \frac{hL}{k}$ ) is less than 0.1, where  $L$  is the length scale of the sample which can be estimated as  $L = \frac{V}{A}$ ,  $h$  is the convection coefficient, and  $k$  is the thermal conductivity. An example of this  $J_V(T)$  extraction procedure is discussed in Section 6. We emphasize that this procedure is also valid for surface-dominated nucleation, in which case Eq. 2 would be normalized by the surface area instead of the volume and the result is  $J_A(T)$  rather than  $J_V(T)$ . To determine whether volume-based or surface-based nucleation dominates, the nucleation rate can be measured for multiple, different sized samples in a DSC pan and should be normalized by both the volume and the surface area. The volume-normalized ( $J/V$ ) and surface-area-normalized ( $J/A$ ) measured nucleation rates can then be plotted against supercooling temperature, and whichever normalization collapses on a single line with zero intercept is the dominant nucleation mechanism.

Equation 2 can be evaluated numerically, but in Sections 2-5 it will prove useful to have an analytical form of the nucleation rate. To that end, it is convenient to define a fitting function to the normalized nucleation rate [24]:

$$J_V(T) = \gamma \Delta T^n \quad 3.3$$

where  $\Delta T$  is the difference between the thermodynamic equilibrium phase change temperature  $T_m$  and the actual temperature at any instant in time, i.e., the supercooling. Equation 3 captures the

nucleation behavior of a material with just two empirical parameters,  $\gamma$  and  $n$ . We argue that it is important that researchers report  $\gamma$  and  $n$ , or some other description of the *function*  $J_V(T)$ , when characterizing new PCMs, rather than simply a single number declared to be “the” supercooling temperature. As will be shown, once  $\gamma$  and  $n$  are known, the supercooling behavior of the material in an arbitrary thermal and geometric system can be predicted.

## 2. Predicting supercooling for arbitrary thermal and geometric systems – General theory

Using the nucleation rate determined in Section 1, the goal is to determine the average time it will take for a PCM to nucleate given the system geometry, volume, material properties, and thermal boundary conditions.

In Section 1 we established that the volumetric nucleation rate can be described by just two parameters and the subcooling temperature,  $J_V(T) = \gamma\Delta T^n$ , characterized at the lab scale (e.g. DSC). At this scale ( $V \approx 10 \mu L$ ), we can ensure that the temperature distribution within the PCM is approximately uniform by controlling the sample thickness ( $L < 1 \text{ mm}$ ) and the cooling rate ( $\beta \approx 10 \frac{^\circ\text{C}}{\text{min}}$ ). By doing this, the nucleation probability,  $J_V(T)$ , also becomes approximately uniform in space, ensuring accurate volumetric nucleation rates. In a general system at larger scale, however, the temperature of the material varies considerably with both position and time, and consequently, so does the nucleation probability. *The system’s nucleation probability is therefore inherently coupled to thermal transport phenomena.*

Qualitatively, this indicates that the subcooling probability in each material element  $i$  within the PCM is governed by its own statistical distribution, dependent only on the local subcooling history at that point,  $T(\mathbf{x}_i, t)$ , where the vector  $\mathbf{x}_i$  represents the location of material element  $i$ . Each distribution is characterized by its Poisson rate parameter,  $\lambda_i$  and resides over volume element  $dV_i$ . To determine the global nucleation probability of the material, the distributions must be combined into one. It is known that the combined probability distribution of the sum of independent random variables is equal to the convolution of their individual distributions. Fortunately, for a non-homogeneous Poisson process, the convolution is simply the sum of the individual rate parameters [25]:

$\chi_l(T) = e^{-\frac{V}{\beta} \int_{T_m}^T J_l(T_l) dT_l}$	$\chi_{l+1}(T) = e^{-\frac{V}{\beta} \int_{T_m}^T J_{l+1}(T_{l+1}) dT_{l+1}}$
$\chi_{l+2}(T) = e^{-\frac{V}{\beta} \int_{T_m}^T J_{l+2}(T_{l+2}) dT_{l+2}}$	$\chi_{l+3}(T) = e^{-\frac{V}{\beta} \int_{T_m}^T J_{l+3}(T_{l+3}) dT_{l+3}}$

Figure 3.2. Discretization of a material into multiple non-homogeneous poisson distributions for metastable analysis

$$\sum_i^N \text{Poisson}(\lambda_i) = \text{Poisson}\left(\sum_i^N \lambda_i\right) \quad 3.4$$

where  $N$  is the total number of independent distributions; here,  $N$  is the number of discrete material elements considered. We can then define a global, or an effective, rate parameter,  $\lambda_{eff}(t) = \sum_{i=1}^N \lambda_i(x, y, z, t)$ , or  $\lambda_{eff}(t) = \sum_{i=1}^N J_i(x, y, z, t) V_i(x, y, z)$ . Passing into the limit of infinitesimally small volume elements, so that summation becomes integration, the effective rate parameter of the system at a given time can be rewritten as:

$$\lambda_{eff}(t, \gamma, n) = \int \int \int J(x, y, z, t) dx dy dz = \int \int \int \gamma(T(x, y, z, t) - T_m)^n dx dy dz \quad 3.5$$

and the CDF becomes

$$DF(t, \gamma, n) = 1 - e^{-\int_0^t \lambda_{eff}(t') dt'} \quad 3.6$$

The probability density function (PDF) is obtained directly from Eq. 6 as  $PDF(t) = \frac{dCDF(t)}{dt}$ . The average time that it takes for the first nucleation event to occur can be calculated as the first moment of the PDF, and the standard deviation as the second:

$$t_{avg}(\gamma, n) = \int_0^{\infty} t PDF(t) dt \quad 3.7$$

$$\sigma_t^2(\gamma, n) = \int_0^{\infty} (t - t_{avg})^2 PDF(t) dt \quad 3.8$$

Thus, if  $T(x, y, z, t)$  is known, by applying Eqs. 5-8 the average time until the first nucleation event of the system, as well as the standard deviation of the distribution of these nucleation-onset times, can be calculated from only the two nucleation parameters determined in Section 1. We note that the parameterization of  $J_v$  from Eq. 3 is not unique, and the same procedure (equations 5-8) can be followed with an arbitrary parametrization of  $J_v$ .

Analytical solutions for  $T(x, y, z, t)$  are available only for the simplest geometries and boundary conditions, so in general this procedure must be carried out numerically. Equations 5-8 are naturally discretized in space (index  $i$ ) and time, and can be easily incorporated into existing numerical schemes for PCMs such as finite element methods, the enthalpy method [14], effective heat capacity method [26], and the heat source method [27]. Using any of these methods,  $T(x, y, z)$  can be determined at each time step, and the integral of the nucleation rate as a function of  $T(x, y, z)$  over the volume in Eq. 5 can be calculated to determine the effective global nucleation rate at time  $t$ . Then stepping through time,  $\lambda_{eff}(t)$  can be calculated, and finally from  $\lambda_{eff}(t)$ , the CDF, PDF, and then average time to nucleation can be determined.

This output can then be used to identify when to trigger nucleation in subsequent simulations with single-phase initial conditions, thus providing high resolution and high-fidelity initial conditions for crystallization studies, or nucleation triggers for cyclic performance simulations of PCMs. Conversely, the probability of nucleation at each discrete element and time step can be calculated from equations 5-7, which makes this analysis suitable for Monte Carlo based nucleation simulations. Incorporating either workflow into numerical models will take into account the hysteresis inherent in PCM cycling caused by supercooling and enable more realistic calculations of PCM charge/discharge times, both of which are critical in predicting PCM performance in real-world applications.

### 3. Approximate Solution – Uniform Temperature Distribution

Analytical solutions to Eqs. 5-8 are intractable for most boundary conditions. However, for a spatially uniform i.e. lumped, temperature distribution such that  $T(x, y, z, t) = T(t)$ , and a constant cooling rate  $\beta$ , equation 5 is greatly simplified and the CDF can be evaluated analytically:

$$CDF(T) = 1 - e^{-\frac{V}{\beta} \int_{T_m}^T J(T) dT} = 1 - e^{-\frac{V}{\beta} \frac{\gamma(T-T_m)^{1+n}}{1+n}} \quad 3.9$$

Using this CDF, equations 6-8 can be evaluated (with dependent variable T instead of t), and it has been shown [24,28,29] that the temperature at which nucleation will occur on average, i.e. the average supercooling temperature, as a function of volume and cooling rate can be expressed as:

$$\Delta T_{avg}(V, \beta) = \beta^{\frac{1}{n+1}} \left( \frac{n+1}{\gamma V} \right)^{\frac{1}{n+1}} \Gamma \left( \frac{n+2}{n+1} \right) \quad 3.10$$

where  $\Gamma$  is the gamma function. The average time until nucleation is triggered is then  $t_{avg}(V, \beta) = \frac{1}{\beta} (T_m - T_{avg}(V, \beta))$ :

$$t_{avg}[s] = \frac{1}{\beta} \left( \beta^{\frac{1}{n+1}} \left( \frac{n+1}{\gamma V} \right)^{\frac{1}{n+1}} \Gamma \left( \frac{n+2}{n+1} \right) \right) \quad 3.11$$

Equations (10a) and (11) highlight how even for a single material (fixed  $n$  and  $\gamma$ ), as either  $V$  or  $\beta$  changes, so too will  $t_{avg}$  and the subcooling  $\Delta T_{avg}$ . Note that when  $\beta$  has its traditional units of [ $^{\circ}\text{C}/\text{min}$ ], this expression for  $t_{avg}$  will be in units of [min]. It also is important that the same units are used for  $V$  in both Eq. (10b) and the definition of  $J_V$  used in evaluating  $\gamma$  from Eq. (3), whether [L] and [L], [ $\text{m}^3$ ] and [ $\text{m}^3$ ], etc.

We emphasize that for PCMs in large-scale applications, a lumped temperature distribution is generally a bad approximation. It is valid when  $\frac{hL}{k} < 0.1$ . For natural convection a typical value of  $h \approx 10 \frac{W}{m^2K}$  and for PCMs  $k \approx 0.1 - 0.5 \frac{W}{m \cdot K}$ , so the thickness of the PCM must be less than  $\sim 1 - 5$  mm to justify the lumped approximation, which is not generally useful for large-scale applications. For small-scale applications such as micro-encapsulation,  $L \approx 1 \mu\text{m}$  so equation 10 is generally valid if volumetric nucleation dominates. Furthermore, our statistical approach assumes that the system volume is much larger than the critical nucleus dimension ( $\sim 10\text{nm}$ ), so for composites with nanoscale confinement, further studies should be done to investigate the minimum critical system dimension for the statistical approach to be valid. We can use equation 10 then to interpret the well-known phenomenon that micro-encapsulated PCMs typically exhibit much larger supercooling than a macroscopic-volume sample. We see from equation 10a that  $\Delta T_{avg}$  scales inversely with volume, specifically  $\Delta T_{avg} \propto V^{-\left(\frac{1}{1+n}\right)}$ , so for a smaller volume the supercooling increases, which has crippled many micro-encapsulation efforts [4,30]. This scaling occurs because a reduction in volume implies a reduction in the number of nucleation sites, and the probability of nucleation decreases with the decrease in the number of nucleation sites. Equation 10 can be used as a guide, therefore, in determining promising candidates for micro-encapsulation applications. It is important to note, however, that the volume dominated nucleation may be eclipsed by surface nucleation sites as the length scale decreases. In fact, this has been used to combat supercooling problems in microencapsulated PCMs. To do this, researchers choose

micro-encapsulation materials that have lower surface energies with the PCM, promoting surface nucleation [31,32]. Equation 10a can then be seen as a worst-case scenario supercooling temperature for micro-encapsulation. If the nucleation does not become surface dominated by whatever means, then the degree of supercooling predicted by equation 10a is the largest average supercooling temperature expected. Any surface effects would serve to decrease the extent of supercooling.

#### 4. A Standardized Definition for the Supercooling Temperature

The supercooling temperature is fundamentally different than the phase transition temperature  $T_m$ . The phase transition temperature is determined by information embedded in the atomic details of the system and is well-described by deterministic equilibrium thermodynamics. The supercooling temperature, on the other hand, is *not* a fundamental property of the material because it depends on the kinetics. Phenomenologically, the kinetics are dictated by the distribution of nucleation sites and the energy barriers associated with those sites relative to the thermal energy scale  $k_B T$ , where  $k_B$  is the Boltzmann constant. The number of nucleation sites scales with the volume and/or surface area of the material, and the rate at which those nucleation sites gain access to the available thermal energy from the environment is strongly material and problem dependent. The volume/surface-area scaling, coupled to a strong material-transport dependence, makes defining a meaningful supercooling temperature for a given material challenging. To date, many researchers report supercooling values observed in DSC/DTA, but this value provides only a single point in a complex space defined by equations 6-8. For this reason, researchers testing the same material under different experimental conditions often observe and report different supercooling temperatures.

To make more meaningful comparisons, it would be helpful for the thermal energy storage community to agree upon a standardized reference system for which a supercooling temperature can be defined. Here we choose a reference system that has a volume of 1L with cooling rate  $\beta = 1 \frac{^{\circ}\text{C}}{\text{min}}$  as a demonstration. Treating the system as lumped, we use the solution for a uniform temperature distribution (equation 10a), to obtain an expression for the supercooling temperature of this reference system:

$$\Delta T_{\text{Supercooling, std}} = \left( \frac{1}{60} \left[ \frac{^{\circ}\text{C}}{\text{s}} \right] \right)^{\frac{1}{n+1}} \left( \frac{n+1}{\gamma \cdot 10^{-3} [\text{m}^3]} \right)^{\frac{1}{n+1}} \Gamma \left( \frac{n+2}{n+1} \right) \quad 3.12$$

*To be clear, this definition says that a 1L volume of PCM cooled uniformly at  $1 \frac{^{\circ}\text{C}}{\text{min}}$  will nucleate at  $\Delta T_{\text{Supercooling, std}}$ . With this standardization of  $\beta$  and  $V$ , this definition of  $\Delta T_{\text{Supercooling, std}}$  depends only on  $\gamma$  and  $n$ . Researchers testing the same material under different experimental conditions will still observe different supercooling temperatures, but by determining the nucleation*

parameters  $n$  and  $\gamma$  they can now agree on the supercooling temperature of this reference system. The supercooling performance of a PCM can then be compared by comparing the supercooling behavior of each PCM in this reference system. To summarize, we recommend that researchers report  $\Delta T_{Supercooling, std}$  as well as  $n$  and  $\gamma$  (or some other parameterization of the  $J_V(T)$  function), when studying a new material.

We note that the nomenclature surrounding supercooling phenomena is not standardized. For instance, supercooling temperature, degree of supercooling, subcooling, metastable zone width, degree of metastability, crystallization temperature, hysteresis width, induction time, etc. are often used interchangeably in the literature. Induction time is used when the independent variable is time, so it's less appropriate for this framework. Metastable zone width and degree of metastability are more common in solution crystallization studies, and crystallization temperature is typically limited to solid-liquid phase change phenomena. For these reasons, we opt for "supercooling temperature" because we believe it is appropriately broad to describe general first-order phase transition systems (solid-liquid, solid-solid, liquid-liquid), and common enough such that its meaning is readily understood by the thermal energy storage community.

## 5. NPG Supercooling Characterization

### 5.1 Experimental Characterization of NPG

To validate the methodology outlined in Sections 1-4, we characterize the nucleation rate of neopentyl glycol's (NPG) solid-solid phase change using DSC and then perform larger-scale cooling experiments to test the predictions of Sections 3 and 4. We choose NPG because its transition from one crystal phase to the other crystal phase is sharp, near room temperature ( $T_m = 40.8\text{ }^\circ\text{C}$ ), and it doesn't interact with the aluminum DSC pans so volumetric nucleation dominates. We note that NPG transition is polymorphic, transitioning between two crystalline phases NPG was acquired from Sigma Aldrich at 99% purity, and TA Instrument's DSC 2500 with indium temperature calibration was used. 10 mg of NPG was cycled 150 times from  $25^\circ\text{C}$  to  $50^\circ\text{C}$  in DSC at a heating and cooling rate of  $10\frac{^\circ\text{C}}{\text{min}}$ . The cooling curves from all 150 runs are shown in Fig. 1a. The supercooling temperatures were determined as the first deviation from the linear baseline heat flow signal ( $\frac{W}{g}$ ) that exceeded the minimum accuracy of heat flow on the DSC (first detectable deviation). For the DSC 2500, the minimum deviation is  $20\ \mu\text{W}$ . There was no sign of aging (see Supplementary Information Section 1).

### 5.2 Model Characterization of NPG

The set of 150 supercooling temperatures was then used to calculate the survivor function by taking the number of non-nucleated (surviving) samples at a given temperature and dividing by the total number of samples. For temperatures greater than  $29.3^\circ\text{C}$ , zero samples out of the 150 had nucleated, so the survivor function is equal to 1 (all samples survived) for  $T > 29.3^\circ\text{C}$ , that is  $\Delta T < 11.5^\circ\text{C}$ . Similarly, for temperatures below  $27.1^\circ\text{C}$ , all samples have nucleated, so the survivor function is equal to zero (no samples survived) for  $T < 27.1^\circ\text{C}$  ( $\Delta T > 13.7^\circ\text{C}$ ), as shown in figure 1b. From the survivor function, the nucleation rate as a function of temperature was

calculated using equation 2 and fitted to the power law,  $J_v(T) = \gamma \Delta T^n$ , resulting in  $\gamma = 4.2 * 10^{-33} \frac{1}{K^n sm^3}$  and  $n = 35.87$  as shown in figure 4.3d. To show the goodness of fit, the survivor function (equation 1) is plotted using  $J_v(T) = 4.2 * 10^{-33} \Delta T^{35.87}$  in figure 4.3b. The smooth line shows the survivor function given by the fitted analytical nucleation rate. There is good agreement between the fit and the data. Using equation 11, the standardized supercooling temperature for the reference system defined in Section 5 for NPG is then  $\Delta T_{Supercooling,std} = 8.85^\circ C$  below the equilibrium transition temperature of  $40.8^\circ C$ . It is noteworthy that this  $\Delta T_{Supercooling,std}$  is smaller than the range of supercoolings observed in Fig. 1b ( $\Delta T \sim 12.0 - 13.5^\circ C$ ). This is because the standardized definition of Eq. 11 presumes a larger volume and a slower cooling rate, both of which facilitate nucleation and reduced  $\Delta T$ .

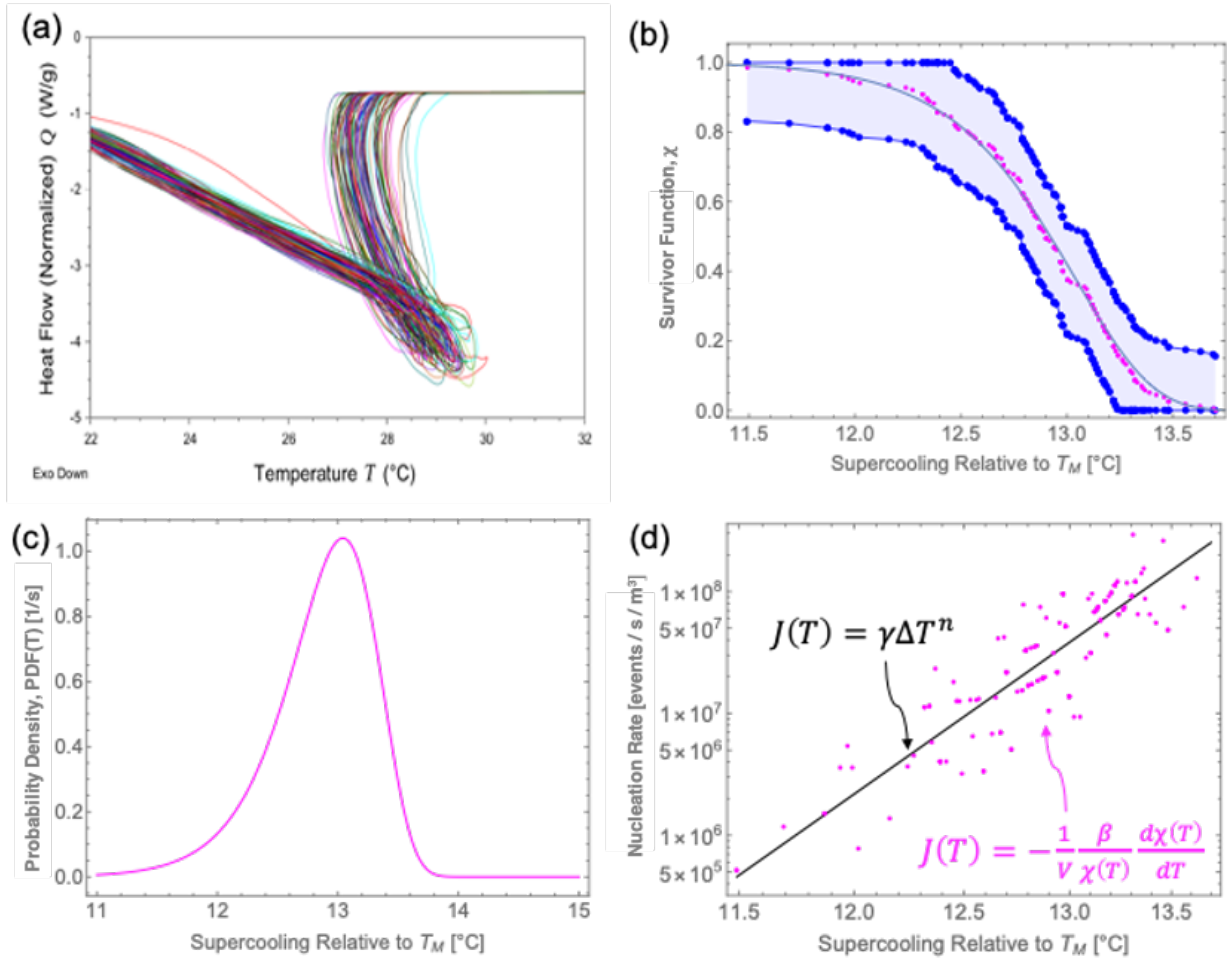


Figure 3.3 (a) Raw DSC data for 150 cooling cycles of 10 mg of NPG at  $\beta=10 \frac{^{\circ}\text{C}}{\text{min}}$ . Each cooling curve exhibits a phenomenon known as recalescence, in which immediately after the onset of a phase transition the rate of heat released is temporarily greater than the rate of cooling, so the material heats itself up for a short time. From these curves, the distribution of supercooling temperatures is recorded. (b) shows the survivor function (magenta) discussed in Section 1, which was calculated from the distribution of supercooling temperatures given by the DSC data in (a). A 95% confidence interval using the DKW inequality is shown in blue surrounding the empirical survivor function. The solid black line shows the fitted CDF from the nucleation parameters,  $\gamma$  and  $n$  using equation 9. (c) The PDF computed from the survivor function,  $PDF(t) = \frac{dCDF(t)}{dt}$ . (d) shows the pointwise nucleation rate (magenta) calculated using a two-point finite difference form of equation 2, and its fit (black solid line) using equation 3. Panels (b)-(d) are referred to  $T_m = 40.8 \text{ }^{\circ}\text{C}$ .

## 6. Experimental Validation of the Model on Solid-Solid Phase Transitions

### 6.1 Experimental Procedure for Validation of Uniform Temperature Distribution Approximation

Using the nucleation parameters characterized via DSC, we can predict how the supercooling temperature will change with volume and cooling rate from equation 10a. To test this prediction, we run cooling experiments for NPG at different volumes spanning 3 orders of magnitude ( $V = 6.0 * 10^{-9}, 2.6 * 10^{-6}, 1.3 * 10^{-5} m^3$ ). For these experiments, the appropriate volume of NPG was melted in an oven and poured into aluminum weigh-boats such that the thickness  $L$  was uniform and less than  $0.5 mm$ , ensuring a uniform temperature distribution during cooling. Three thermocouples with uncertainty  $\pm 0.1^\circ C$  were taped to the opposite sides of each aluminum pan, and the samples were cycled 20 times in an oven at a cooling rate of  $\beta = 0.1 \frac{^\circ C}{min}$ . Nucleation temperatures were recorded as the average supercooling value from each thermocouple for a given sample. We note that the crystal growth rate in NPG appears to be very fast, so that all thermocouples record the nucleation event within 5 seconds of each other and thus there is close agreement among the measurements.

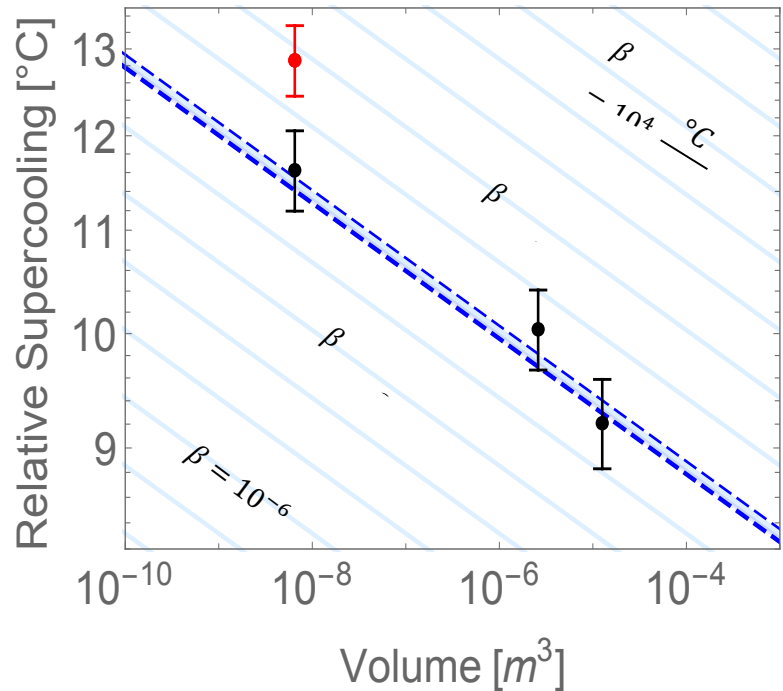


Figure 3.4: Experimental vs. predicted supercooling temperatures (relative to  $T_m$ ) for NPG at different volumes and cooling rates for the uniform temperature distribution approximation. The black dots represent the experimental averages and the vertical lines their standard deviations, all for an experimental cooling rate of  $\beta = 0.1 \frac{^\circ C}{min}$ . The shaded blue region and the dashed blue lines represent the average predicted supercooling temperatures from equation 10a for a cooling rate of  $0.1 \frac{^\circ C}{min}$ , bounded by one predicted standard deviation, using  $\gamma = 4.2 * 10^{-33}$  and  $n = 35.87$  determined from

## 6.2 Experimental Procedure for validation of General Theory

To test the predictions in Section 4 we keep the volume constant at  $V = 2.6 * 10^{-6} m^3$  but vary the aspect ratio, so that the transient cooling is no longer lumped. By varying the geometry, we change the local thermal conditions at each nucleation site. To do this, we iteratively melted  $2.6 * 10^{-6} m^3$  of NPG in an oven and cast them into PTFE tubes of varying diameter, ranging from 0.635 to 1.588 cm. We

note that the PTFE was chosen because the tubes do not interact with NPG, and they are non-stick for easy removal.

Once removed from the PTFE forms, the NPG cylinder (shown in blue in Fig 3) was bridged between two columns of foam (diagonal black hatched lines) such that

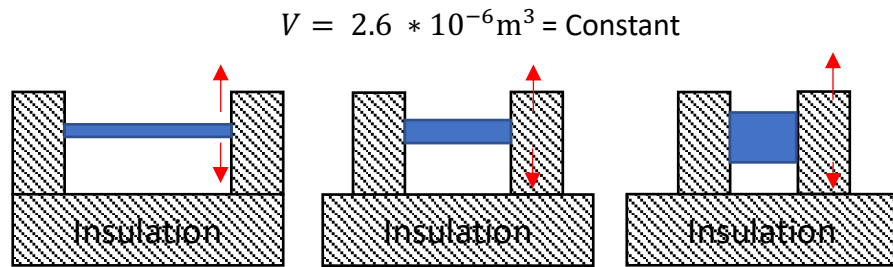


Figure 3.5: Experimental setup to test the general non-lumped theory of Section 4. NPG (blue) was cast into cylinders of varying lengths and diameters, but constant volume. The cylinders were suspended between two foam insulation columns such that the end faces were insulated. Heat transfer is in the radial direction (red arrows) during these cooling experiments.

its end faces were insulated, while its circumferential surface was open to the environment (i.e convective boundary conditions). Thermocouples were placed behind aluminum foil contacting one face of the cylinder, so that the thermocouple tip had no direct contact with the NPG. The NPG cylinders were then equilibrated at  $T_o = 50^{\circ}C$  in an oven for several hours. Then each cylinder was transferred to an environment held at  $T_{\infty}=25^{\circ}C$  to cool by free convection, and the time until nucleation was recorded for each aspect ratio and compared against the predictions given by equations 6-8. For these predictions, edge effects were important, so we used COMSOL Multiphysics to calculate  $T(x, y, z, t)$ . To make these predictions, we first calibrated for the free convection coefficient by placing a thermocouple on the outer surface of an NPG cylinder and measuring the temperature vs time curve and fitting numerical solutions for temperature vs time curves to that data to determine  $h$ . This calibration yielded  $h = 18 \frac{W}{m^2K}$ , taken as constant, which is a reasonable value for free convection and was used for the predictions in figure 4.5.

## 6.3 Results

The experimental results for the uniform temperature distribution approximation are plotted against the predictions made from the nucleation parameters in Figure 4.4. Variations of the prediction with  $\beta$  are shown, and it can be seen that changing  $\beta$  simply offsets the curve, but not the slope, in this log-log plot. Experimental vs predicted values for constant volume but varying  $\beta$  are shown in figure 4.4 for  $\beta = 10^{-1} \frac{^{\circ}C}{s}$  (the three black points) and  $\beta = 10^1 \frac{^{\circ}C}{s}$  (the red point), and the predicted values agree closely with experimental results for the effects of both  $V$  and  $\beta$ .

The predictions of equations 6-8 describing the more general theory are plotted (solid blue line) against experimentally determined nucleation times (black dots) in Figure 4.6. The shaded blue region denotes predictions that are one standard deviation above and below the average nucleation time. There is excellent agreement between equations 6-8 and experimental values. We include two additional curves on the figure to contextualize the importance of including temperature gradients and convective boundary conditions, as described next.

Previous related work [24,28,29] had two key simplifying assumptions: (i) a lumped temperature response (that is,  $T(t)$  only); (ii) constant cooling rate,  $\beta$ . The present work focuses on relaxing both of these requirements by considering non-lumped temperature response (that is,  $(T(x, y, z, t))$ ) and convectively coupled cooling which leads to variable cooling rate. To demonstrate the effect of relaxing these requirements, we show two additional predictions in Figure 4. First, we compare to the lumped constant cooling rate case, where the average nucleation time is given by equation 10b. Because the physical system experienced convective cooling and not constant cooling rate, we approximated a constant cooling rate,  $\beta$ , by evaluating the convective cooling rate at  $t = 0$  from Newton's Law of Cooling. This gives  $\frac{dT}{dt} \Big|_{t=0} = -\beta = -\frac{hA}{mC_p} (T_o - T_\infty)$ . We used this  $\beta$  and the system volume,  $V = 2.6 * 10^{-6} m^3$ , as inputs into equation 10b and the results are plotted as the gray dotted line in figure 4. It can be seen that using the lumped approximation with constant cooling rate gives average nucleation times that are  $\sim 1.5x$  lower than that given by the more detailed treatment of the non-lumped ( $T(x, y, z, t)$ ) with equations 5-8.

Next, we maintained the lumped approximation and relax the constant cooling rate assumption by using Newton's law of cooling  $T(t) = T_\infty + (T_o - T_\infty)e^{-\left(\frac{hA}{mC_p}\right)t}$  to describe the time-dependent convective cooling, which was used as the input into equations 6-8. This ensures that the sample is convectively-coupled to the surroundings with the same value of  $h = 18 \frac{W}{m^2K}$  used in the more detailed simulations. The predictions for this lumped, convective cooling are shown as the gray dashed line in figure 4, and now overpredict the actual cooling time by around a factor of 2. It overpredicts because the lumped assumption ignores large temperature gradients which generally arise near the material surface. The large temperature gradients lead to much lower temperature near the surface, which catalyzes nucleation. Because the lumped assumption ignores these temperature gradients, the catalyzed effect on nucleation is missed, leading to over-prediction. We show these comparisons to highlight the fact that the lumped assumption can easily cause large ( $\sim 2x$ ) errors. Thus, accounting for the temperature gradients within the sample during cooling is very important for an accurate description of a sample's supercooling behavior.

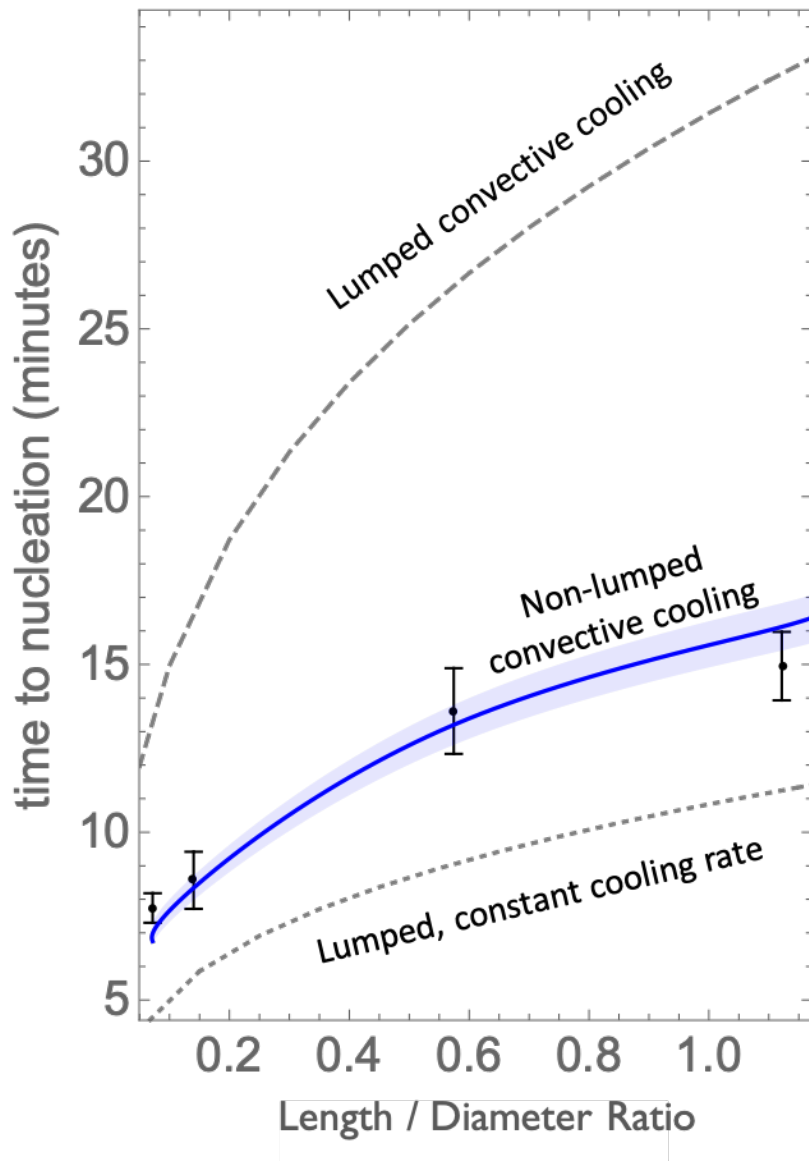


Figure 3.6: Experimental (points) vs predicted (lines) supercooling times for NPG at fixed volume with varying aspect ratio (unitless). See figure 3 for schematic of the experiment. The black points represent the experimental averages and their standard deviations on the vertical. The solid blue line represents the predicted supercooling times from equations 5-8 using  $\gamma = 4.2 \times 10^{-33}$  and  $n = 35.87$ . The blue shaded zone represents  $\pm 1$  standard deviation from equation 8. The gray dashed and dotted lines show predictions for lumped convective and lumped constant cooling cases, and are included to highlight the importance of taking into account temperature gradients (non-lumped) to correctly predict the supercooling behavior of a system.

## 7.) Experimental Validation of the Model on Solid-Liquid phase transitions

The methodology developed in this chapter was shown to work on a solid-solid phase change of neopentyl glycol (NPG)<sup>21</sup>. The solid-solid phase change, however, has limited applications for TES due to its relatively low latent heat. In this section, we further validate the statistical framework with a larger class of PCMs.

I'd like to first emphasize that the upcoming results presented in this section were gathered by Youngsup Song, a Postdoc in our group that I worked with to help extend the validity of this supercooling framework. Many of the words below were directly written by him in preparation of a manuscript. I include this section here because it serves as important validation of the equations developed in this chapter.

To investigate the applicability of our approach for multiple material types, we first characterize the nucleation behaviors for two types of PCMs: an organic and an inorganic material, in this case, a fatty acid and a salt hydrate. Fatty acids have shown potential for TES with great chemical stability and reproducibility over long thermal cycles.<sup>19</sup> Salt hydrates, which are inorganic compounds, have great thermo-physical properties for TES applications, e.g., high latent heat of fusion, thermal conductivity, and density; however, salt hydrates experience significant supercooling, limiting their use in TES despite the great thermo-physical properties.<sup>19</sup> In this section, we test decanoic acid (also known as capric acid) and  $\text{MgCl}_2 \cdot 6\text{H}_2\text{O}$  for the study of fatty acids and salt hydrates, respectively. Based on the statistical analysis of supercooling values ( $\theta_s$ ) from more than one hundred heating-cooling cycles using DSC, we show that nucleation behaviors of both material types can be characterized by a non-homogeneous Poisson distribution. With the statistical characterization of nucleation, we demonstrate the  $\theta_s$  prediction for large-scale  $\text{MgCl}_2 \cdot 6\text{H}_2\text{O}$  samples under both isothermal and non-isothermal conditions. The experimental results showed excellent agreement with our prediction.

At the material level, we characterized both materials in the same manner that we did with NPG using the DSC. We then turned it through the statistical crank developed in the preceding sections, and the survivor function, probability distribution, and nucleation rates are shown in Fig 4.7. For each material, we collected data for three conditions by changing the mass ( $m$ ) and  $\beta$  to investigate the effects of sample size and cooling rate on  $\theta_s$ . For example, in the case of  $\text{MgCl}_2 \cdot 6\text{H}_2\text{O}$  (Figure 2(a – c)), Sample 1 (blue) and Sample 2 (red) have different  $m$  of 1.4 and 19.8 mg, respectively, but the same  $\beta$  of 10 °C/min. Similarly, Sample 2 (red) and Sample 3 (yellow) have the same  $m$  of 19.8 mg but different  $\beta$  of 10 and 1 °C/min, respectively. The results of  $\text{MgCl}_2 \cdot 6\text{H}_2\text{O}$  clearly show the effects of sample size and cooling rate on  $\theta_s$  in Figure 4.7 (a) and 2(b).  $\text{MgCl}_2 \cdot 6\text{H}_2\text{O}$  samples show a wide spread of  $\theta_s$ , ranging from  $\approx 15$  to 40 °C. Compared to Sample 1 (blue), both  $\chi(\theta_s)$  and  $f(\theta_s)$  of Sample 2 (red) shifted to the left, indicating the decrease in  $\theta_s$  with increase in the sample size for the same cooling rate. Likewise, the slower cooling rate of Sample 3 (yellow) resulted in the left-shift of  $\chi(\theta_s)$  and  $f(\theta_s)$  of Sample 3 compared to those of Sample 2 (red) for the same sample size. The results are consistent with our qualitative understanding, that is,  $\theta_s$  decreases with the increase in sample size and decrease in cooling rate. Specifically, a larger sample has a higher probability for nucleation as it has spatially more nucleation sites. Likewise, a slower cooling rate results in a higher probability for nucleation because there are more nucleation attempts. We found a similar result regarding the sample size

with decanoic acid, that is, the decreased  $\theta_s$  with the increase in  $m$  (Sample 1 and Sample 2). The effect of cooling rate, however, was not obvious for decanoic acid. For example, Sample 2 (red) showed a very close  $\theta_s$  distribution with Sample 3 (yellow) with a ten-times slower cooling rate.

Finally, we plotted all the data points of nucleation rate as a function of  $\theta_s$  and fitted them resulting in  $\gamma = 3.17 \times 10^{-10} \text{ } ^\circ\text{C}^{-n} \text{ min}^{-1} \text{ m}^{-3}$  and  $n = 12.38$  for  $\text{MgCl}_2 \cdot 6\text{H}_2\text{O}$  (Figure 2(c)) and  $\gamma = 4.85 \times 10^{-4} \text{ } ^\circ\text{C}^{-n} \text{ min}^{-1} \text{ m}^{-3}$  and  $n = 6.44$  for decanoic acid.

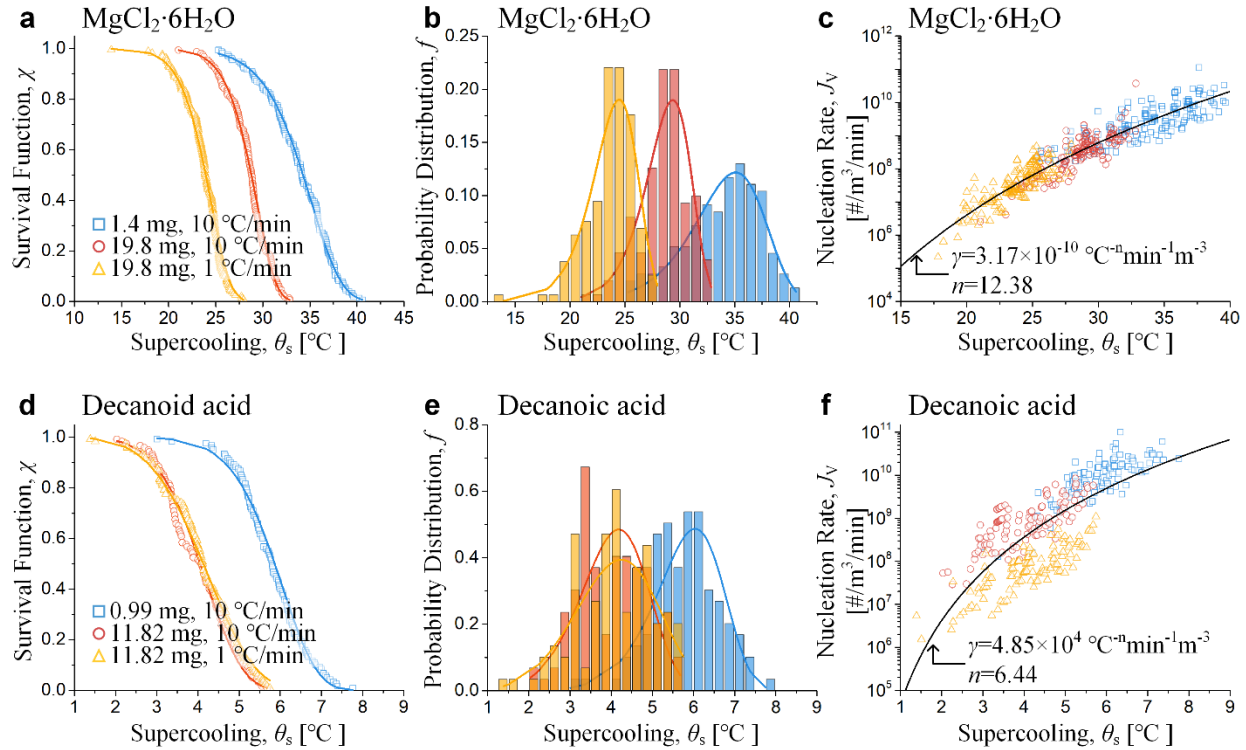


**Figure 3.7** Statistical distributions of  $\theta_s$  and nucleation rates of  $\text{MgCl}_2 \cdot 6\text{H}_2\text{O}$  and decanoic acid obtained by DSC analysis. (a) Survival function and (b) probability distribution function of  $\text{MgCl}_2 \cdot 6\text{H}_2\text{O}$  as a function of  $\theta_s$ . Sample 1 (blue) and Sample 2 (red) have the same  $\beta$  of 10  $^\circ\text{C}/\text{min}$  but different  $m$  of 1.4 and 19.8 mg, respectively. In contrast, Sample 2 (red) and Sample 3 (yellow) have the same  $m$  of 19.8 mg but different  $\beta$  of 10 and 1  $^\circ\text{C}/\text{min}$ , respectively.  $\theta_s$  distributions of three samples show that  $\theta_s$  decreased with the increase of  $m$  and decrease of  $\beta$ . Data points are experimental data. Solid lines show the fitting results of the experimental data with the power law function of  $J_V$ . (c) Volume-specific nucleation rate  $J_V$  of  $\text{MgCl}_2 \cdot 6\text{H}_2\text{O}$  calculated from the survival function. Fitting (black solid line) of all experimental data with the power law  $J_V(\theta_s) = \gamma\theta_s^n$  results in  $\gamma = 3.17 \times 10^{-10} \text{ } ^\circ\text{C}^{-n} \text{ min}^{-1} \text{ m}^{-3}$  and  $n = 12.38$ . (d) Survival function and (e) probability distribution function of decanoic acid. Sample 1 (blue), Sample 2 (red), and Sample 3 (yellow) have  $m$  of 0.99, 11.82, and 11.82 mg and  $\beta$  of 10, 10, and 1  $^\circ\text{C}/\text{min}$ , respectively. While the decrease of  $\theta_s$  from Sample 2 to Sample 3 by the decrease of  $\beta$  is not as apparent as  $\text{MgCl}_2 \cdot 6\text{H}_2\text{O}$ , a similar decreasing trend of  $\theta_s$  was found with the increase of  $m$ . (f)  $J_V$  of decanoic acid calculated from the survival function. The black solid line shows the power-law fit of experimental data with  $\gamma = 4.85 \times 10^{-4} \text{ } ^\circ\text{C}^{-n} \text{ min}^{-1} \text{ m}^{-3}$  and  $n = 6.44$ .

To validate our prediction of the model for scaling to larger sizes, we performed large-scale experiments for  $\text{MgCl}_2 \cdot 6\text{H}_2\text{O}$  in an oven (**Figure 4.8a**). We first filled two different masses (265.7 and 1776 mg) of  $\text{MgCl}_2 \cdot 6\text{H}_2\text{O}$  in a tubing made of the same material (Alodine®-coated aluminum) as a pan and lid used for DSC. This mass is  $\sim 10\text{x}$  higher than that used in DSC. The inner and outer diameters of the tubing were 5.24 and 5.95 mm, respectively. The  $Bi$  of  $\text{MgCl}_2 \cdot 6\text{H}_2\text{O}$  in the

tubing can be evaluated as  $Bi = \frac{d_{PCM}/k_{PCM}}{(t_{Al}/k_{Al})+(1/h)}$ , where  $d_{PCM}$ ,  $k_{PCM}$ ,  $t_{Al}$ ,  $k_{Al}$ , and  $h$  are the diameter and thermal conductivity of  $MgCl_2 \cdot 6H_2O$ , aluminum tubing wall thickness, aluminum thermal conductivity, and convection heat transfer coefficient. Because of the small wall thickness ( $t_{Al}$  of 0.355 mm) and high thermal conductivity of aluminum ( $k_{Al} \approx 170$  W/mK), we can neglect  $t_{Al}/k_{Al}$  compared with  $1/h$  in the denominator as  $Bi \cong \frac{d_{PCM}/k_{PCM}}{(1/h)}$ .  $d_{PCM}$  is equivalent to the inner diameter of tubing (5.24 mm) and the thermal conductivity of liquid phase  $MgCl_2 \cdot 6H_2O$  ( $\approx 0.570$  W/mK) is used for  $k_{PCM}$ .<sup>10</sup> For a typical  $h$  value of 10 W/m<sup>2</sup>K, the  $Bi$  is less than 0.1. Four thermocouples were attached to the outer wall of the tubing to detect the phase change from a sudden change in temperature. The tubing was vertically hung in the oven and tested at two different  $\beta$  of 8 and 0.1 °C/min. We tested 25 cooling cycles for the  $\beta$  of 8 °C/min and 6 cooling cycles for the  $\beta$  of 0.1 °C/min.

We compared the predictions made using the framework with experimental results of oven tests (squares) along with DSC data (circles) in Figure 4.8b. The black solid line indicates the equivalence between the prediction and experiments and grey dashed lines show the  $\pm 20\%$  deviation range. We evaluated the uncertainty of prediction using the DKW inequality and represented the uncertainty as error bars in the plot. Error bars for experimental data represent standard deviations. For all cases, experimental data showed an excellent agreement with our prediction. Also, the oven tests confirmed the dependency of  $\theta_s$  on the system size and  $\beta$  again – larger oven samples showed lower  $\theta_s$  values than DSC samples and the  $\beta$  of 0.1 °C/min resulted in a lower  $\theta_s$  compared to the  $\beta$  of 8 °C/min.

Figure 4.8c and 4.8d show the average and standard deviation of  $\theta_s$  of  $MgCl_2 \cdot 6H_2O$  using Equation with  $\gamma$  and  $n$  values obtained from the DSC analysis. The plots clearly show that both average and standard deviation of  $\theta_s$  decrease with increasing volume and decreasing cooling rate, with the scaling relationship as  $\sim V^{-\frac{1}{n+1}}$  and  $\sim \beta^{\frac{1}{n+1}}$ . These contour maps can serve as *a priori* design guidelines for the optimization of PCM-based applications.

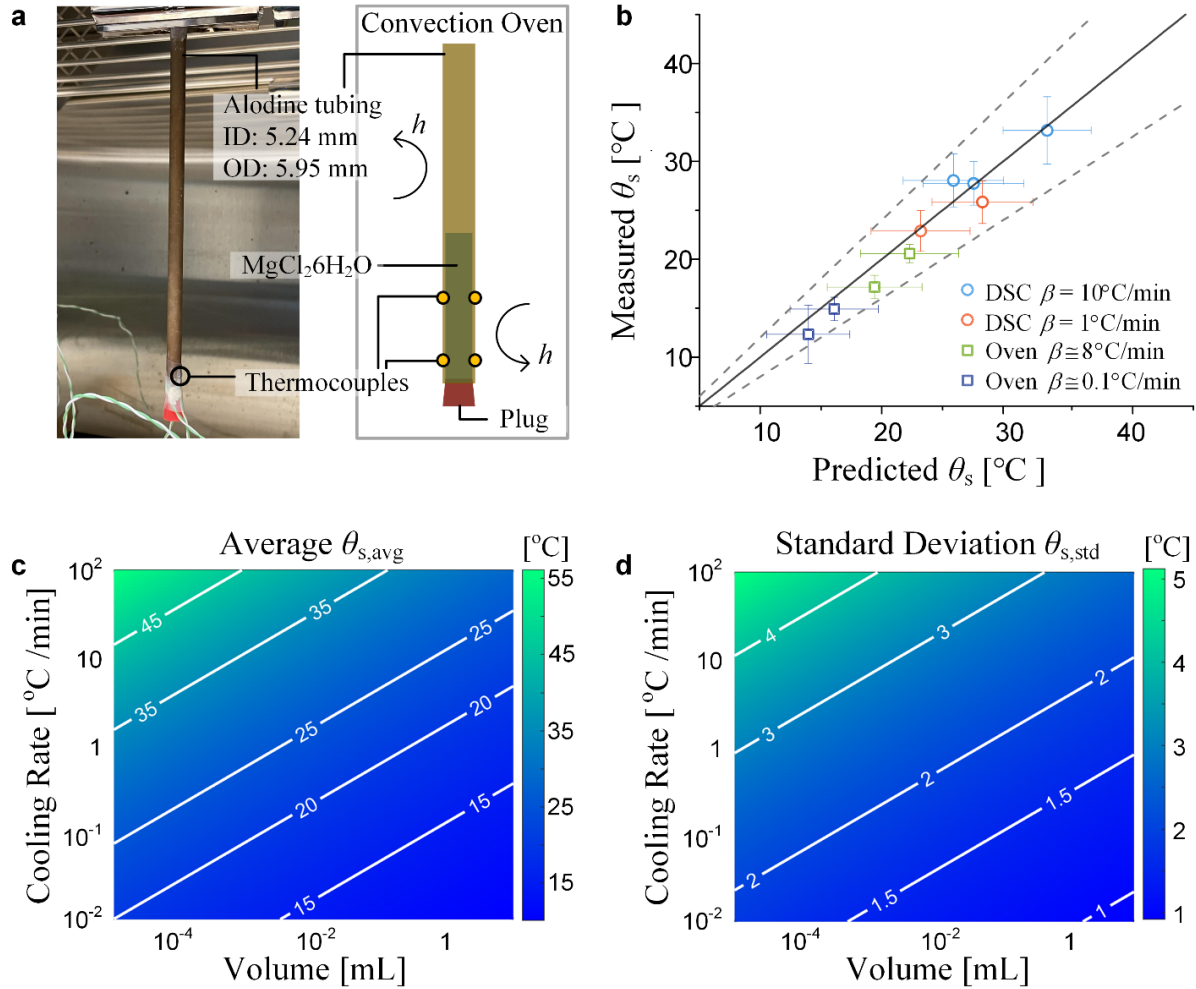


Figure 3.8: Prediction of  $\theta_s$  for lumped thermal capacitance cases. (a) Experimental setup to measure  $\theta_s$  values of large but lumped thermal capacitance samples. An Alodine®-coated aluminum tubing was filled with  $\text{MgCl}_2 \cdot 6\text{H}_2\text{O}$  and vertically hung in an oven. Tubing dimensions were chosen to make sure the  $Bi$  of  $\text{MgCl}_2 \cdot 6\text{H}_2\text{O}$  in the tubing is less than 0.1. Two different  $m$  (265.7 and 1776 mg) and  $\beta$  (8 and 0.1 °C/min) were tested. Four thermocouples were attached to the outer wall to detect the phase change. (b) Experimental results of  $\theta_s$  values (y-axis) measured for large samples in an oven (squares) as well as DSC samples (circles) compared with our prediction (x-axis). A black solid line indicates the equivalence of experiments and prediction. Grey dashed lines show the  $\pm 20\%$  deviation range. Error bars for prediction were evaluated based on the DKW analysis (further details in Section III of Supplemental Information). Error bars for experimental data are standard deviations of measurements. (c) Contour maps of average and (d) standard deviation of  $\theta_s$  as a function of  $V$  and  $\beta$  in log-log scale. Both the average and standard deviation follow the scaling relationship with  $V$  and  $\beta$  as  $\sim V^{-\frac{1}{n+1}}$  and  $\sim \beta^{-\frac{1}{n+1}}$ .

To test our prediction for a non-uniform temperature case (general case), we fabricated an aluminum plate-fin heat exchanger and embedded 31 g of  $\text{MgCl}_2 \cdot 6\text{H}_2\text{O}$  between the fins (**Figure 3.9a**). To prevent corrosion, the entire surface of the heat exchanger was covered with a roughly 500-nm-thick Parylene C layer deposited by chemical vapor deposition. The length ( $l$ ), width ( $w$ ), and height ( $h$ ) of the fins were 30, 3, and 15 mm, respectively. The gap between the fins was 12 mm. We also created four 15 mm-deep holes in two fins and inserted thermocouples to measure temperature change and detect a phase change. After embedding the  $\text{MgCl}_2 \cdot 6\text{H}_2\text{O}$  between the fins, we covered the heat exchanger with a lid and sealed the gap between the lid and heat exchanger using Teflon tape to prevent the loss of vapor. The whole device including the lid had a width of 93 mm, depth of 39 mm, and height of 24.4 mm. We put the PCM-embedded heat exchanger in an oven at 130 °C for  $\approx 210$  min to melt  $\text{MgCl}_2 \cdot 6\text{H}_2\text{O}$  and thermalize the whole device. Then, we took the heat exchanger out and cooled it down at room temperature by natural convection to freeze  $\text{MgCl}_2 \cdot 6\text{H}_2\text{O}$ . We ran eight heating-cooling cycles; on average, the first nucleation occurred in 327 sec with a standard deviation of 41.5 sec. Figure 3.9c shows the temperature change of the first heating-cooling cycle, where a temperature plateau between 45 and 67 min shows the melting, and a temperature spike around 228 min indicates the freezing of  $\text{MgCl}_2 \cdot 6\text{H}_2\text{O}$ .

To get the temperature distribution for  $\theta_s$  prediction, we applied the same conditions for a numerical simulation using COMSOL, that is, the initial temperature condition of 130 °C and cooling by natural convection. The density, heat capacity, and thermal conductivity of  $\text{MgCl}_2 \cdot 6\text{H}_2\text{O}$  were set to be 1460 kg/m<sup>3</sup>, 2250 J/(kg·K), and 0.570 W/(m·K), respectively.<sup>10,32,33</sup> The heat transfer coefficients for natural convection of sidewalls, top, and bottom surfaces were set as 12, 8.8, and 6.6 W/(m<sup>2</sup>·K), respectively, which were measured by separate experiments). Figure 3.9d shows the resulting temperature distribution of the  $\text{MgCl}_2 \cdot 6\text{H}_2\text{O}$  with a horizontal slice-view after 354 sec of cooling. We then calculated the global nucleation rate in time by taking the volume integral of temperature using Equation (13), from which we obtained the PDF. Figure 3.9e shows the resulting PDF in time with  $t_{\text{avg}}$  at 354.3 sec (red vertical line) and  $t_{\text{std}}$  of 18.1 sec (red shadow region). Compared with experimental results ( $327 \pm 41.5$  sec), our prediction ( $354.3 \pm 18.1$  sec) shows an excellent agreement with only  $\approx 8\%$  deviation. As an example, we compared our prediction with the freezing point of the first cooling experiment in Figure 3.9f. Figure 3.9f shows the temperatures measured by four thermocouples during the cooling period of Figure 3.9c along with our prediction of  $t_{\text{avg}}$  (red vertical line) and  $t_{\text{std}}$  (red shadow region). In this case, the nucleation occurred at 358 sec with only 4 sec difference from our prediction. The excellent agreement with experimental measurements confirms the prediction capability of our framework for a system with an arbitrary geometry and thermal conditions.

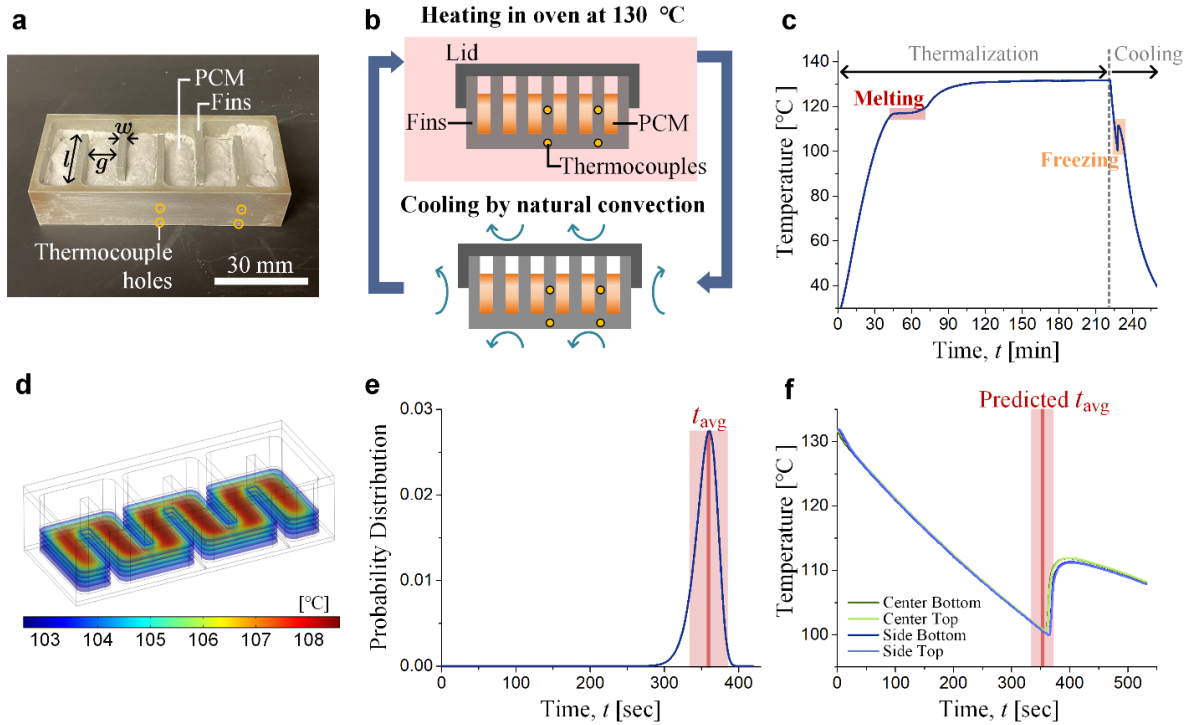


Figure 3.9: Prediction of  $t_{avg}$  and experimental validation for a PCM ( $MgCl_2 \cdot 6H_2O$ ) with non-uniform temperature distribution. (a) A PCM-embedded plate-fin heat exchanger. The heat exchanger is made of aluminum with  $\approx 50$ -nm-thick Parylene C covering the entire surface to protect from corrosion. Four thermocouples were inserted into the fins to measure the temperature change. (b) A schematic of heating-cooling cycle experiments. During heating, the PCM melts and the whole device thermalizes at 130 °C in an oven; then, the device was cooled at room temperature by natural convection for nucleation. (c) A temperature profile of a heating-cooling cycle measured by embedded thermocouples. The red shadow region between 45 and 67 min shows the phase transition from solid to liquid at the melting temperature, and the yellow shadow region around 228 min shows the temperature spike due to the freezing. (d) A COMSOL simulation of temperature distribution in the PCM after 354 sec of cooling from the initial temperature of 130 °C. (3) A PDF of nucleation calculated from COMSOL simulation. The  $t_{avg}$  for nucleation was calculated as 354.3 sec with the  $t_{std}$  of 18.1 sec. (f) Comparison of experimental data of the first cooling experiment with our prediction. Four lines show the temperature profile measured by thermocouples. The freezing point (temperature spike) at 358 sec shows an excellent agreement with our prediction of 354.3 sec.

## Conclusion

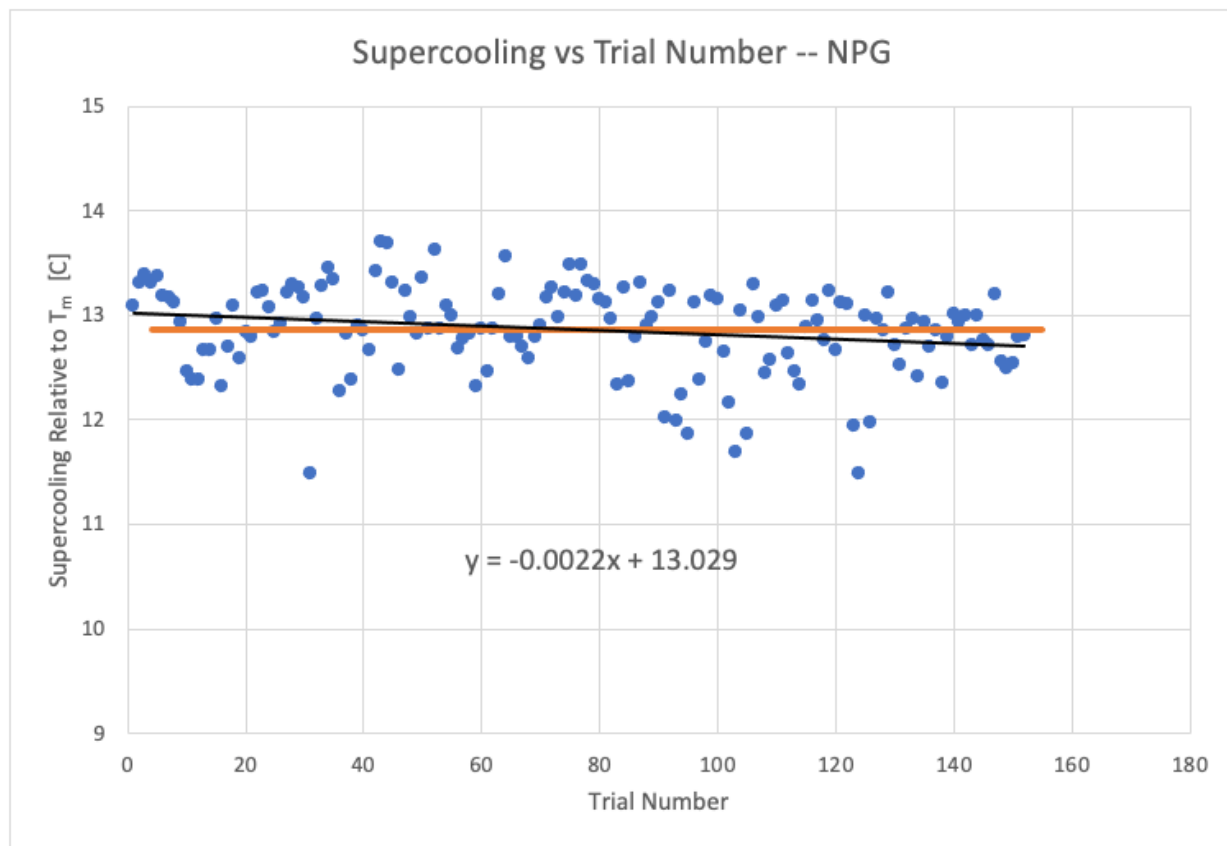
Using lab scale experimental data to predict supercooling performance in large scale thermal energy storage applications is crucial for the analysis and prediction of PCM performance metrics. This chapter has outlined experimental characterization techniques for supercooling in thermal energy storage applications and developed a theoretical framework to use that characterization for prediction of supercooling in a generalized system, which may be much larger than the lab scale

and include substantial temperature gradients. The analysis can be used in conjunction with existing numerical methods to accurately incorporate supercooling into phase change models, thus combining material modeling with system modeling. This framework has been validated by comparing to experimental results in neopentyl glycol, salt hydrates, and fatty acids, which shows how the model successfully predicts the changes in subcooling temperature across a large range of cooling rates (2 orders of magnitude) and volumes (3 orders of magnitude). To expand this framework, future efforts should explore the characterization of more exotic and complex materials (e.g. polymers, mixtures).

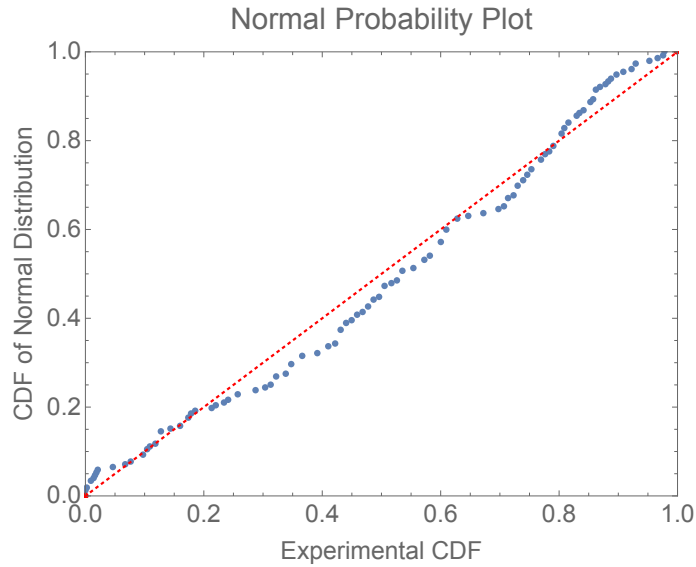
## Additional Information

### 1. Experimental Supercooling Data and Quality of Distribution

10mg of NPG was cycled 150 times from 25°C to 50°C in a DSC at a heating and cooling rate of  $10 \frac{^{\circ}\text{C}}{\text{min}}$ . The cooling curves from each run are shown in figure 1 of the main text. The supercooling temperatures were determined as the first deviation from the heat capacity that exceeded the minimum accuracy of heat flow on the DSC (first detectable deviation). For the DSC 2500, the minimum deviation is  $20 \mu\text{W}$ . The extracted values are plotted below as a function of trial number.

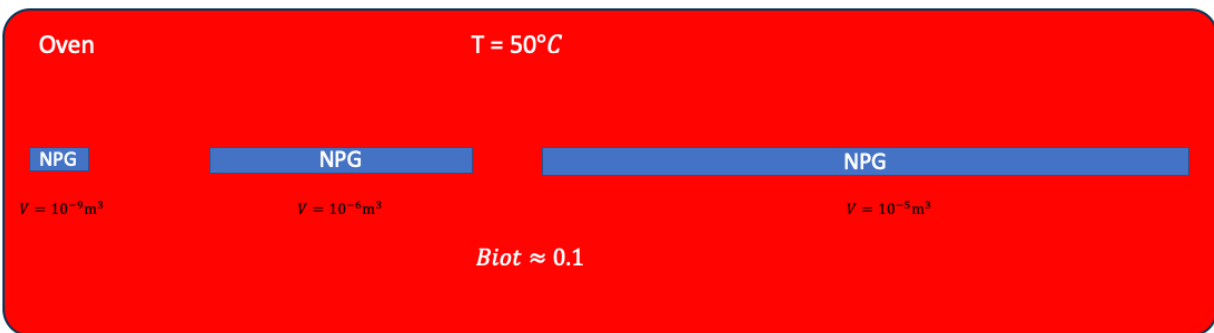


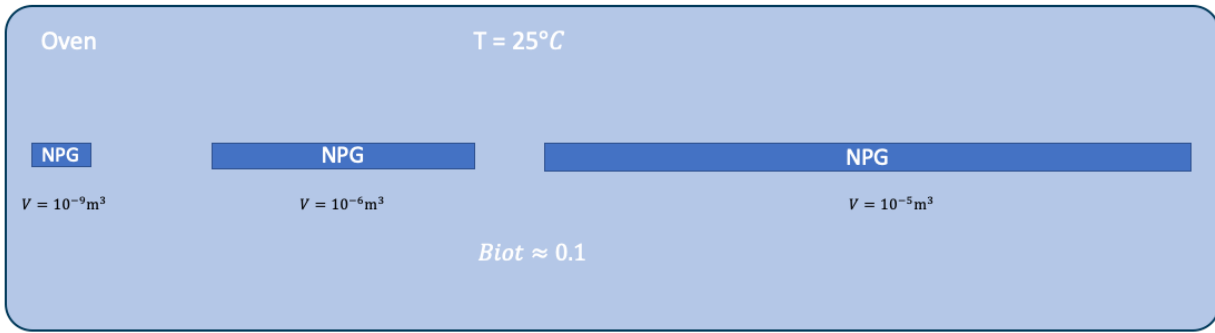
To check for signs of material aging, we provide a linear fit (black solid line) to the data, and compare that with the average of the distribution (orange solid line). It is seen that the average fit is nearly constant vs trial number, indicating little to no aging. In addition, we take the raw data and generate a normal probability plot. This plots the CDF of the experimental data vs the CDF of a theoretical normal distribution. If the experimental data is perfectly normally distributed about the mean, the plot would show a straight 45° line. As can be seen from the normal probability plot below, the experimental data is approximated well by a normal distribution, indicating that there is negligible aging or systematic bias.



## 2. Experimental Setup for Uniform Temperature Distribution Approximation

The figure below depicts the hot and cold conditions used to cycle the NPG samples for the uniform temperature distribution approximation experiments.



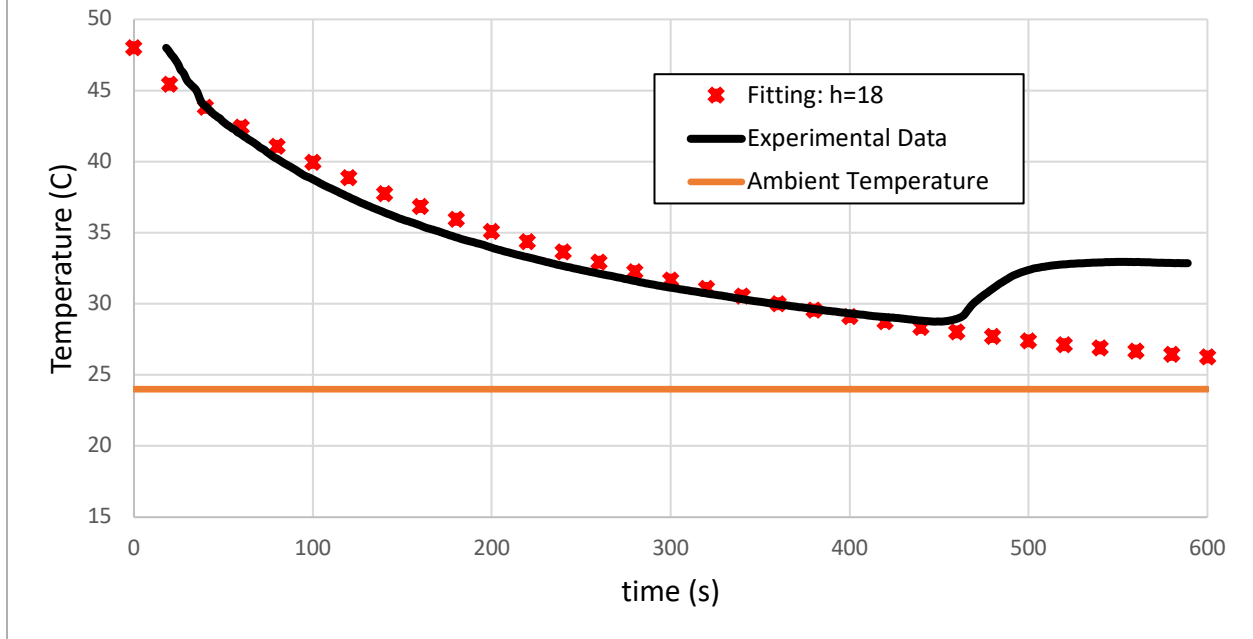


Cycled 20x

### 3. Convection Heat Transfer Coefficient Calibration

To make the predictions in figure 4, we needed to calibrate for the convection coefficient. We calibrated by placing a thermocouple on the outer surface of a  $\frac{3}{8}$ " diameter NPG cylinder, equilibrating the NPG at  $50^{\circ}\text{C}$ , and then measuring the temperature vs time curve after it was brought to ambient at  $24^{\circ}\text{C}$ . To find the convection heat transfer coefficient associated with the experiment, we solved for the temperature vs time of the equivalent physical and geometric system in COMSOL Multiphysics, and fitted the numerical solutions to the experimental data to determine  $h$ . The calibration yielded  $h = 18 \frac{\text{W}}{\text{m}^2\text{K}}$  which is a reasonable value for free convection and was used for the predictions in figure 4. The abrupt spike in temperature around 450 seconds indicates that the lower temperature NPG phase has nucleated. Once nucleated, the NPG releases its latent heat. The temperature rises abruptly because the rate of energy release is greater than the rate of cooling (recalescence), so the material will self-heat until it reaches its equilibrium melting temperature.

## Heat Transfer Coefficient Calibration



Symbol	Meaning	Units
CDF	Cumulative Distribution Function	Unitless
PDF	Probability Density Function	$\frac{1}{s}$
$\chi(t)$	Survivor Function	Unitless
$\lambda(T)$	Total system nucleation rate	$\frac{\text{nucleation}}{s}$
$J_V(t)$	Total system nucleation rate divided by the volume of the system	$\frac{\text{nucleation}}{s \cdot m^3}$
$J_A(t)$	Total system nucleation rate divided by the area of the system	$\frac{\text{nucleation}}{s \cdot m^2}$
$\beta$	Cooling rate for uniform temperature approximation	$\frac{^\circ C}{s}$
$Bi$	Biot Number	Unitless
$L$	Length Scale of system	m
h	Convective heat transfer coefficient	$\frac{W}{m^2 K}$
k	Thermal conductivity	$\frac{W}{m \cdot K}$
$\gamma$	Fitting parameter in $J_V(T) = \gamma \Delta T^n$	$\frac{\text{nucleation}}{s \cdot m^3 \cdot K^n}$
n	Fitting parameter in $J_V(T) = \gamma \Delta T^n$	Unitless
V	Volume of PCM system	$m^3$
$T_m$	Equilibrium melting point	C
A	Surface area of PCM system	$m^2$
t	Time elapsed as system is cooled from equilibrium melting point	S
i	Representative statistical distribution for each material element (see equation 4)	Unitless
$x_i$	Coordinate vector specifying the position at which the statistical distribution is evaluated	m

Table 3: List of Symbols and Variables

## References

- [1] I. Gur, K. Sawyer, and R. Prasher, *Science* (80-. ). **335**, 1454 (2012).
- [2] A. Henry, R. Prasher, and A. Majumdar, *Nat. Energy* **5**, 635 (2020).
- [3] A. S. B. Ankit Gupta, *Thermal Energy Storage Market Size By Storage Material (Water, Molten Salt, PCM), By Technology (Sensible Heat, Latent Heat, Thermochemical), By Application (Power Generation, District Heating & Cooling, Process Heating & Cooling), By End-Use (Residential)* (2018).
- [4] A. Safari, R. Saidur, F. A. Sulaiman, Y. Xu, and J. Dong, *Renew. Sustain. Energy Rev.* **70**, 905 (2017).
- [5] Y. Peng and Y. Cui, *Joule* **724** (2020).
- [6] A. K. Stark and J. F. Klausner, *Joule* **1**, 416 (2017).
- [7] Z. Ling, Z. Zhang, G. Shi, X. Fang, L. Wang, X. Gao, Y. Fang, T. Xu, S. Wang, and X. Liu, *Renew. Sustain. Energy Rev.* **31**, 427 (2014).
- [8] F. Souayfane, F. Fardoun, and P. H. Biwole, *Energy Build.* **129**, 396 (2016).
- [9] J. Pereira da Cunha and P. Eames, *Appl. Energy* **177**, 227 (2016).
- [10] V. I. Kalikmanov, in (Springer, Dordrecht, 2013), pp. 17–41.
- [11] G. Wilde, J. L. Sebright, and J. H. Perepezko, *Acta Mater.* **54**, 4759 (2006).
- [12] W. Sun and G. Ceder, *CrystEngComm* **19**, 4576 (2017).
- [13] K. Biswas, J. Lu, P. Soroushian, and S. Shrestha, *Appl. Energy* **131**, 517 (2014).
- [14] S. Morales-Ruiz, J. Rigola, C. Oliet, and A. Oliva, *Appl. Energy* **179**, 1006 (2016).
- [15] X. Jin, M. A. Medina, and X. Zhang, *Appl. Therm. Eng.* **103**, 1057 (2016).
- [16] K. D'Avignon and M. Kummert, *Appl. Therm. Eng.* **99**, 880 (2016).
- [17] S. Jiang and J. H. Ter Horst, *Cryst. Growth Des.* **11**, 256 (2011).
- [18] A. Filippini, A. Di Cicco, and E. Principi, *Phys. Rev. E - Stat. Nonlinear, Soft Matter Phys.* **86**, (2012).
- [19] V. Bhamidi, P. J. A. Kenis, and C. F. Zukoski, (2017).
- [20] J. Bokeloh and G. Wilde, (n.d.).
- [21] J. Bokeloh, R. E. Rozas, J. Horbach, and G. Wilde, *Phys. Rev. Lett.* **107**, (2011).
- [22] G. M. Maggioni and M. Mazzotti, *Cryst. Growth Des.* **17**, 3625 (2017).
- [23] G. M. Maggioni, L. Bosetti, E. Dos Santos, and M. Mazzotti, *Cryst. Growth Des.* **17**, 5488 (2017).
- [24] N. Kubota, *J. Cryst. Growth* **418**, 15 (2015).
- [25] J. Kingman, *Poisson Processes* (1993).
- [26] D. Heim, *Renew. Energy* **35**, 788 (2010).
- [27] F. Mathieu-Potvin and L. Gosselin, *Int. J. Therm. Sci.* **48**, 1707 (2009).
- [28] N. Kubota, Y. Fujisawa, and T. Tadaki, *J. Cryst. Growth* **89**, 545 (1988).
- [29] N. Kubota, *J. Cryst. Growth* **345**, 27 (2012).
- [30] E. Günther, L. Huang, H. Mehling, and C. Dötsch, *Thermochim. Acta* **522**, 199 (2011).
- [31] F. Cao and B. Yang, (2013).
- [32] X. Tang, W. Li, X. Zhang, and H. Shi, *Energy* **68**, 160 (2014).

## Chapter 4. Manipulation of thermochemistry for enhanced thermal fluids and pumpable thermal energy storage

Thermal fluids are used as heat transfer fluids and thermal energy storage media in many energy technologies ranging from solar thermal heating to battery thermal management. The heat capacity of state-of-the-art thermal fluids remains  $\sim 50\%$  of water (which suffers from a limited operation range between  $0\text{ }^{\circ}\text{C}$  and  $100\text{ }^{\circ}\text{C}$ ) and their viscosities are typically more than one order of magnitude higher than that of water. Our results demonstrate that the heat capacity of the proposed thermochemical fluid is significantly higher than state-of-the-art thermal fluids over a broad temperature range and is also higher than that of water between  $60$  and  $90\text{ }^{\circ}\text{C}$ . The viscosity of our liquid is only 3 times higher than that of water and the operating temperature range is between  $-90\text{ }^{\circ}\text{C}$  –  $135\text{ }^{\circ}\text{C}$ . Furthermore, a model was developed allowing for novel design of thermochemical thermal fluids in the future with even higher heat capacity.

### Introduction

Approximately  $90\%$  of world's current energy technologies involve thermal processes<sup>1</sup>. Examples include conversion of solar energy to heat<sup>2</sup>, conversion of waste heat to electricity<sup>3</sup>, thermal storage<sup>4</sup>, cooling and heating of buildings<sup>5</sup> and thermal management of various energy devices such as batteries<sup>6</sup>, microelectronics, electrical transformers<sup>7</sup>. For example, there is significant interest in using solar thermal processes to decarbonize industrial heating; it is expected that industrial processes requiring medium temperature ( $< \sim 150\text{ }^{\circ}\text{C}$ ) heat can be economically decarbonized using solar thermal processes. For high power microelectronics<sup>8</sup> and high energy density and fast charging lithium ion batteries<sup>9</sup>, thermal management plays a very important role for reliable operation of these technologies. Other examples of thermal management include cooling of both traditional<sup>7</sup> and solid state<sup>10</sup> electrical transformers. Thermal fluids play a dominant role in all these energy technologies. Thermal fluids are used both as heat transfer fluid (HTF) and as thermal energy storage (TES) for different temperature ranges in solar thermal<sup>11</sup> and building applications. A good thermal fluid should possess: i) a high specific heat ( $C_p$ ), ii) a low freezing temperature, iii) a higher boiling point (depending on the application), iv) a higher thermal conductivity ( $k$ ), and v) a low viscosity. Both the cooling power and thermal storage capacity of thermal fluids are proportional to  $C_p$  whereas thermal and fluid resistance are dependent on thermal conductivity and viscosity, respectively. There is more freedom in designing systems with lower thermal resistance as it also depends on heat exchanger design. For example, microchannel-based heat exchangers have much smaller thermal resistance for a given fluid than larger heat exchangers<sup>12</sup>.

Among various thermal fluids used in practice and investigated in the literature, water has some of the best properties. The  $C_p$  of current thermal fluids (usually less than  $2\text{ J/g}\cdot\text{K}$ ) has remained significantly below that of water ( $4.2\text{ J/g}\cdot\text{K}$ ). The viscosity of these thermal fluids is also much larger than water. Despite possessing great thermal and flow properties, the use of pure water as thermal fluid is rather limited because of its high freezing point ( $0\text{ }^{\circ}\text{C}$ ) and low boiling point ( $100\text{ }^{\circ}\text{C}$ ). Therefore, water is typically mixed with antifreeze liquids such as ethylene or propylene glycols which significantly degrades its' thermal properties. From a molecular point of view, water has very high  $C_p$  due to hydrogen bonds ( $10\text{--}30\text{ kJ/mol}$ ) whereas other thermal fluids such as mineral oil have low  $C_p$  due to weak van der Waals bonds ( $< 5\text{ kJ/mol}$ ). Covalent bonds typical have bond strengths of hundreds of  $\text{kJ mol}^{-1}$ . This makes thermochemical heat transfer fluids based

on the formation and breaking of covalent bonds in the liquid phase very attractive as it can potentially lead to higher effective  $C_p$ .

### **Use of Diels-Alder thermochemical reaction for thermal fluids**

In the 1980s, the idea of using reversible liquid-phase chemical reactions to store heat was proposed and some initial efforts were attempted<sup>13-16</sup>. Using calorimetry, Sparks and Poling<sup>16</sup> measured the heat of reaction and equilibrium constant for the Diels-Alder reaction between maleic anhydride and dilute 2-methyl furan. Based on measured heat of reaction and equilibrium constant and an equilibrium theoretical model they proposed that a hypothetical reaction mixture at a high concentration (7 mol/L) could achieve an apparent  $C_p$  of 7.37 J/cm<sup>3</sup>·K, 76% higher than that of water. However due to the lack of theoretical/first principle calculations and experimental tools the potential of Diels-Alder thermal fluids was never realized and many technologically and scientifically relevant questions were never answered. Those are: 1) Direct measurement of  $C_p$  for Diels-Alder reactions as a function of temperature is still missing. 2) Since no measurement of  $C_p$  has ever been made, the impact of cycling and reversibility on the performance is not known – both of which are critical from the technological point of view 3) Lacking experimental data, it is not clear if the equilibrium model holds or if kinetics become important 4) Viscosity of these liquids was also not reported, which is important from the technological point of view to understand the pressure drop and pumping requirements.

The concept has since been largely overlooked by the research community and little progress has been made in this area. We recently proposed theoretically that the specific heat of liquids can be greatly enhanced by reversible chemical reactions<sup>17</sup> by combining density functional theory (DFT) calculations with an equilibrium thermal model. More recently, we used density functional theory (DFT) calculations to virtually screen for thermally reversible Diels–Alder reactions that could take place in water and identified several candidate reactions for the potential applications in HTF and TES<sup>18</sup>.

Here, we present experimental results for the enhancement of specific heat capacity of liquids enabled by reversible Diels–Alder reactions in an organic solvent. To the best of our knowledge, this is the first direct experimental validation of this concept and offers evidence for the future development of high specific heat storage and transfer liquids based on thermally reversible chemical reactions. We also conducted cycling experiments and viscosity measurements to answer the questions raised above. We report the results of preparing several concentrations of the 2-methylfuran and maleic anhydride in a solution of dimethylformamide (DMF) and performing calorimetry tests. We have also modified the macroscale  $C_p$  model based on the equilibrium model proposed by Sparks and Poling<sup>16</sup> and further developed by us<sup>17</sup> to include chemical kinetics as the equilibrium model does not match in trend and magnitude with the experimental data. Furthermore, the macroscale  $C_p$  model including chemical kinetics is combined with first principles calculations using density functional theory (DFT) for chemical parameters such as transition state enthalpy and entropy to validate the experimental results. Finally, we conclude this chapter with a discussion on the future outlook and potential research directions.

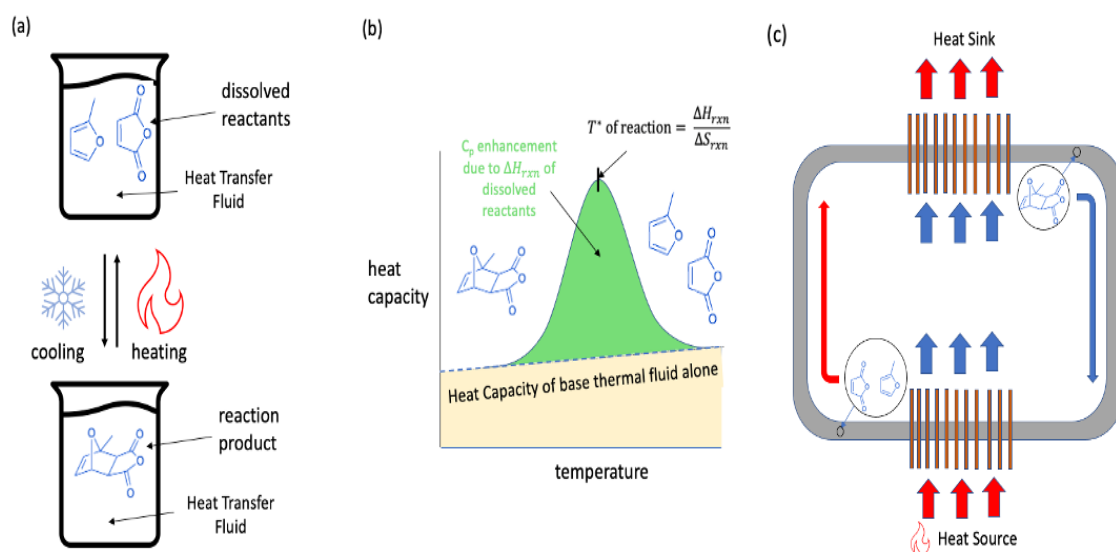


**Figure 4.1:** The heat capacity of a heat transfer fluid is enhanced by adding reactants that absorb energy when heated and release energy when cooled. (a) shows the physical mechanism of the enhancement in which the reactants break weak covalent bonds to form a rigid ring (b) depicts the thermodynamic effect on the heat capacity where the transition enthalpy is distributed over a large temperature range as a result of equilibrium between the reactants and products. (c) shows how the heat transfer fluid behaves at the system level, absorbing extra energy from the heat source by breaking the ring structure of the reaction product, and subsequently transferring extra energy to the heat sink by re-forming the ring structure.

The basic concept for using reversible Diels–Alder reactions to enhance the specific heat of liquids is illustrated in **Figure 4.1**. Two or more reactants are dissolved in a base solution where they form some equilibrium combination of reactants and products. As the mixture is heated, excess enthalpy is required to split the product molecule into the reactants; when the mixture is cooled, this stored reaction enthalpy is released as the forward Diels-Alder reaction occurs to produce more product. Diels-Alders reactions involve a simultaneous  $\pi$  to  $\sigma$  covalent bond transition accompanying a ring formation. This process involves the breaking of two weak covalent bonds ( $\pi$  bond) to form two strong covalent bonds ( $\sigma$  bond), which result in a high  $\Delta H_{rxn}$  as compared to that of hydrogen bonds or van der Waals interactions in conventional thermal fluids, manifesting as high heat capacities. The formation of a rigid ring from conformationally flexible structures combined with the reduction in molecularity greatly reduces the molecular degrees of freedom. This leads to a high  $\Delta S_{rxn}$  within the liquid phase. The high  $\Delta S_{rxn}$  is critical because it ensures that the turning temperature of the reaction,  $T^*$ , is not too high and remains within the liquid temperature range of the mixture. Thus, although many types of liquid phase chemical reactions could in theory achieve high  $\Delta H_{rxn}$  alone, Diels-Alder reactions are ideal for this concept because they also have high  $\Delta S_{rxn}$ .

### **Experimental results of Diels-Alder enhanced thermal fluid**

The effective heat capacity of 2M, 3M, and 3.5M mixtures of maleic anhydride and 2-methylfuran in DMF were determined using differential scanning calorimetry (See Methods). We begin by discussing the properties of the 3.5M mixture as plotted in Figure 4.2a. The region of heat capacity enhancement over that of DMF alone is represented by the blue shaded region in Figure 4.2a. The 3.5M solution has an enthalpy change of  $\sim 345$  J/g from  $20^\circ - 135^\circ C$ , which is about 99 J/g greater than that of pure DMF ( $\sim 246$  J/g) and represents a total enthalpy enhancement of approximately 40% due to the presence of the reactive species. The heat capacities of the 3.5M mixture, pure DMF, ethylene glycol, propylene glycol, mineral oil, and water are also compared in Fig. 2a. The heat capacity of the 3.5M mixture exceeds that of even water ( $4.18$  J/gC) from  $\sim 60^\circ - 90^\circ C$ , peaking at  $\sim 5.0 \frac{J}{g^\circ C}$ , which is approximately 20% higher than water. Figure 4.2a shows that the heat capacity of the 3.5M mixture is substantially higher than the heat capacity of propylene glycol and ethylene glycol from  $\sim 45^\circ - 100^\circ C$ , demonstrating the large improvement in the energy transfer and storage capacity over traditional heat transfer fluids.

The viscosity of the mixtures was measured using a standard parallel plate rheometer and is plotted in Figure 4.2b. The mixtures remain approximately Newtonian for both high and low shear regimes, making them favorable for thermal applications ranging from thermal storage (slow shear rate) to classical applications in heat transfer fluids (high shear rate). Pure DMF exhibits a very low viscosity of  $0.8$  mPa-s at  $T = 25^\circ C$ , roughly equal to that of pure water, making it an excellent choice as a base fluid to host the Diels-Alder reactants. The viscosity increases approximately linearly with increasing reactant concentration, and at 3.5M is equal to  $3.04$  mPa-s @  $T = 25^\circ C$ . This represents a significant improvement over other traditional heat transfer fluids, such as propylene glycol ( $40.4$  mPa-s), ethylene glycol ( $17.1$  mPas), 50/50 water and propylene glycol ( $4.5$  mPa-s), and mineral oil ( $14.1$  mPa-s), all taken at room temperature. Thus, such mixtures are attractive not only for their enhanced heat capacity but also potentially for their flow properties.

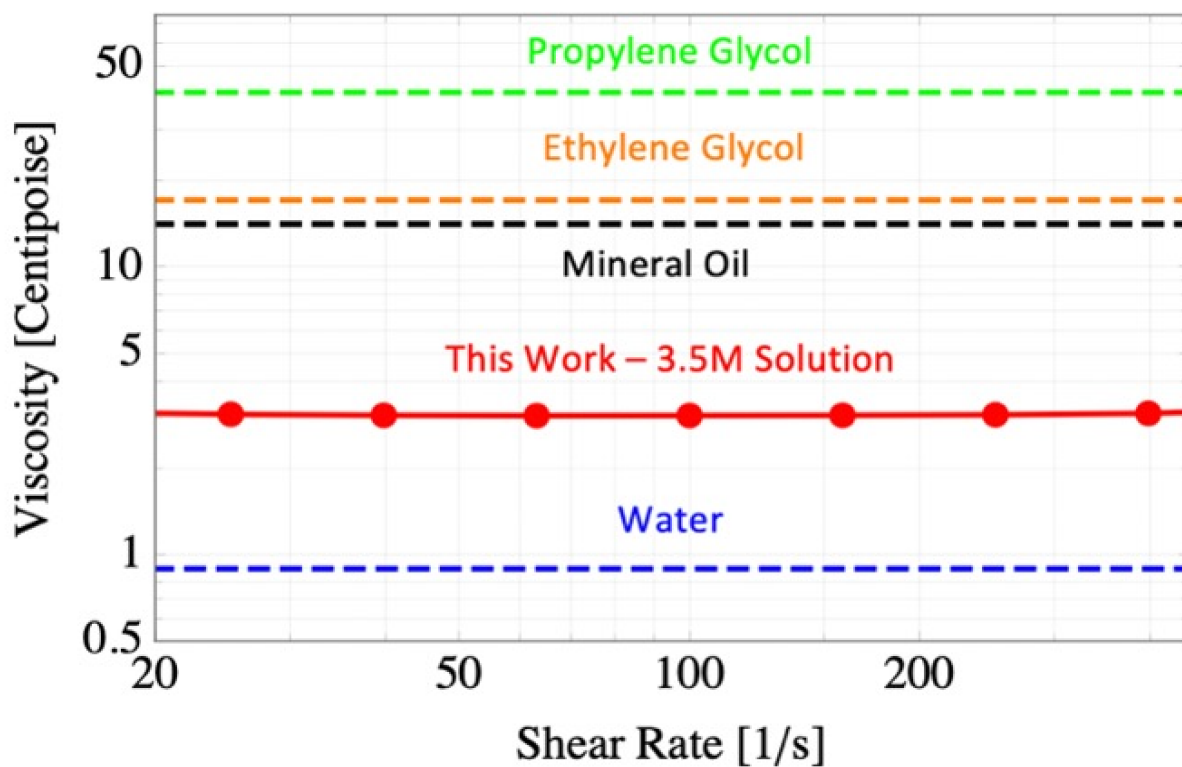
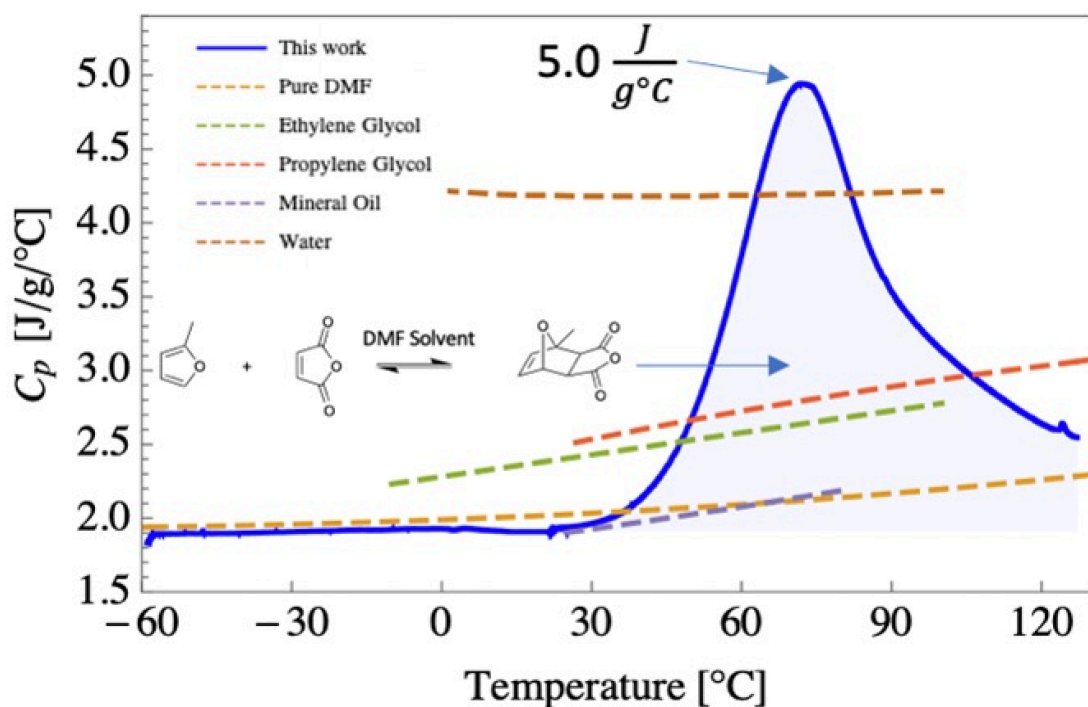


Figure 4.2 a) Effective heat capacity of 3.5M maleic anhydride and 2-methylfuran in DMF (solid blue) compared to the heat capacities of common thermal fluids (water, ethylene glycol, propylene glycol, mineral oil, and pure DMF). The blue shaded region indicates the enhancement provided by the chemical reaction taking place between the maleic anhydride and 2-methylfuran. (b) Viscosity of the 3.5M mixture over shear rates 20-600 1/s showing a Newtonian response. We include water, mineral oil, ethylene glycol, and propylene glycol data for comparison.

## Predictions using DFT

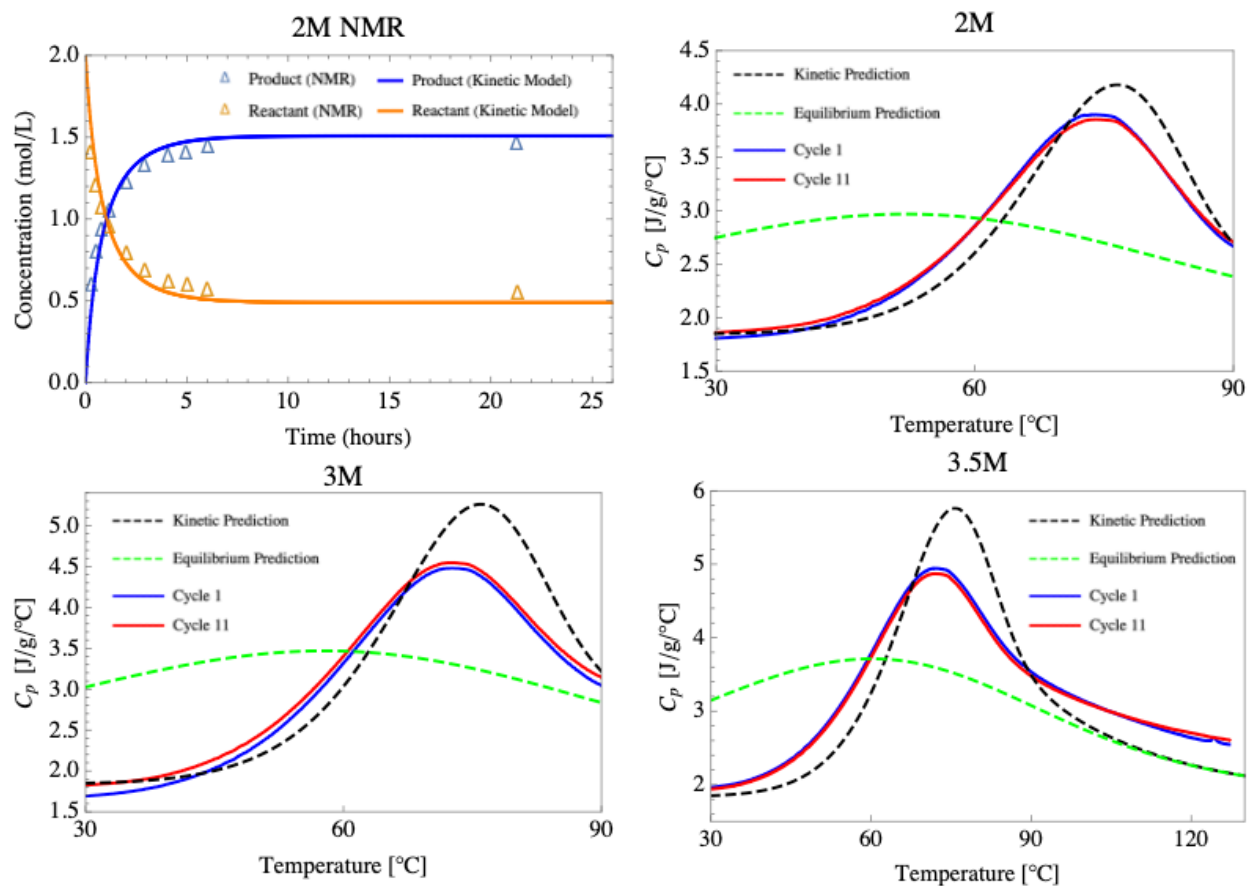
We note that the properties of these mixtures can be accurately predicted from first-principles calculations, making it feasible to design such mixtures using different reactive species *in silico*<sup>18</sup> and also confirming mechanistic understanding of the heat capacity enhancement. For example, in Fig 3a we compare nuclear magnetic resonance (NMR) measurements of the time-dependent concentration profiles of 2M maleic anhydride and 2-methylfuran in DMF at 26°C against predictions made using the molecular parameters in Table 1 determined from density functional theory calculations (see Methods). The kinetic model (see Eq. SI.1) tracks the NMR-determined concentration profiles very closely for both the rapid transience observed over short time scales ( $t < 10$  hours), and the asymptotic approach toward equilibrium thereafter. The agreement, which is obtained without any fitting parameters, demonstrates that the reactions are indeed occurring as would be expected based on the fundamental properties of the overall reaction.

Table 4.1: Calculated properties from density functional theory of the reaction between maleic anhydride and 2-methylfuran, which are used to model the expected heat capacity curves.

	$\Delta H_{rxn}$ [Kcal/mol]	$\Delta S_{rxn}$ [cal/mol]	$\Delta H^\ddagger$ [Kcal/mol]	$\Delta S^\ddagger$ [cal/mol]
2-methylfuran + maleic anhydride	-14.44	44.63	12.04	-35.88

Furthermore, the theoretical calculations allow prediction of the full heat capacity profile. Using again the molecular parameters in Table 4.1 determined from DFT, we compare in Figure 4.3b-d the model predictions to experimental heat capacity data. Figure 4.3b-d shows that the  $C_p$  model based on equilibrium model previously proposed by Sparks and Poling<sup>16</sup> and further developed by us<sup>17</sup> grossly underrepresents the data. Note that the equilibrium model only depends on  $\Delta H_{rxn}$  and  $\Delta S_{rxn}$  given in Table 4.1. To resolve this discrepancy, we modify the macroscopic  $C_p$  model to account for chemical kinetics (see Methods) which depends on all four parameters given in Table 4.1. Given that the theoretical prediction using kinetic model uses no empirical fitting parameters, the agreement is quite good for the 2M concentration (peak heat capacity difference of 6.9%, temperature of peak heat capacity difference of 2.2 degrees C). However, the model shows larger deviations for the 3.5M concentration; in particular, the experimental peak heat capacity enhancement is not as high as expected. This could potentially be due to mass transport limitations<sup>19</sup> and further investigation is needed to determine if the full theoretical heat capacity can be unlocked at high concentrations. Nevertheless, the excellent agreement validates the DFT determined molecular parameters and is encouraging for future DFT-based thermochemical screening efforts.

All samples were cycled 11 times, and the effective heat capacity of the first and last cycle are plotted in Figure 4.3b-d. No appreciable degradation was observed over the 11 cycles, indicating a highly reversible reaction. Finally, we note that the thermal window of the Diels-Alder mixtures is greatly enhanced relative to water. The freezing point of pure DMF is  $-61^\circ\text{C}$ . However, with a high concentration of reactants dissolved into it as in our work, it exhibits a large freezing point depression as no nucleation was observed as low as  $-90^\circ\text{C}$ . Although the boiling point of pure DMF is  $T = 153^\circ\text{C}$ , we observed boiling at  $T = 145^\circ\text{C}$ ; we attribute this to the 2-methylfuran boiling, given its low nominal boiling point out of solution ( $63^\circ\text{C}$ ). The effective thermal window



**Figure 4.3** (a) NMR data (triangles) showing the concentration vs time of the maleic anhydride and 2-methylfuran isothermal reaction at 26 $^{\circ}$ C. The solid lines indicate the predictions given by Eq. SI.1 using inputs determined from density functional theory calculations. (b-d) DSC measurements of 2M, 3M, and 3.5M mixtures. The blue solid line indicates the first measurement, and the red solid line shows the performance after 10 heating and cooling cycles. The black dashed line shows the predicted heat capacity using equation 1 (see Methods) and the green dashed line shows the predicted equilibrium heat capacity from previous work<sup>17</sup>. The thermodynamic inputs were determined from density functional theory calculations.

for the Diels-Alder mixtures is then  $-90^{\circ}\text{C} - 145^{\circ}\text{C}$ , which is much larger than that of water and traditional water-glycol mixtures.

Overall, the mixtures exhibited enhanced heat capacity (and thereby greater stored enthalpy) over 11 cycles, low viscosity, and an extended thermal stability window as compared to typical heat transfer fluids. A summary of the properties are listed in **Table 4.2**.

**Table 4.2:** Comparison of energy stored and other properties of 3.5M mixture vs water and 50/50 propylene glycol and water mixture

	This work [3.5M]	Water	50/50 propylene glycol and water mixture
$E_{\text{stored}}$ (J)	354.5 (20 – 135 °C)	314.2 (20 – 95 °C)	315.8 (20 – 105 °C)
Viscosity @25 °C (mPa-s)	3.04	0.8	4.53
$C_{p,\text{avg}}$ (J/kg-°C)	3.08 (20 – 135 °C)	4.19 (20 – 95 °C)	3.70 (20 – 105 °C)
$C_{p,\text{max}}$ (J/kg-°C)	5.00	4.21	3.86
Melting Temperature	-90 °C	0 °C	-34 °C
Boiling Temperature	145 °C	100 °C	105 °C

### Future Outlook

We have demonstrated that by dissolving a reactive species in a base solution, we can greatly enhance the effective heat capacities of thermal fluids. To further improve the performance of these thermal fluids and look toward their application as energy storage and heat transfer materials, we must seek higher energy density mixtures. Good agreement between the DFT model and experimental data allows for quick screening of existing molecules as well as design of new molecules for enhanced  $C_p$ . From the theoretical model, there are six parameters which decide heat capacity of the thermochemical fluid: i) the base heat capacity of the solution, ii) the heat of reaction ( $\Delta H_{\text{rxn}}$ ) and the entropy of reaction ( $\Delta S_{\text{rxn}}$ ), iii) the transition state enthalpy ( $\Delta H^{\ddagger}$ ) and the transition state entropy ( $\Delta S^{\ddagger}$ ), and iv) the solubility of the reactants in the solvent. The overall energy density can be improved in several ways: (i) Using a solution with higher base heat capacity, such as using water as solvent. In a previous work<sup>18</sup> where we theoretically screened

potential reactants using DFT for use in an aqueous solvent; although high heat capacities were theoretically possible, the temperature range of such solutions will likely be limited by the liquid range of water. ii) Using existing molecules or designing molecules with high  $\Delta H_{\text{rxn}}$  and appropriate  $\Delta H^\ddagger$  and  $\Delta S^\ddagger$  for better kinetics but retaining an appropriate turning temperature by also increasing  $\Delta S_{\text{rxn}}$ . In our previous computational study<sup>18</sup> using DFT we screened existing molecules as well as evaluated the performance of new molecules using various functional groups such as methyl, methoxy, and formyl groups. Although our previous work did not take kinetics into considerations, it showed that the design space for Diels-Alder thermochemical thermal fluids is huge.

We have conducted experiments in a static manner to measure  $C_p$ , however in application settings HTFs will be flowing. The impact of advection on reaction kinetics and solubility and how it impacts effective  $C_p$  remains unknown. A system with a condensed phase reaction occurring during flow is a complex system both from molecular<sup>19</sup> and macroscopic points of view. One will have to develop coupled thermal, fluidic and chemical macroscopic model to understand the system level performance of these thermochemical HTFs. From a molecular point of view, the reaction rate may increase due to increased diffusion of species<sup>19</sup>. Analogous to the static model where we have combined macroscale thermodynamic and kinetic model with molecular models of basic chemical parameters, potentially a dynamic model can be developed. Some of these open questions should be explored after conducting a thorough study of these thermochemical HTF in flowing conditions.

#### *Heat Capacity Measurements*

The heat capacity was measured using differential scanning calorimetry (DSC) at a scan rate of  $10 \frac{^\circ\text{C}}{\text{min}}$  with  $10\mu\text{L}$  samples in hermetically sealed non-reacting pans. The heat capacity measurements were calibrated using NIST reference data for DMF, sapphire, and water<sup>20</sup>.

#### *Cycling procedure*

After initial mixing, each solution was equilibrated at  $25^\circ\text{C}$  for 12 hours. Once equilibrated, the solutions were cycled in a DSC between  $-60^\circ\text{C}$  and  $135^\circ\text{C}$  10 times at both a heating and cooling rate of  $10 \frac{^\circ\text{C}}{\text{min}}$ . After 10 cycles, the solutions were again equilibrated at  $25^\circ\text{C}$  for 12 hours, and then ramped from  $-60^\circ\text{C}$  to  $135^\circ\text{C}$  at  $10 \frac{^\circ\text{C}}{\text{min}}$ .

#### *DFT Molecular modeling to predict transition states*

Initial molecular structures of the reactants and product were constructed using Avogadro (Avogadro: an open-source molecular builder and visualization tool. Version 1.2.0. <http://avogadro.cc/>) and optimized using the MMFF94 force field<sup>21</sup>. These initial structures were then optimized using the  $\omega\text{B97X-D}^{22}$  density functional and the 6-31G basis set as implemented in the Q-Chem 4.4 software package using the keyword OPT. The transition state structure was constructed from the product structure by elongating the forming bonds to 2.0 Å and then optimized using the keyword TS. Subsequent vibrational frequencies were calculated using the keyword FREQ to obtain entropies and thermal corrections for enthalpy at 298.15 K. Single-point

energy calculations were performed with a larger basis set 6-311++G(d,p) and with the PCM implicit solvation model<sup>23</sup> (dielectric constant  $\epsilon = 38.25$  for DMF<sup>24</sup>).

### NMR

The samples for NMR analysis were prepared by dissolving 2-methylfuran (1 mmol) and maleic anhydride (1 mmol) in 500  $\mu\text{L}$  of DMF-*d*7. <sup>1</sup>H NMR spectra were recorded on a Bruker 300 or 400 MHz spectrometer. <sup>1</sup>H chemical shifts are reported in parts per million relative residual protiated solvent as a reference (DMF in DMF-*d*7: 2.86 ppm).

### Kinetic Heat Capacity Model

The Eyring equation<sup>25</sup> was used to describe the change in concentration with time in Eqn SI.3, and was solved using the equilibrium concentration governed by the Van't Hoff equation<sup>26</sup> as the initial condition. See SI for more information. The equilibrium heat capacity as a function of reactant concentration and temperature can be related<sup>17</sup> to the chemical equilibrium governed by the Van't Hoff equation, which relates the equilibrium constant ( $K_{\text{eq}}$ ) to the enthalpy ( $\Delta H_{\text{rxn}}$ ) and entropy ( $\Delta S_{\text{rxn}}$ ) of reaction. Heat transfer fluids are typically heated and cooled very rapidly, so in a typical application the state of the chemical reaction will be far from equilibrium. To account for the kinetics, the number of bonds formed over a temperature interval multiplied by the enthalpy change associated with bond formation can be related to the chemical-based enhancement to the heat capacity of the solution at a given temperature:

$$C_{p,\text{kinetic}}(T) = \frac{\Delta H_{\text{rxn}}}{\rho} \frac{dc}{dT} + C_{p,\text{fluid}} = \frac{\Delta H_{\text{rxn}}}{\rho} \frac{\left(\frac{dc}{dt}\right)}{\left(\frac{dT}{dt}\right)} + C_{p,\text{fluid}} = \frac{\Delta H_{\text{rxn}}}{\rho} \frac{\left(\frac{dc}{dt}\right)}{\beta} + C_{p,\text{fluid}} \quad 4.1$$

where  $\beta$  is the ramp rate in the DSC. In equation 4.1,  $c$  is the molar concentration which can be predicted by kinetic theory,  $T$  is the temperature in Kelvin,  $\Delta H_{\text{rxn}} = H_{\text{product}} - \sum H_{\text{reactant}}$ ,  $\rho$  is the density of the mixture, and  $C_{p,\text{fluid}} = \chi_{\text{base fluid}} C_{p,\text{base fluid}} + \sum_i \chi_i C_{p,i}$  where  $\chi$  represents the volume fraction of a given species.

### Equilibrium and Kinetic Thermodynamic Model to predict Energy Storage Enhancement

Upon heating, the dissolved species reversibly react to form covalent bonds. At each temperature there exists an equilibrium between the reactants and products dissolved in solution, and the change in that equilibrium with the change in temperature determines the number of reactants that form products over a given temperature interval. The change in concentration can be related to the change in heat capacity of a thermal fluid. In reality, heat transfer fluids are heated/cooled quickly so the reaction is unlikely to observe equilibria at a given temperature. More generally, then, the number of bonds formed over a temperature interval multiplied by the enthalpy change associated with bond formation can be related to the chemical-based enhancement to the heat capacity of the solution at a given temperature by 4.1.

To evaluate 4.1 we can predict the change in concentration with time (i.e. kinetics of the reaction) using the Eyring equation:

$$\frac{dc}{dt} = \frac{k_b T(t)}{h} e^{-\frac{\Delta G_f}{RT(t)}} (c_{\max} - c(t))^2 - \frac{k_b T(t)}{h} e^{-\frac{\Delta G_{rev}}{RT(t)}} c(t) \quad 4.2$$

Where  $k_b$  is the Boltzmann constant,  $h$  is Planck's constant,  $T(t) = T_o + \beta t$ ,  $\Delta G_f = \Delta H_f - T\Delta S_f$  and  $\Delta G_{rev} = (\Delta H_f - \Delta H_{rxn}) - T(\Delta S_f - \Delta S_{rxn})$ . Equation 4.2 is a nonlinear first order ODE. We choose the equilibrium concentration of reactants as the initial condition, which can be derived from the Van't Hoff equation:

$$c(T_o) = \frac{1}{2} \left( 2c_{\max} + \frac{1}{K_{eq}(T_o)} \right) - \frac{1}{2} \sqrt{\left( 2c_{\max} + \frac{1}{K_{eq}(T_o)} \right)^2 - 4c_{\max}^2} \quad 4.3$$

$T_o$  is the initial temperature at which the solution was equilibrated and  $c_{\max}$  is the concentration of the reactants before the reaction has begun. Equation 4.2 can then be numerically solved using 4.3 as the initial condition, the result of which can be inserted into equation 4.1 to determine the heat capacity as a function of temperature for a given starting concentration of reactants, and at a prescribed heating/cooling rate.

*Viscosity of 2.0M, 3.0M, and 3.5M solutions.*

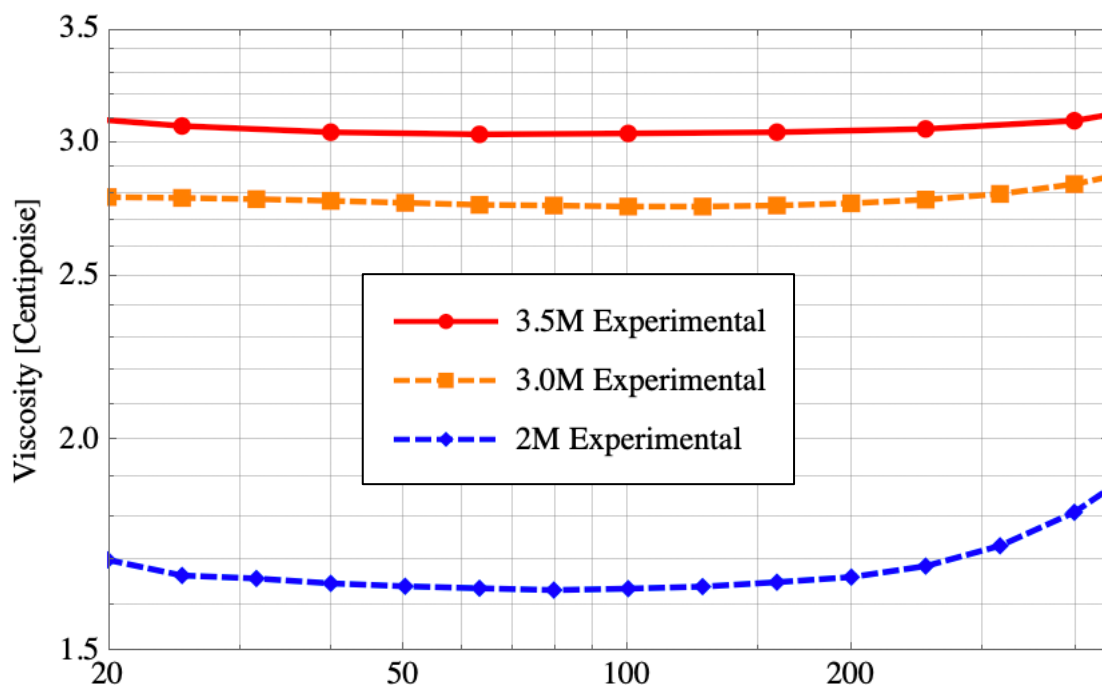


**Figure 4.4:** Viscosity of DMF with respect to concentration of diels alder reactants. As can be seen, the increase is approximately linear with reactant concentration

## References

1. Henry, A., Prasher, R. & Majumdar, A. Five thermal energy grand challenges for decarbonization. *Nature Energy* **5**, 635–637 (2020).
2. Sharma, A. K., Sharma, C., Mullick, S. C. & Kandpal, T. C. Solar industrial process heating: A review. *Renewable and Sustainable Energy Reviews* **78**, 124–137 (2017).
3. Hung, T. C. Waste heat recovery of organic Rankine cycle using dry fluids. *Energy Convers. Manag.* **42**, 539–553 (2001).
4. Woods, J. *et al.* Rate capability and Ragone plots for phase change thermal energy storage. *Nat. Energy* **6**, 295–302 (2021).
5. Booten, C., Rao, P., Rapp, V., Jackson, R. & Prasher, R. Theoretical Minimum Thermal Load in Buildings. *Joule* **5**, 24–46 (2021).
6. Xia, G., Cao, L. & Bi, G. A review on battery thermal management in electric vehicle application. *Journal of Power Sources* **367**, 90–105 (2017).
7. Meshkatodd, M. R. Aging Study and Lifetime Estimation of Transformer Mineral Oil. *Am. J. Eng. Appl. Sci.* **1**, 384–388 (2008).
8. Sohail Murshed, S. M. & Nieto de Castro, C. A. A critical review of traditional and emerging techniques and fluids for electronics cooling. *Renewable and Sustainable Energy Reviews* **78**, 821–833 (2017).
9. Zeng, Y., Chalise, D., Lubner, S. D., Kaur, S. & Prasher, R. S. A review of thermal physics and management inside lithium-ion batteries for high energy density and fast charging. *Energy Storage Mater.* (2021). doi:10.1016/j.ensm.2021.06.008
10. She, X., Huang, A. Q. & Burgos, R. Review of solid-state transformer technologies and their application in power distribution systems. *IEEE J. Emerg. Sel. Top. Power Electron.* **1**, 186–198 (2013).
11. Steinmann, W.-D. Thermal energy storage systems for concentrating solar power plants. in *Concentrating Solar Power Technology Principles, Developments, and Applications A volume in Woodhead Publishing Series in Energy* (eds. Lovegrove, K. & Stein, W.) (2020).
12. Kandlikar, S. G. *et al.* Heat transfer in microchannels - 2012 status and research needs. *J. Heat Transfer* **135**, (2013).
13. Wentworth, W. E. & Chen, E. Simple thermal decomposition reactions for storage of solar thermal energy. *Sol. Energy* **18**, 205–214 (1976).
14. Lenz, T. G. & Hegedus, L. S. MODERATE TEMPERATURE SOLAR THERMOCHEMICAL SYSTEMS - AN APPLICATION OF DIELS-ALDER CHEMISTRY. in *Electric Power Research Institute (Report) EPRI EA* **1**, 154–158 (1979).
15. Lenz, T. G., Hegedus, L. S. & Vaughan, J. D. Liquid phase thermochemical energy conversion systems—An application of Diels-Alder chemistry. *Int. J. Energy Res.* **6**, 357–365 (1982).
16. Sparks, B. G. & Poling, B. E. Energy storage capacity of reversible liquid-phase Diels Alder reaction between maleic anhydride and 2-methyl furan. *AIChE J.* **29**, 534–537 (1983).
17. Yu, P., Jain, A. & Prasher, R. S. Enhanced Thermochemical Heat Capacity of Liquids: Molecular to Macroscale Modeling. *Nanoscale Microscale Thermophys. Eng.* **23**, 235–246 (2019).

18. Spotte-Smith, E. W. C., Yu, P., Blau, S. M., Prasher, R. S. & Jain, A. Aqueous Diels–Alder reactions for thermochemical storage and heat transfer fluids identified using density functional theory. *J. Comput. Chem.* **41**, 2137–2150 (2020).
19. Wang, H. *et al.* Boosted molecular mobility during common chemical reactions. *Science* (80-. ). **369**, 537–541 (2020).
20. Domalski, E. & Hearing, E. Condensed Phase Heat Capacity Data. in *NIST Chemistry WebBook, NIST Standard Reference Database Number 69*, Eds. P.J. Linstrom and W.G. Mallard
21. Halgren, T. A. Merck molecular force field. I. Basis, form, scope, parameterization, and performance of MMFF94. *J. Comput. Chem.* **17**, 490–519 (1996).
22. Chai, J. Da & Head-Gordon, M. Long-range corrected hybrid density functionals with damped atom-atom dispersion corrections. *Phys. Chem. Chem. Phys.* **10**, 6615–6620 (2008).
23. Mennucci, B. *et al.* Polarizable continuum model (PCM) calculations of solvent effects on optical rotations of chiral molecules. *J. Phys. Chem. A* **106**, 6102–6113 (2002).
24. Lide, D. R. *CRC handbook of chemistry and physics*. **85**, (CRC press, 2004).
25. Espenson, J. H. *Chemical kinetics and reaction mechanisms*. **102**, (Citeseer, 1995).
26. Atkins, P. & De Paula, J. *Atkins' Physical chemistry* 8th edition. (2006).

## Chapter 5. Nonequilibrium stabilization of Thermochemical Energy Materials during Hydration/Dehydration

Thermochemical materials (TCMs) undergo a solid-gas reversible chemical reaction. In this chapter, we focus on stabilizing reactions with water vapor to store and release energy with high storage capacities ( $600 \text{ kWh/m}^3$ ) and negligible self-discharge that makes TCM uniquely suited as compact, stand-alone units for daily or seasonal storage. Currently, TCMs suffer from mechanical and thermal instabilities at the material and reactor level, resulting in poor multi-cycle efficiencies and high-levelized cost of storage. In this chapter, we develop a model to predict how nonequilibrium behavior leads to mechanical decay. Specifically, we derive an equation that identifies a critical particle size that we call the pulverization limit or  $R_{\text{crit}}$  for various salt hydrates, that considers both the thermal and mass transport of the dehydration process in tandem with the equilibrium material properties. The model was tested on multiple TCM salt hydrates with different water content and hydration shells, and provides robust design criteria for future TCM efforts.

In this work, I collaborated with Andrew Martin (postdoc) who did all the experimental characterizations shown in this chapter.

### 1. Introduction

Thermal energy storage can be broadly divided into 3 classes: (1) sensible materials, (2) phase change materials (PCMs) and (3) thermochemical materials (TCMs).<sup>[4]</sup> TCMs have the fundamental advantage of having significantly higher theoretical energy densities ( $200$  to  $600 \text{ kWh/m}^3$ ) compared to sensible and latent ( $50$  to  $150 \text{ kWh/m}^3$ ) storage because the energy is stored in reversible reactions.<sup>[5]</sup> For building applications, a low charge-discharge temperature is highly desirable in thermal energy storage materials, and sorption-based TCMs fulfill this need. Depending upon the type of reaction, sorption based TCMs can be divided into two categories: **absorption** materials (example: inorganic salt hydrates)<sup>[6]</sup> or **adsorption** (example: zeolites or silica gel).<sup>[7]</sup> In **absorption** TCMs energy is stored or released by reversible solid-gas reaction (chemisorption) which involves breaking and restoring strong bonds (such as covalent bonds) between the constituents throughout the bulk of the material, whereas in **adsorption** TCMs the reversible reaction is based on weak van der Waals interactions between solid and gas (physisorption) and is limited to the surface of the solid. Consequentially, absorption based TCMs, such as inorganic salts ( $\text{SrCl}_2 \cdot 6\text{H}_2\text{O}$ ,  $\text{MgSO}_4 \cdot 7\text{H}_2\text{O}$ ,  $\text{K}_2\text{CO}_3 \cdot 1.5\text{H}_2\text{O}$ , etc.) have higher energy densities ( $\sim 500 \text{ kWh/m}^3$ ) when compared to adsorption TCMs ( $\sim 200 \text{ kWh/m}^3$ ) as shown in Figure 5.1a. This work focuses on absorption TCMs utilizing the chemisorbed water reaction. These inorganic salt hydrate TCMs are uniquely suited for on-site TES in buildings because in addition to having high energy densities, they have negligible self-discharge and can be charged at temperatures below  $100^\circ\text{C}$ . Furthermore, since they are made from earth abundant materials, they are very economical. Figure 5.1b shows an example for the implementation of salt hydrates as TCM-thermal storage that can be charged using solar energy or excess grid electricity and

discharged for thermal end-uses in buildings such as space and water heating by harvesting moist air from the surroundings.

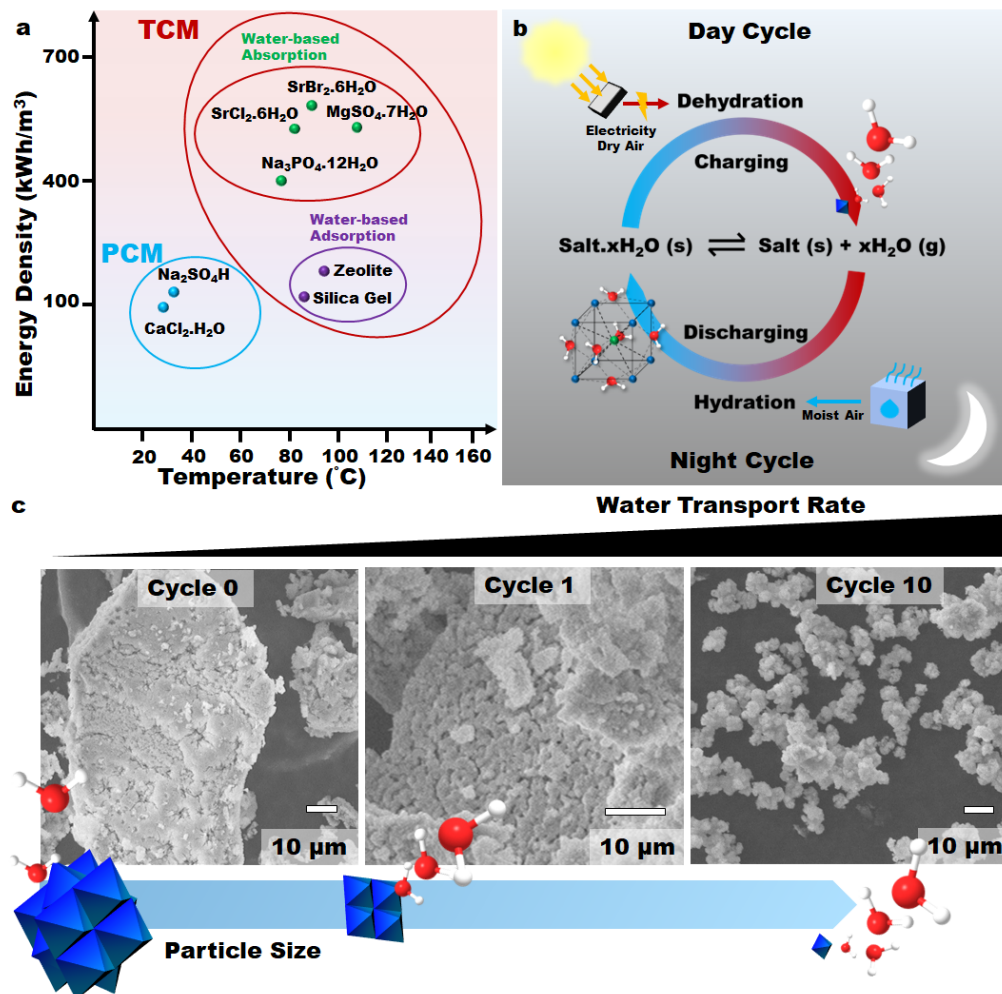


Figure 5.1 (a) Energy density comparison between various thermal energy storage materials including phase change materials (PCM), water-based adsorption and absorption thermochemical materials (TCM). (b) Illustration for use of TCMs in buildings and charge-discharge cycle of salt hydrates where the salt hydrates can be dehydrated using the energy generated through solar power and then rehydrated at night with outside humid air or a humidifier. (c) SEM image and illustration of the change in salt hydrate (SrCl<sub>2</sub>·6H<sub>2</sub>O) morphology and size during cycling.

At the material level, the greatest challenge working with TCMS has to do with the stability of the salt hydrate. Structural and volumetric changes, slow reaction kinetics, and high hygroscopicity of salt hydrates under operating conditions can all induce instability in salt hydrates. For example, structural changes from crystalline to amorphous phases reduce the water capacity of the hydrate and the salt energy density. Similarly, large volume changes during hydration and

dehydration are highly undesirable as they lead to crack formation (Fig. 6.4) and ultimately pulverization of the host material, which affects the cycling efficiency and lifetime of the storage media.

Operating conditions at the reactor level also couple critically to reaction kinetics at the material level, and sub-optimal operating conditions can significantly reduce reaction rate and the storage capacity. For example, it has been shown that during the dehydration step, higher heat flux at the system level could result in incongruent melting of salt hydrates if the heat transport at the material level happens faster than the mass transport (i.e. if water vapor cannot escape quickly). Also, since this is a solid-gas reaction, the formation of any liquid phase of the salt (melting/deliquescence) is undesirable as it leads to salt leakage, agglomeration, and structural modifications, which renders the material inactive. These issues can be avoided by establishing relationships between operating conditions at the reactor level with the equilibrium reaction thermodynamics at the material level.

To improve thermal and mass transport at the particle level, typically salt hydrates are impregnated into a host matrix such as expanded graphite or vermiculite (referred hereafter as composite TCMs). So far, limited success has been achieved with these approaches as the composite TCMs disintegrate after limited cycling. Under repeated cycling the composite TCM particles expand and contract by 30%- 150% by volume due to intake of water molecules which leads to many different mechanical failure modes such as cracking of the expanded graphite matrix. In previous works, to reduce the mechanical stress due to particle expansion, the particle loading in the composite was greatly reduced which leads to significantly lower effective energy density (<70 kWh/m<sup>3</sup>) at the reactor level. Since the LCS is inversely proportional to energy density, this is not a desirable strategy. Even with significantly lower salt loading previous attempts have not led to enhanced number of cycles. Thus, there is a clear need to develop an in-depth detailed fundamental understanding of mechanical strength of the materials which has largely been ignored by the TCM community so far.

So far, many studies have reported the pulverization of TCMs with cycling,<sup>[11e, 13]</sup> but none have provided a mechanistic understanding or physical insights into predicting such behavior. In typical salt hydrates, water can account for approximately 1/4 – 1/2 the mass of the salt hydrate itself. For example, in a commonly investigated salt TCM for building applications such as MgSO<sub>4</sub>·7H<sub>2</sub>O,<sup>[13f]</sup> water occupies approximately 51% of the salt hydrate's mass, this causes large volume and porosity change when water molecules are removed and reintroduced (approx. 71.8% volume reduction during dehydration).

Previous investigation of the transitions undergone by TCM salt hydrates between various hydrate phases has shown that different salts may undergo different mechanisms during both dehydration and hydration. The hydration of salt can follow different pathways (i.e. a direct solid-solid transition or a dissolution and a recrystallization process),<sup>[5, 15]</sup> however, salt dehydration for most salts are common with a diffusion of water molecules out of the salt hydrate crystal. Consequentially, this removal of water from the crystal induces a solid-state transformation and causes a degree of mechanical stress and strain on the crystal itself, causing defects (i.e.

dislocation and formation of cracks) that in the long run can result in the self-pulverization of salt.<sup>[16]</sup> Thus, whilst both hydration and dehydration may contribute in the deterioration of salt hydrates over cycling due to the large morphological changes, dehydration is considered to be the largest contributor towards the pulverization of salt hydrate.

In this work, SrCl<sub>2</sub>·6H<sub>2</sub>O is chosen and investigated for building application as it has low charging temperature (<100°C) when compared to MgSO<sub>4</sub>·7H<sub>2</sub>O, and higher stability owing to its higher deliquescence point. Figure 1c and S1 shows the effect of cycling on SrCl<sub>2</sub>·6H<sub>2</sub>O (in here, water accounts for 1/3 mass of the salt hydrate) where the particle size gets reduced from > 400 μm (as received) to < 10 μm after just 10 cycles. This 40-fold reduction in particle size creates significant change in the surface area of the salt hydrates and shift the dynamics of the reaction. Here, we developed a model to predict the pulverization limit (i.e., critical size, R<sub>crit</sub>) of salt hydrates and validated it for various salt hydrates. We also demonstrated the effect of R<sub>crit</sub> on the dehydration and hydration kinetics as well as provided insights into the long-term stability of salt hydrates and its composites.

## 2. Results and Discussion

To determine how much the salt hydrates will pulverize due to expansion during cycling, a theoretical model for a single spherical particle was developed by solving the coupled mechanical stress and mass diffusion equations. This model is developed based on the mechanical response of the particle to water generation (i.e. dehydration), which leads to internal expansion gradients within the particle core. To begin, we assume that the salt hydrate is a perfectly spherical, defect-free particle with isotropic material properties. As it will be shown, the results of the model do not depend strongly on material properties, but instead on the rate of dehydration. Thus, although a real salt hydrate is not perfectly spherical, and certainly does not have perfectly isotropic material properties, this assumption will be of little consequence to the final model predictions. First, we consider the well-known stress response due to thermal expansion within a sphere:

$$\sigma_{rr} = \frac{2E\alpha_T}{1-\nu} \left\{ \frac{1}{R^3} \int_0^R \theta(r)r^2 dr - \frac{1}{r^3} \int_0^r \theta(r)r^2 dr \right\} \quad 5.1$$

$$\sigma_{\phi\phi} = \frac{E\alpha_T}{1-\nu} \left\{ \frac{1}{r^3} \int_0^R \theta(r)r^2 dr - \frac{2}{R^3} \int_0^r \theta(r)r^2 dr - C(r) \right\} \quad 5.2$$

Where  $E$  is the Young's modulus,  $\alpha_T$  is the linear coefficient of thermal expansion,  $\nu$  is the Poisson ratio,  $R$  is the radius of the sphere, and  $\theta(r) = T(r) - T_o$ , where  $T_o$  is the reference temperature. Equations 5.1 and 5.2 give the thermomechanical response to an arbitrary temperature gradient induced in a solid sphere at steady state. To get the mechanical response

to water generation, we can write the mass transfer analogue of equations 5.1 and 5.2. First, we recognize that the strain gradient is induced via the dehydration reaction, which occurs volumetrically. Thus, the mass analogue to  $\theta(r)$  corresponds to  $C(r) - C_o$ , where  $C(r)$  is the number of water molecules at position  $r$ , and  $C_o$  is the reference number of dehydrated water molecules, which is equal to zero (e.g. the hydrated state). Next, we substitute  $\alpha_T$  for  $\alpha_{H_2O}$ , which represents the expansion per water molecule generated. Thus, when  $\alpha_{H_2O}$  is multiplied with the expression in the brackets in equations 5.3-5.4, we are multiplying the expansion per water molecule by the number of water molecules at position  $r$ , which gives us the strain. Multiplying the strain by  $\frac{E}{1-\nu}$  then yields the stress:

$$\sigma_{rr} = \frac{2E\alpha_m}{1-\nu} \left\{ \frac{1}{R^3} \int_0^R C(r)r^2 dr - \frac{1}{r^3} \int_0^r C(r)r^2 dr \right\} \quad 5.3$$

$$\sigma_{\phi\phi} = \frac{E\alpha_m}{1-\nu} \left\{ \frac{1}{r^3} \int_0^R C(r)r^2 dr - \frac{2}{R^3} \int_0^r C(r)r^2 dr - C(r) \right\} \quad 5.4$$

From equations 5.3-5.4, it is clear that the stress gradient is a function of the location within the sphere. To evaluate equations 5.3-5.4, the distribution of water molecules generated throughout the sphere must be known at steady state. This can be solved for using Fick's law, assuming uniform mass (vapor) generation.

$$D_{ab}\nabla^2 C = N \frac{m'(t)}{M_{H_2O}} \quad 5.5$$

Where  $D_{ab}$  is diffusivity between the salt and the water vapor,  $m'(t)$  represents the total mass generation of water molecules within the sphere per second [ $\frac{g}{s}$ ],  $M_{H_2O}$  is the molar mass of water, and  $N$  is Avogadro's number -- which makes the right-hand side describe the total number of water molecules per second. Assuming the same 1D spherical geometry as in equations 6.1-4, equation 5.5 can be readily solved by enforcing axisymmetry such that the gradient,  $C'(r = 0) = 0$ , which caps vapor generation from blowing up at the center, and by setting the number of water molecules at the sphere's boundary equal to the number of water molecules in the air  $C(R) = C_\infty$ , which provides a "mass sink" to equation 5.5. The resulting profile of water molecules is:

$$C(r) = \frac{Nm'R^2}{6D_{ab}} \left( 1 - \frac{r^2}{R^2} \right) + C_\infty \quad 5.6$$

Equation 5.6 is then fed into the mechanical response equations (5.3 and 5.4) with an assumption that salt hydrates' volume changes approximately 10% per water molecule when it is calculated based on the mass change of salt hydrate during dehydration assuming constant density (i.e. linear expansion coefficient becomes  $0.1/3 = 0.033$ ). To determine the critical particle size, we

first note that the principal stress in the azimuthal direction is always larger than in the radial direction, so we focus only on equation 5.4. By evaluating the integrals in equation 5.4 and solving for the position,  $r$ , that maximizes the stress, we can now determine the critical particle size ( $R_{crit}$ ) by equating the maximum stress experienced by the sphere to the ultimate stress of the salt lattice. To be clear,  $R_{crit}$  defines the maximum size above which the particle will pulverize because of the internal stress due to salt contraction with water output will exceed the ultimate strength of the salt. The equation is as follows:

$$R_{crit} = 1.29 \left( \frac{\sigma_{yield} D_{ab} M_{H_2O}}{(1 - \nu) \alpha_m E N m'(t)} \right)^{\frac{1}{5}} \quad 5.7$$

Where  $\sigma_{yield}$  is yield strength of salt hydrate and  $M_{H_2O}$  is the molar mass of water.  $\sigma_{yield}$  ranges between 15 to 40 MPa for different salts hydrates,<sup>[17]</sup>  $D_{ab}$  is assumed to be approximately  $10^{-6}$  cm<sup>2</sup>/s,<sup>[18]</sup>  $\nu$  is Poisson's ratio (neglected due to insignificance to the overall result),  $\alpha$  is approximated at  $10^{-4}$  K<sup>-1</sup> and  $E$  varies between 5 to 50 GPa for different salts.<sup>[17-19]</sup> The model predicts the mechanical response and failure condition of the salt hydrates based on their mechanical properties, coupled with diffusion rate and charge/discharge. Figure 5.2a shows the  $R_{crit}$  as a function of  $m'(t)$  where both the lower and higher end of material constant values were taken into consideration to represent the range of mechanical and intrinsic properties for various salt hydrates.<sup>[17a, 17c, 18-19]</sup> Due to the nature of mass generation of water vapor during dehydration, the largest contributor of  $R_{crit}$  within this equation comes from the amount of H<sub>2</sub>O within the salt hydrate and their mass generation rate ( $m'(t)$ ).

This model is experimentally validated by testing various salt hydrates (K<sub>2</sub>CO<sub>3</sub>·1.5H<sub>2</sub>O, MgSO<sub>4</sub>·7H<sub>2</sub>O, SrCl<sub>2</sub>·6H<sub>2</sub>O and Na<sub>3</sub>PO<sub>4</sub>·12H<sub>2</sub>O) under the similar testing conditions where different  $m'(t)$  were generated as each salt hydrate had different molar mass of the water to lose in the same time window. Specifically, each salt hydrate was experimentally cycled between 25°C to 80°C and then rehydrated back at 25°C with 60% RH. The charging rate for all the salts were kept constant at 1°C/min. The  $m'(t)$  was calculated based on the amount of water which are lost during the dehydration period. K<sub>2</sub>CO<sub>3</sub>·1.5H<sub>2</sub>O and Na<sub>3</sub>PO<sub>4</sub>·12H<sub>2</sub>O showed the most extreme behavior as the former only generates 1.5H<sub>2</sub>O and the latter generates 12H<sub>2</sub>O in a very short period. As expected, the salt hydrates pulverized during cycling and significant reduction in particle size was observed for all the salt hydrates after 10 cycles (Figure 5.2b-e). The mean particle sizes for cycled salts correspond well with the  $R_{crit}$  predicted by the model as shown in Figure 5.2a. Although there is a size distribution for all salt hydrates after 10 cycles, it is anticipated that the larger particles (> $R_{crit}$ ) will continue to pulverize further with cycling until they reach the respective critical particle size as predicted by the model.

For a given salt hydrate,  $m'(t)$  can only be varied by changing operating conditions such as temperature ramp rate and/or relative humidity. Thus, we further investigated correlation between  $R_{crit}$  and  $m'(t)$  for SrCl<sub>2</sub>·6H<sub>2</sub>O under various operating conditions for different sized particles.

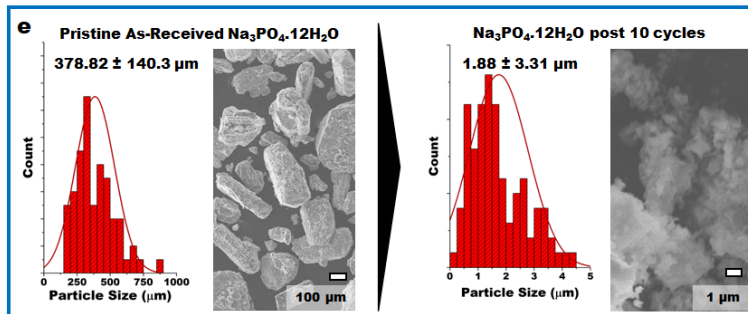
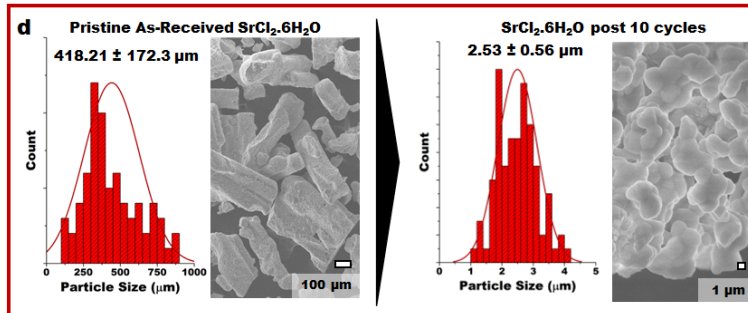
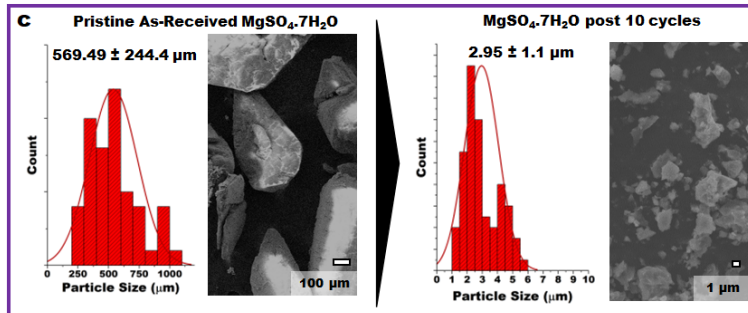
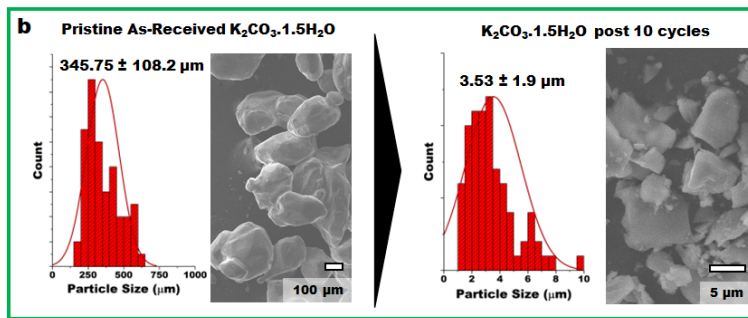
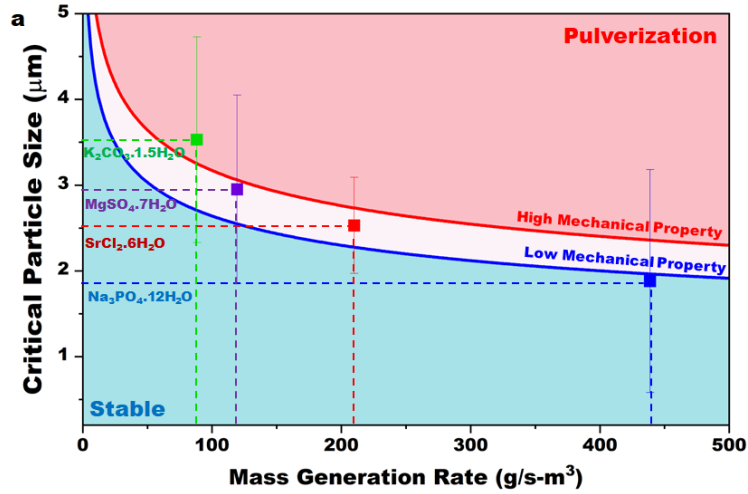


Figure 5.2. (a) Model along with experimental data on the critical particle size of salt hydrates. Two set of material constant values were taken to represent the range of mechanical and intrinsic properties for various salt hydrates. Size distribution and SEM image for pristine (as received) to post 10 cycles of (b)  $K_2CO_3 \cdot 1.5H_2O$  (c)  $MgSO_4 \cdot 7H_2O$ , (d)  $SrCl_2 \cdot 6H_2O$ , and (e)  $Na_3PO_4 \cdot 12H_2O$ . Cycling was done between 25°C, 60% RH and 80°C, 0% RH at 1°C/min ramp rates.

### 2.1. Correlation of Particle Size and $m'(t)$

To understand the effect of particle size on  $m'(t)$  in salt hydrates, multiple batches of  $SrCl_2 \cdot 6H_2O$  in various sizes were prepared by ball milling and sieving (which will be referred here as pre-conditioning of salt) which allows for more control over particle size as opposed to self-pulverization of salt hydrates through cycling. As expected, the smaller size particles completed their transitions at lower temperature, whereas for larger ones there was a shift to higher temperature. In other words, as opposed to 10 mins for smaller particles, it took 35 mins for the larger particles to complete the first transition ( $6H_2O$  to  $2H_2O$ ). Similarly, there was time lag for the second and third transitions based on size of the particle, but since these transitions happened at relatively high temperatures compared to the first transition, the effect of particle size on water transport kinetics was less significant. Table 5.1 provides the transition temperatures of each hydrate forms for different average particle size.

Table 5.1 Transition temperatures of each hydrate forms for different particle size averages

Transitions	Particle Size Average					
	2.63 $\mu m$	10.1 $\mu m$	42.2 $\mu m$	70.9 $\mu m$	151.3 $\mu m$	560.2 $\mu m$
$6H_2O \rightarrow 2H_2O$	35.3°C	35.8°C	43.9°C	48.1°C	58.1°C	60.8°C
$2H_2O \rightarrow H_2O$	67.5°C	68.3°C	72.8°C	73.4°C	80.2°C	82.2°C
$H_2O \rightarrow$ Anhydrous	103.1°C	103.2°C	106.1°C	109.7°C	117.9°C	119.7°C

From an operational perspective, the time required to charge (dehydration) and discharge (hydration) thermal energy storage material is crucial, especially the discharge time as it determines the power density of the storage. Given that the transition steps are modulated by temperature and vapor pressure,<sup>[20]</sup> we investigated the effect of these variables by comparing the performance of the as-received salts (approximately 560.2  $\mu m$ ) with the pre-conditioned salt

of size near  $R_{crit}$ . Figure 5.3a-c shows the effect of particle size on dehydration times with the increase in the temperature ramp rates, whereas larger particles require more time to dehydrate when compared to smaller particles at same ramp rates, indicating that the process is diffusion limited for larger particles. For small sized particles, mass generation rate increases linearly with the ramp rates reaching up to  $826 \text{ g/s}\cdot\text{m}^3$  (Figure 5.3c), indicating fast mass (water vapor) transport owing to large surface area. This similar behavior is also observed in the hydration process where dehydrated salt hydrates were rehydrated back to  $6\text{H}_2\text{O}$  under different conditions of relative humidity and temperature (Figure 5.3d). Performing a size study on these salt hydrates as shown in Figure 5.3e results in a trend where larger salt hydrates take significantly longer to get back to its original mass with 6 molecules of water (approximately 150 min) whereas the pre-conditioned salts can reach it quite rapidly (approximately 60 min) under the same hydration conditions. In fact, by increasing the RH further it is possible to hydrate the small sized particles in 30 mins. Figure 5.3f displays the result of this faster reaction rate where the overall power density of the material improves significantly ( $227 \text{ kW/m}^3$  vs  $630 \text{ kW/m}^3$  between the smallest and largest- sized particles).

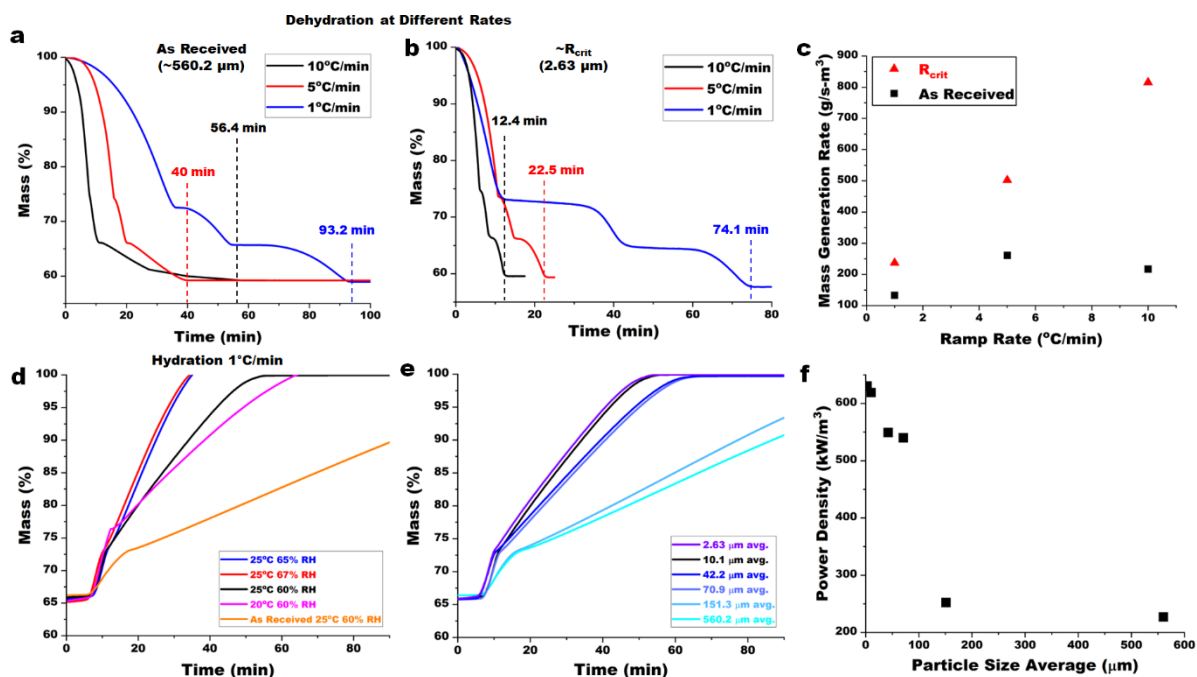


Figure 5.3: Dehydration and hydration behavior of  $\text{SrCl}_2\cdot 6\text{H}_2\text{O}$  with various average starting size and ramp rates. (a) Dehydration time from  $6\text{H}_2\text{O}$  to anhydrous of as-received particles at various temperature ramp rates. (b) Dehydration time from  $6\text{H}_2\text{O}$  to anhydrous of pre-conditioned particles close to  $R_{crit}$  at various temperature ramp rates. (c) Relation between mass generation rate and ramp rates for as received and pre-conditioned particles. (d) Hydration times for pre-conditioned and as-received particles with different temperature and relative humidity conditions. (e) Hydration times for particles with different initial sizes. (f) Effect of particle size on power density. As the relative humidity and/or temperature were increased, the hydration rate for small particles increased whereas large particles lagged behind owing to slower water transport. Thus, having the salt hydrates within the critical size not only allows for increased

mechanical stability but also provides more flexibility in parametric space of operations at the reactor level for both dehydration and hydration processes

## 2.2. Self-Pulverization vs. Preconditioning of Salt Hydrate

Since the salt hydrates can be pre-conditioned or self-pulverized during initial cycling period to reach optimal size ( $R_{crit}$ ), we investigated the effect of these two different approaches to achieve the  $R_{crit}$  on the performance of  $SrCl_2 \cdot 6H_2O$ . The first ten cycles of  $SrCl_2 \cdot 6H_2O$  (as received) and preconditioned (10  $\mu m$ ) particle size are shown in Figure 5.4a-b. The shift in dehydration of as received  $SrCl_2 \cdot 6H_2O$  is apparent in the thermogravimetric data, where the transition temperature continually shifts to lower temperature as the cycling continues for 10 cycles (Figure 5.4a). This is mainly due to improved kinetics (faster mass transport) due to self-pulverization of the salt hydrates resulting in smaller particles with increased surface area as the cycling happens. As expected, no significant shifts were observed in case of pre-conditioned salt (approximately 10  $\mu m$ ) as the particle size is already small enough and close to the  $R_{crit}$ , resulting in the steady kinetics. The mass vs. time evolution (20 cycles) for these two samples are shown in Figure 5.4c-d. The difference in the change in dehydration and hydration times with cycling for as-received and pre-conditioned salt hydrate is highlighted in Figure 5.4e-h. Owing to large size distribution in the as received  $SrCl_2 \cdot 6H_2O$ , dehydration time for the first cycle for different batches of salt samples varied between 49 to 57 mins but nonetheless for all the batches tested, the dehydration time reduced significantly during initial cycling and stabilized at approx. 46 mins for the ramp up rate of 1°C/min. For preconditioned salt, the dehydration time was steady between 44-46 mins. The larger contrast, however, comes from the differences in hydration behavior between the two (Figure 5.4g-h) where the hydration time for as-received salt hydrate continues to decrease in 20 cycles (from 127 mins to 107 mins) whereas the pre-conditioned salt experiences a constant hydration time (78 mins) in all cycle. The reason behind longer times for self-pulverized salt is the morphology of the as-received salt hydrate after 20 cycles, which looked different from preconditioned salts and resembled “pomegranate structure” which comprise of primary particles approximately 2.63  $\mu m$  in size, stuck together as larger secondary particle size (similar pomegranate structure in battery electrode).<sup>[21]</sup> Due to this hierarchical structure, the surface area of self-pulverized salt hydrates was smaller when compared to pre-conditioned salt hydrate and thus requires more hydration times (Figure 5.4g). The signature crystalline peaks of  $SrCl_2 \cdot 6H_2O$  are apparent and present throughout cycling. Although Brunauer-Emmett-Teller (BET) analysis of self-pulverized salt hydrates also indicates an increase in both surface area and porosity with cycling, we anticipate that the surface area will continue to increase as the secondary particles break down further to primary particles and finally reaching similar surface areas as preconditioned salt hydrates.

Please note that the disparity between dehydration and hydration times (46 and 78 mins, respectively) for pre-conditioned salt can be explained through the different parameters required to induce the reactions. The dehydration of salt hydrates takes place at high temperature where reaction rates are higher whereas the hydration happens at low temperature (25°C) and is driven by a constant vapor pressure. As mentioned earlier and shown in Figure 5.3, both of these times can be controlled by varying appropriate parameters.



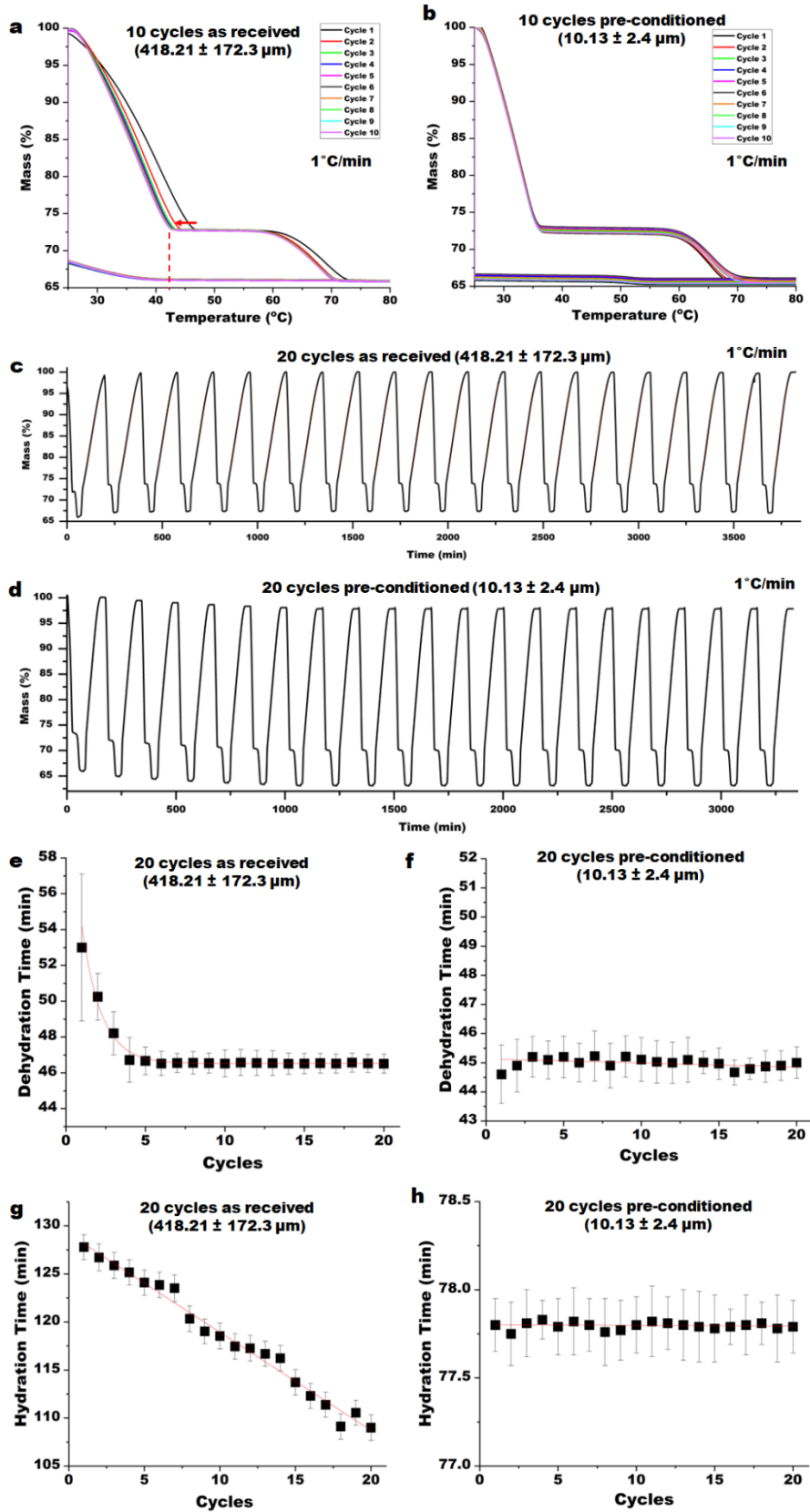


Figure 5.4: Gravimetric data of (a) as-received  $\text{SrCl}_2 \cdot 6\text{H}_2\text{O}$  and (b) pre-conditioned  $\text{SrCl}_2 \cdot 6\text{H}_2\text{O}$  cycled 10 times. Mass vs. time evolution of (c) as received  $\text{SrCl}_2 \cdot 6\text{H}_2\text{O}$  and (d) pre-conditioned  $\text{SrCl}_2 \cdot 6\text{H}_2\text{O}$  cycled 20 times at  $1^\circ\text{C}/\text{min}$  between  $25^\circ\text{C}$ , 60% RH and  $80^\circ\text{C}$ , 0% RH. Change in dehydration time for (e) as-received  $\text{SrCl}_2 \cdot 6\text{H}_2\text{O}$  and (f) pre-conditioned  $\text{SrCl}_2 \cdot 6\text{H}_2\text{O}$ . Change in hydration time for (g) as-received  $\text{SrCl}_2 \cdot 6\text{H}_2\text{O}$  and (h) pre-conditioned  $\text{SrCl}_2 \cdot 6\text{H}_2\text{O}$ .

The preliminary results of our ongoing work for making TCM composites with pre-conditioned salt shows that the composites made using pre-conditioned salt hydrates were mechanically intact and stable for >40 cycles as opposed to 20 cycles when the composites are made with as-received salt hydrates. These samples are continued to be cycled and display prolonged mechanical stability. Using preconditioned salts minimizes the formation of cracks, slipping and changes in expansion/contraction behavior within the host matrix, this allows for a more predictable mechanical behavior during cycling which could result into better long-term performance of the composite TCMs.

### 3. Conclusion

This work demonstrates that model-based understanding of  $R_{\text{crit}}$  of salt hydrates that would be mechanically stable during cycling. This is very crucial as it provides not only pathways to make TCM composites using more energy efficient method of solid state (dry) mixing but also results in TCM composites which are more mechanically robust and have high multi-cyclic efficiency. Thus, predicting  $R_{\text{crit}}$  mitigates the one of the major limitations TCM composites that hinders their more general usage. Furthermore, reaching  $R_{\text{crit}}$  induces faster hydration and dehydration reactions, thus allowing for a broader parametric space for reactor design optimizations.

### 4. Experimental Section

*Materials:* Strontium chloride hexahydrate (99%), magnesium sulfate heptahydrate (99.5%), potassium carbonate sesquihydrate (99%), sodium phosphate dodecahydrate (98%) were purchased from Sigma-Aldrich. Expandable graphite flakes were purchased from Alfa Aesar.

*Sample Preparation:* Salt hydrates were either used as received or grinded into desirable particle size. Prepared salts were grinded using mortar and pestle and sieved using various grade sieves to achieve desirable particle size average.

*Thermogravimetric Analysis (TGA) and Differential Scanning Calorimetry (DSC):* Dehydration experiments were done using TGA/DSC SDT650 (TA Instruments). Prepared salt hydrates were placed in an open alumina crucible and then heated to  $150^\circ\text{C}$  at  $1^\circ\text{C}/\text{min}$ . Nitrogen purge gas at 100 ml/min was used throughout the run. Data was analyzed using the TA Instrument TRIOS software. Rehydration and cyclic runs were done using a DSC/TGA 3+ (Mettler Toledo) with a modular humidity generator (MHG, ProUmid) extension. Prepared salt hydrates were placed in an open aluminum sample pan, heated to  $80^\circ\text{C}$  at  $1^\circ\text{C}/\text{min}$  at 0%RH, then cooled down to  $25^\circ\text{C}$

at 5°C/min with 60 %RH at the end, the samples were then held at 25°C 60 %RH for 90 minutes. Data was analyzed using the Mettler Toledo Star-e software.

*Scanning Electron Microscopy (SEM)*: JEOL 7500F SEM with EDS was used for microscopy analysis. Samples were deposited onto a carbon tape on the sample holder. 10 mm working distance at 15 kV 10  $\mu$ A was used for most imaging needs. Spot size was increased to 20  $\mu$ A for EDS analysis to enhance signal.

## References

- [1] a) P. Albertus, J. S. Manser, S. Litzelman, *Joule* **2020**, *4*, 21-32; b) M. A. Pellow, C. J. M. Emmott, C. J. Barnhart, S. M. Benson, *Energy Environ. Sci.* **2015**, *8*, 1938-1952.
- [2] The heat is on. *Nature Energy* **2016**, *1*, 16193.
- [3] A. Odukomaiya, J. Woods, N. James, S. Kaur, K. R. Gluesenkamp, N. Kumar, S. Mumme, R. Jackson, R. Prasher, *Energy Environ. Sci.* **2021**, *14*, 5315-5329.
- [4] a) A. Sharma, V. V. Tyagi, C. R. Chen, D. Buddhi, *Renew. Sust. Energ. Rev.* **2009**, *13*, 318-345; b) S. M. Hasnain, *Energy Convers. Manag.* **1998**, *39*, 1127-1138.
- [5] K. Linnow, M. Niermann, D. Bonatz, K. Posern, M. Steiger, *Energy Procedia* **2014**, *48*, 394-404.
- [6] a) K. E. N'Tsoukpoe, T. Schmidt, H. U. Rammelberg, B. A. Watts, W. K. L. Ruck, *Appl. Energy* **2014**, *124*, 1-16; b) C. Barreneche, A. I. Fernández, L. F. Cabeza, R. Cuypers, *Energy Procedia* **2014**, *48*, 273-279.
- [7] a) K. Johannes, F. Kuznik, J.-L. Hubert, F. Durier, C. Obrecht, *Appl. Energy* **2015**, *159*, 80-86; b) Y. Zhang, R. Wang, *Energy Storage Mater.* **2020**, *27*, 352-369; c) H. Deshmukh, M. Maiya, S. S. Murthy, *Appl. Therm. Eng.* **2017**, *111*, 1640-1646.
- [8] a) X. Xu, H. Cui, S. A. Memon, H. Yang, W. Tang, *Energy Build.* **2017**, *156*, 163-172; b) K. Shahbaz, I. AlNashef, R. Lin, M. Hashim, F. Mjalli, M. Farid, *Sol. Energy Mater. Sol. Cells* **2016**, *155*, 147-154; c) X. Zhang, X. Li, Y. Zhou, C. Hai, Y. Shen, X. Ren, J. Zeng, *Energy Fuels* **2018**, *32*, 916-921.
- [9] a) A.-J. de Jong, F. Trausel, C. Finck, L. Van Vliet, R. Cuypers, *Energy procedia* **2014**, *48*, 309-319; b) W. Li, M. Zeng, Q. Wang, *Sol. Energy Mater. Sol. Cells* **2020**, *210*, 110509; c) P. A. J. Donkers, L. Pel, O. C. G. Adan, *J. Energy Storage* **2016**, *5*, 25-32.
- [10] a) R.-J. Clark, M. Farid, *Sol. Energy Mater. Sol. Cells* **2021**, *231*, 111311; b) T. Yan, T. Li, J. Xu, J. Chao, R. Wang, Y. I. Aristov, L. G. Gordeeva, P. Dutta, S. S. Murthy, *ACS Energy Lett.* **2021**, *6*, 1795-1802.
- [11] a) J. Zhu, C. Gao, F. Kong, K. Zhang, Z. Bai, J. Guo, *Sol. Energy Mater. Sol. Cells* **2021**, *229*, 111118; b) P. D'Ans, E. Courbon, A. Permyakova, F. Nouar, C. Simonnet-Jégat, F. Bourdreux, L. Malet, C. Serre, M. Frère, N. Steunou, *J. Energy Storage* **2019**, *25*, 100881; c) H. Ait Ousaleh, S. Sair, S. Mansouri, Y. Abboud, A. Faik, A. El Bouari, *Sol. Energy Mater. Sol. Cells* **2020**, *215*, 110601; d) H. Zhou, D. Zhang, *Sol. Energy* **2019**, *184*, 202-208; e) A. I. Shkatulov, J. Houben, H. Fischer, H. P. Huinink, *Renew. Energy* **2020**, *150*, 990-1000.
- [12] R.-J. Clark, A. Mehrabadi, M. Farid, *J. Energy Storage* **2020**, *27*, 101145.
- [13] a) L. C. Sögütoglu, P. A. J. Donkers, H. R. Fischer, H. P. Huinink, O. C. G. Adan, *Appl. Energy* **2018**, *215*, 159-173; b) M. Stanish, D. Perlmutter, *AIChE Journal* **1984**, *30*, 56-62; c) R. Fisher, Y.

- Ding, A. Sciacovelli, *J. Energy Storage* **2021**, *38*, 102561; d) P. A. Kallenberger, K. Posern, K. Linnow, F. J. Brieler, M. Steiger, M. Fröba, *Adv. Sustainable Syst.* **2018**, *2*, 1700160; e) P. A. J. Donkers, S. Beckert, L. Pel, F. Stallmach, M. Steiger, O. C. G. Adan, *J. Phys. Chem. C* **2015**, *119*, 28711-28720; f) V. Van Essen, H. Zondag, J. Gores, L. Bleijendaal, M. Bakker, R. Schuitema, W. Van Helden, Z. He, C. Rindt, *J. Sol. Energy Eng.* **2009**, *131*.
- [14] a) A. Shkatulov, R. Joosten, H. Fischer, H. Huinink, *ACS Appl. Energy Mater.* **2020**, *3*, 6860-6869; b) M. Graham, J. Smith, M. Bilton, E. Shchukina, A. A. Novikov, V. Vinokurov, D. G. Shchukin, *ACS Nano* **2020**, *14*, 8894-8901; c) V. Mamani, A. Gutiérrez, S. Ushak, *Sol. Energy Mater. Sol. Cells* **2018**, *176*, 346-356.
- [15] L.-C. Sögütöglu, M. Steiger, J. Houben, D. Biemans, H. R. Fischer, P. Donkers, H. Huinink, O. C. G. Adan, *Cryst. Growth Design* **2019**, *19*, 2279-2288.
- [16] S. Chizhik, A. Matvienko, A. Sidelnikov, *Cryst. Eng. Comm.* **2018**, *20*, 6005-6017.
- [17] a) V. Kanchana, G. Vaitheeswaran, A. Svane, *J. Alloys Compd.* **2008**, *455*, 480-484; b) A. D. Fortes, K. S. Knight, I. G. Wood, *Acta Crystallogr. B* **2017**, *73*, 47-64; c) P. M. Grindrod, M. J. Heap, A. D. Fortes, P. G. Meredith, I. G. Wood, F. Trippetta, P. R. Sammonds, *J. Geophys. Res.* **2010**, *115*.
- [18] J. Ding, L. Du, G. Pan, J. Lu, X. Wei, J. Li, W. Wang, J. Yan, *Appl. Energy* **2018**, *220*, 536-544.
- [19] a) H. Lauer Jr, K. Solberg, D. Kühner, W. Bron, *Phys. Lett. A* **1971**, *35*, 219-220; b) H. Ghaedi, M. Ayoub, S. Sufian, A. M. Shariff, B. Lal, C. D. Wilfred, *J. Chem. Thermodyn.* **2018**, *118*, 147-158.
- [20] M. Steiger, *J. Chem. Thermodyn.* **2018**, *120*, 106-115.
- [21] a) N. Liu, Z. Lu, J. Zhao, M. T. McDowell, H.-W. Lee, W. Zhao, Y. Cui, *Nat. Nanotechnol.* **2014**, *9*, 187-192; b) Q. Xu, J. Y. Li, J. K. Sun, Y. X. Yin, L. J. Wan, Y. G. Guo, *Adv. Energy Mater.* **2017**, *7*, 1601481; c) T. Shen, X.-h. Xia, D. Xie, Z.-j. Yao, Y. Zhong, J.-y. Zhan, D.-h. Wang, J.-b. Wu, X.-l. Wang, J.-p. Tu, *J. Mater. Chem A* **2017**, *5*, 11197-11203.

## Chapter 6. Ionocaloric Refrigeration

Developing high efficiency heating and cooling with safe, low global warming potential refrigerants is a grand challenge for tackling climate change. Vapor-compression (VC) technology has dominated refrigeration for the past century by using (HFCs). The heating and cooling industries do not have a viable replacement for hydrofluorocarbons (HFCs), and HFCs must be phased out globally under the Kigali Amendment of the Montreal Protocol. It is predicted that by 2050, HFC emissions will account for up to 20% of equivalent CO<sub>2</sub> emissions due to rapid growing demand for refrigeration in the world. Other alternatives to HFCs are being implemented in parts of the world, but these low GWP refrigerants are still slightly flammable, have smaller power densities and efficiencies compared to HFCs, and pose other environmental concerns. This leaves the heating and cooling industries with a refrigerant problem. In fact, in 2017, a team of more than 200 scholars, scientists, policymakers, and business leaders ranked solutions to global warming based on immediate environmental impact. As part of this project, the team measured and modeled the carbon impact of more than 100 solutions through the year 2050. Among all the possible solutions, including wind turbines, tropic forest reforestation, and food waste reduction – refrigerant management was ranked the number one solution to mitigate global warming.

Nearly all heating and cooling technologies employ vapor compression. Initial vapor compression technologies used chlorofluorocarbons (CFCs), which – if unfettered by legislation – would have led to 500 million cases of skin cancer and 63 million cases of cataracts in America by 2100. The Montreal Protocol curbed the use of CFCs world-wide and transitioned heating and cooling technologies to HFCs, which are on track to account for about 25% of our global warming budget by 2050. Legislation has now been signed into law (Kigali Amendment) to curb HFC use and transition the world to a next generation refrigerant. That next generation refrigerant is a choice between HFOs, which acidify our water (irreparably), or natural refrigerants such as propane, which are explosive. The heating and cooling industries must wean off HFCs, but they do not have an acceptable alternative. Thus, vapor compression itself needs to be curbed – not just the refrigerants that drive it. This is where ionocaloric heating and cooling comes in.

In this chapter, we develop a new method for refrigeration and heat pumping that we call “ionocaloric refrigeration.”

The concept was born out of our previous work on the dynamic tunability of phase change materials<sup>1</sup>. In that work, we sought to modulate the temperature of a solid/liquid phase transition using some sort of applied stimulus for applications in the building envelope.

The best way to go about changing the solid/liquid phase transition for this storage application was not obvious. We can do a simple thermodynamic scaling analysis to see why there are limited options. To fix the scaling analysis, we will examine the first order phase transition from liquid water to ice 1h as an example.

### Scaling of Phase Equilibria in a Closed System

We begin by examining the stabilization of the liquid water phase relative to the solid ice Ih phase, i.e. the depression of this melting point. The change in equilibria from the melting point under various thermodynamic conditions is subject to the constraint  $d\Phi_{water} = d\Phi_{ice}$ , from which a generalized Clausius Clapeyron equation can be written, assuming the intensive variables are experimentally independent such that  $d\Phi = -SdT + VdP - pdE - MdH$ :

$$-S_{water}dT + V_{water}dP - pdE - M_{water}dH = -S_{ice}dT + V_{ice}dP - p_{ice}dE - M_{ice}dH \quad 6.1$$

According to the Gibbs-Duhem equation, each term in the above equation is dependent on all other terms – so the equation is heavily coupled. Moreover, the extensive parameters are generally strong functions of their conjugate intensive coupling (e.g. the magnetization is a strong function of the applied field, H) so an integral formulation is needed to relate any of the above quantities. To make simple scaling arguments, however, we assume independence of all variables, so the differential quantities can be integrated out. Isolating  $\Delta T$ , we get:

$$\Delta T_{depression} = \frac{\Delta V_{ice \rightarrow water} \Delta P_{applied} - \Delta p_{ice \rightarrow water} \Delta E_{applied} - \Delta M_{ice \rightarrow water} \Delta H_{applied}}{\Delta S_{ice \rightarrow water}} \quad 6.2$$

Now, we can use the above relation to determine the pressure, electric field, or magnetic fields needed to depress the melting point by an amount  $\Delta T$  when applied independently to the material. Using data from the SeaFreeze equations of state, we can choose an arbitrary target depression of the melting point of ice Ih (here 10°C). We may now proceed to estimate the relative effects of different modes of thermodynamic work on this same water-ice equilibrium by considering each in isolation. Examples of pressure, electric, elastic, and pressure work modes are shown in Figure 6.1

If we want to change water's melting point by  $10^{\circ}\text{C}$ , we would need to apply:

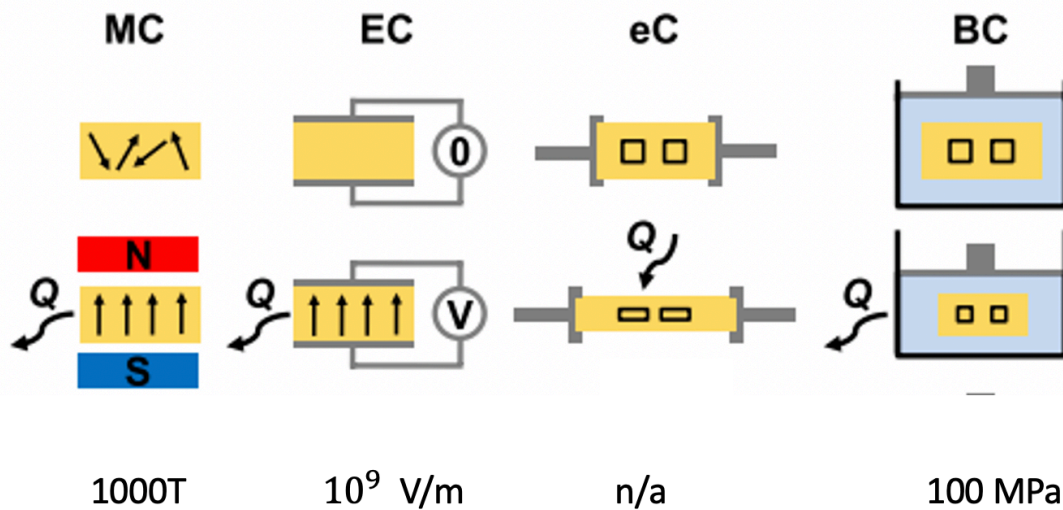


Figure 6.1. Magnitude of Applied field strength needed to shift water's melting point by 10 degrees using magnetic, electric, elastic, and pressure fields.

To shift the melting point of ice by  $10^{\circ}\text{C}$ , an electric field of  $10^9 \frac{\text{V}}{\text{m}}$  must be applied to the bulk system. Because water breaks down above  $1.2\text{V}$ , the length-scale of the water system would need to be  $\approx 1\text{nm}$  to generate  $10^9 \frac{\text{V}}{\text{m}}$ . However, dielectric breakdown in water occurs on the order of  $10^7 \frac{\text{V}}{\text{m}}$ , so even for the rare nanoscale application, an electric field wouldn't be sufficient to shift phase equilibria. Likewise, the water must support a magnetic field of about  $1000 \text{ Tesla}$ , which would break the current record for a magnetic field produced in a lab using superconductors by about  $20\times$  – so the magnetic field has an extremely weak energetic effect on the ice  $\rightarrow$  water phase stabilization. Pressure, on the other hand, is the only thermodynamic toggle in a closed system that is even remotely experimentally viable; However,  $100 \text{ MPa}$  is still a tremendous pressure (for context, iron begins yielding at  $50 \text{ MPa}$ ), and generating that would require special hydraulic equipment.

#### Scaling of Phase Equilibria in an Open System

To bypass the thermodynamic limitations of electrical, magnetic, and pressure based work modes, we can “open” the system to chemical work. This presents a unique thermodynamic nuance: while for most work modes the *intensive* variable is considered tunable and the *extensive* variable considered a function of the fixed difference between material properties, the *intensive* variable of chemical work, the chemical potential, is itself a function of a tunable *extensive* variable, the amount or concentration of an added solute. In an open system, equilibria is expressed by the equality of chemical potentials,  $\mu_{\text{water}} = \mu_{\text{ice}}$  such that  $\mu_o^{\text{water}} + RT\ln(1 - \chi_b) = \mu_o^{\text{ice}}$ , where  $R$  is the ideal gas constant,  $T$  is temperature, and  $\chi_b$  is the mole fraction of some other species introduced into the water system. This can be manipulated further to give the melting point depression as a function of solute concentration:

$$\Delta T_{depression} = \frac{RT_{m,o}^2 \chi_a}{\Delta H_{ice \rightarrow water}} = \frac{zRT_{m,o}^2}{\Delta H_{ice \rightarrow water}} [m] \quad 6.3$$

Where  $[m]$  is the molality and  $z$  is the number of particles the solute splits into when dissolved. This yields a concentration of about 2.5M to achieve at 10°C melting point depression, which is easily realized using standard salts (e.g. NaCl, CaCl<sub>2</sub>, NaI, etc). However, to make a real system work, we need a way to modulate the salt concentration, just as in the closes systems the pressure/magnetic/electric fields can be modulated. For that, we can couple the electrochemical potential to other field vairables.

### Thermodynamic Couplings for Phase Stabilization

Couplings between thermodynamic variables may be used to lower applied field strengths for equivalent phase stabilization applications. We start with the well-known (linearized) osmotic coupling:

$$P = z[m]_{solute}RT \quad 6.4$$

In which P is the osmotic pressure,  $z$  is number of ions dissociated,  $[m]_{solute}$  is the molar concentration, and R is the ideal gas constant. Substituting equation 6.8 in for  $[m]_{concentrate}$ , we take advantage of the coupling between solute concentration, osmotic pressure, and phase stabilization:

$$\Delta T = \frac{T_{m,o}}{2} \left( \frac{1 + \sqrt{\Delta H_{ice \rightarrow water} - 4MP_{applied}}}{\sqrt{\Delta H_{ice \rightarrow water}}} \right) \approx = \frac{P_{applied}MT_{m,o}}{\Delta H_{ice \rightarrow water}} \quad 6.5$$

To achieve  $\Delta T = 10^\circ C$  an applied pressure of about 20 MPa is required, which is about 5x less than the nominal pressure required without the coupling!

A similar thermodynamic “lever” can be introduced for the electrical work mode. In an electrochemical cell, the coupling between voltage and concentration is of the form:

$$V = \frac{RT}{zF} \ln \left( \frac{[m]_{solute,concentrate}}{[m]_{solute,dilute}} \right) \quad 6.6$$

Where F is Faraday’s constant,  $[m]_{solute}$  is the molal concentration of concentrated solute and  $[m]_{dilute}$  is the molal concentration of dilute solute in the electrochemical cell. Substituting equation 6.3 in for  $[m]_{concentrate}$ , we take advantage of the electrochemical coupling for phase stabilization:

$$\Delta T \approx \frac{e^{\frac{FVz}{RT_{m,o}}} M_{H_2O} [m]_{dilute} RT_{m,o}^2 z}{\Delta H_{ice \rightarrow water}}$$

If we set the purification on the dilute side to be  $[m]_{solute,dilute} = 0.1m$ , then  $V_{applied} \approx 0.036V$  to get  $\Delta T = 10^\circ C$ . The term  $e^{\frac{FVz}{RT_{m,o}}}$  represents the ratio of  $\frac{[m]_{solute,concentrate}}{[m]_{solute,dilute}}$ , and scales exponentially with voltage. If  $V$  is set to  $1V$ ,  $e^{\frac{FVz}{RT_{m,o}}} \approx 10^{38}$ , so you can get near-complete purification of solute next to one electrode and arbitrarily high concentration of solute on the other.

**This coupling presents a tremendous thermodynamic lever; *With just  $\approx 0.1V$ , virtually any shift in phase equilibria can be achieved for systems of any size, whereas in the closed system with no coupling,  $\approx 0.1V$  would lack sufficient energetic response even at the atomic scale!***

Now, armed with this simple thermodynamic scaling information, the relative potential of different work modes to stabilize liquid water at low temperatures becomes clear. Practically achievable mechanical and chemical work, requiring pressures of  $\sim 100MPa$  or solute concentrations of  $\sim 2-2.5M$  respectively, can reach the relevant energy scale. However, electrical and magnetic work modes require extreme field strengths to achieve equal energy scales, which may themselves be unachievable at the industrial or laboratory scale (e.g. a magnetic field strength of  $1000T$ ) or may otherwise be unattainable due to limitations of the material. However, these “weak” fields can regain their utility by acting as a thermodynamic lever when coupled to electro-chemical work modes. **Applying a voltage emerges as by far the most powerful thermodynamic toggle for phase stabilization when coupled to ion concentration, and its energetic interaction scales exponentially with voltage.** Coupling pressure to ion concentration for phase stabilization is also effective (can see a  $5x$  reduction in applied pressure for the water system), but the energetic interaction scales only linearly with pressure. Thus, voltage is king for phase stabilization in electrochemical systems, and pressure is king for phase stabilization in pure / non electro-active solutions.

Because voltage has the most favorable energetic scaling for modulating the solid to liquid transition, in our study investigating the dynamically tunable phase change materials, we designed a dual-ion battery (DIB) as shown in Figure 6.2 to electrochemically modify the concentration of salt in a PCM and its melting point in a reversible and dynamic manner. In a DIB, a PCM with a high initial salt concentration and low melting point serves as the electrolyte for the device.

## Tunable Phase Change Material (PCM)

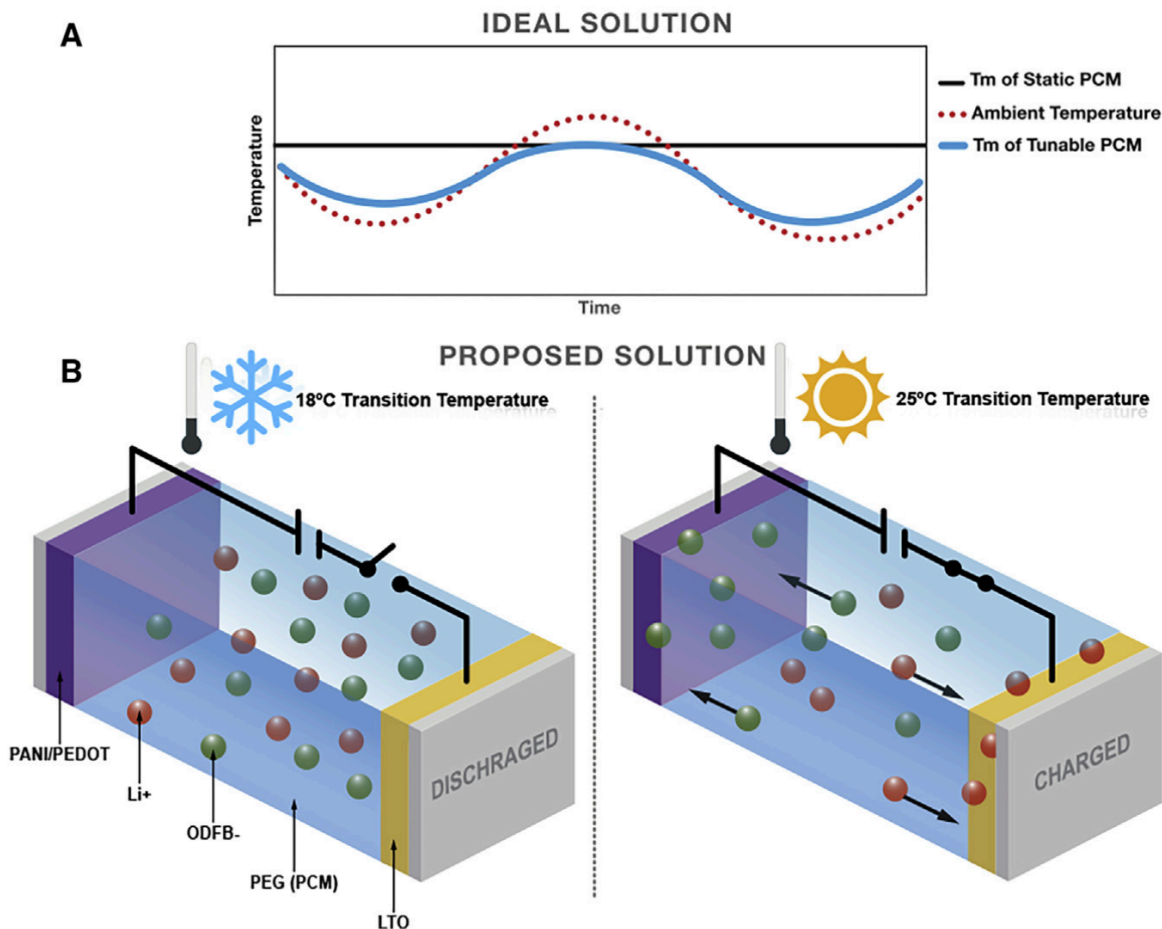


Figure 6.2 Voltage modulated ion concentration fo dynamic tunability of a solid to liquid phase transition

Electrochemical charging stores the cations and anions in the negative and positive electrodes, respectively. This decreases the nominal salt concentration in the PCM/ electrolyte itself, raising its melting point. The device can then be electrochemically discharged to reverse the process and lower the melting point to its original value. The state of charge (SOC) controls the magnitude of the melting point. DIBs store cations and anions from the bulk electrolyte via redox reactions. This enables much higher charge storage capacities and greater changes to the salt concentration of the bulk electrolyte in DIBs. The storage of ions via faradic reactions also reduces the self-discharge of the device and may obviate the need for a constant applied voltage to maintain a

chosen melting point. For a DIB to work as a dynamically tunable TES device, there are three components—PCM, salt, and electrodes—that need to be selected and manipulated for optimized performance.

## **Ionocalorics**

Using this work as a launch pad, we developed a solid-liquid based thermodynamic cycle that we call “ionocaloric refrigeration,” which utilizes the ionocaloric effect by changing the concentration of a salt in a mixture to modulate a material’s melting point, and therefore heat content. We’ve defined the ionocaloric effect as a thermal response to an applied electrochemical field (i.e. ionic field). Ionocaloric heating/cooling utilizes the ionocaloric effect within an appropriate thermodynamic cycle (e.g. Reverse Carnot or Stirling cycle).

Ionocaloric heating and cooling provides a completely new method or platform by which technologies can heat and cool across all industries. There is never any vapor produced in ionocaloric cooling, thus there is no refrigerant that can harm our atmosphere. The first demonstrated prototype is CO<sub>2</sub> negative, environmentally benign, non-hazardous, zero-GWP, non-toxic, and non-flammable. Without vapor leaking into the atmosphere, and toxic/hazardous/flammable components, the ionocaloric technologies have the potential to break the perilous environmental cycle vapor compression cannot seem to escape.

Caloric-effect based cooling, such as magneto- or electro- caloric refrigeration are promising technologies but often require large applied fields for a relatively low coefficient of performance and adiabatic temperature change., We propose using the ionocaloric effect and the accompanying thermodynamic cycle as a caloric-based, all condensed-phase cooling technology. Theoretical and experimental results show a higher adiabatic temperature change and entropy change per unit mass and volume compared to other caloric effects, under low applied field strengths. We demonstrated the viability of a practical system using an Ionocaloric Stirling Refrigeration Cycle. Our experimental results show a coefficient of performance of 30% relative to Carnot, and a temperature lift as high as 25°C using a voltage strength of ~0.22V.

## **Introduction**

Vapor-compression (VC) technology has dominated refrigeration for the past century by using hydrofluorocarbons (HFCs) as liquid refrigerants<sup>2</sup>. HFCs, however, have global warming potential (GWP) greater than 2000 times that of CO<sub>2</sub>, and by 2050 HFC emissions are predicted to account for up to 20% of equivalent CO<sub>2</sub> emissions due to rapid growing demand for refrigeration in the world<sup>3,4</sup>. Other liquid based alternatives to HFCs, such as HFOS, are being implemented in parts of the world, but these low GWP refrigerants are still slightly flammable, have smaller power densities and coefficients of performance (COP) compared to HFCs, and pose other environmental concerns<sup>5-7</sup>. To overcome these challenges, researchers have turned to solid-state materials that provide a refrigeration effect upon the application of an external field<sup>8,9</sup>. These materials – often referred to as caloric materials—generally require large field strengths, and their accompanying thermodynamic cycles have thus far yielded low coefficient of performance (COP), small adiabatic temperature changes, and lower power outputs relative

to a typical VC cycles<sup>9-15</sup>. We report a different caloric effect that we term the ionocaloric effect, and demonstrate better performance than previously reported caloric materials.

In general, a caloric effect refers to an isothermal entropic response to an external field applied to its conjugated energetic variable, such as an electric polarization in response to an electric field. The magnetocaloric effect, for example, refers to a thermal response driven by a magnetic field<sup>16</sup>; the electrocaloric effect, driven by an electric field<sup>17</sup>. Physically, the magnetic field induces an entropy change by aligning the material's magnetic dipoles; the electric field, the electric dipoles. Likewise, we define the "ionocaloric" effect as the thermal response to a changing ionic environment surrounding a solid phase, driven by an electrochemical field. The ionocaloric effect induces an entropy change through the electrochemical mixing of species. As with other caloric effects, the isothermal entropy change ( $\Delta S_T$ ) and adiabatic temperature change ( $\Delta T_s$ ) can be well defined for the ionocaloric effect using Maxwell relations. Maxwell relations can be constructed for the electrochemical field and its corresponding conjugated quantity of chemical species (See<sup>18</sup> section I.1), leading to:  $\Delta T_s = \int_{\Delta\mu} \frac{T}{C_\mu} \left( \frac{\partial n}{\partial T} \right)_\mu d\mu$  and  $\Delta S_T = - \int_{\Delta\mu} \left( \frac{\partial n}{\partial T} \right)_\mu d\mu$  where  $\mu$  is the electrochemical potential,  $T$  the temperature,  $C_\mu$  the constant electrochemical potential heat capacity, and  $n$  is the molar quantity.

Compared to conventional caloric effects, the ionocaloric effect presents a distinct thermodynamic nuance; while for other caloric systems, the applied field induces an energetic response by interacting with its conjugate pair, the ionocaloric system operates in reverse. The electrochemical potential cannot be directly controlled, as an electric, magnetic, or pressure field can. Instead, the effect is calculated from the concentration of chemical species (conjugate variable) using  $\mu = RT \ln(\gamma x)$  where  $\gamma$  is the activity coefficient of the species and  $x$  is the mole fraction. The chemical species, however, can be added/removed from the system through couplings to other field variables, such as temperature (e.g. distillation), pressure (e.g. reverse osmosis), and voltage. We use voltage in our demonstration for the coupling.

Physically, the ionocaloric effect manifests within first-order, solid-liquid phase boundaries by lowering the melting point of a solid below the ambient temperature upon the addition of ions to its surroundings (i.e. applying an electrochemical field). Under this field, the solid melts because the liquid phase becomes more stable, which requires energy to do so. If the system is insulated from its surroundings (adiabatic), it must trade its own internal energy to melt the solid phase, upon which it lowers its own temperature by endothermically converting some solid to the liquid phase. This process will continue until the solid's temperature is equal to its new melting temperature, which is dictated both by the strength of the applied electrochemical field and caloric material's solid-liquid phase boundaries. The reverse effect, observed by removing ions from the caloric material's surroundings (or, conversely, by adding more caloric material), will increase the melting point of the liquid phase. The liquid, which is now most stable as a solid, crystallizes -- releasing energy to do so. Under adiabatic conditions, it will release energy to itself, increasing the temperature and exothermically converting some liquid to the solid phase. This process will continue until the liquid's temperature is equal to the new melting/crystallization temperature.

The ionocaloric effect is not to be confused with electrochemical cooling. In the ionocaloric effect, the entropy change is achieved using a reversible phase transition, and exhibits

a field-induced phase transition temperature change enabled by the electrochemical field. In traditional electrochemical refrigeration, cooling is driven by the “thermogalvanic effect” which

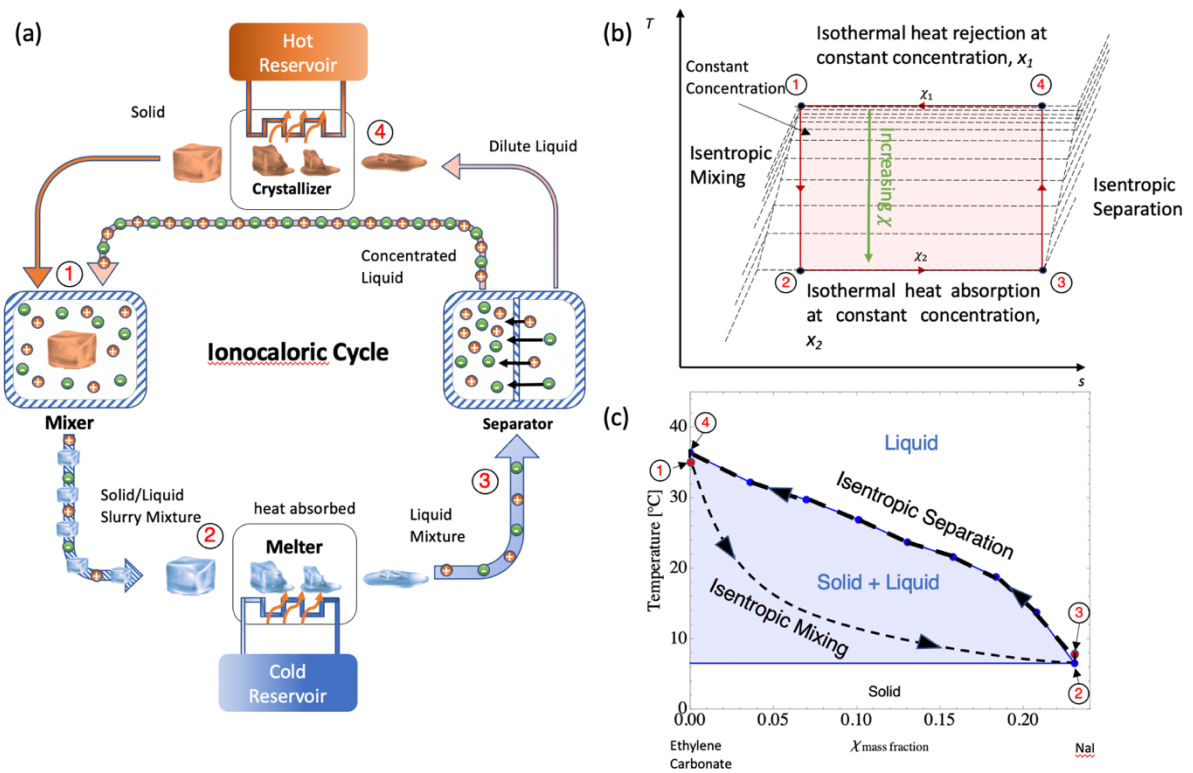


Figure 6.3: Overview of the ionocaloric cycle. (A) Schematic of the 4 steps involved in ionocaloric refrigeration (separation, crystallization, mixing, and melting). (B) T-S diagram for an ideal, reversible ionocaloric cycle. (C) The T-X binary phase equilibria for the ethylene carbonate-sodium iodide system, along with state points corresponding to various points on the T-S diagram and schematic in (A).

utilizes the entropy change of ions participating in redox reactions to generate a temperature difference from applied work. In thermogalvanic cooling, ions participate in the cooling and the liquid solvent serves to enable ion transport. Although the entropy change per unit ion is large, the entropy change per unit mass and volume is very low because of the large amount of liquid solvent present in the system. Therefore, the temperature lift is expected to be very small. Recent experimental demonstrations<sup>19,20</sup> have shown that the highest temperature lift achieved to date is  $0.15^{\circ}\text{C}$ , with a relative Carnot COP  $<0.002$ . In our proposed idea the solvent is participating in a first order phase transition, and very large entropy/enthalpy and adiabatic temperature changes can be achieved because the whole medium is participating in the entropy change.

The ionocaloric effect can cool/heat a material under an applied/removed electrochemical field, but to provide continuous refrigeration it must be embedded into an appropriate thermodynamic cycle. In physical terms, this can be done in 4 steps(Fig. 1A): (i) mixing a salt with a solid, which cools the solid to its now-lower melting point (ii), melting the solid at the lower melting point (iii), separating the salt from the liquid, thereby heating the solution, and raising its melting point (iv): and crystallizing the solid from the liquid at the now-higher melting point. To make this Carnot-like (Fig 1B), this must be done via (i) Isentropic (adiabatic and reversible) mixing, (ii) Isocompositional and isothermal heat absorption (iii) isentropic separation, and (iv) Isocompositional and isothermal heat rejection. We depict the T-S diagram of the ionocaloric cycle along different lines of constant composition (Fig. 1B) and show the traversal of each step on the systems Temperature-Composition (T-X) phase boundaries at different electrochemical fields (mass fractions) (Fig. 1C). We determined the systems T-X phase equilibria (Fig 1C) by differential scanning calorimetry (17, section 3).

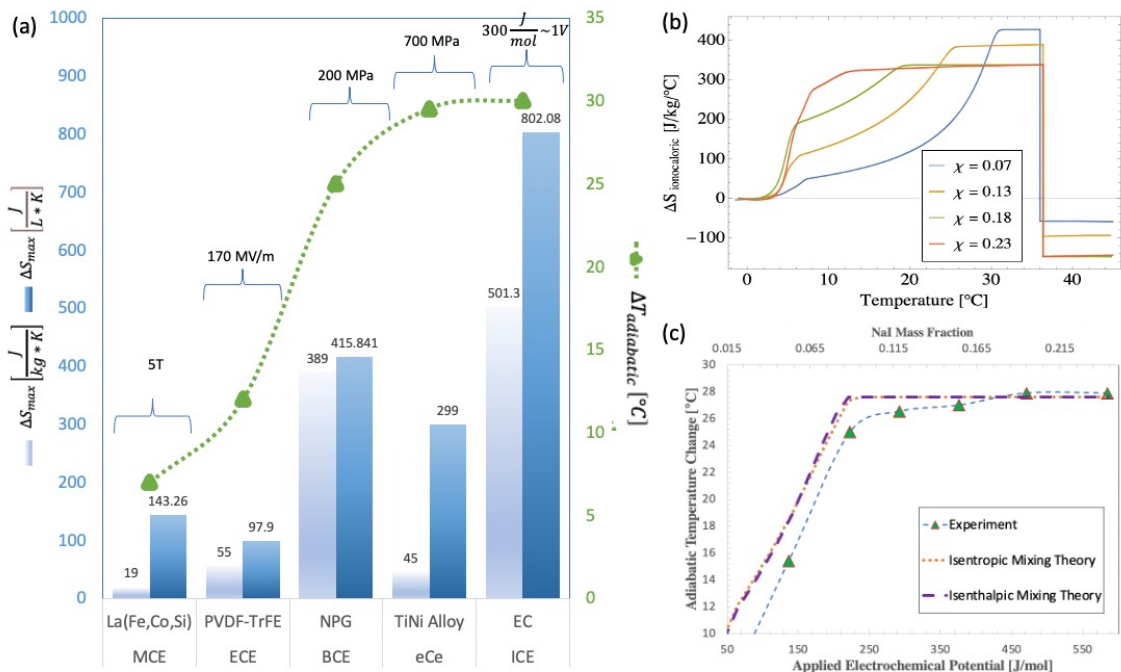


Figure 6.4: The ionocaloric effect of the ethylene carbonate-sodium iodide system. (A) Comparison of the maximum entropy change (per kg and L) and adiabatic temperature change of EC/Nal to the state of the art in magnetocaloric (MCE), electrocaloric (ECE), elastocaloric (eCe), and barocaloric (BCE) literature<sup>22–25</sup>, along with the applied field strengths to achieve the effect. The data shown for other caloric materials are typical values based on three criteria: (i) simultaneous measurement of entropy and adiabatic temperature change on the same system (ii) measurement taken near room temperature and (iii) reversible material changes. Detailed data sets for all other possible cases are available in references<sup>26,28,29</sup> (B) Ionocaloric entropy change for various mass fractions of NaI. (C) Directly measured adiabatic temperature change of ethylene carbonate as a function of the applied electrochemical potential (bottom axis) and mass fraction (top axis).

The maximum and minimum operating temperatures of the cycle are dictated by the pure caloric materials' melting point and the lowest melting point of the binary salt mixture. The refrigeration capacity, or the amount of heat absorbed per cycle, is determined by the caloric material's enthalpy of fusion. The ideal ionocaloric material will have a melting point above room temperature, a eutectic (or some other invariant point) well below room temperature, and a high enthalpy of fusion. Ideal ionocaloric materials should also have high cryscopic constants<sup>21</sup> so that large temperature changes can be achieved using small amounts of electrolyte. Based on these criteria we identified the ethylene carbonate-sodium iodide system as a promising ionocaloric system (17, section 2) with a pure melting point of  $T_{melt} = 36.4^{\circ}C$ , a eutectic transition at  $T_{eutectic} = 6.4^{\circ}C$ , and a relatively high latent heat of fusion,  $\Delta H_{fus} = 204.6 \frac{J}{mL}$  (as compared to  $\Delta H_{fusion} \approx 330 \frac{J}{mL}$  for water, which has one of the highest entropies of fusion of known near-room temperature molecules). We note that the EC-Nal system is a  $CO_2$  negative,

environmentally benign, non-hazardous, zero-GWP, non-toxic, and non-flammable mixture. EC is a common additive to battery electrolytes (e.g. Li-ion), and can be made stable over a long life-time and has shown good cyclability and stability however more studies are needed for cooling applications. The material compatibility in the liquid state with other materials is not well characterized.

The ionocaloric effect (ICE), characterized by  $\Delta S_{isothermal}$  and  $\Delta T_{adiabatic}$  of the EC/NaI system, is better than other caloric effects reported in the literature (Figure 6.4A)<sup>22-29</sup>. We determined  $\Delta S_{isothermal} = 802.08 \frac{J}{L \cdot K}$  by calorimetry (17, Section 3) which is roughly two times larger than the neopentyl glycol based barocaloric effect (BCE), which has one of the highest  $\Delta S_{isothermal}$  reported<sup>23</sup>. In addition,  $\Delta S_{isothermal}$  per unit mass (Figure 6.4A, B) is over ten times the state of the art for magneto-, electro-, and elasto- caloric effects (Figure 6.4A). For the EC/NaI system, we directly measured  $\Delta T_{adiabatic}$  (Figure 6.4C) of 28°C using an electrochemical potential of ~450 J/mol (i.e. at NaI mass fraction of ~0.18 using  $= RT \ln(\gamma x)$ ). This is larger than other caloric effects (Figure 6.4A). Multicalorics is an emerging field in which entropy changes from multiple applied fields can potentially increase  $\Delta T_{adiabatic}$  and  $\Delta S_{isothermal}$ , however the reported performances<sup>30</sup> are still smaller than what has been found for the best caloric materials. Our theoretical model for  $\Delta T_{adiabatic}$  (17, section 4-5) matches well our data (Figure 6.4C). To modulate the electrochemical potential in a real system, the ion concentration can be controlled by applying a voltage in an electrolytic cell (e.g. dual ion battery) where the applied voltage is typically ~1V. This stimulus is considerably milder than those used in magnetic, electric, and pressure based caloric systems.

We determined the maximum  $COP = \frac{Q_{cool}}{W_{in}}$  for the EC/NaI system by the minimum energy needed to reversibly separate the solution, which is given by the free energy of mixing, and the cooling energy,  $Q_{cool}$ , is related to the enthalpy of fusion of ethylene carbonate (17, section 7). Neglecting any work output available during the isentropic mixing step (analogous to using an expansion valve instead of a turbine in a vapor-compression cycle) and assuming perfect regeneration (17, section 6), we compute the relative Carnot COP ( $COP_C$ ) to be roughly 0.9 for temperature spans of 10 – 30°C (17, section 7).

While the theoretical reversible properties of the EC/NaI system are competitive with that of other caloric materials, and the theoretical performance in an ideal thermodynamic cycle can reach very high efficiencies, the performance in practice will be strongly impacted by the details of the separation process, which can be viewed as a desalination step. Desalination technologies<sup>31,32</sup> are mature and plentiful and include both thermal, mechanical, and electrochemical techniques. Thermal separation techniques are inherently less efficient than mechanical techniques due to 2<sup>nd</sup> law penalties of three-temperature systems. Mechanical techniques<sup>33</sup>, such as reverse osmosis, can operate at efficiencies as high as 50% of the theoretical limit of separation in commercial plants but require relatively high operating pressures. Electrochemical techniques, such as electrodialysis, also routinely operate at high efficiencies (~50%), but do not require high operating pressures/fields<sup>34</sup>. For this reason, electrodialysis was used in the separation step in this study to show the feasibility of a practical system.

Electrodialysis separates ions by applying an electric field across perm-selective ion-exchange membranes. In our EC/NaI system, the electrodialysis process is a system broken up into the working fluid and electrode compartments (Figure 6.5A). The electrode compartments are each

filled with 0.5M  $NaI_3$  and 1.5M  $NaI$ , forming a symmetric cell. Current is driven across the cell using an Iodide/Triiodide redox couple (well-studied for applications in dye-sensitized solar cells). At the negative electrode triiodide is reduced, following  $I_3^- + 2e^- \rightarrow 3I^-$  and at the positive electrode, iodide is oxidized such that  $3I^- \rightarrow I_3^- + 2e^-$ . Because they are symmetric reactions, the change in Gibbs free energy between the oxidized/reduced states is zero, and the reaction proceeds at any non-zero voltage applied across the electrodes. At higher potentials ( $\sim 1V$  higher than the iodide/triiodide couple vs SCE)(17, section 6), triiodide is further oxidized to pure iodine,  $2I_3^- \rightarrow 3I_2 + 2e^-$ .  $I_2$  is soluble in EC, so it dissolves back into the electrode solution, and upon circulation, either combines with an  $I^-$  to re-form  $I_3^-$ , or gets reduced at the negative electrode to the same result. Positive ions ( $Na^+$ ) will then be driven toward the negative electrode upon reduction of  $I_3^-$ .  $Na^+$  can cross the cation exchange membranes (Figure 6.5A, red) but are prevented from crossing the anion exchange membrane (Figure 6.5A, green) by Donnan exclusion. Likewise, the negative  $I^-$  ions will be driven toward the positive electrode upon oxidation of  $I^-$ , and may cross the anion exchange membrane, but are prevented

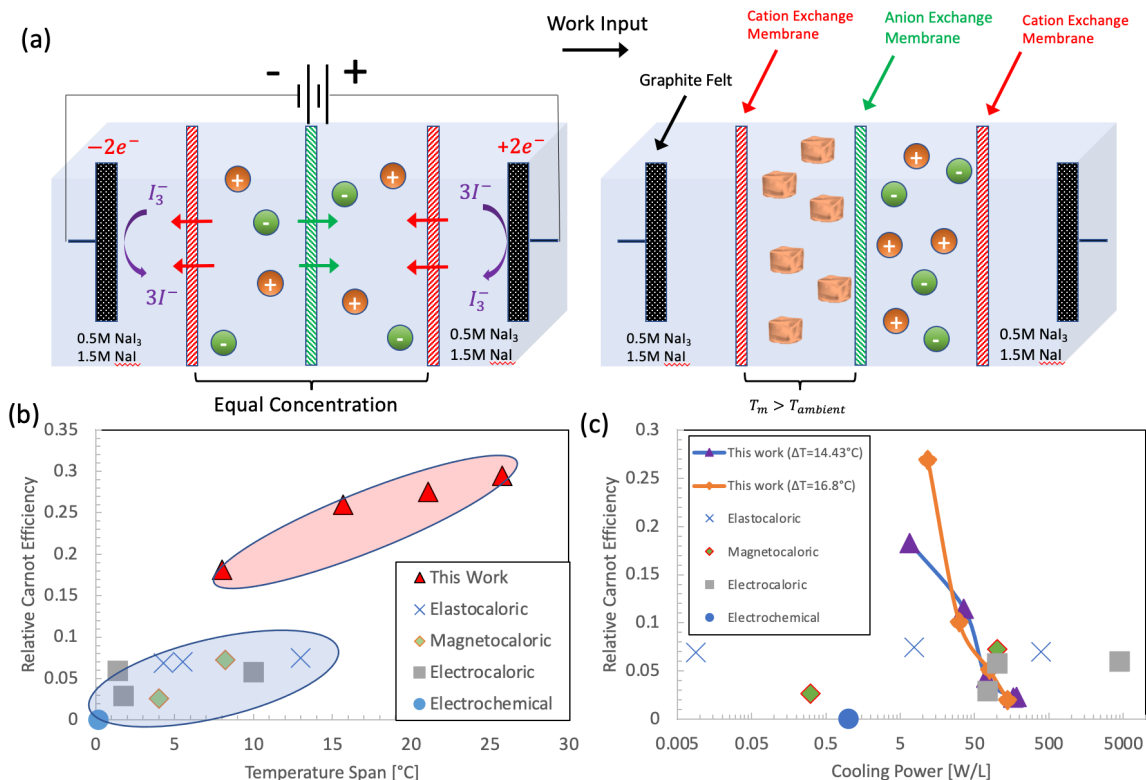


Figure 6.5: Experimental setup and results. (A) Electrodesalination cell used for the separation process of the ionocaloric cycle. (B and C) Relative Carnot efficiency vs temperature span and relative Carnot efficiency vs cooling power per liter of the device compared against that of other elastocaloric magnetocaloric, electrocaloric, and electrochemical prototypes reported in literature<sup>15,19,20,35–40</sup>. The data shown were curated from the literature where COP, Temperature Span and Cooling power were simultaneously reported. Detailed data sets for other conditions can be obtained from<sup>29</sup>

from crossing the cation exchange membranes. Because the membranes are selective to only one type of ion, one compartment will eventually become completely depleted of ions, while the other becomes concentrated.

This cell setup was run until depletion of one compartment for various EC/NaI concentrations and current densities. We note that these experiments assume a regenerative ionocaloric cycle (17, section 6) so that the separation process was done isothermally instead of isentropically. As the concentration of the diluent is decreased, the melting point will increase until it is equal to the temperature of the external sink, upon which crystallization of the diluent rejects heat to the external sink. At the end of the separation process, the diluent is predominantly solid while the concentrate is liquid (17, section 10). The work input into the separation process is directly calculated by the I-V work done at the electrodes. The temperature of the cold side is dictated by the final concentration of the two solutions when mixed such that all energy was absorbed at the system's liquidus temperature (solid/liquid phase boundary). The energy absorbed at the liquidus temperature is correlated to the amount of solid coming out of the electrodesalination cell

(17, section 10). The experimental COP was then calculated from the work input measured and the cooling energy provided.

We show the relative Carnot COP ( $COP_c$ ) vs temperature and cooling power of the ionocaloric device compared to the performance of devices made utilizing other caloric effects<sup>15,19,20,35-40</sup> (Figure 6.5B,C). The performance of the ionocaloric device operated at a temperature span,  $\Delta T_{span} = (T_{hot} - T_{cold})$ , of  $25.76^\circ C$  is 29.5% relative to Carnot with a cooling power of  $5.75 \frac{W}{L}$ . The best device level performance utilizing other caloric effects is reported at 7.4% relative to Carnot at a much smaller temperature span of  $13^\circ C$  (Figure 6.5B). Compared to elastocaloric devices at 7% efficiency, the ionocaloric device's cooling power is at least an order of magnitude larger (Figure 6.5C). However, an electrocaloric device operating at  $\Delta T_{span} = 1.6^\circ C$  has a cooling power over an order of magnitude larger than that of the ionocaloric device. This difference is expected, as they operated at a much lower temperature span than the ionocaloric device.

The largest challenge to overcome using electro dialysis in the ionocaloric cycle is the cooling power output. The membrane resistance for the EC/NaI electrolyte is roughly 100x larger than a typical membrane resistance in an aqueous system (17, section 13), posing a hurdle for achieving high cooling power densities at high efficiencies. Most ion-exchange membranes are designed for aqueous systems, so developing low-resistance membranes specifically made for organic electrolytes would be needed to increase the cooling power density. For additional perspective, some high efficiency aqueous vanadium redox flow batteries operate at  $800 \text{ mA/cm}^2$ ; the ionocaloric device operated at  $\approx 0.5 \text{ mA/cm}^2$  for its highest efficiency results. If, for example, it operated at  $800 \text{ mA/cm}^2$  like in the aqueous system, the cooling power output would be equal to  $9.2 \frac{kW}{L}$ .

The largest benefit of using electro dialysis in the separation step is in lowering the needed strength of the applied field. Magnetocaloric devices use incredibly strong magnetic fields (up to 5T) (Fig. 2A) which are difficult to generate using permanent magnets alone. In electrocaloric devices, electric fields of  $\approx 200 \frac{MV}{m}$  are common (over 50x larger than the dielectric strength of air) and can only be generated by applying voltages across micron-sized films in the kV range. Elastocaloric devices with high  $\Delta T_{span}$  operate at stresses of 800 MPa; barocaloric, at stresses around 200 MPa. For context, the yield strength of steel is 350 MPa. In the ionocaloric device the applied field is  $\sim 0.22 \text{ V}$  which is relatively modest. As a comparison, a lithium ion battery operates at  $\sim 4\text{V}$ . Such lowering of the applied field will have significant impact on reducing the cost of refrigeration technology based on the ionocaloric cycle proposed here. The experimental device demonstration is based on the regenerative system, which is completely analogous the Stirling cycle (17, section 6). Therefore, we can term our experimentally demonstrated cycle is an Ionocaloric Stirling Refrigeration Cycle.

We have shown how the ionocaloric effect can lead to higher performance as compared to other caloric materials. Even higher COP, temperature lift ( $\Delta T$ ), and power density are possible with additional improvements. For example, the maximum adiabatic temperature change of ethylene carbonate is about  $100^\circ C$  ( $\Delta T_{adibatic} \approx \frac{\Delta H_{fus}}{C_p} \approx 100^\circ C$ ), but we were only able to achieve  $30^\circ C$ . This limitation comes from the phase boundaries (Figure 6.3C). A ternary or quaternary eutectic system can push these phase boundaries to lower temperatures if a larger

adiabatic temperature change is needed. Similarly, power density can potentially be increased by 100x if commercial membranes could be designed to have similar resistance values for EC as they do for water (17, section 13). As the resistance is decreased, and the selectivity of the membranes improves, higher efficiencies can be achieved for the same power output, leading to increased COP.

## Part 2: The Nitty Gritty

### 1 Adiabatic Temperature Change and Isothermal Entropy Change

First, we choose a fundamental thermodynamic relation of the form  $S = S(T, P, \mu)$ . The differential is then:

$$dS = \left(\frac{\partial S}{\partial T}\right)_{P,\mu} dT + \left(\frac{\partial S}{\partial P}\right)_{T,\mu} dP + \left(\frac{\partial S}{\partial \mu}\right)_{T,P} d\mu \quad 6.7$$

And the heat capacity is defined as  $C_{p,\mu} = T \left(\frac{\partial S}{\partial T}\right)_{P,\mu}$  such that

$$dS = \frac{C_{p,\mu}}{T} dT + \left(\frac{\partial S}{\partial P}\right)_{T,\mu} dP + \left(\frac{\partial S}{\partial \mu}\right)_{T,P} d\mu \quad 6.8$$

To define the adiabatic temperature change from the change in entropy with respect to the change in electrochemical potential at constant pressure and temperature,  $\Delta T_{adiabatic}$ , we set  $dS = 0$  and solve for  $dT$ :

$$dT = -\frac{T}{C_{p,\mu}} \left(\frac{\partial S}{\partial \mu}\right)_{T,P} d\mu \quad 6.9$$

And integrating we get:

$$\Delta T_{adiabatic} = -\int \frac{T}{C_{p,\mu}} \left(\frac{\partial S}{\partial \mu}\right)_{T,P} d\mu \quad 6.10$$

Now, we can construct a Maxwell relation using the differential of the thermodynamic function to get rid of  $\left(\frac{\partial S}{\partial \mu}\right)_{T,P}$ . The differential of the thermodynamic function corresponding to the fundamental relation  $S(T, P, \mu)$  can be expressed as:

$$d\Phi = -SdT + VdP - nd\mu \quad 6.11$$

Since  $d\Phi$  is the exact differential type, we know that mixed second-order partial derivatives are independent of the order in which they compute, we can write:

$$\left(\frac{\partial S}{\partial \mu}\right)_{T,P} = \left(\frac{\partial n}{\partial T}\right)_{\mu,P} \quad 6.12$$

Which we can substitute into equation 6.10:

$$\Delta T_{adiabatic} = - \int \frac{T}{C_{p,\mu}} \left( \frac{\partial n}{\partial T} \right)_{\mu,P} d\mu \quad 6.13$$

Likewise, to determine the isothermal entropy change,  $\Delta S_{isothermal}$ , we set  $dT = 0$  in equation 2 at constant pressure  $dP = 0$ , such that:

$$dS = \left( \frac{\partial S}{\partial \mu} \right)_{T,P} d\mu \quad 6.14$$

Integrating, and substituting in equation 6.12 we get:

$$\Delta S_{isothermal} = - \int \left( \frac{\partial n}{\partial T} \right)_{\mu,P} d\mu \quad 6.15$$

## 2 Ionocaloric Material Selection

Ideal refrigerants in the ionocaloric cycle should experience large adiabatic temperature changes and isothermal entropy changes. This allows for high temperature spans and large refrigeration capacities (the amount of heat absorbed per cycle). In addition, the materials' melting point dictates the maximum operating temperature of the cycle, so only materials with melting points above room temperature should be considered. The lowest operating temperature in the cycle is determined by either (1) The max adiabatic temperature change, or (2) the maximum melting point depression that can be achieved for a given material/salt combination.

The maximum adiabatic temperature change for the ionocaloric material, independent of the salt used in conjunction with the material, scales with the ratio of latent heat to specific heat,  $\Delta T_{max} \approx \frac{\Delta H_{sl}}{C_p}$ . However, the amount of salt needed to drive this melting point depression is related to the ionocaloric material's cryoscopic constant<sup>21</sup>,  $k_f = \frac{RT_m^2}{\Delta H_{sl}}$ , which can be used to relate (to first order) the expected melting point depression to the molality for a given solvent/salt combination:  $\Delta T_D = -ik_f[m]$ , where R is the ideal gas constant, M is the molar mass of the ionocaloric material,  $T_m$  is the melting point,  $\Delta H_{sl}$  is the enthalpy of fusion,  $i$  is the van't Hoff Factor (number of particles the salt dissociates into), and  $[m]$  is the molality.

These simple relations demonstrate that a material with a high enthalpy change will enable large adiabatic temperature changes but will require higher salt concentrations to move the phase boundary. To support the higher salt concentrations needed to move the phase boundaries for lower to moderate cryoscopic constant materials, the ionocaloric material must have high salt solubility. Ionic solubility can be predicted from solution theory, but this usually requires many experimental fitting parameters. Instead, the material's dielectric constant can be used as a broad indicator of a material's ability to solubilize ionic compounds. In general, materials with higher dielectric constants are more likely to exhibit high solubilities<sup>41</sup>.

When searching for an ideal ionocaloric material, we can apply these simple rules to identify materials with (1) Melting point greater than ambient temperature, (2) Large enthalpy of fusion (3) High Cryoscopic Constant (4) Large maximum adiabatic temperature change, and (5) Large dielectric constant.

A list of materials meeting at least several of these criteria is listed in table 1<sup>42</sup>. Ethylene carbonate has the best balance between the various factors, with a melting point similar to the hot side temperature of many air conditioning environments, a large enthalpy of fusion, moderate cryoscopic constant, and an extraordinarily high dielectric constant of 89.78 at 40°C

<sup>43</sup>.

<b>Chemical</b>	<b><math>T_{m,o}</math> (Celsius)</b>	<b><math>\Delta H_{sl}</math> (J/g)</b>	<b><math>k_f</math></b>
<b>Cyclohexanol</b>	25	17	43.47
<b>Phenol</b>	40.5	127	6.44
<b>t-butanol</b>	25.82	91	8.17
<b>Cetyl Alcohol</b>	49.27	238	3.63
<b>menthol</b>	40	80	10.19
<b>Ethylene Carbonate</b>	35	155	5.09
<b>Sulfolane</b>	27.5	10	75.15
<b>Methyl anthranilate</b>	24	60	12.24
<b>p-Cresol</b>	35	116	6.81
<b>Guaiacol</b>	28	120	6.28
<b>DMSO</b>	19	184	3.86

Table 6.1 Ionocaloric material Selection

For these reasons, we identified ethylene carbonate as the most promising candidate for initial experiments. Our goal was to drive the ionocaloric effect using small applied field strengths, so we opted for electro dialysis to drive the separation in the ionocaloric cycle. Electro dialysis is complex, but broadly speaking it works best with ion/solvent pairs with high ionic conductivity and monovalent dissociation. Ethylene carbonate is widely used in battery electrolyte solutions, so many of its' electrochemical properties are well characterized for various ion pairs<sup>44</sup> ( see Table 6.2 below).

<b>Salt</b>	<b>Solubility (gr/100g Ethylene Carbonate)</b>	<b>Ionic conductivity (<math>\mu\text{S}/\text{cm}</math>)</b>
<b><math>\text{ZnCl}_2</math></b>	33	n/a
<b><math>\text{HgCl}_2</math></b>	49	n/a
<b><math>\text{KCNS}</math></b>	$\approx 0$	n/a
<b><math>\text{KMnO}_4</math></b>	$\approx 0$	n/a
<b><math>\text{K}_2\text{Cr}_2\text{O}_7</math></b>	$\approx 0$	n/a
<b><math>\text{Cu}(\text{Br})_2</math></b>	$\approx 0$	n/a
<b><math>\text{NaI}</math></b>	37.6	11000
<b><math>\text{NaBr}</math></b>	0.31	94.6
<b><math>\text{CaCl}_2</math></b>	0.2	8.66
<b><math>\text{KI}</math></b>	11.16	15000

Table 6.2 Salt Combinations with Ethylene Carbonate

$\text{ZnCl}_2$  and  $\text{HgCl}_2$  both have excellent solubilities, which would allow for very large temperature spans. Because both cations carry a  $2^+$  charge, they will experience more difficulty crossing cation exchange membranes, making them less attractive. In addition, the  $\text{Cl}^-$  anion poses problems if it reaches the positive electrode, as it will convert into a toxic chlorine gas.  $\text{NaI}$  and  $\text{KI}$  both have high solubilities and extremely high ionic conductivity relative to most organic electrolytes (for reference, 1M aqueous solutions have  $\sim 10\times$  the conductivity). Both would be suitable in an ionocaloric device, but we opted for  $\text{NaI}$  because of its higher salt solubility.

### 3. Temperature-Composition Binary Phase Equilibria

Binary phase equilibria for the Ethylene Carbonate-sodium iodide system was determined via differential scanning calorimetry using a TA instruments DSC 2500 ( $\sim 40\mu\text{W}$  resolution,  $0.01^\circ\text{C}$  Temperature precision,  $0.1^\circ\text{C}$  temperature accuracy). The temperature scale was calibrated in accordance with the calibration procedure recommended by an IUPAC technical report on calibration standards for differential scanning calorimetry<sup>45</sup>. Temperature correction coefficients were calculated using pure analytical grade indium and water as reference materials, which were subsequently used by the DSC 2500's software in analysis of temperature onsets.

Samples were prepared by mixing ethylene carbonate and sodium iodide (both  $>99.9\%$  purity from Sigma Aldrich) to make binary solutions incremented by 0.25 molal (m).  $10\mu\text{L}$  of each solution was transferred into TA instruments Tzero alodined aluminum pans and then hermetically sealed. Each sample was ramped to  $-60^\circ\text{C}$  at  $2^\circ\text{C}/\text{min}$ , held isothermally for 5

minutes to bring the sample to equilibrium, and then heated at  $0.5^{\circ}\text{C}/\text{min}$  until the sample reached  $45^{\circ}\text{C}$ .

The eutectic temperature was identified as the first peak in each thermogram, and the precise value was determined by the tangent construction method<sup>46</sup>. In several of the higher concentration thermograms, a double peak near the eutectic is observed. Because the  $I^{-}/I_3^{-}$  conversion is photoactive, and DSC sample preparation requires a high surface/volume sample ratio, a small concentration of  $I_3^{-}$  appears before the sample is hermetically sealed, as evidenced by a slight purple tint to the solution. The presence of low concentrations of  $I_3^{-}$  is likely responsible for the split-peak observed in the thermograms. The eutectic temperature was further verified by vigorously mixing solid EC and NaI at a eutectic composition in a large quantity (80g of EC) in an insulated container, and measuring the lowest temperature reached via thermocouples. Both methods give a eutectic temperature of  $6.4^{\circ}\text{C}$ . The liquidus temperature corresponds to the second peak in each thermogram, and its temperature is determined by the peak value<sup>46,47</sup>. In the constructed phase diagram (Figure 6.7), the solid/salt mixture is not shown because the solubility of salt in the solid phase is negligible.

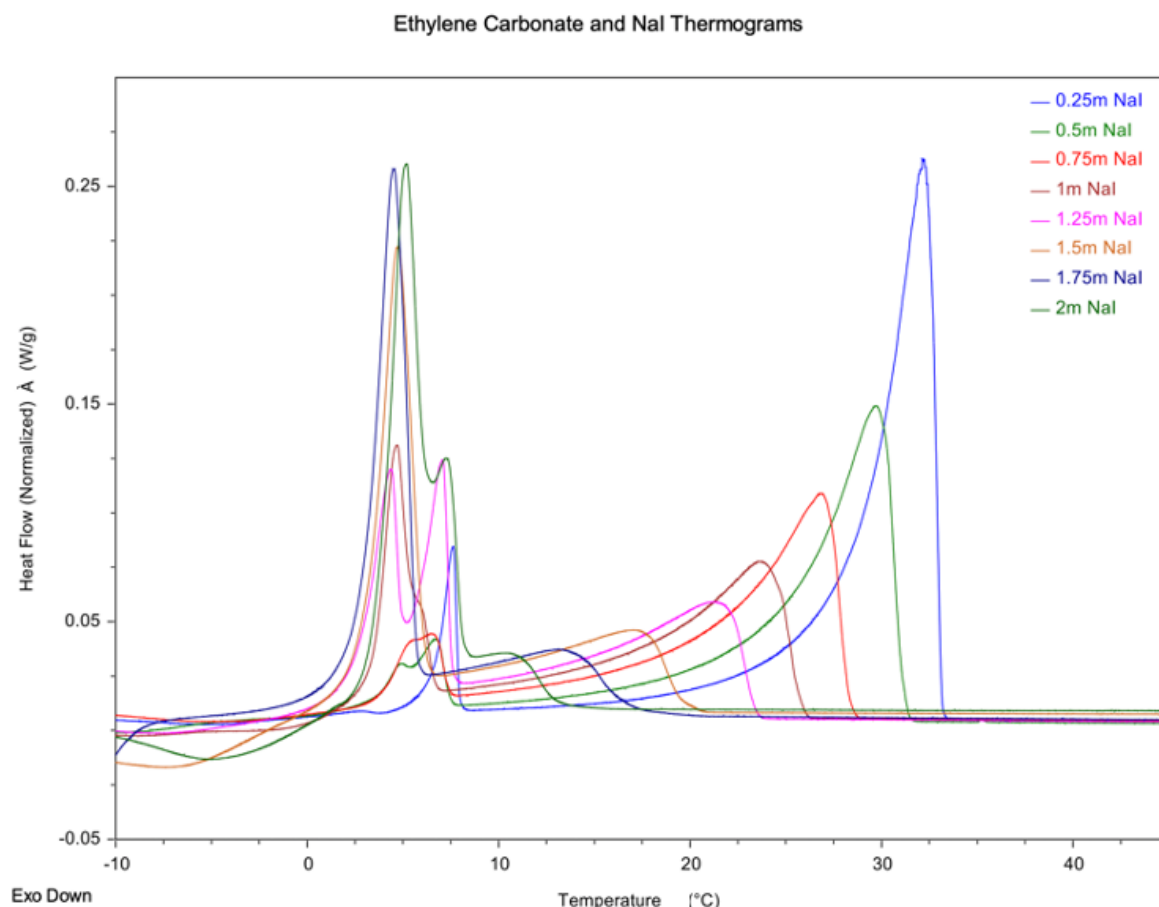


Figure 6.6 DSC Thermograms

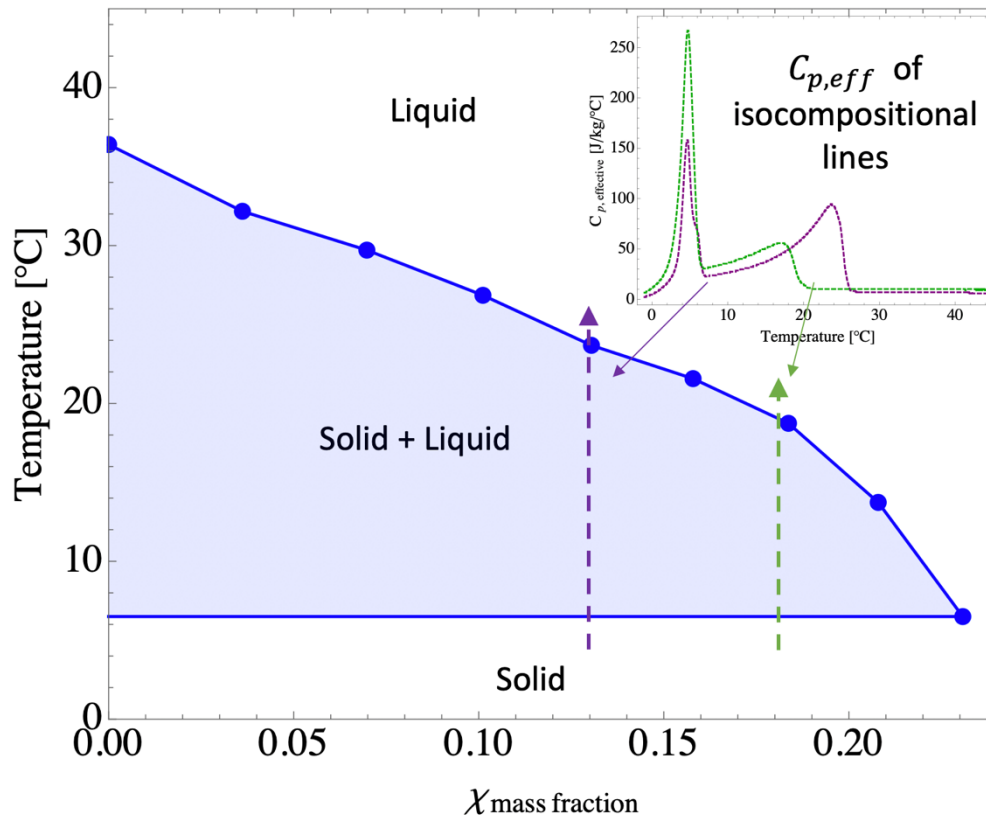


Figure 6.7 EC + NaI Binary Phase Equilibria

#### 4. Adiabatic Temperature Change Experiments and Theory

**Measurement of adiabatic temperature change:** To measure the adiabatic temperature change of Ethylene Carbonate under various applied electrochemical fields, a home-built adiabatic mixing chamber was constructed. The mixing chamber was built using a combination of highly insulating fiber glass and styofam insulation and was mounted on a vortex mixer. For each experiment, 70g of ethylene carbonate was pre-heated to 35°C along with pure sodium iodide salt (mass varied for each experiment), and then transferred into the adiabatic chamber at the start of each experiment. The chamber was then sealed, and the vortex mixer was turned on such that the two solids were vigorously mixed. Three embedded thermocouples recorded the temperature vs time of the resulting solid/liquid solution, and the steady state value of all three was averaged and recorded as the final temperature. This was subtracted from the starting temperature (35°C) to determine the adiabatic temperature change, and these values are shown in Figure 6.4c for various mass fractions / applied electrochemical fields. This was then compared

to the output of equations 6.16 and 6.23, which predict the adiabatic temperature change of the ionocaloric material under both isenthalpic and isentropic conditions.

**Theory for Adiabatic Non-reversible (Isenthalpic) Mixing:** In a practical device, the mixing step is not done reversibly, just as in a vapor compression system an expansion valve is used instead of a turbine/expander. This is because the amount of useful work that can be extracted from the mixing step / expansion step in vapor compression is very small compared to the total work input of the separator/compressor, and work recovery device would be very expensive. For this reason, we analyze adiabatic (but not reversible) and therefore isenthalpic mixing. An isenthalpic process has the same enthalpy before and after, so at the system level:

$$H_{initial} = H_{final} \quad 6.16$$

Where the initial enthalpy is a summation of the enthalpies of the two components to be mixed:

$$H_{initial} = \sum m_i h_i = m_s h_s + m_{ic} h_{ic} \quad 6.17$$

Here subscript “ic” refers to “ionocaloric,” representing the active material undergoing freezing/melting in the cycle (in this study, that is ethylene carbonate), and subscript “s” refers to “salt”, which could be pure salt or a concentrated salt solution. m represents the mass and h represent the enthalpy per unit mass. We note that in the general case, the ionocaloric material is not a pure solid entering the adiabatic mixing step as perfect separation of salt and ionocaloric material is not possible. Also depending on the hot side temperature and the liquidus temperature, in general the ionocaloric material will be a solid-liquid mixture. This is made clearer by considering the phase diagram in Figure 6.3c; If the incoming solution to be mixed is not 100% purified, a finite amount of salt will push the phase-equilibria into the two phase region (governed by the lever rule). Thus, in general, the entering ionocaloric material must be considered a solid-liquid mixture with some amount of salt present in it. That basically means that the ionocaloric material at state 1 in Figure 7c is in the solid+liquid phase region and has a small amount of salt in it. Similarly, after the mixing with the salt (highly concentrated salt solution) the ionocaloric material may not completely reach eutectic point as shown in Figure 7c. It may be somewhere in the solid+liquid phase region with a very high amount of salt in it.

After mixing, the final enthalpy of the system is the enthalpy of the mixed solid-liquid solution:

$$H_f = m_f h_f \quad 6.18$$

where subscript f refers to “final” and  $m_f$  is the final mass of the solution.

In the following analysis, we choose the global reference point for all these enthalpy curves to be with respect to the pure material melting point temperature of ethylene carbonate in the liquid phase (see Fig SI.3 Purple curve for visualization of the reference enthalpy). We have arbitrarily assumed the  $h_{ref}$  to be zero. Since the ic material is in the solid+liquid region (shown by yellow star on the green curve in Figure 6.8) to calculate the enthalpy with respect to the reference temperature (melting temperature of the pure ic material,  $T_{m,o}$ ) we need to consider 4 enthalpy terms: 1.) enthalpy of mixing ( $\Delta H_{mix}$ ) 2.) enthalpy change from  $T_{m,o}$  to  $T_{liquidus}$  3.) enthalpy change of the liquid in the solid-liquid region which will be weighted by the phase fraction of the liquid present in the solid-liquid region 4.) enthalpy change of the solid weighted by the phase fraction of the solid.

The mass fraction of the solid phase ( $\phi_m$ ) can be found by applying the lever rule to the solution's phase diagram. This is expressed as:

$$\phi_m(T, \chi) = \frac{\chi_{liq}(T) - \chi_m}{\chi_{liq}(T) - \chi_o} \quad 6.19$$

where  $\chi_o$  is the solubility limit of the salt in the solid phase of the ionocaloric active material which is we have assumed to be zero as discussed earlier (Figure 6.7),  $\chi_m$  is the mass fraction of the salt in the ic+salt solution before the mixing chamber (in the ideal case  $\chi_s = 1$ ) and  $\chi_{liq}(T)$  is the mass fraction of the liquidus line at a given temperature. Therefore

$$\phi_m(T, C) = 1 - \frac{\chi_m}{\chi_{liq}(T)} \quad 6.20$$

Therefore, the enthalpy of the ic material in the solid+liquid region (shown by the star on green curve) is given by:

$$h_{ic} = -\Delta H_{mix} + \int_{T_{m,o}}^{T_{Liq}} C_{p,l} dT + \int_{T_{Liq}}^{T_{start}} (1 - \phi_m) C_{p,l} dT + \int_{T_{Liq}}^{T_{start}} \phi_m C_{p,s} dT - \phi_m \Delta H_{sl} \quad 6.21$$

We note that  $h_s$ , the enthalpy function of the pure salt or concentrated salt solution can also be expressed using equation 6.21, using the appropriate temperature and phase fraction fractions.

In equation 6.21,  $C_{p,l}$  is the heat capacity of the liquid+ salt solution,  $C_{p,s}$  is the heat capacity of the solid phase (we have assumed no salt in the solid phase as discussed earlier) and  $\Delta H_{sl}$  is the enthalpy of fusion. We further assume that the  $\Delta H_{mix}$  can be neglected as it's very small compared to other terms. In addition, although  $C_{p,l}$  is different than pure liquid due to the partial molar heat capacity of salt, we have assumed it to be same as that of pure liquid. These assumptions are justified because  $h_{ic}$  is dominated by  $\Delta H_{sl}$  in practical applications. Therefore, the initial enthalpy of ic material before the mixing chamber is given by

$$h_{ic,init} = \int_{T_{m,o}}^{T_{Liq,init}} C_{p,l} dT + \int_{T_{Liq,init}}^{T_{start}} (1 - \phi_{m,init}) C_{p,l} dT + \int_{T_{Liq,init}}^{T_{start}} \phi_{m,init} C_{p,s} dT - \phi_{m,init} \Delta H_{sl} \quad 6.22$$

where *init* denotes terms evaluated at the initial concentration of the salt in the ic material before entering the mixing chamber.

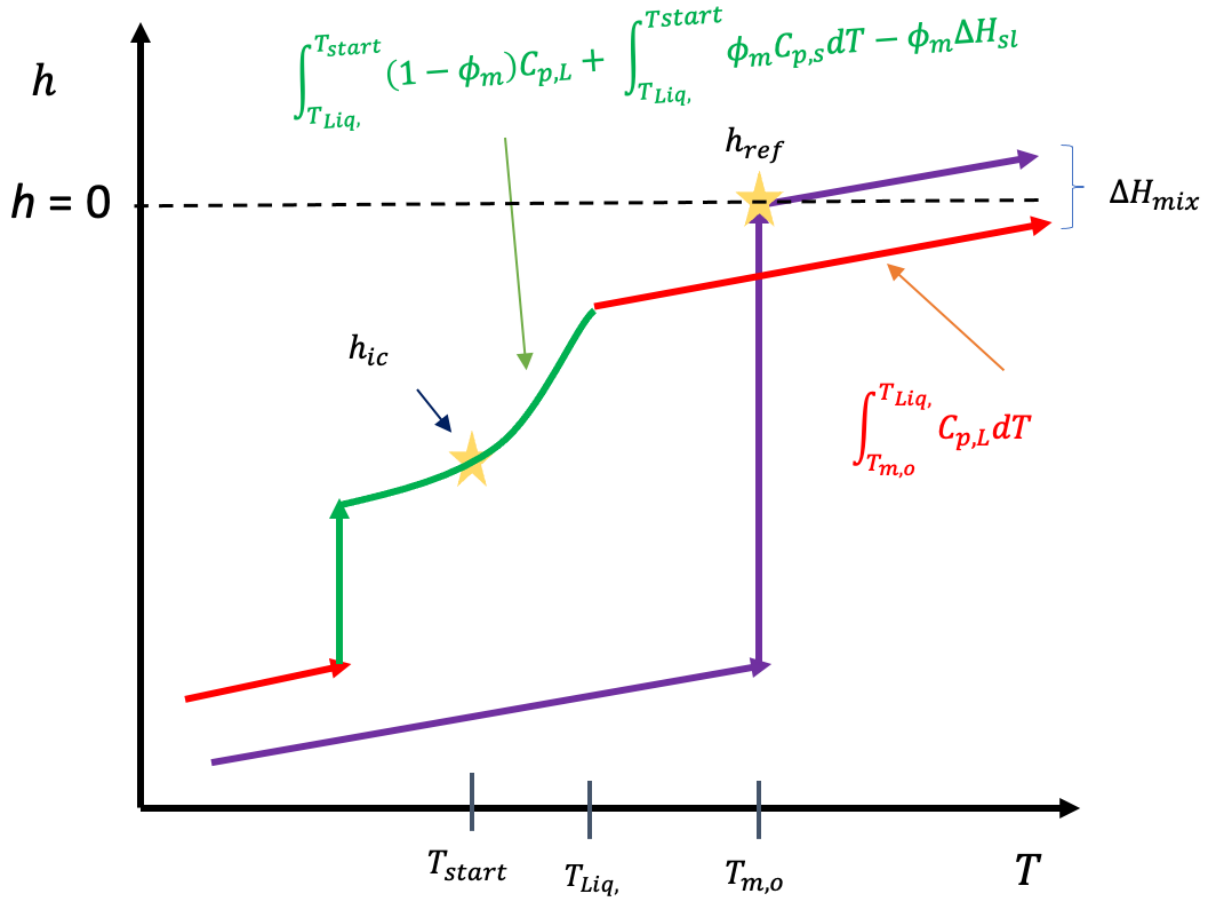


Figure 6.8: Enthalpy Path relative to reference curve

The final enthalpy of the solution can likewise be expressed by considering a solid-liquid mixture, so we can then write an analogous expression for  $H_f$ :

$$H_f = (m_s + m_{ic})h_f \quad 6.23$$

$$h_f = \int_{T_{m,o}}^{T_{Liq,f}} C_{p,L} dT + \int_{T_{Liq,f}}^{T_f} (1 - \phi_{m,f}) C_{p,L} dT + \int_{T_{Liq,f}}^{T_f} \phi_{m,f} C_{p,s} dT - \phi_{m,f} \Delta H_{sl} \quad 6.24$$

Where  $f$  denotes final state after the mixing chamber and  $T_f$  is the final temperature after adiabatic mixing and  $T_{Liq,f}$  is the liquidus temperature at the final concentration resulting from the mixing. A compatibility equation determines  $\chi_f$ , the final concentration of the mixed solution:

$$m_s \chi_s + m_{ic,init} \chi_{ic,init} = (m_s + m_{ic,init}) \chi_f \quad 6.25$$

Therefore

$$\chi_f = \frac{m_s \chi_s + m_{ic,init} \chi_{ic,init}}{m_s + m_{ic,init}} \quad 6.26$$

Finally, we solve equation 6.16 for  $T_f$ , which for non-linear  $\chi_L(T)$  will require numerical solutions.

## 5. Theory for Adiabatic and Reversible (Isentropic) Mixing

Isentropic mixing assumes that the entropy before and after mixing is the same (i.e. no entropy generation), such that the path on a T-S diagram is completely vertical and Carnot-like. Isentropic mixing follows a very similar analysis to isenthalpic mixing, which we re-iterate below for clarity:

At the system level:

$$S_{initial} = S_{final} \quad 6.27$$

Consistent with the iso-enthalpic analysis, we choose the global reference point for all these entropy curves to be with respect to the pure material melting point temperature of ethylene carbonate in the liquid phase

Using the expression for the entropy of a pure phase relative to the global reference, analogous to the enthalpy equation (Eq. 6.21-6.22) the initial entropy is given as:

$$S_{ic,init} = \int_{T_{m,o}}^{T_{Liq}} \frac{C_{p,L}}{T} dT + \int_{T_{Liq,init}}^{T_{start}} \frac{(1 - \phi_{m,init})C_{p,L}}{T} dT + \int_{T_{Liq,init}}^{T_{start}} \frac{\phi_{m,init}C_{p,s}}{T} dT - \frac{\phi_{m,init}\Delta H_{sl}}{T_{start}} \quad 6.28$$

The final enthalpy of the solution can likewise be expressed by considering a solid-liquid mixture, so we can then write an analogous expression for  $S_f$ :

$$S_f = \int_{T_{m,o}}^{T_{Liq,f}} \frac{C_{p,L}}{T} dT + \int_{T_{Liq,f}}^{T_f} \frac{(1 - \phi_{m,f})C_{p,L}}{T} dT + \int_{T_{Liq,f}}^{T_f} \frac{\phi_{m,f}C_{p,s}}{T} dT - \frac{\phi_{m,f}\Delta H_{sl}}{T_{start}} \quad 6.29$$

Where  $T_f$  is the final temperature after adiabatic mixing and  $T_{Liq,f}$  is the liquidus temperature at the final concentration resulting from the mixing.

Finally, we solve equation 20 for  $T_f$ , which for non-linear  $\chi_l(T)$  will require numerical solutions.

## 6. Thermodynamic Analysis of Ideal Ionocaloric Cycle with Regeneration

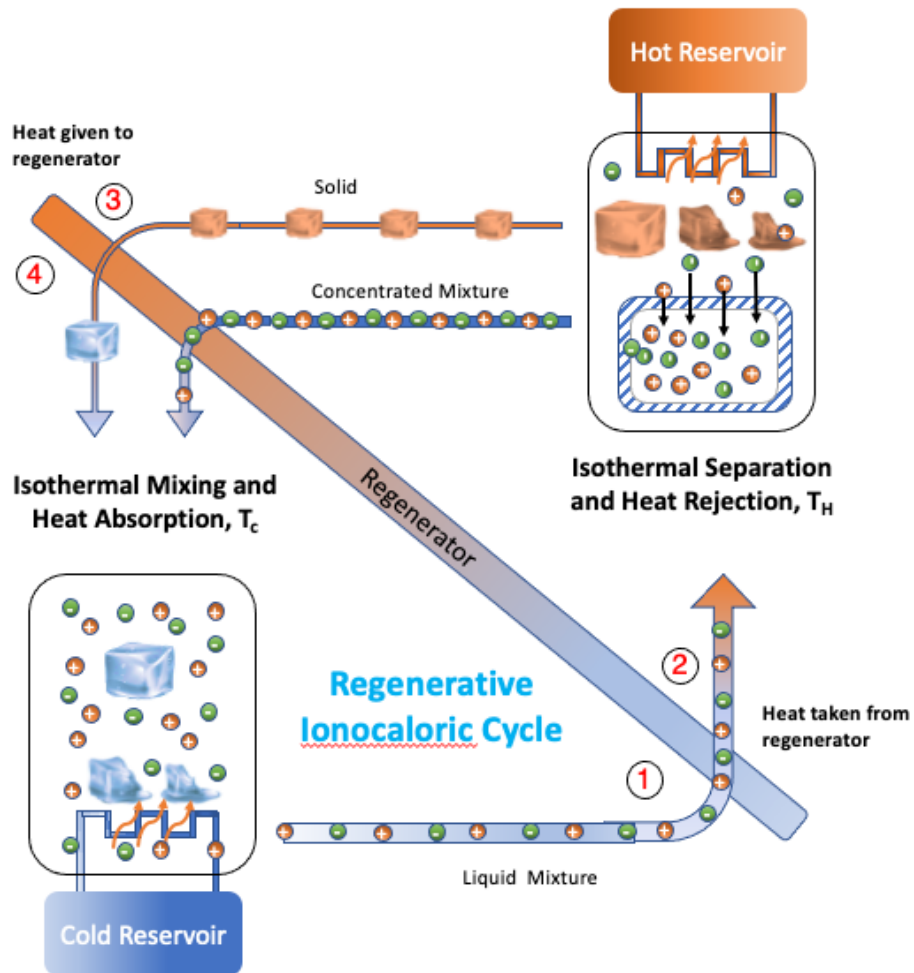


Figure 6.9 Schematic of Regenerative Ionocaloric Cycle

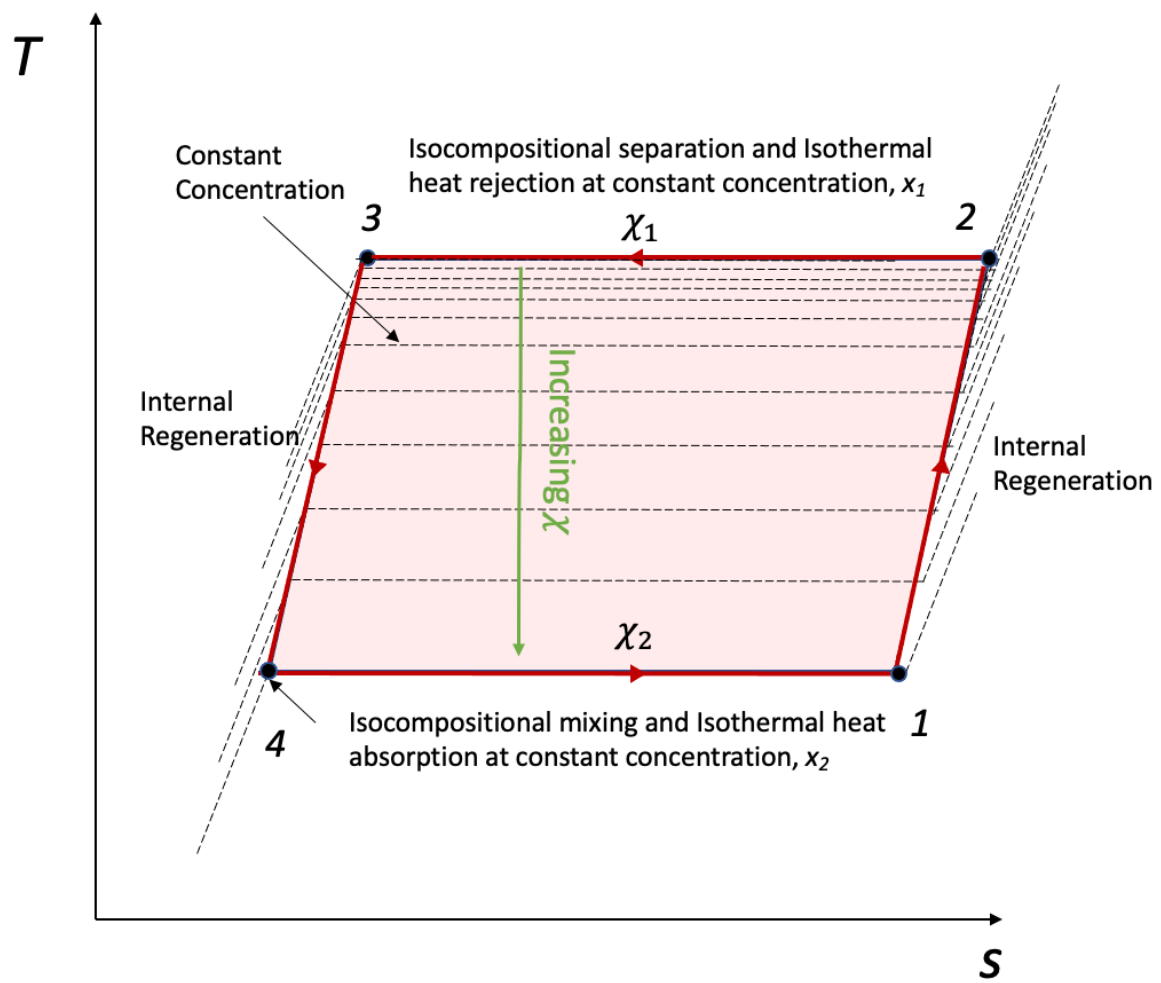


Figure 6.10 TS Diagram of an Ideal Regenerative Ionocaloric Cycle

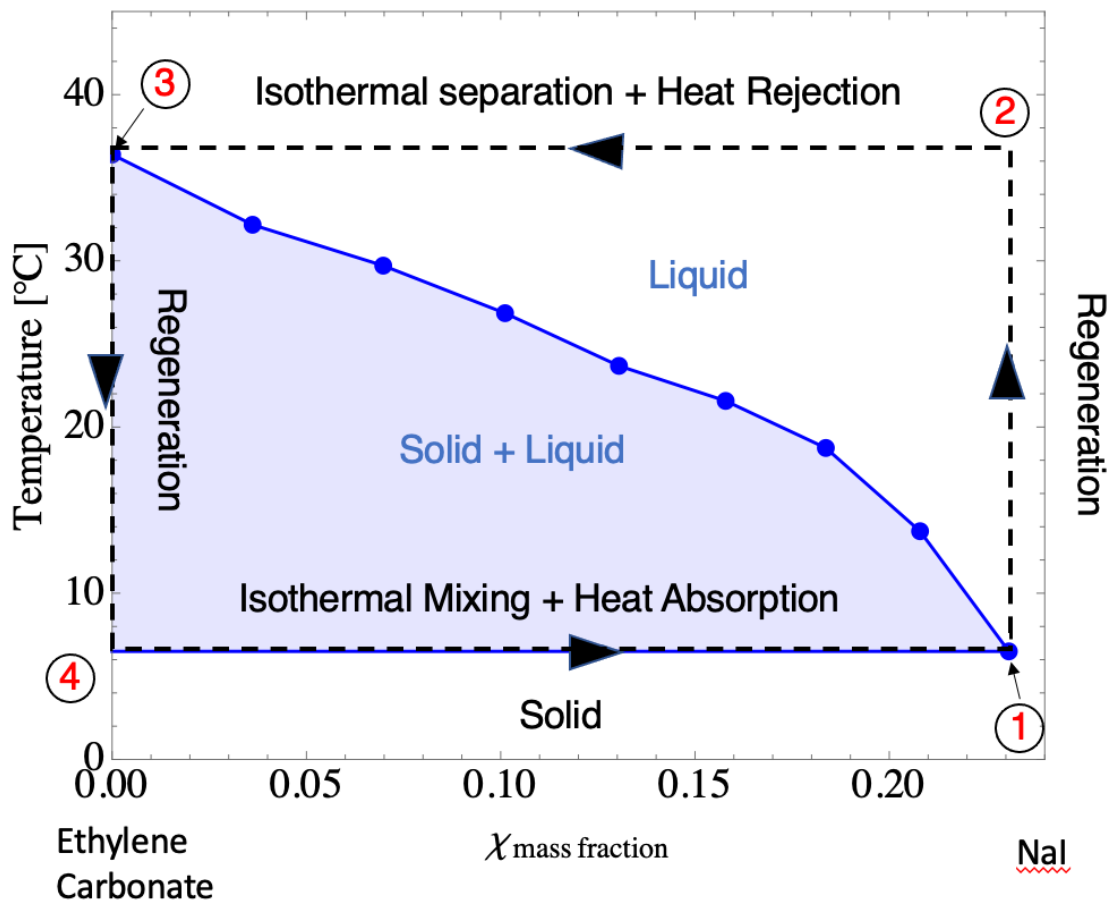


Figure 6.11 Traversal of Phase Diagram for Ideal Regenerative Ionocaloric Cycle

The ideal regenerative cycle is composed of four steps:

1. Process 1 → 2: Isocompositional regeneration where internal heat transfer takes place from the regenerator to the ionocaloric mixture
2. Process 2 → 3: Isothermal separation where work is added to the system to separate the constituents of the ionocaloric mixture, during which the crystallization of the fluid rejects heat to the external sink.
3. Process 3 → 4: Isocompositional regeneration where internal heat transfer takes place from the ionocaloric mixture to the regenerator.
4. Process 4 → 1: Isothermal mixing of the crystal and salt, where the melting of the crystal absorbs heat from an external source. Note the cycle shown in Figure 6.10 is the ideal cycle

which means that theoretically work can be extracted during the mixing step however in our device we have irreversible mixing. Therefore, no work can be extracted.

The cycle shown in Figure 6.10 can be thought of as an Ionocaloric Stirling cycle. Analogous to the Stirling cycle, the processes  $2 \rightarrow 3$  and  $4 \rightarrow 1$  are similar because heat transfer with the external system and work input/output in the cycle are taking place at the same time. Similarly, processes  $1 \rightarrow 2$  and  $3 \rightarrow 4$  in the Stirling cycle are iso-volumetric processes, whereas in our case these steps are iso-compositional.

### Temperature

In this cycle,  $T_h$  and  $T_c$  are the hot and cold reservoirs, where  $T_h = T_2 = T_3$  and  $T_c = T_1 = T_4$  (i.e., isothermal heat rejection and absorption). The temperature difference between the hot side and the cold side,  $\Delta T_{span}$ , is governed by the temperature difference between the crystallization/melting temperatures between two different compositions. For complete separation in process  $2 \rightarrow 3$ ,  $T_h \rightarrow T_{m,o}$ , the melting point of the pure ionocaloric material, however in reality complete separation will not take place and some amount of salt will be present (See theoretical section on adiabatic temperature change).  $T_c$  is then determined by the liquidus temperature of the ionocaloric mixture at the mixed composition, such that  $T_c = T_l(\chi)$ , which is governed by the binary phase equilibria. The largest temperature span will be when  $T_c$  is same as the eutectic temperature as shown in Figure 6.11.

### Heat and Work Flows

Process  $1 \rightarrow 2$  and  $3 \rightarrow 4$  are adiabatic with respect to the boundaries of the total system, but allow for internal heat exchange such that  $Q_{ext} = 0$  and  $Q_{1 \rightarrow 2} = -Q_{3 \rightarrow 4}$ , yielding  $T_2 - T_1 = T_4 - T_3$ , assuming equal heat capacities of the two streams. Thus, there is no net transfer of heat or work to/from the system or the environment, just internal heat generation is taking place.

Process  $2 \rightarrow 3$  requires work into the system to separate the constituents of the ionocaloric mixture. The energy to reversibly separate the ionocaloric mixture is equal to minus the energy released upon mixing, which is governed by the Gibb's Free energy of mixing so that  $W_{in} = -\Delta G_{mix}$ . The energy required for removing one mole of the working fluid from an infinitely large volume of the salt/working fluid solution (the concentration of which is not changed by the removal of the ionocaloric material), is given by  $\Delta G = \Delta \mu_{ic} = RT_{mix} \ln \gamma_{ic}(x_{ic})x_{ic}$ , where  $\gamma_{ic}(x_{ic})$  is the activity coefficient of the ionocaloric material at a given concentration. During separation, crystallization of the ionocaloric material in the mixture will reject heat to the external reservoir. Using the First law of Thermodynamics,  $W_{in} = Q_h - Q_c$ , so  $Q_h = W_{in} + Q_c$ , and  $Q_c$  is determined by Process  $4 \rightarrow 1$ . Note we have assumed irreversible mixing in Process  $4 \rightarrow 1$ . Therefore there is no work output from this step.

Process 4→1 absorbs energy from the surroundings at  $T_c$ . The amount of energy absorbed is equal to the amount of energy required to melt the crystal-phase of the ionocaloric material in the working fluid solution. The enthalpy of melting of the crystal in solution, or  $Q_c$ , can be expressed as  $Q_c = \Delta H_{sl} - \Delta C_{p,s \rightarrow L}(T_{m,o} - T_c) - \Delta H_{mix}$ , (see section 7 for detailed derivation).  $\Delta H_{sl}$  is the latent heat of fusion of the solid as a pure substance, and  $\Delta C_{p,s \rightarrow L} = C_{p,s} - C_{p,l}$  represents the enthalpy change between the solid and liquid phase between the pure ic melting point and the liquidus, which is the difference between the heat capacity of the solid and liquid phases of the crystal evaluated at the cold side temperature. The enthalpy of mixing,  $\Delta H_{mix} = -\Delta G_{mix} - \Delta S_{ideal} = RT_{mix} \ln \gamma_{ic}(x_{ic}) = RT_c \ln \gamma_{ic}(x_{ic})$

## 7. Ideal Material Coefficient of Performance Calculations

The coefficient of performance, or COP, is defined as  $COP = \frac{Q_c}{W_{in}}$ . For the ideal regenerative ionocaloric cycle,  $Q_c$  is governed by process 4→1, and  $W_{in}$  by 2→3. The expression for the work is described in section 6. The expression for  $Q_c$  requires a more detailed explanation. To calculate  $Q_c$ , we must evaluate the isothermal enthalpy change upon melting of the ionocaloric material:

$$Q_c = h_{ic,1} - h_{ic,4} \quad 6.30$$

Equation 6.30 represents the enthalpy change associated with the melting of all solid ionocaloric material at the cold side temperature. For the ideal case the solid fraction  $\phi = 1$  at state 4 in Figure 6.11 and  $\phi = 0$  at state 1.

In section 4 we derived an expression for  $h_{ic}$ , but will copy it below for reference:

$$h_{ic} = -\Delta H_{mix} + \int_{T_{m,o}}^{T_{Liq}} C_{p,l} dT + \int_{T_{Liq}}^{T_c} (1 - \phi_m) C_{p,l} dT + \int_{T_{Liq}}^{T_c} \phi_m C_{p,s} dT - \phi_m \Delta H_{sl} \quad 6.31$$

At state 4 since  $\phi = 1$ , then  $\phi = 0$  (Eq. 6.20) i.e. there is no salt mixing in the solid (as discussed earlier)  $\Delta H_{mix}$  can be neglected and  $T_{Liq} = T_{m,o}$  because the solid is pure (without any salt in it). Therefore

$$h_{ic,4} = \int_{T_{m,o}}^{T_c} C_{p,s} dT - \Delta H_{sl} \quad 6.32$$

Similarly,  $h_{ic,1}$  for  $\phi = 0$  is

$$h_{ic,1} = -\Delta H_{mix} + \int_{T_{m,o}}^{T_{Liq}} C_{p,l} dT + \int_{T_{Liq}}^{T_c} C_{p,l} dT = -\Delta H_{mix} + \int_{T_{m,o}}^{T_c} C_{p,l} dT \quad 6.33$$

Therefore

$$Q_c = -\Delta H_{mix} + \int_{T_{m,o}}^{T_c} (C_{p,l} - C_{p,s})dT + \Delta H_{sl} \quad 6.34$$

If we approximate  $C_{p,s}$  and  $C_{p,L}$  as constants independent of temperature, and substitute in  $\Delta H_{mix} = -RT_c \ln \gamma_{ic}(\chi_{ic})$ , which gives the enthalpy change of the ionocaloric material and salt, respectively, then we arrive at:

$$Q_c = \Delta H_{sl} - \Delta C_{p,s \rightarrow L}(T_{m,o} - T_c) + RT_c \ln \gamma_{ic}(\chi_{ic}) \quad 6.35$$

The material COP is therefore calculated as:

$$COP_{ideal} = \frac{\Delta H_f^o - \Delta C_{p,s \rightarrow L}(T_{m,o} - T_c) + RT_c \ln \gamma_{ic}(\chi_{ic})}{RT_h \ln \gamma_{ic}(\chi_{ic})\chi_{ic}} \quad 6.36$$

The inputs to the material parameters are as follows:

$\Delta H_f^o \frac{J}{g}$	$\Delta C_{p,s \rightarrow L} \frac{J}{g \cdot K}$	$T_{m,o} \text{ } ^\circ C$
155	~0.3	36.4

And  $\gamma_{ic}(\chi_{ic})\chi_{ic}$  is determined in section 8. The results as a function of temperature span are shown in Figure 6.12 below. Note  $T_c$  is for temperature greater than  $T_{eutectic}$  is  $T_{liq}$  (liquidous temperature) at a given salt concentration which is varied in the calculation for Figure 6.12.

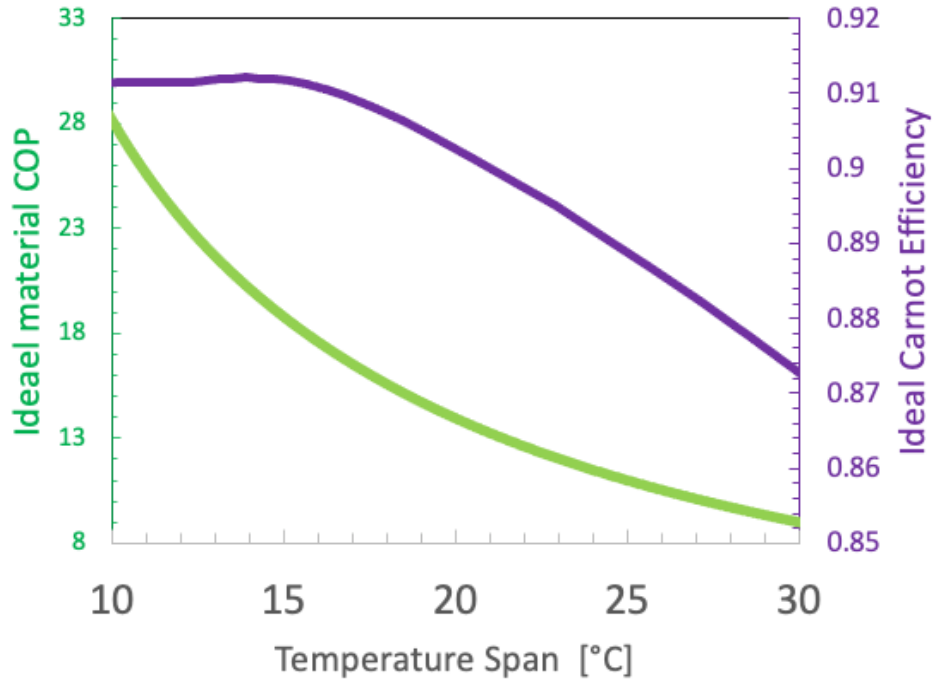


Figure 6.12 Ideal Material COP and Carnot Efficiency for Ethylene Carbonate and Sodium Iodide System

### SI.8 Determination of Activity Coefficients

At the freezing point of a solution, the chemical potential of the solvent in the liquid solution is equal to the chemical potential of the solid phase of the pure solvent. By equating the chemical potentials and representing non-idealities using activity coefficients, we can arrive at the following equation to express the dependence of the solvent's activity as a function of temperature<sup>48</sup>:

$$\ln(\gamma_i x_i) = \frac{\Delta H_{sl}}{R} \left( \frac{1}{T_{m,o}} - \frac{1}{T} \right) + \frac{\Delta C_{p,s \rightarrow L}}{R} \left( \ln \left( \frac{T}{T_{m,o}} \right) + \frac{T_{m,o}}{T} - 1 \right) \quad 6.37$$

Where  $\gamma_i$  is the activity coefficient as a function of mole fraction,  $\Delta H_{sl}$  is the enthalpy of fusion of the pure ionocaloric material,  $R$  is the ideal gas constant,  $T_{m,o}$  is the melting point of the pure material,  $T$  is the new melting point (Liquidus temperature) as a function of mole fraction,  $\Delta C_p = C_p^L - C_p^S$ , and  $x_i$  is the mole fraction.

To solve for the activity coefficient when the liquidus as a function of concentration is known, we simply rearrange and make  $T = T(x_i)$ :

$$\gamma_i(x_i) = \frac{1}{x_i} \exp \left\{ \frac{\Delta H_{sl}}{R} \left( \frac{1}{T_{m,o}} - \frac{1}{T(x_i)} \right) + \frac{\Delta C_{p,s \rightarrow L}}{R} \left( \ln \left( \frac{T(x_i)}{T_{m,o}} \right) + \frac{T_{m,o}}{T(x_i)} - 1 \right) \right\} \quad 6.38$$

Which gives the following activity coefficients:

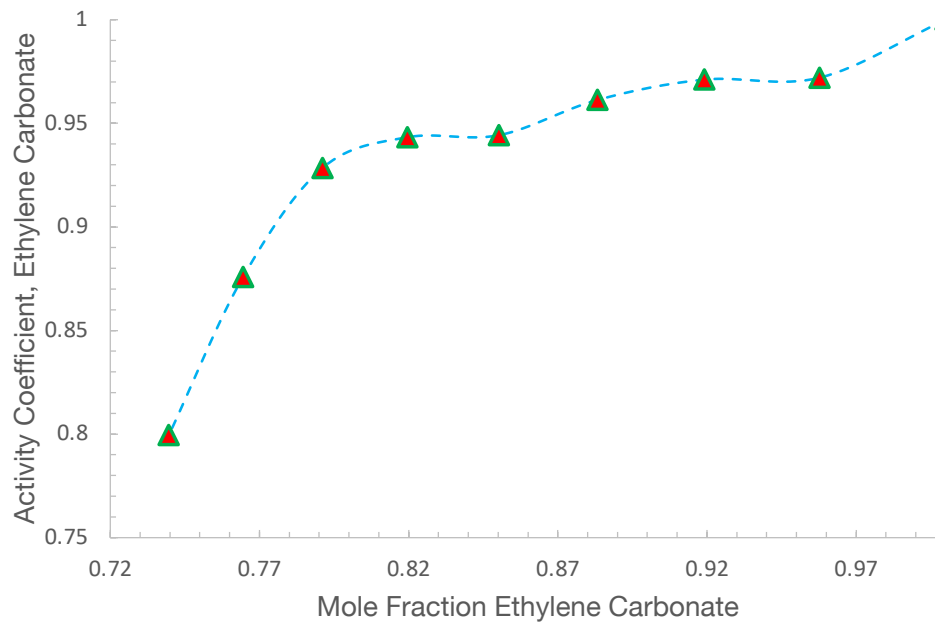


Figure 6.13 Activity Coefficients of EC in EC + NaI mixture

## 9. Isocompositional entropy change and the Ionocaloric Effect

The ionocaloric effect can be calculated from the calorimetric data carried out over various concentrations. First, the Isocompositional entropy change,  $\Delta S_{isocomp}$ , must be computed as a function of temperature relative to a reference temperature:

$$\Delta S_{isocomp} = S(T, \chi) - S(T_o, \chi) = \int_{T_o}^T \frac{1}{T} \frac{Q(\chi)}{T'(t)} dT \quad 6.39$$

Here,  $Q(\chi)$  is the heat flux measured by the calorimeter at different concentrations,  $T'(t)$  is the heating rate, and  $T_o$  is the reference temperature. Using this, the following isocompositional entropy change curves are generated:

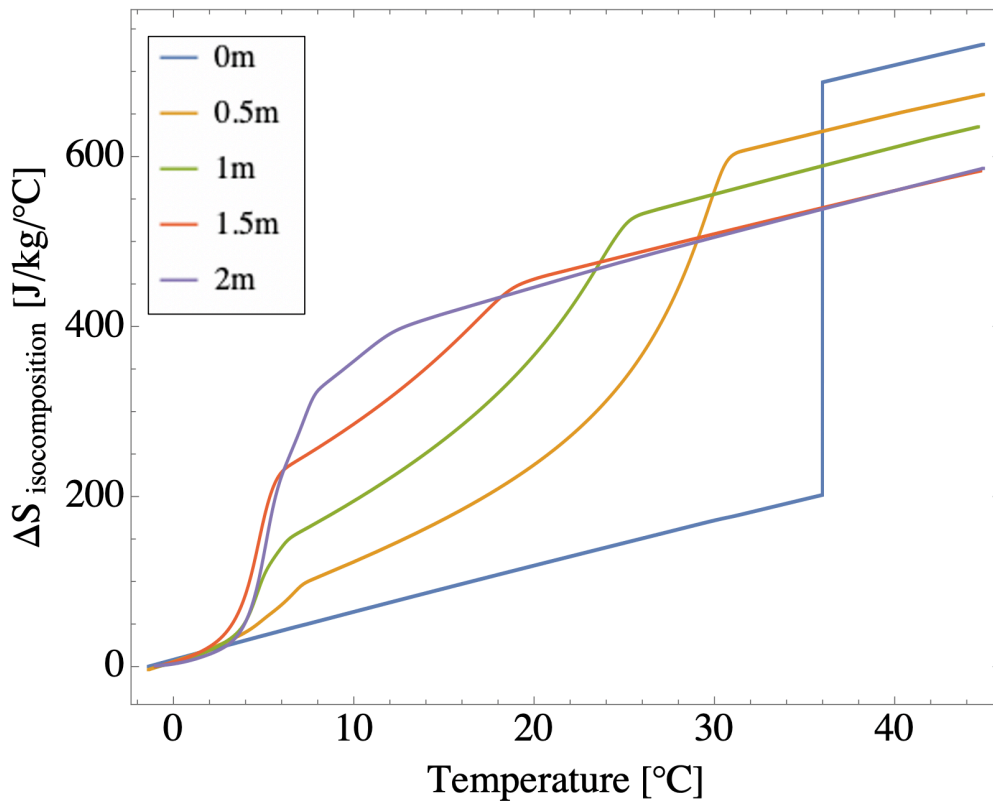


Figure 6.14 Entropy vs Temperature for various NaI concentrations in EC

The corresponding ionocaloric entropy change (shown in Figure 6.4b in the manuscript), which is defined as the isothermal entropy change induced by ion addition, can be calculated as the difference between the ionocompositional entropy change at a given concentration and the ionocompositional entropy change of the pure substance:

$$\Delta S_{ionocaloric} = \Delta S_{isocomp}(\chi) - \Delta S_{isocomp}(\chi = 0)$$

6.40

## 10. Experimental Methods

### *Electrodialysis Cell Setup*

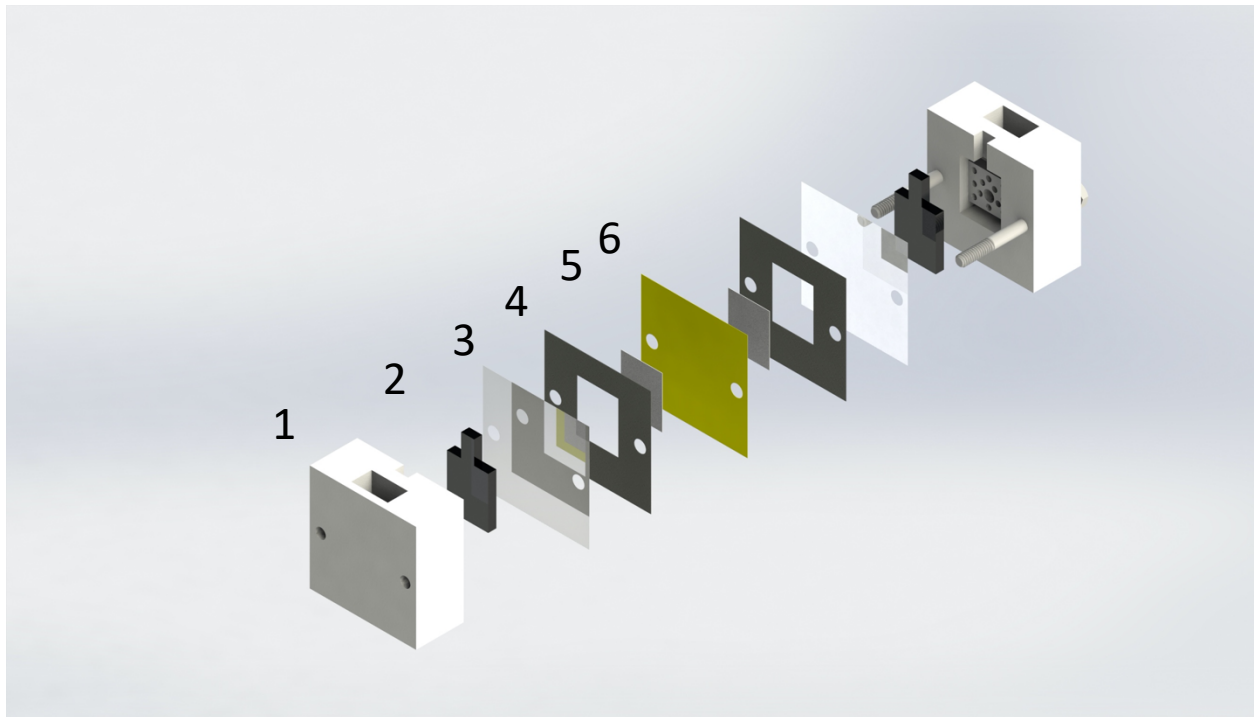


Figure 6.15 Electrodesalination Experimental Setup

## Materials

ID	Component	Material	Thickness
1	Electrode Housing	Onyx (3D Printed from Mark Forge)	28.5mm
2	Electrodes	AvCarb G600A Soft Graphite Battery Felt	6.1mm
3	Cation Exchange Membrane	Nafion 212	50.8 $\mu\text{m}$
4	Outer Separator	Clear Static Cling PVC Film,	200 $\mu\text{m}$
5	Inner Separator	Whatman <sup>®</sup> glass microfiber filters, Grade GF/C	220 $\mu\text{m}$
6	Anion Exchange Membrane	Fujifilm AEM Type 1	135 $\mu\text{m}$

Table 6.3 Electrodialysis Material List

### Membrane Preparation

Nafion 212 was boiled in 3% Hydrogen peroxide solution for an hour. It was then rinsed in deionized water for 30 minutes, after which it was transferred to a 1M aqueous NaOH solution for 7 days. The membrane was then removed, rinsed again with deionized water, and dried overnight. Once all the water was removed, it was transferred into a 2M NaI solution in ethylene carbonate, where it stayed for at least 7 days. Finally, the membrane was fitted into an H-cell filled with the electrode rinse and cycled at a current density of  $10\text{mA}/\text{cm}^2$  for 12 hours (1 cycle per hour).

The Fujifilm AEM type 1 membrane was directly added to a 1M aqueous NaI solution for 7 days, and then rinsed with deionized water. After drying overnight, it was transferred to a 2M NaI solution in ethylene carbonate for 7 days. It was then added to a membrane stack with the following arrangement: |electrode| Electrode Rinse|Nafion| 1M NaI in EC|FujFilm| 1M NaI in EC|Nafion|Electrode Rinse| Electrode|. By surrounding the Fujifilm membrane with NaI solution instead of the electrode rinse solution, we prevent it from undergoing ion exchange with the  $I_3^-$  in the electrode rinse, and instead condition it to only allow transport of  $I^-$ . It was then cycled at a current density of  $10\text{mA}/\text{cm}^2$  for 12 hours (1 cycle per hour).

### Experimental Procedure

The cell in Figure 6.15 was assembled in the following fashion:

- 1.) After soaking in the electrode rinse for 20 minutes at  $40^\circ\text{C}$ , the graphite felt electrodes were press-fit into the electrode housing.

- 2.) Nafion 212 was transferred from an electrolyte solution to a paper towel to wipe off excess, and then the membrane was pressed against the membrane housing in the manner shown in Figure 6.15.
- 3.) A set of inner and outer separators were then added to the stack. 350 $\mu$ L of electrolyte solution (solution concentration varies across experiments) was dispensed onto the inner separator (glass fiber), which was quickly absorbed by the material.
- 4.) Fujifilm AEM Type 1 was then added to the stack and pressed firmly against the separator, upon which excess electrolyte was squeezed out.
- 5.) A set of inner and outer separators were then added to the stack. 350 $\mu$ L of electrolyte solution (solution concentration varies across experiments) was dispensed onto the inner separator (glass fiber), which was quickly absorbed by the material.
- 6.) Nafion 212 was added to the stack, in the same manner as (2).
- 7.) The second electrode housing was added to the stack and then the bolts were tightened to clamp the stack together (both nuts were torqued down to 0.7 lbs-in).
- 8.) 25ml of Electrode rinse was then added to both electrode housing compartments

The assembled cell was then thermalized in a temperature chamber at 35.5°C. We note that the inner separators were measured on a micro balance before cell assembly. The porous graphite felt electrodes require conditioning before use. Without conditioning, the electrode resistance approximately doubles. To condition the system, the cell was connected to a potentiostat and underwent the following procedure:

- 1.) Constant current of 20mA for 50 seconds.
- 2.) Constant current of -20 mA for 50 seconds.
- 3.) Repeat 5x

Typically, by the 5<sup>th</sup> cycle, the voltage response to the applied current converges. Next, the cell was “charged” at constant current with a voltage limit set to 10% above the nominal charging voltage. The current was integrated with respect to time to monitor the charge passed into the system, and after a “threshold charge” was passed (determined by the molality of the solution), the potentiostat was returned to an open circuit.

### ***Experimental Processing***

The cell was then quickly disassembled by pipetting out the electrode rinse, loosening the nuts, pulling off the electrode housing, and then peeling back the membranes/separators sequentially. By doing this, the inner separator (glass fiber) was extracted from each compartment, which contained all the electrolyte in those compartments. The picture below shows the results of a typical experiment:

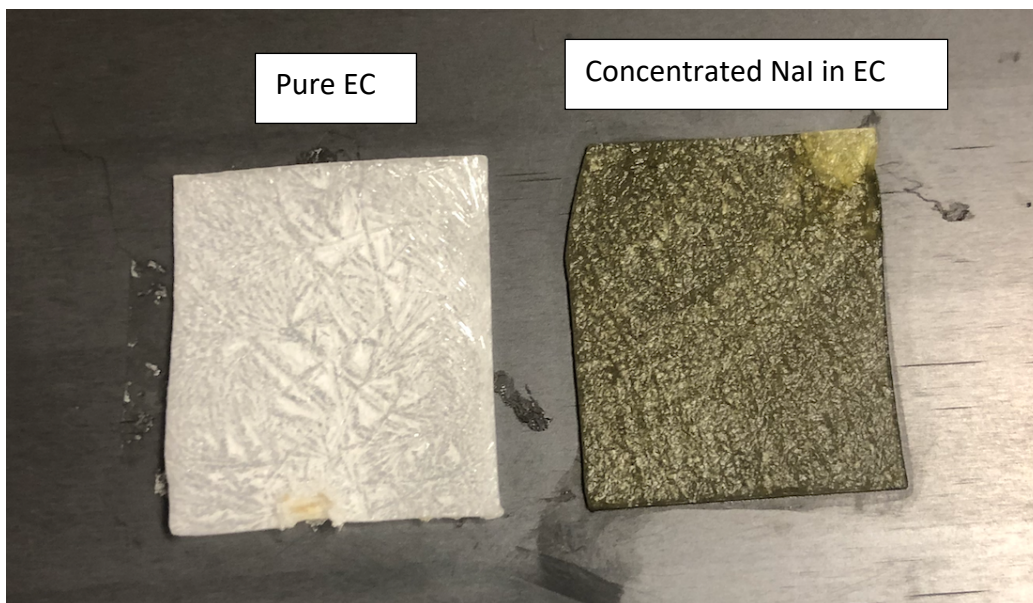


Figure 6.16 Output of a typical electrodialysis experiment.

The left-hand side is the purified ethylene carbonate. During the separation process, the melting point of the solution increased such that the solution spontaneously crystallized. On the right, the solution is strongly concentrated (in some cases, super-saturated or even salted-out). The concentrated solutions melting point is much lower (in this case, it was about  $9^{\circ}\text{C}$ ), so it remains in its liquid form, soaked into the glass fiber paper. Furthermore, concentrated sodium iodide in ethylene carbonate has a yellow tint, which is clearly seen here.

*Determining the concentration of the diluent:*

The purified solution (left) is then weighed on a micro balance. The mass of the filter paper (pre-measured) is subtracted out, and the total mass of the ethylene carbonate + sodium iodide is directly determined. Typically, it was around  $\sim 300 - 350\text{mg}$ .

The purified solution is then kept on a hot plate at  $50^{\circ}\text{C}$  overnight in a fume hood, and the ethylene carbonate is slowly evaporated out. To remove trace amounts of the remaining ethylene carbonate, it is moved to a vacuum-oven and held at  $100^{\circ}\text{C}$  for 6 hours, and then the filter paper is re-measured on the micro balance. Again, subtracting out the weight of the filter paper, the mass of the remaining sodium iodide is measured. From this, the concentration can be directly calculated as  $\frac{m_{\text{NaI}}}{m_{\text{solution}}}$ , and was typically less than 1wt%.

*Determining Total energy input:*

The total work input was equal to the electrical work across the graphite felt electrodes. To calculate this, we integrate the power signal with respect to time:  $W_{in} = \int_0^t I(t)V(t)dt$ .  $W_{in}$  ranged from 10-100 joules across all experiments. In our system,  $W_{in} = W_{rev} + Losses$  where

$W_{rev} = RT \ln(\gamma\chi)$ . The losses are driven by the overpotential that we had to apply to achieve ion separation at a finite rate. The overpotential was governed by the resistance values of the electrochemical circuit. These include electrolyte resistances, membrane resistances, and kinetic electrode resistances – which are characterized in sections 13 and 14. We concluded that the membrane resistances dominate the total cell resistance. Thus, for a given power, the work input can be lowered – and the efficiency increased – by reducing the membrane resistance.

*Determining  $Q_{abs}$ , COP, and  $\Delta T_{span}$  for Experimental Setup:*

The cold side temperature is determined by the initial concentration. If the initial electrolyte used had a concentration of  $\chi = 0.1578$  (mass fraction), then by conservation of mass, when the solutions of the two compartments are re-combined, they will re-combine with a final mass fraction of  $\chi = 0.1578$ . In practice, however, the two outer membranes allow a small amount of mass and solvent transport between the concentrate/diluent and the electrode rinse. Because the electrode rinse has a total molality of 2m, and the concentrate compartment is generally held at 2m or less, the activities of both are very similar, and there is little driving force for the transfer of ions or solvent. The dilute compartment at the end of the separation process is close to 0m, so in this case there is a strong driving force for solvent to transport from the dilute compartment to the electrode rinse (note: any ions transporting into the diluent will be transported out by the electrodialysis process, but will lower the current efficiency). This would serve to increase the overall concentration of the total electrolyte solution (diluent + concentrate) to be greater than the initial concentration. In aqueous systems, the solvent transport can be significant when working with large concentration gradients, due to high water permeability and mass transfer coefficients within the membrane. In the ethylene carbonate system, however, both the mass and solvent transport due to concentration polarization between the electrode rinse and diluent/concentrate is insignificant relative to the electrochemically driven transport between the diluent and concentrate compartments. This is because the resistance of the membranes in ethylene carbonate is  $\sim 100$ - $200$ x larger than in water. Thus, the system generally obeyed conservation of mass across the two compartments, which was verified by measuring the total solution mass and concentration in the concentrated compartment using the same procedure for determining the concentration of the diluent.

In the regenerative cycle, the maximum cooling occurs when  $T_c = T_i(\chi)$ , because  $T_i(\chi)$  is the new equilibrium melting point for the solid ethylene carbonate.  $T_i$  is obtained from the phase diagram for various salt concentrations.

The hot side temperature is determined by the experiment. If the dilute compartment is completely purified, such that there is no sodium iodide remaining, then full crystallization will occur at Ethylene carbonate's pure melting point of  $36.4^\circ\text{C}$ . If it is not completely pure, it will form a two-phase solution with solid mass fraction depending on temperature, as given by the lever rule when applied to the binary phase diagram in Figure 6.7

Before we discuss the determination of  $Q_{cold}$ , we must describe this important parameter in relation to the theory developed in sections 4-7.

$Q_{cold}$  for non-ideal cycle i.e. incomplete separation ( $\phi \neq 1$ )

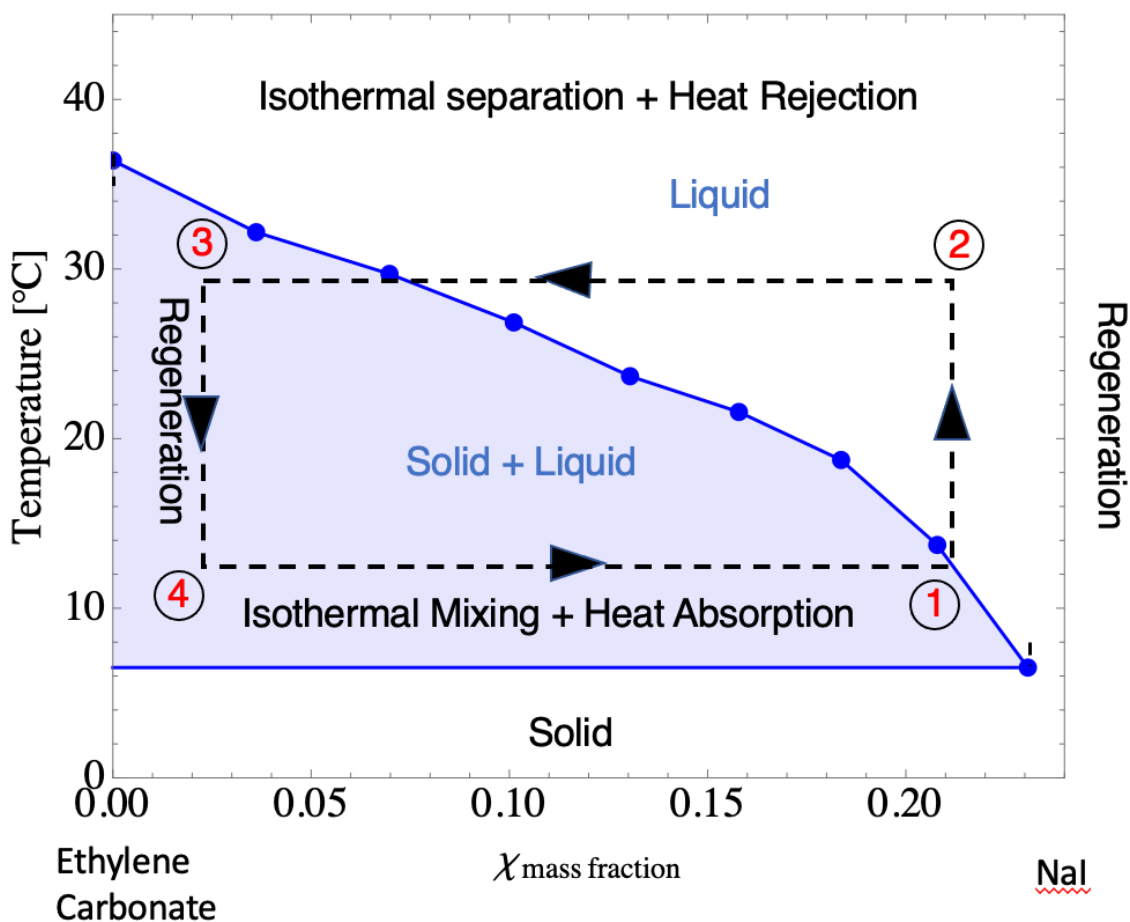


Figure 6.17: Temperature-composition representation of a non-ideal regenerative system

The foregoing analysis in sections 4-7 did not consider incomplete separation. In actual experiments, the ethylene carbonate is not 100% dilute, and some sodium iodide will always remain. The remaining sodium iodide will lower the phase fraction of solid ethylene carbonate, lowering the refrigeration capacity of EC as shown in Figure 6.17. We can analyze this scenario by computing  $Q_c(\phi \neq 1) = h_1 - h_4$ .

First, we describe the enthalpy of the solution at state 1, in which all the solid ethylene carbonate has melted and the solution exists completely in the liquid phase. The enthalpy at this state is:

$$h_1 = -\Delta H_{mix} + \int_{T_{m,o}}^{T_c} C_{p,l} dT \quad 6.41$$

Likewise, the enthalpy of state 4, in which both the solid and liquid phases are present in the mixture ( $\phi \neq 1$ ) is described as (see equation 6.31 for context of equation 6.42):

$$h_4 = -(1 - \phi)\Delta H_{mix} + \int_{T_{m,o}}^{T_{liq}(\chi_4)} C_{p,l}dT + \int_{T_{liq}(\chi_4)}^{T_c} (1 - \phi)C_{p,l}dT + \int_{T_{liq}(\chi_4)}^{T_c} \phi C_{p,s}dT - \phi\Delta H_{sl} \quad 6.42$$

Where the above terms take on the meanings detailed in sections 4-7. This expression can be expanded to make grouping terms clearer:

$$h_4 = -\Delta H_{mix} + \phi\Delta H_{mix} + \int_{T_{m,o}}^{T_{liq}(\chi_4)} C_{p,l}dT + \int_{T_{liq}(\chi_4)}^{T_c} C_{p,l}dT - \int_{T_{liq}(\chi_4)}^{T_c} \phi C_{p,l}dT + \int_{T_{liq}(\chi_4)}^{T_c} \phi C_{p,s}dT - \phi\Delta H_{sl} \quad 6.43$$

As is clear, all the terms weighted by the phase fraction can be grouped together, which will be important when subtracting from the enthalpy at state 1

$$h_4 = -\Delta H_{mix} + \int_{T_{m,o}}^{T_c} C_{p,l}dT - \phi \left( \int_{T_{liq}(\chi_4)}^{T_c} C_{p,l}dT - \int_{T_{liq}(\chi_4)}^{T_c} C_{p,s}dT + \Delta H_{sl} - \Delta H_{mix} \right) \quad 6.44$$

Now that both  $h_4$  and  $h_1$  are established, we can compute  $Q_c$  for arbitrary phase fraction.

$$Q_c(\phi \neq 1) = h_1 - h_4 = -\Delta H_{mix} + \int_{T_{m,o}}^{T_c} C_{p,l}dT - \left\{ -\Delta H_{mix} + \int_{T_{m,o}}^{T_c} C_{p,l}dT - \phi \left( \int_{T_{liq}(\chi_4)}^{T_c} C_{p,l}dT - \int_{T_{liq}(\chi_4)}^{T_c} C_{p,s}dT + \Delta H_{sl} - \Delta H_{mix} \right) \right\} \quad 6.45$$

which results in:

$$Q_c(\phi \neq 1) = h_1 - h_4 = \phi \left( \int_{T_{liq}(\chi_4)}^{T_c} C_{p,l} dT - \int_{T_{liq}(\chi_4)}^{T_c} C_{p,s} dT + \Delta H_{sl} - \Delta H_{mix} \right) \quad 6.46$$

Assuming constant heat capacity in the solid and liquid states, the integrals can be evaluated such that:

$$Q_c(\phi \neq 1) = \phi (\Delta H_{sl} - \Delta C_{p,s \rightarrow l} (T_{liq}(\chi_4) - T_c) - \Delta H_{mix}) \quad 6.47$$

To validate Eqn. (40) we conducted further calorimetry for  $T_h = 36.4^\circ\text{C}$  where near complete separation in the electro dialysis was observed ( $\phi \rightarrow 1$ , it was  $\sim 0.97$  in the experiment) for different salt concentrations. The results are shown in Fig. SI.13 below. Figure SI.13 shows an excellent agreement with Eq. 40.

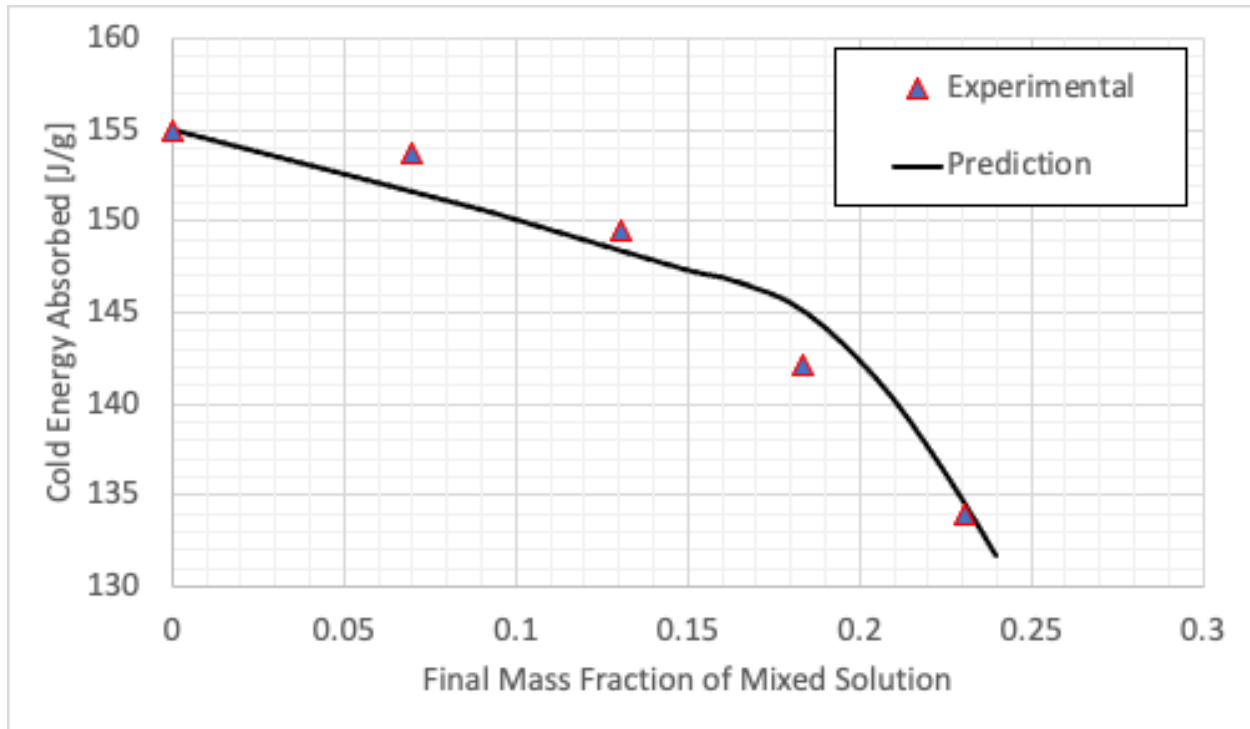


Figure 6.18 Comparison of Eqn. 6.47 with calorimetry data for  $T_h = 36.4^\circ\text{C}$ .

To compute  $Q_c$  (cold side heat absorption) and then the COP as a function of  $T_h$  in the experiments, the following procedure was used:

- 1.) Choose  $T_h$
- 2.) Compute the fraction of solid formed in the purified ethylene carbonate by using the lever rule, such that  $\phi_{solid} = 1 - \frac{\chi_s}{\chi_{liq}(T_h)}$ , where  $\chi_{liq}(T_h)$  is the mass fraction of the liquidus line at  $T_h$  and  $\chi_s$  is the mass fraction of the salt in the purified ethylene carbonate solution.
- 3.) Compute the heat absorbed at  $T_c$  using equation 6.47
- 4.) Compute the COP using  $COP = \frac{Q_c}{W_{in}}$ , where  $W_{in}$  is the electrical work input determined from the experiment.

The results for the absolute value of the COP vs  $\Delta T_{span}$  for four different concentrations are shown in Figure 6.19:

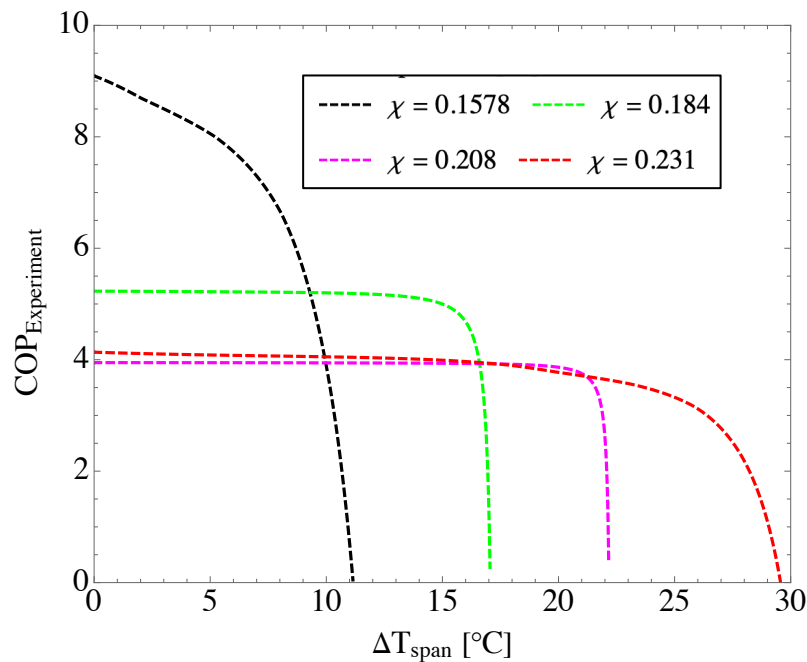


Figure 6.19 Experimental COP vs Temperature Span for various experiments operating using different concentrations

The curves generally saturate after a few °C: This behavior is explained through the COP equation:  $COP = \frac{\phi(\Delta H_{sl} - \Delta C_{p,s \rightarrow l}(T_{liq}(\chi_4) - T_c) - \Delta H_{mix})}{W_{in}}$ . When operating at fixed concentration, the COP only depends on the phase fraction, which depends on the degree of purification, or the

final mass fraction of the dilute stream during the separation step ( $\phi_{solid} = 1 - \frac{\chi_s}{\chi_{liq}(T_h)}$ ). So when  $\chi_{liq}(T)$  is small, the phase fraction increases, and the COP increases for all  $\Delta T_{span}$ . For this reason, for highly dilute solutions the phase fraction of solid formed will approach 1 very quickly as the temperature is lowered from the pure substance melting point, and in these experiments, the ethylene carbonate was highly purified by the electro dialysis separation process.

In Fig SI.15, we plot the same results relative to the Carnot COP ( $COP_C$ ):

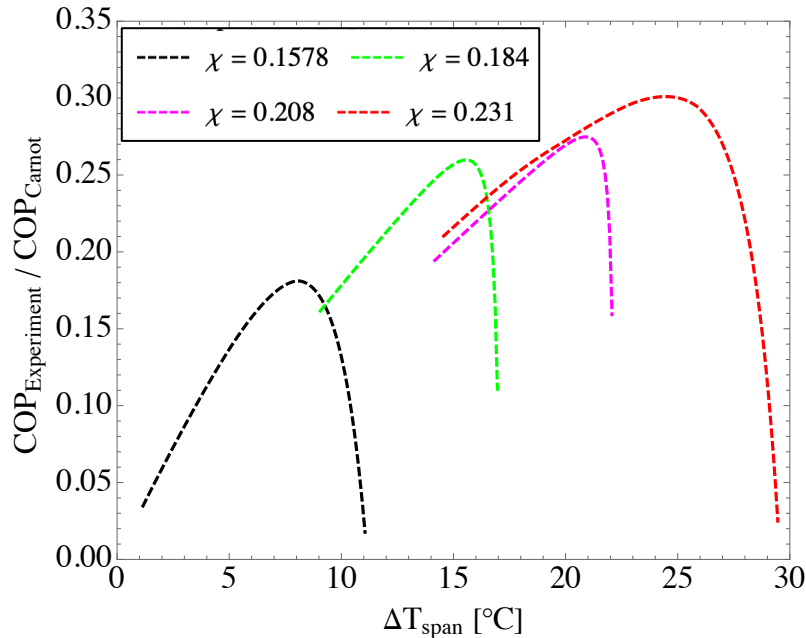


Figure 6.20 Carnot Efficiency vs Temperature Span for various experimental conditions

This curve shows a maximum because both the Carnot COP and the experimental COP in Figure 6.17 are monotonically decreasing functions of  $\Delta T_{span}$ , albeit at different rates (Carnot COP is far more hyperbolic with respect to temperature span), so there will be a unique maximum value. If the diluent were perfectly dilute, the maximum value will correspond to the full temperature span given by  $\Delta T_{span} = T_{m,o} - T_l(\chi)$  for a given concentration. In reality, because it is difficult to get full purification, the optimization procedure will result in a maximum efficiency that is less than the temperature span, because the material will crystallize at lower temperatures, and  $\Delta T_{span} = T_h - T_l(\chi)$ , where  $T_h < T_{m,o}$ .

## 11. Efficiency vs Power Output

The procedure in section 10 was repeated at different current densities. The cooling load ( $Q_{abs}$ ) was divided by the total separation time to calculate the cooling power. The plots shown in figure Figure 6.19 and Figure 6.20 were constructed for each experiment, and the maximum relative carnot efficiency was extracted. The results are shown below, normalized per unit volume of ionocaloric material and per unit area of membrane in a compartment.

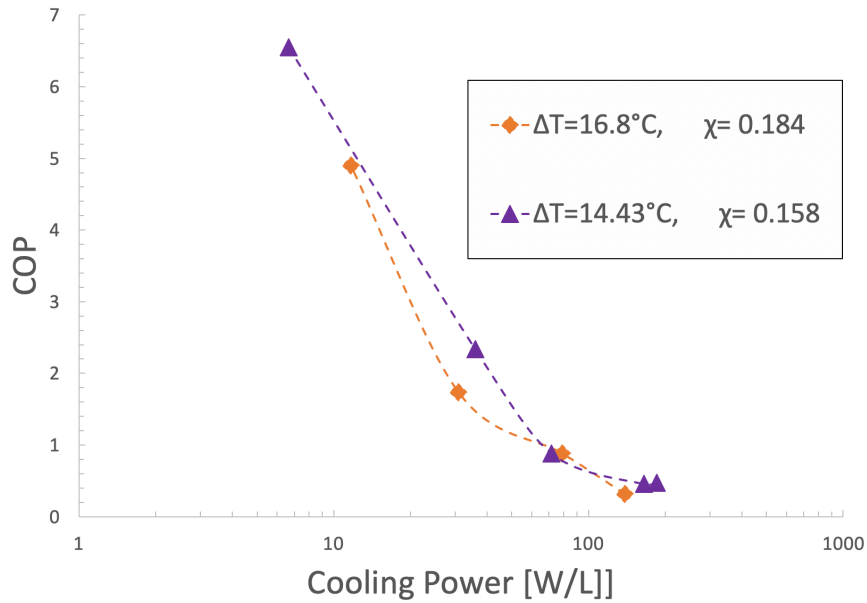


Figure 6.21 COP vs Cooling Power for experiments run at different concentrations

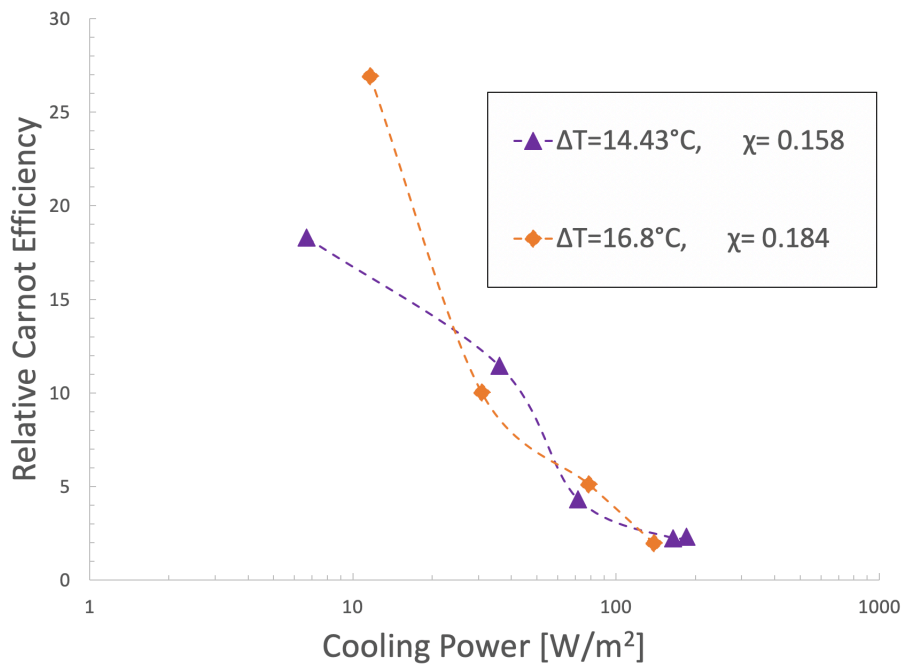


Figure 6.22 Relative Carnot Efficiency vs Cooling Power for experiments run at different concentrations

## 12. Thermal Conductivity Measurements

The thermal conductivity of a caloric material greatly impacts the practical limits of its power output. It has been shown<sup>49</sup> in simulations of magnetocaloric materials that the thermal conductivity affects  $\tau$ , the time constant of temperature change, which ultimately limits the maximum frequency of a refrigerant cycle – even under the assumption of perfect heat exchange. The thermal conductivity, therefore, represents an important metric for any caloric material, benchmarking its power density. To compare ethylene carbonate to other caloric materials, we measure its thermal conductivity using the transient plane source method, also known as the “hot-disk” method<sup>50</sup>. The experiment and analysis followed ISO 22007-2:2015<sup>51</sup>, a standardized methodology for the determination of the thermal conductivity and thermal diffusivity.

Ethylene Carbonate (99.9% purity) was melted at 60°C and cast into aluminum pans. The liquid cooled via natural convection at room temperature, and the solid was slowly crystallized under these ambient conditions. Once fully crystallized, the solid slabs were removed from the aluminum and used to sandwich a Kapton embedded plane Hot Disk 4922, spiral (6.4mm radius) sensor, connected to the TPS 2200 thermal constants analyser. The slabs were clamped from both sides, ensuring an even pressure against the Hot Disk sensor, and mitigating thermal contact resistance. A thermal load of 60mW was applied over 20 seconds, and the temperature rise vs time was recorded at the Hot Disk sensor. The temperature signal was then fitted to the analytical solution to the symmetric semi-infinite domain boundary conditions of the heat equation. A heat capacity of  $1.38 \frac{J}{g \cdot K}$  (measured in this work and confirmed with NIST tabulated data) was used as an input to the fitting of the thermal diffusivity, yielding a fit of  $\alpha = 0.2690 \frac{mm^2}{s}$ , and a thermal conductivity of  $k = 0.4843 \frac{W}{m \cdot K}$ . The thermal probing depth was 4.52mm, well within the limit of the slab thickness (~1cm).

In Table 6.4 we compare ethylene carbonates solid thermal conductivity to that of other caloric effects. Relative to Baro- and Electro-, it is very competitive. However, it is about 10x lower than that of the Magneto- and Elasto-, which often employ metals/ metal alloys. Fortunately, because the ionocaloric cycle employs solid/liquid phase change, the active material is often embedded in a liquid mixture, so convection can be utilized to increase the heat transfer coefficient.

Thermal Conductivity (W/m/K)				
This Work	Magnetocaloric	Elastocaloric	Electrocaloric	Barocaloric
0.456	(1-10) <sup>49</sup>	(0.4-18) <sup>52</sup>	(0.1-1.1) <sup>53</sup>	(0.1-0.6) <sup>54,55</sup>

*Table 6.4 Comparison of thermal conductivity for different caloric effects*

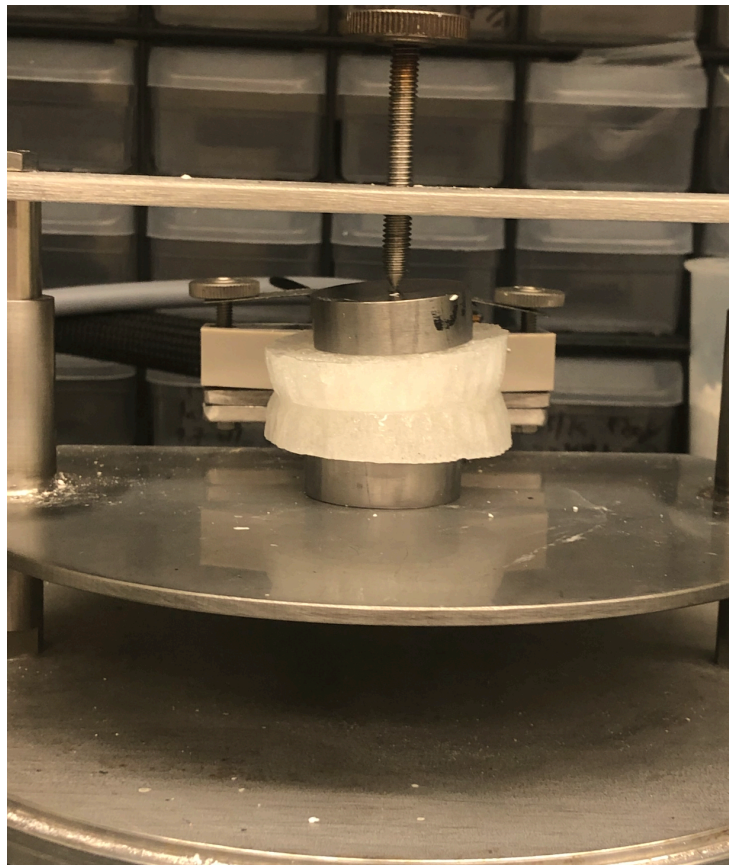


*Figure 6.23 Hot Disc Experimental Setup*

### 13. Membrane Characterizations

A symmetric H-cell was constructed using the same graphite felt electrodes used for all experiments. The electrodes were separated by 0.125 inches, and electrochemical impedance spectroscopy (EIS) was performed galvanostatically at 10mA (electrodes had a geometric area of 5.25cm<sup>2</sup>). The apparatus was equilibrated in an oven at 25°C before all experiments. The frequency was swept from 100mHz to 100kHz, and the resulting Nyquist plot was fitted to a Randles circuit modified with an additional Warburg Impedance. First, the Nyquist plot of the H-cell with no membrane was determined. From this plot, the left most intercept of the real part of the impedance was extracted, and the total cell resistance (4.6Ω) was computed. The cell was then deconstructed, and a pre-conditioned membrane was inserted to partition the H-cell in half. The same electrolyte solution (0.5m NaI3, 1.5m NaI) was re-added to the cell, which was then again equilibrated at 25°C, and an identical EIS Measurement was then taken. The results for the two membranes used in all experiments (cation exchange membrane = Nafion 212, anion exchange membrane = FujFilm AEM Type 1) are shown below.

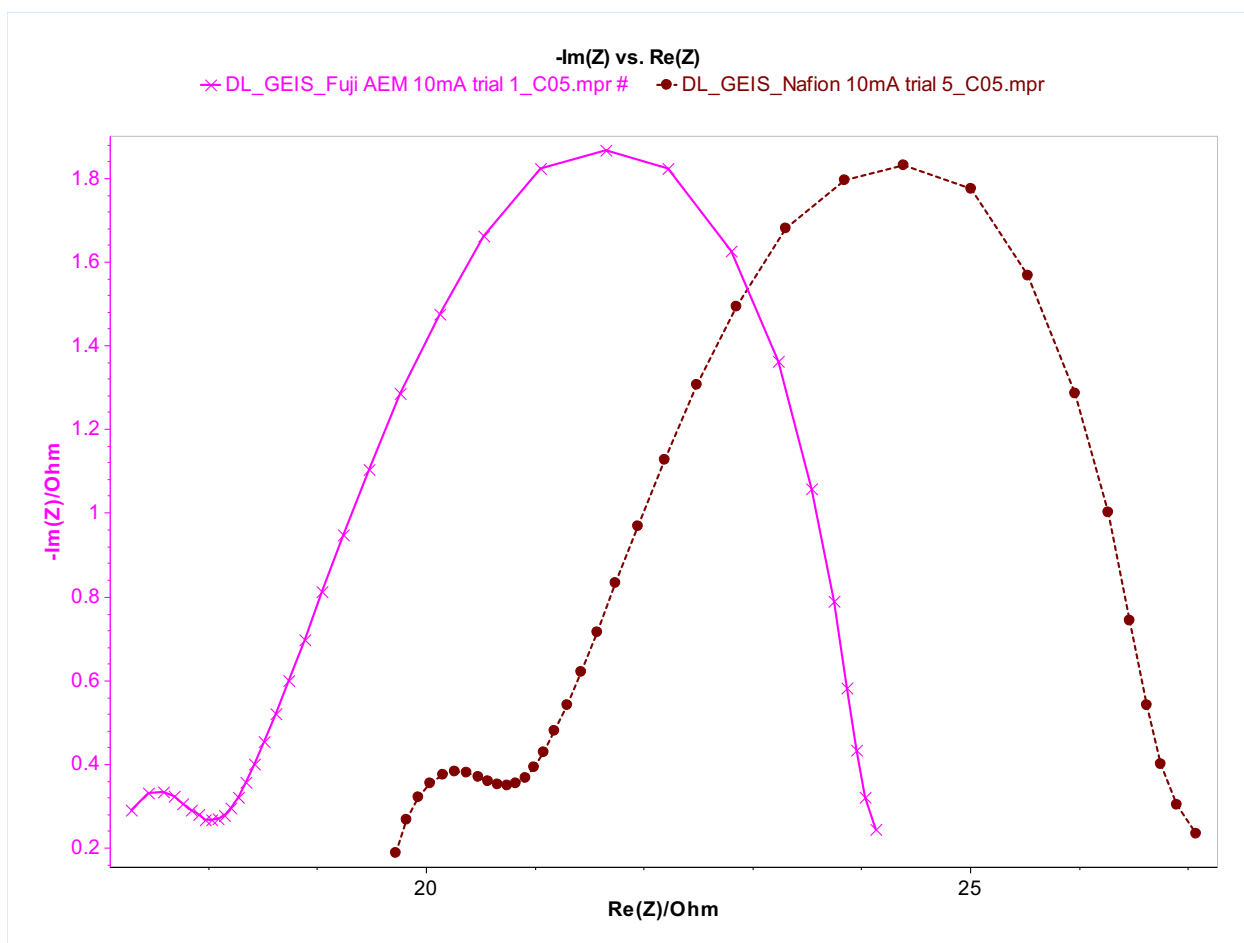


Figure SI.6.24 Nyquist Plot created using electrochemical impedance spectroscopy to determine the ionic conductivity of the membranes used in electro dialysis

By subtracting the cell constant from the resistance values determined with the membranes partitioning the H-cell, we can calculate the resistance added to the cell due to the membrane.

	<b>Nafion 212</b>	<b>FujiFilm AEM I</b>
<b>Absolute Resistance <math>\Omega</math></b>	<b>15.9</b>	<b>13.0</b>
<b>Area Resistance <math>\Omega * cm^2</math></b>	<b>83.475</b>	<b>68.25</b>
<b>Area Resistance in Water <math>\Omega * cm^2</math></b>	<b>~0.5-1</b>	<b>~0.5-2</b>

*Table SI.5 Resistance values for the membranes used in electro dialysis*

For comparison, the resistance of the membranes is 50-100x higher in Ethylene Carbonate than in water. The high resistance of these membranes in ethylene carbonate is expected because they are designed for use in aqueous media.

#### 14. Kinetic Resistance of Graphite Felt Electrodes

Electrochemical impedance spectroscopy was used to determine the kinetic resistance of the  $I^-/I_3^-$  reaction at the electrode interface. A symmetric H-cell was constructed using the same graphite felt electrodes used for all experiments. The electrodes were separated by  $\frac{1}{8}$ " , and the experiments were performed galvanostatically such that the current amplitude supplied was swept from 0.1mA to 400mA (electrodes had a geometric area of  $5.25cm^2$ ). The frequency was swept from 100mHz to 100kHz, and the resulting Nyquist plot was fitted to a Randle's circuit. The right most intercept of the real part of the impedance was extracted, and the kinetic resistance as a function of current density is shown in Figure 6.26

As can be seen, the kinetic resistance decreases linearly from  $\sim 0.01 - 1 mA/cm^2$ , and then decreases exponentially from  $\sim 10 - 100 mA/cm^2$ . This is typical for the kinetics of faradaic processes, as described by the Butler-Volmer model. These results, coupled with the resistances of the electrolyte and membranes, can be used in an electro chemical transport model to predict performance metrics at different current densities/ over potentials.

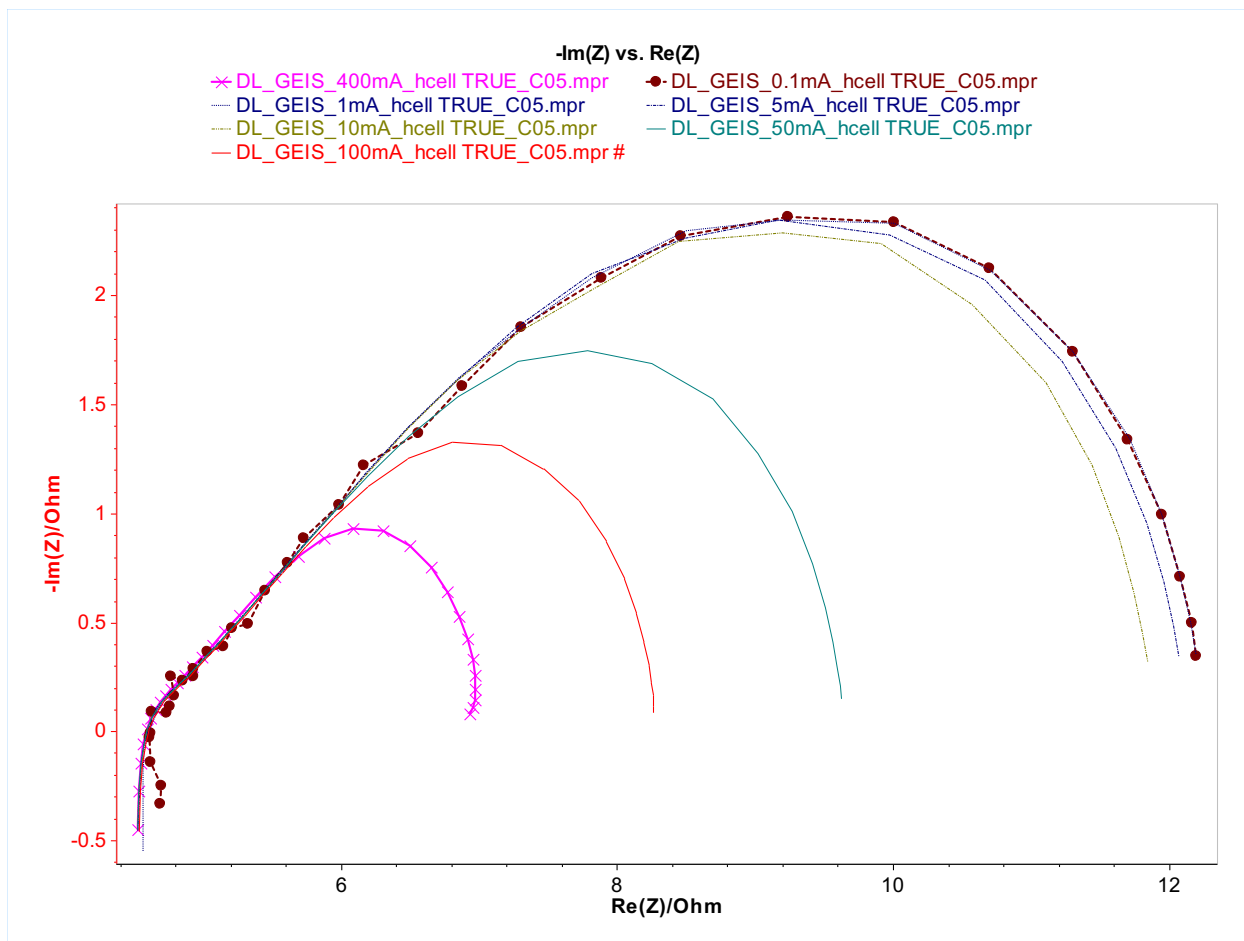


Figure 6.25 Nyquist Plots created using electrochemical impedance spectroscopy with an H cell using Graphite Felt electrodes at various current densities

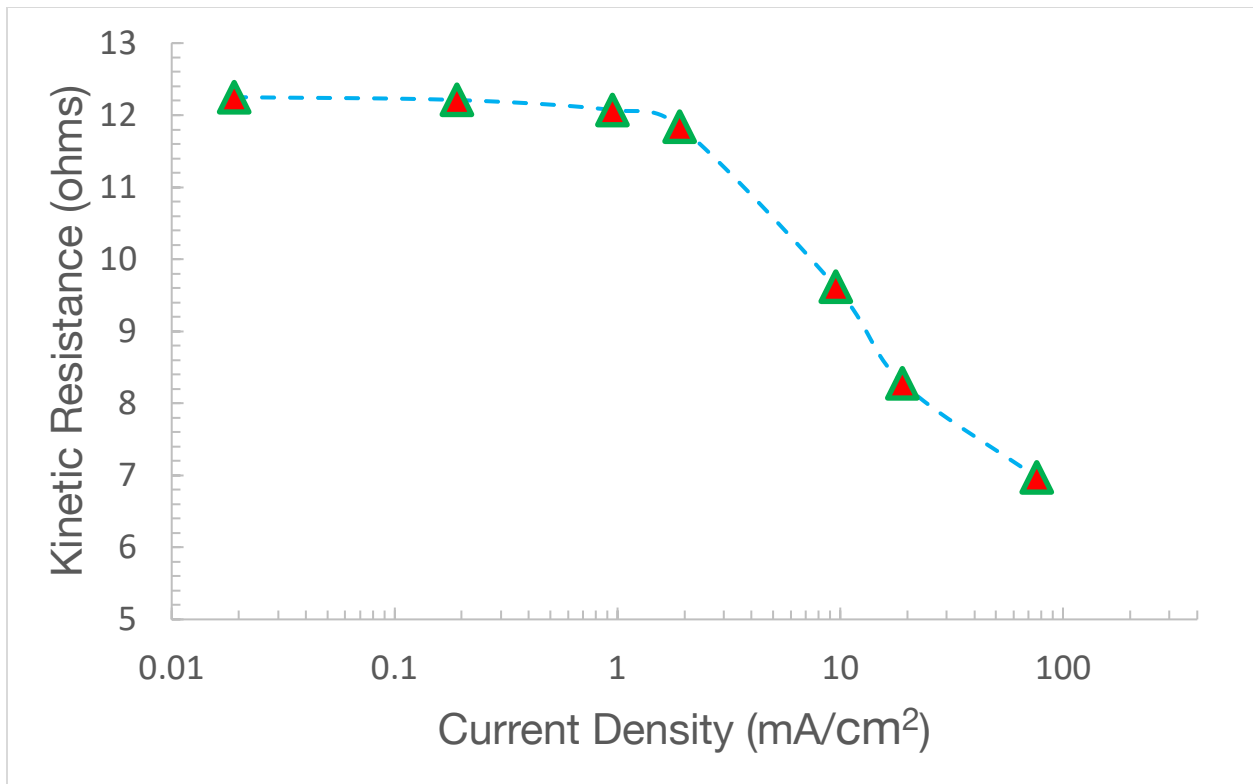


Figure 6.26 Kinetic Resistance of the Graphite Felt electrodes as a function of current density

## 15. Viscosity of Ethylene Carbonate and Sodium Iodide Solutions

The viscosity of the ethylene carbonate and sodium iodide solutions was measured at 25°C using a standard parallel plate rheometer on TA instrument's HR-20. The mixtures remain approximately Newtonian for both high and low shear regimes (10-500s<sup>-1</sup>). Pure ethylene carbonate at its melting point (36.4°C) has a viscosity of  $2.0 \times 10^{-3}$  Pa\*s, which is roughly 10x lower than the viscosity of the most concentrated solution. Moreover, the concentrated solution is approximately 25x more viscous than pure water at the equivalent temperature. Thus, the hydraulic losses in a traditional electro dialysis stack will be much larger for the same flow rate and channel size. The relatively high viscosity of the EC/NaI mixture will likely move the minimum channel thickness, which is usually about 200µm for salt water, to larger values, and will therefore lead to higher electrical losses.

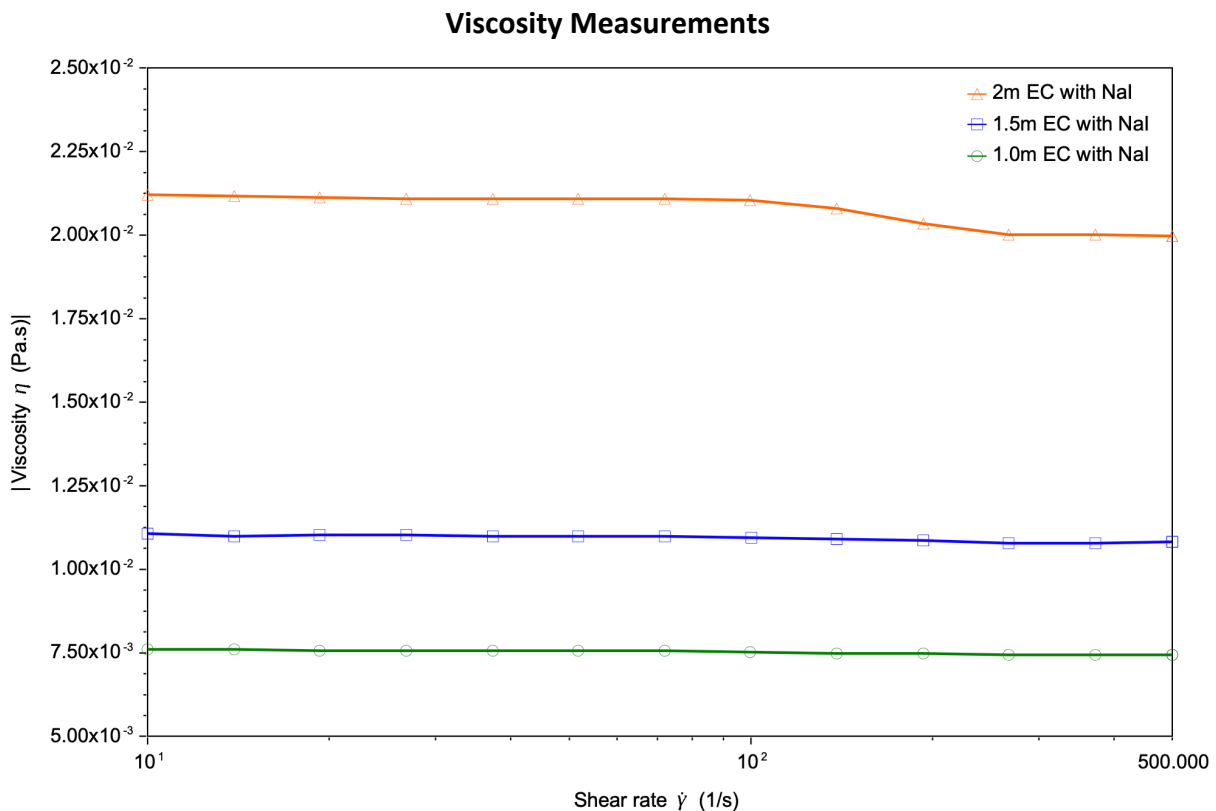


Figure 6.27 Viscosity of Ethylene Carbonate as a function of shear rate taken at 25 degrees celsius for 1m, 1.5m and 2m concentrations

## 16. Cyclic Voltammetry of Electrode Rinse

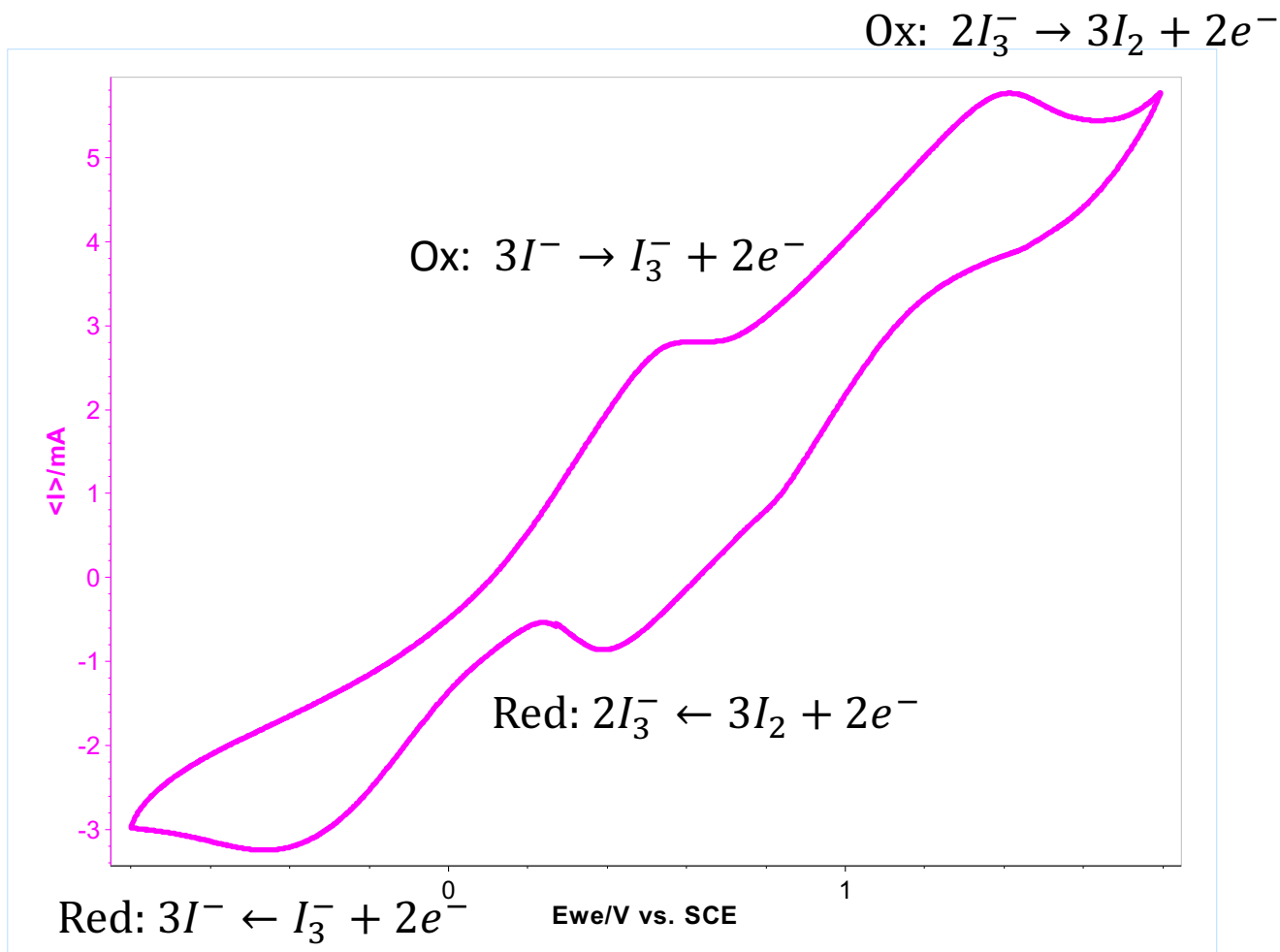


Figure 6.28. Cyclic Voltammetry of Ethylene Carbonate and sodium iodide + triiodide system, showing reversible reactions.

To understand the electrode reactions more thoroughly, cyclic voltammetry was performed on the electrode rinse solution (0.5m NaI<sub>3</sub>, 1.5m NaI). Conductive graphite rods were used as the working and counter electrodes (~1cm<sup>2</sup> of exposed area for the working electrode), and a saturated calomel electrode was used as the reference. The plot above shows the cyclic voltammogram for the solution at the scan rate of 20  $\frac{mV}{s}$ . Two pairs of oxidation/reduction peaks were observed in the CV curves. The first reduction/oxidation peak pair corresponds to the oxidation and reduction of  $I^-/I_3^-$ , described by:



The nearly identical integral area of the redox pair in the CV indicates excellent reversibility for the redox reaction. The second reduction/oxidation peak corresponds to the oxidation and reduction of  $I_3^-/I_2$  :



This reaction is less reversible, as the iodine solid that forms upon triiodide oxidation is electrically insulating, and dissolution back into the ethylene carbonate, and subsequently recombination with an iodide ion to re-form triiodide, is sluggish. This is captured in the asymmetry of the redox peaks. The increase in current density following the oxidation and reduction peaks, as opposed to the asymptotic decrease typical of aqueous solutions, is indicative of slow ion diffusion. Because the ionic conductivity of the electrode rinse is about 10-20 times smaller  $\sim 16,660 \frac{\mu S}{cm}$ , this is expected.

## 17. Uncertainty Analysis of Results

In this chapter we report on ethylene carbonates  $\Delta S_{isothermal}$ ,  $\Delta T_{adiabatic}$ ,  $\eta_{relative\ carnot}$ , and power density.  $\Delta S_{isothermal} = \frac{\Delta H_{sl}}{T_m}$ . We got values for both from a NIST database, and validated the NIST data on our own differential scanning calorimetry. Our DSC is rated for an accuracy of  $\pm 0.01\%$  on enthalpy measurements, but from experience we'll be conservative as we can typically reproduce NIST data to within about 1.5%. The accuracy of  $T_m$  is rated to be  $\pm 0.01^\circ C$ , but again we'll be conservative and say it's about  $\pm 0.1^\circ C$ . This makes the uncertainty of  $\Delta S_{isothermal} \approx \pm 4 \frac{J}{kg \cdot K}$ .  $\Delta T_{adiabatic}$  was measured directly via large scale calorimetry with k-type thermocouples that had  $\pm 0.1^\circ C$  accuracy.

COP calculations were made from experimental data,  $COP = \frac{Q_{cold}}{W_{in}}$ .  $Q_{cold}$  was measured directly from calorimetry with  $\pm 1.5\%$  accuracy, and  $W_{in}$  was measured by integrating the IV curve of a potentiostat. The potentiostat we used was high-precision (intended for battery research), with both  $\pm 10 \mu V$  and  $\pm 0.1 mA$ . Nominal power in was on the order of 1W, so the uncertainty in  $W_{in}$  is negligible compared to the uncertainty of  $Q_{cold}$ . Thus, the uncertainty of the COP is approximately  $\pm 1.5\%$  of the reported values. Likewise, the power density reported in Figure 6.5c was calculated by dividing  $\frac{Q_{cold}}{t}$ . The uncertainty in experimental time was negligible relative to the 1.5% uncertainty of  $Q_{cold}$ , so the power output also carries an uncertainty of about 1.5%.

## Nomenclature

Symbol	Meaning
S	Entropy
P	Pressure
T	Temperature
$\mu$	Electrochemical potential
$C_{p,\mu}$	Constant pressure / electrochemical potential heat capacity
$\Delta T_{adiabatic}$	Adiabatic Temperature Change
$d\Phi$	Differential of governing thermodynamic function
n	Molar quantity
$\Delta S_{isothermal}$	Isothermal Entropy Change
$\Delta T_{max}$	Maximum adiabatic temperature change possible for a given ionocaloric material
$\Delta H_{sl}$	Enthalpy of fusion of pure ionocaloric material
$C_p$	Constant pressure heat capacity
$k_f$	Cryoscopic constant
R	Ideal Gas Constant
M	Molar Mass of ionocaloric material
$T_{m,o}$	Melting point of pure ionocaloric material
$\Delta T_D$	Melting Point Depression
$i$	Van't Hoff factors
[m]	molality
H	System enthalpy
h	Enthalpy per unit mass
m	Mass
$\chi$	Mass fraction
$\chi_o$	Solubility limit of salt in solid phase (mass fraction)
$\varrho_m$	Mass fraction of salt before the mixer to calculate adiabatic temperature change
$\varrho_s$	Mass fraction of the salt after separation in the electro dialysis
$\varrho_{liq}$	Mass fraction of salt at liquidous temperature
$\phi_m$	Phase fraction (mass fraction) of the solid phase
$\Delta H_{mix}$	Enthalpy of mixing of ionocaloric solution
$T_{liq}$	Liquidus temperature of the ionocaloric solution at a given salt concentration
$T_{start}$	The temperature at which the ionocaloric solution is at before being mixed
$C_{p,s}$	Constant pressure heat capacity of the solid phase of the ionocaloric material
$C_{p,l}$	Constant pressure heat capacity of the liquid phase of the ionocaloric material
$T_f$	Final temperature of the ionocaloric mixture after mixing
$\gamma$	Activity coefficient
$T_h$	Hot side temperature of refrigeration cycle
$T_c$	Cold Side temperature of refrigeration cycle
$Q_c$	Heat absorbed on the cold side of the refrigeration cycle
$Q_h$	Heat rejected by the hot side of the refrigeration cycle
$W_{in}$	Work input to the refrigeration cycle
COP	Coefficient of Performance
$\Delta C_{p,s \rightarrow L}$	Different in heat capacities between the solid and liquid phases of the ionocaloric material
$\Delta S_{isocomp}$	Isocompositional entropy change
$Q(\chi)$	Heat flux measured by DSC at different concentrations
$T'(t)$	Heating rate in DSC
$T_o$	Reference temperature
$\Delta S_{ionocaloric}$	Ionocaloric Entropy Change

$\Delta T_{span}$	Difference between hot side and cold side temperatures in the refrigeration cycle
-------------------	-----------------------------------------------------------------------------------

*Table 6.5 Symbols and associated meanings used throughout this chapter*

## References

- <sup>1</sup> J. Lau, J.K. Papp, D. Lilley, P. Khomein, S. Kaur, C. Dames, G. Liu, and R. Prasher, *Cell Reports Phys. Sci.* **2**, 100613 (2021).
- <sup>2</sup> IEA, *Futur. Cool. Oppor. Energy-Efficient Air Cond.* 92 (2018).
- <sup>3</sup> G.J.M. Velders, D.W. Fahey, J.S. Daniel, M. McFarland, and S.O. Andersen, *Proc. Natl. Acad. Sci. U. S. A.* **106**, 10949 (2009).
- <sup>4</sup> L.T. Biarreau, L.W. Davis, P. Gertler, and C. Wolfram, *Nat. Sustain.* **3**, 25 (2020).
- <sup>5</sup> M.O. McLinden, J.S. Brown, R. Brignoli, A.F. Kazakov, and P.A. Domanski, *Nat. Commun.* **8**, (2017).
- <sup>6</sup> D. Behringer, F. Heydel, B. Gschrey, S. Osterheld, W. Schwarz, K. Warncke, F. Freeling, K. Nödler, S. Henne, S. Reimann, M. Blepp, W. Jörß, R. Liu, S. Ludig, I. Rüdener, and S. Gartiser, *Persistent Degradation Products of Halogenated Refrigerants and Blowing Agents in the Environment : Type , and Fate with Particular Regard to New Halogenated Substitutes with Low Global Warming Potential* (2021).
- <sup>7</sup> M.O. McLinden, C.J. Seeton, and A. Pearson, *Science (80-. )*. **370**, 791 (2020).
- <sup>8</sup> A. Kitanovski, U. Plaznik, U. Tomc, and A. Poredoš, *Int. J. Refrig.* **57**, 288 (2015).
- <sup>9</sup> A. Greco, C. Aprea, A. Maiorino, and C. Masselli, *Int. J. Refrig.* **106**, 66 (2019).
- <sup>10</sup> P. Lloveras and J.-L. Tamarit, *MRS Energy Sustain.* (2021).
- <sup>11</sup> A. Chauhan, S. Patel, R. Vaish, and C.R. Bowen, *MRS Energy Sustain.* **2**, (2015).
- <sup>12</sup> A. Torelló, P. Lheritier, T. Usui, Y. Nouchokgwe, M. Gérard, O. Bouton, S. Hirose, and E. Defay, *Science (80-. )*. **370**, (2020).
- <sup>13</sup> X. Qian, D. Han, L. Zheng, J. Chen, M. Tyagi, Q. Li, F. Du, S. Zheng, X. Huang, S. Zhang, J. Shi, H. Huang, X. Shi, J. Chen, H. Qin, J. Bernholc, X. Chen, L.Q. Chen, L. Hong, and Q.M. Zhang, *Nature* **600**, 664 (2021).
- <sup>14</sup> C. Aprea, A. Greco, A. Maiorino, and C. Masselli, *Energy* **165**, 439 (2018).
- <sup>15</sup> Y. Meng, Z. Zhang, H. Wu, R. Wu, J. Wu, H. Wang, and Q. Pei, *Nat. Energy* **5**, 996 (2020).
- <sup>16</sup> N.R. Ram, M. Prakash, U. Naresh, N.S. Kumar, T.S. Sarmash, T. Subbarao, R.J. Kumar, G.R. Kumar, and K.C.B. Naidu, *J. Supercond. Nov. Magn.* **31**, 1971 (2018).
- <sup>17</sup> R. Ma, Z. Zhang, K. Tong, D. Huber, R. Kornbluh, Y.S. Ju, and Q. Pei, *Science (80-. )*. **357**, 1130 (2017).
- <sup>18</sup> D. Lilley and R. Prasher, (n.d.).
- <sup>19</sup> I.S. McKay, L.Y. Kunz, and A. Majumdar, *Sci. Rep.* **9**, 1 (2019).
- <sup>20</sup> A. Rajan, I.S. McKay, and S.K. Yee, *Nat. Energy* **7**, 320 (2022).
- <sup>21</sup> John R. Rumble, *CRC Handbook of Chemistry and Physics*, 102nd ed. (CRC Press/Taylor & Francis, Boca Raton, FL, 2021).
- <sup>22</sup> S.G. Lu, B. Rožič, Q.M. Zhang, Z. Kutnjak, R. Pirc, M. Lin, X. Li, and L. Gorny, *Appl. Phys. Lett.* **97**, 202901 (2010).
- <sup>23</sup> B. Li, Y. Kawakita, S. Ohira-Kawamura, T. Sugahara, H. Wang, J. Wang, Y. Chen, S.I. Kawaguchi, S. Kawaguchi, K. Ohara, K. Li, D. Yu, R. Mole, T. Hattori, T. Kikuchi, S. ichiro Yano, Z. Zhang, Z. Zhang, W. Ren, S. Lin, O. Sakata, K. Nakajima, and Z. Zhang, *Nature* **567**, 506 (2019).

- <sup>24</sup> V.K. Pecharsky and K.A. Gschneidner, *Phys. Rev. Lett.* **78**, 4494 (1997).
- <sup>25</sup> D. Cong, W. Xiong, A. Planes, Y. Ren, L. Mañosa, P. Cao, Z. Nie, X. Sun, Z. Yang, X. Hong, and Y. Wang, *Phys. Rev. Lett.* **122**, 255703 (2019).
- <sup>26</sup> A. Torelló and E. Defay, *Adv. Electron. Mater.* **8**, (2022).
- <sup>27</sup> L. Mañosa and A. Planes, *Appl. Phys. Lett.* **116**, (2020).
- <sup>28</sup> J. Lyubina, *J. Phys. D: Appl. Phys.* **50**, 53002 (2017).
- <sup>29</sup> H. Hou, S. Qian, and I. Takeuchi, *Nat. Rev. Mater.* **7**, 633 (2022).
- <sup>30</sup> Z. Li, Z. Li, D. Li, J. Yang, B. Yang, Y. Hu, D. Wang, Y. Zhang, C. Esling, X. Zhao, and L. Zuo, *Acta Mater.* **192**, 52 (2020).
- <sup>31</sup> A.T. Bouma and J.H. Lienhard, *Desalination* **445**, 280 (2018).
- <sup>32</sup> A. Campione, L. Gurreri, M. Ciofalo, G. Micale, A. Tamburini, and A. Cipollina, *Desalination* **434**, 121 (2018).
- <sup>33</sup> S.K. Patel, P.M. Biesheuvel, and M. Elimelech, *ACS ES&T Eng.* **1**, 851 (2021).
- <sup>34</sup> H. Strathmann, *Desalination* **264**, 268 (2010).
- <sup>35</sup> F. Greibich, R. Schwödauer, G. Mao, D. Wirthl, M. Drack, R. Baumgartner, A. Kogler, J. Stadlbauer, S. Bauer, N. Arnold, and M. Kaltenbrunner, *Nat. Energy* **6**, 260 (2021).
- <sup>36</sup> F. Bruederlin, H. Ossmer, F. Wendler, S. Miyazaki, and M. Kohl, *J. Phys. D: Appl. Phys.* **50**, 424003 (2017).
- <sup>37</sup> S. Jacobs, J. Auringer, A. Boeder, J. Chell, L. Komorowski, J. Leonard, S. Russek, and C. Zimm, in *Int. J. Refrig.* (Elsevier, 2014), pp. 84–91.
- <sup>38</sup> P. Clot, D. Viallet, F. Allab, A. Kedous-Lebouc, J.M. Fournier, and J.P. Yonnet, *IEEE Trans. Magn.* **39**, 3349 (2003).
- <sup>39</sup> U. Plaznik, M. Vrabelj, Z. Kutnjak, B. Malič, B. Rožič, A. Poredoš, and A. Kitanovski, *Int. J. Refrig.* **98**, 139 (2019).
- <sup>40</sup> Ž. Ahčin, S. Dall'Olio, A. Žerovnik, U.Ž. Baškovič, L. Porenta, P. Kabirifar, J. Cerar, S. Zupan, M. Brojan, J. Klemenc, and J. Tušek, *Joule* **2338** (2022).
- <sup>41</sup> J. Newman and K.E. Thomas-Alyea, *Electrochemical Systems* (John Wiley & Sons, 2012).
- <sup>42</sup> J.F.L. P.J. Linstrom and W.G. Mallard James S. Chickos, William E. Acree, Jr., *NIST Chemistry WebBook, NIST Standard Reference Database Number 69, Heat of Fusion Data* (n.d.).
- <sup>43</sup> E.R. Logan, E.M. Tonita, K.L. Gering, L. Ma, M.K.G. Bauer, J. Li, L.Y. Beaulieu, and J.R. Dahn, *J. Electrochem. Soc.* **165**, A705 (2018).
- <sup>44</sup> G. Pistoia, M. De Rossi, and B. Scrosati, *J. Electrochem. Soc.* **117**, 500 (1970).
- <sup>45</sup> G. Della Gatta, M.J. Richardson, S.M. Sarge, and S. Stølen, in *Pure Appl. Chem.* (De Gruyter, 2006), pp. 1455–1476.
- <sup>46</sup> G. Höhne, J.L. McNaughton, W. Hemminger, H.-J. Flammersheim, and H.-J. Flammersheim, *Differential Scanning Calorimetry* (Springer Science & Business Media, 2003).
- <sup>47</sup> T. Kousksou, A. Jamil, Y. Zeraoui, and J.-P. Dumas, *Chem. Eng. Sci.* **62**, 6516 (2007).
- <sup>48</sup> K.S. Pitzer and C.R.C. Press, *Activity Coefficients in Electrolyte Solutions* (CRC press Boca Raton, FL, 1991).
- <sup>49</sup> G. Porcari, K. Morrison, F. Cugini, J.A. Turcaud, F. Guillou, A. Berenov, N.H. Van Dijk, E.H. Brück, L.F. Cohen, and M. Solzi, *Int. J. Refrig.* **59**, 29 (2015).
- <sup>50</sup> Q. Zheng, S. Kaur, C. Dames, and R.S. Prasher, *Int. J. Heat Mass Transf.* **151**, 119331 (2020).
- <sup>51</sup> ISO, *Annu. B. OfASTM Stand.* **2008**, 17 (2008).
- <sup>52</sup> F. Wendler, H. Ossmer, C. Chluba, E. Quandt, and M. Kohl, *Acta Mater.* **136**, 105 (2017).

- <sup>53</sup> G. Zhang, Q. Li, H. Gu, S. Jiang, K. Han, M.R. Gadinski, M.A. Haque, Q. Zhang, and Q. Wang, *Adv. Mater.* **27**, 1450 (2015).
- <sup>54</sup> A. Serrano, M. Duran, J.L. Dauvergne, S. Doppiu, and E.P. Del Barrio, *Sol. Energy Mater. Sol. Cells* **220**, 110848 (2021).
- <sup>55</sup> N. Zhang, Y. Song, Y. Du, Y. Yuan, G. Xiao, and Y. Gui, *Adv. Eng. Mater.* **20**, 1800237 (2018).

## Chapter 7. Final Thoughts

It's been a wild ride, and I was incredibly fortunate to work alongside world-class scientists and engineers from every discipline. Over my PhD, I've collaborated with materials scientists, organic and polymer chemists, computational physicists, electrochemists, chemical engineers, bioengineers, and physicists from all sorts of backgrounds. The exposure I had to these various fields through them was instrumental in my studies as a student, and I cannot emphasize enough the massive role this special scientific soup had in forming my skillset and thought processes as a researcher. For this opportunity, I will be forever grateful.

Now, as my time as a student ends, I've got a few parting thoughts for the next generation that chooses to pick up the torch.

### *On Liquid Physics*

I spent a considerable time investigating the physics of the liquid state. I was new to the subject, and my first approach was naïve. I thought that because we have good descriptions of the solid and gas states, and that because the liquid state is intermediate between the two, we could somehow massage the two descriptions of the bounding states to describe the intermediate one. I can confidently say now that this is not a productive endeavor.

The problem is that we are used to describing energetics within a large condensed interacting system through a phonon spectrum. But to work with phonon spectra analytically, we need to make quite a few assumptions. For this reason, solid state physicists love their "gas" models. In the solid state, because the vibration amplitude is small, vibration amplitudes are generally harmonic and thus the phonon spectra can be diagonalized and each phonon mode treated as if it didn't interact with the others (e.g. phonons abstractly emulate the characteristics of an ideal gas). In liquids, vibration amplitudes are large so any attempt at using a gas model goes out the window. Without a non-interacting gas model describing a fundamental excitation, a physicist's analytical toolkit gets a whole lot smaller.

Likewise, when we treat actual gasses from a fundamental stat mech / excitation perspective, we generally rely on the fact that the interatomic potential between gas molecules is small relative to their kinetic energy, and thus we can simplify them as ideal gasses, or at least use simple virial expansions to describe denser gasses. In liquids, interactions are almost as strong as in solids, so we can't make use of this trick either.

Given the lack of a small parameter to exploit, it is of my opinion that further pursuit of the liquid state through a "phonon" picture will not prove effective. Our analytical toolkit for phonons is insufficient given the reality of the strongly interacting and highly anharmonic liquid state. There are generally two ways to describe a systems thermodynamics. The first is through the modelling of a partition function, which generally assumes independent coordinates for each atom. In a solid, this assumption is good because we can diagonalize the dynamics of the system and find independent eigen modes, and then use the eigen coordinates as the independent coordinates

in the solid state partition function. This is very effective and leads to famous results like the Debye or Einstein models.

In a gas, the momenta coordinates are inherently independent/decoupled, so again the partition function formulation is very effective, and leads to famous results like the Ideal gas or van der waals equation of state, Sackur-Tetrode equation, etc.

In a liquid, because there is no diagonalization/decoupling possible that would transform your physics into independent coordinates, the partition function approach is analytically intractable using any sort of lattice dynamical approach(although there are some clever ways it can be useful with molecular dynamics).

The second way you can describe the thermodynamics of your system is through fundamental excitations. If you can figure out how to describe the energetics of your system through simple energy counting, you've solved your system. In other words, if you can find some aspect of your system that represents a fundamental quanta of energy by which summing over every quanta in your system will give you your systems total energy, then your description of the system is complete. In solids, phonons are that excitation. In amorphous solids, locons/diffusons are partial-descriptions of that excitation.

In a liquid, it is my opinion that we simply haven't found that fundamental excitation yet. If someone more clever than myself can re-cast the dynamics of the liquid system into an excitation spectra that can be completely diagonalized, their name will sit next to Debye and Van Der Waals in the history of science. If I had to guess where that excitation spectra may be found, I would be inclined to look at whatever the motivating force is behind the local atomic re-arrangement that's occurring on the scale of the vibration frequency.

My thinking is thus: The energy contained in the atom of a solid is equal to that of an atom in a liquid at its melting point. Yet, the solid atom is confined to oscillate around a localized point that changes only over very large time scales. The liquid atom is not. It oscillates around its localized point, but that point moves at very small timescales. This movement of its center of oscillation gives it a larger effective amplitude, even though it's orbital interactions with the neighboring atoms hasn't changed whatsoever. It's rapidly changing its center of oscillation, because over the course of its vibration other atoms have moved positions, and its previous position now represents a higher energy state. Thus, to lower its energy, it "relaxes" into a new equilibrium position. If I had to guess, this "relaxation" energy could be somehow cast into a fundamental excitation. If someone could describe an atom's configurational space in terms of a discrete relaxation energy ladder, I'd think they'd be well on their way to a new description of the liquid state. The phonon picture doesn't have to get completely thrown out, but perhaps just appended.

### *On Thermal Energy Storage*

Overall, I'm very optimistic for what's in store for thermal energy storage over the next few years. The need for load shifting is clear, and I think both government and industry have fully embraced the value thermal storage offers for a fully renewable future. I went through the exercise in chapter 3 on the enthalpy maximization of a condensed phase transition to understand where I should focus my efforts regarding thermal storage, and it gave me some strong insights into what critical research needs might be left. In mechanical engineering, our first move when evaluating any problem is to look at the "reversible" or "ideal" limit. We ask "if I can build a perfect system according to thermodynamics, what would my numbers look like?" This tells us if something is feasible, and identifies target performance metrics, and areas that need to be focused on for improvement. In thermal energy storage, we don't really know how energy dense a material can be. Electrochemists have a very good sense of what the upper limit is. After attempting to come up with an upper limit for thermal storage, which admittedly is very approximate, I think I've convinced myself that some of the most common materials out there are already approaching the upper limit of thermal energy density. Water/ice for cold storage is ~33% of the limit I arrived at. Salt hydrates come close to that number as well, for higher temperatures. I just don't see any new materials being studied that will push the needle much further. For this reason, I think the most fruitful direction for thermal energy storage work is not in materials discovery for better energy density, but in system level modelling to better understand real world performance so that value in a given application is easy to assess and communicate.

Once the appropriate thermophysical characterizations are made on a material, there aren't many material level problems that need further research (besides verifying chemical stability). The biggest materials problem practitioners faced was regarding supercooling. After going the 9 rounds with supercooling during my PhD, I think there is more work to be done there. Especially in connecting the material level metastability properties into system level performance, which usually happens through finite element analysis. It would be great if someone can develop a program that connects the two. More materials level supercooling characterizations must be made first for that to be worthwhile though.

Thermochemical materials, such as the salt hydrates discussed in this thesis are very promising. They require a tremendous amount of engineering before they're ready to hit the shelves though. In addition, at the material level there's a lot of instability that needs to be investigated further. If I had to spend more time on these materials, I would very carefully carve out the equilibrium conditions for each thermochemical phase of interest. Then I would do intense system level transport modelling to ensure that the reactor never forces the material outside the equilibrium phase I'm utilizing in the system. I think this is the only way to ensure stability. Current research efforts in my opinion are missing this point. Stability studies are done in a TGA, and without specifying transport conditions they are difficult to make sense of at the reactor level. I think there needs to be a much stronger connection between the materials scientists doing these characterizations and the chemical/mechanical engineers that will ultimately design and built the storage systems.

Finally, the dissolved reactants in liquid heat transfer fluids presents an incredible opportunity. The design space is absolutely wide open for this field. One of the biggest challenges with thermochemical and phase change materials is just transporting the heat from the stored material to the downstream application. The diels-alder heat transfer fluids presented in chapter 5 solves this problem by always remaining in the liquid state, so that it may be pumped to the downstream application. We were unable to attain the highest theoretical energy density we predicted in that system because of materials problems at higher reactant concentrations. However, if we could have solved that, we would have been able to observe a 50-100% increase in thermal storage over water. That would be game changing, because right now using water's sensible heat is the most common mode of thermal storage across the world. Doubling that storage density by just dropping a few chemicals into the water could be potentially disruptive in many industries. We specifically focused on diels-alder reactants, but any reactant/product that remains soluble in a liquid would work. As a mechanical engineer, I have a limited knowledge on better opportunities in the chemical space for this application. We relied on chemists and DFT guys to suggest materials for screening. I very much hope that this work is continued, and that some chemist might identify greener pastures for this application.

#### *On Refrigeration:*

I have a lot of strong opinions on the research directions and various technologies being investigated for alternative zero-GWP refrigeration, so I'm going to try to use broad strokes here.

Regardless of how its done, I think refrigeration is incredibly difficult to do well and very easy to do poorly. There are many refrigeration cycles and concepts out there (can think of at least 10 off the top of my head), yet in any real-world application we really only use vapor compression (and absorption, but rarely). In my opinion, vapor compression is truly a marvel of engineering. It uses the liquid to vapor transition that has the largest entropy change of any thermodynamic process a material can go through. In addition, its' thermodynamic cycle is extremely Carnot-like so it's inherently efficient and operates using compressors that are highly efficient and power dense.

Many new research directions focus on solid state refrigeration using caloric (or ferroic) effects. My fundamental gripe with this research direction – beyond system level considerations – is that there is simply very little entropy in the solid state. In general, the higher the entropy change the material undergoes during the work input step of the cycle, the better the refrigeration cycle. There is much nuance in this statement though. The efficiency of a cycle is simply related to  $COP = \frac{T\Delta S}{W_{in}}$ . A lot of materials / caloric folks will argue that a small  $\Delta S$  is not a deal breaker, so long as it comes with a small  $W_{in}$  such that a high COP can still be achieved. **I'm going to quote the wise words of Professor Chris Dames here: small compared to what?** If  $W_{in}$  is small compared to  $\Delta S$ , sure we can have high efficiency with that material. *However, it must also be small compared to cycle losses.* Let's take a very simple example to understand why this is so important in real world applications.

Let's assume that a solid state caloric device is embedded in a recuperative cycle (only way it can operate efficiently), let's say a reverse Stirling cycle. Let's further assume that we are trying to maintain a temperature difference of  $40^{\circ}\text{C}$  between the hot and cold sides, which is typical in an air conditioning application, and we assume a heat capacity of the solid material to be  $2 \frac{\text{J}}{\text{g}\cdot\text{K}}$ , then we have  $80 \frac{\text{J}}{\text{g}}$  to recover in just the recuperator. If we assume a heat exchanger effectiveness of 0.9, which is on the very high end, then we get  $8 \frac{\text{J}}{\text{g}}$  lost. Now, if we look at the best caloric materials right now (minus plastic crystals using barocalorics), they get about  $\Delta S \approx 50 \frac{\text{J}}{\text{kg}\cdot\text{K}}$ , or at room temperature a  $\Delta H \approx 14 \frac{\text{J}}{\text{g}}$ . If we assume that the caloric refrigerator would have operated with a  $\text{COP} = 4$ , then the work input is  $W_{in} = 3.5$ . But now, with losses from the recuperator (even using a very good recuperator), we get  $\text{COP} = \frac{\Delta H - \Delta H_{recup}}{W_{in}} = \frac{14 - 8}{3.5} = 1.7$ . In contrast, vapor compression usually sees  $\Delta S$  on the order of 500-1000  $\frac{\text{J}}{\text{kg}\cdot\text{K}}$ , or a  $\Delta H$  of about  $200 \frac{\text{J}}{\text{g}}$ . Let's say we're maintaining a COP of 4 as well. That means the work input is about  $50 \text{ J/g}$ . If we assume the same losses incurred as in the caloric case, we get  $\text{COP} = \frac{200 - 8}{50} = 3.84$ . The vapor compression cycle is barely affected by these losses!

In my opinion, this is why having a high entropy change is so incredibly important for new refrigeration cycles. Low entropy change materials might have high theoretical efficiencies, because the work input is proportional to the entropy change, but at the system level you absolutely need high entropy changes to soak up minor system losses.

The only solid state effect to have an impressive entropy change is the barocaloric effect, utilizing plastic crystals (NPG). This is not surprising to me, because NPG changes from a low entropy solid phase to what is essentially a liquid. I've worked quite a bit with NPG, and the high temperature phase almost appears "wet" – it's as close to a liquid as a solid can get. For this reason, I can't imagine another material is going to come along with a substantially higher entropy change in the solid state, because the solid state simply doesn't have much entropy to give.

This is why we chose to focus on the solid to liquid transition – it is the only other transition that has commensurate entropy changes to current liquid/vapor refrigerants today.

Now my second strong opinion: I think the real opportunity for new disruptive refrigeration technologies lies in heat pumping – not necessarily in air conditioning/cooling. The vapor compression cycle is incredible at cooling and heat pumping near room temperature, where temperature differences never really exceed  $50 - 60^{\circ}\text{C}$ . However, for heat pumping applications in industry where temperature differences easily reach  $100 - 200^{\circ}\text{C}$ , vapor compression has a huge Achilles heel, which is baked right into the physics of the liquid to vapor transition.

In the vapor compression cycle, temperature spans are determined by pressure ratios between the liquid in the evaporator and the vapor exiting the compressor. Thus, the temperature span is limited by a compressor's pressure-ratio constraints. The pressure ratio needed is determined by the refrigerant-specific liquid-vapor dome. For most refrigerants and compressors, this limits the temperature span in vapor compression to about  $60^{\circ}\text{C}$  (can flex up to 80 with select refrigerants and oil-injected/specialized compressors). The vapor compression cycle becomes increasingly more inefficient as temperature spans increase because the change in saturation temperature with respect to the change in pressure ratio,  $\frac{dT_s}{dP_{ratio}}$  increases with increasing saturation temperature, partly due to the concavity of the vapor dome. Thus, as the temperature span increases, each additional degree increase requires a larger increase in pressure ratio. As an illustration, R410a would require a pressure ratio of about 14 at an evaporation temperature of  $-40^{\circ}\text{C}$  and a condensing temperature of  $40^{\circ}\text{C}$ . If the evaporation temperature instead were  $-30^{\circ}\text{C}$ , the compression ratio needed drops to about 8, which is about a 42% decrease from that which was required for  $-40^{\circ}\text{C}$ . An additional  $10^{\circ}\text{C}$  increase such that it evaporates at  $-20^{\circ}\text{C}$  requires a pressure ratio of 6, or a 25% decrease.

This leads to inefficiencies at high temperature spans in the vapor compression cycle because the pressure ratio is directly related to the irreversibility within the compressor. Specifically, as pressure ratio increases, both expansion losses and superheating losses increase (which have a power law relationship with pressure ratio), so if the pressure ratio increases with increasing temperature span, so too will the losses and therefore inefficiency.

Given this relationship with temperature span, vapor compression refrigerants see second law efficiencies that monotonically decrease with temperature span, and suffer greatly at temperature spans nearing  $60^{\circ}\text{C}$ . This is where I see the real opportunity for disruptive refrigeration cycles.

In the ionocaloric cycle, for example, the temperature span is controlled by the concentration difference of ions in the ionocaloric material, or its' binary solid-liquid temperature-composition (T-x) diagram. Most T-x phase equilibria curves have an increasing slope with respect to concentration. This provides the opposite outcome to vapor compression. As the temperature span increases, the concentration difference needed to increment the temperature span further decreases. The inefficiencies in vapor compression are tied to the compression ratio; the inefficiencies in the ionocaloric cycle are tied to the concentration differences needed. Thus, as the temperature span gets larger, and the concentration difference needed to increment the temperature span gets smaller, the inefficiency of the ionocaloric cycle gets smaller with increasing temperature. This makes it uniquely suited for these high temperature lift applications, because its isentropic efficiency reaches its' peak at its' highest temperature span operation (Figure 7.1).

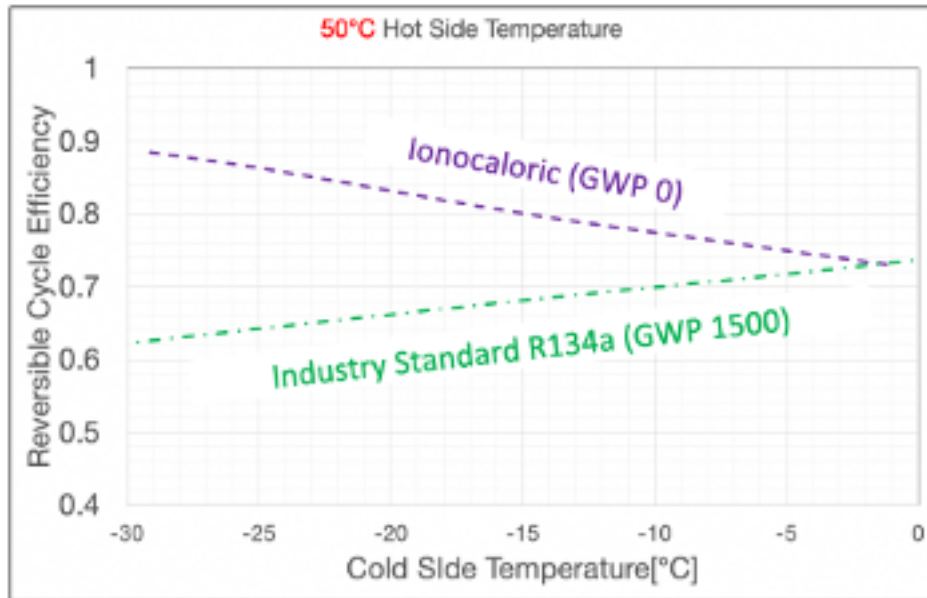


Figure 7.1 Efficiency vs temperature span of vapor compression vs ionocaloric cycle

**And with that, I conclude my thesis!**

